

**FABRICATION AND MODIFICATION OF DEFECTS IN $\text{Cu}_2\text{ZnSnSe}_4$
SINGLE CRYSTALS AND THIN FILMS**

by

Douglas M. Bishop

A dissertation submitted to the Faculty of the University of Delaware
in partial fulfillment of the requirements for the degree of Doctor of Philosophy
in Materials Science and Engineering

Spring 2016

© 2016 Douglas Bishop
All Rights Reserved

ProQuest Number: 10156470

All rights reserved

INFORMATION TO ALL USERS

The quality of this reproduction is dependent upon the quality of the copy submitted.

In the unlikely event that the author did not send a complete manuscript and there are missing pages, these will be noted. Also, if material had to be removed, a note will indicate the deletion.



ProQuest 10156470

Published by ProQuest LLC (2016). Copyright of the Dissertation is held by the Author.

All rights reserved.

This work is protected against unauthorized copying under Title 17, United States Code
Microform Edition © ProQuest LLC.

ProQuest LLC.
789 East Eisenhower Parkway
P.O. Box 1346
Ann Arbor, MI 48106 - 1346

**FABRICATION AND MODIFICATION OF DEFECTS IN $\text{Cu}_2\text{ZnSnSe}_4$
SINGLE CRYSTALS AND THIN FILMS**

by

Douglas M. Bishop

Approved: _____
Darrin Pochan, Ph.D.
Chair of the Department of Materials Science and Engineering

Approved: _____
Babatunde Ogunnaike, Ph.D.
Dean of the College of Engineering

Approved: _____
Ann L. Ardis, Ph.D.
Senior Vice Provost for Graduate and Professional Education

I certify that I have read this dissertation and that in my opinion it meets the academic and professional standard required by the University as a dissertation for the degree of Doctor of Philosophy.

Signed:

Robert Birkmire, Ph.D.
Professor in charge of dissertation

I certify that I have read this dissertation and that in my opinion it meets the academic and professional standard required by the University as a dissertation for the degree of Doctor of Philosophy.

Signed:

William Shafarman, Ph.D.
Member of dissertation committee

I certify that I have read this dissertation and that in my opinion it meets the academic and professional standard required by the University as a dissertation for the degree of Doctor of Philosophy.

Signed:

Robert Opila, Ph.D.
Member of dissertation committee

I certify that I have read this dissertation and that in my opinion it meets the academic and professional standard required by the University as a dissertation for the degree of Doctor of Philosophy.

Signed:

Joshua Zide, Ph.D.
Member of dissertation committee

I certify that I have read this dissertation and that in my opinion it meets the academic and professional standard required by the University as a dissertation for the degree of Doctor of Philosophy.

Signed:

Meijun Lu, Ph.D.
Member of dissertation committee

I certify that I have read this dissertation and that in my opinion it meets the academic and professional standard required by the University as a dissertation for the degree of Doctor of Philosophy.

Signed:

Brian McCandless,
Member of dissertation committee

ACKNOWLEDGMENTS

Every large accomplishment takes a team. Four groups of people made this document possible: staff at the IEC, staff at IBM, my committee, advisor and mentor, and my friends and Family. First, thanks to my committee for agreeing to read this thing and being supportive and available throughout the process. To my advisor Bob Birkmire for making sure I had a salary, and having faith in me from day one. Bob was always available and truly cared about my wellbeing and that of all of his students. Without him and the IEC, I would not be here.

Special thanks to Brian McCandless who was been a fantastic mentor and project lead for most of my graduate research. He has taught me so much both professionally and personally and I feel blessed to carry some of his philosophy and knowledge into my future work and life. Brian brings unique detailed lab wisdom which can't be purchased or read in a book, with theoretical approach of understanding fundamentals and thermodynamics which can only be gathered through reading hundreds of books. Brian trained me, had faith in me, and enabled me to think and work independently. This work is truly half his. He's been a mentor and a good friend.

Lastly, thanks to Mike Lloyd, who has been great to work with, teach, and learn from. Mike is one of the few in the world who has read more than a few pages of this document and actually offered feedback for more than half the pages. He has helped me think by asking tough questions, and challenging assumptions and while are perspectives are not always the same, he brings some balance to my work.

Without the PV team at IBM, this work would certainly not have happened. Since beginning our collaboration only two and a half years ago, they have been imparted direction, knowledge, enthusiasm, and opportunities and new avenues for our research. They have been open to share, willing to train, and inspiring to work with. The four months I spent working at IBM were some of the most productive time of PhD research – although a large part of the work accomplished has been left out this document. Thanks to Priscilla for being a great work partner and helping with back contact passivation and hundreds of exfoliated devices. Thanks to Talia Gershon for training me on photoluminescence, collaborating on numerous publications, and generally giving me an example of what a good young researcher is supposed to do. Thanks to Oki Gunawan for being an equipment wizard and for always being willing to talk and train you about his latest measurement tool. I can't thank Rich Haight enough for allowing and encouraging me to come up to IBM to work, and then after all that, still wanting me to return and helping make sure I got a job. To Yun Seog Lee, Ravin Mankad, and Saurabh Singh for helping with depositions and getting me into the labs when my ID didn't work. Also special thanks to David Mitzi for providing a great example of what a well led project looks like.

At the IEC, thanks to Shannon Fields for helping make the stuff that makes the stuff. It's hard to count all of the places he was involved, but most recently, his furnace building and programming that was central to making crystals. Thanks to John Elliot for teaching me vacuum depositions and repairs, and being always willing to brainstorm new crazy ideas. Also, thanks to Kevin Hart for providing Mo and device depositions for my early thin film work. Thanks to Roddel Remy in the Mackay lab for the training and assistance with TGA experiments used in this work.

Life requires balance, and while the above people helped get the work done, my friends and family supported the other half of my life – without which, I would have run away from this PhD journey long ago. To my Mom, for being a rock, to my dad, for being always interested, and to my brothers Mike, Matt and Odei for inspiring through their examples every day. And thanks to all of the support crew who will go unmentioned and among them: Andre, Mark, Mark, Tucker and Jordan. You guys are the best.

Funding Sources

Thanks to DOE SunShot Initiative for funding portions of this work on fabrication and characterization of single crystals in collaboration with IBM. Special thanks to Dupont for funding me for the first 3 years of my tenure at the IEC through the Dupont Photovoltaic Fellowship. That work is mainly summarized in Chapter 5.

Acknowledgment: The information, data, or work presented herein was funded in part by the U.S. Department of Energy, Energy Efficiency and Renewable Energy Program, under Award Number DE-EE0006334.

Disclaimer: The information, data, or work presented herein was funded in part by an agency of the United States Government. Neither the United States Government nor any agency thereof, nor any of their employees, makes any warranty, express or implied, or assumes any legal liability or responsibility for the accuracy, completeness, or usefulness of any information, apparatus, product, or process disclosed, or represents that its use would not infringe privately owned rights. Reference herein to any specific commercial product, process, or service by trade name, trademark, manufacturer, or otherwise does not necessarily constitute or imply its endorsement, recommendation, or favoring by the United States Government or any agency thereof. The views and opinions of authors expressed herein do not necessarily state or reflect those of the United States Government or any agency thereof.

TABLE OF CONTENTS

LIST OF TABLES	xiv
LIST OF FIGURES	xv
LIST OF ABBREVIATIONS	xxii
ABSTRACT	xxiii

Chapter

1	INTRODUCTION	1
1.1	Motivation	1
1.2	Introduction to CZT(S,Se).....	4
1.3	Challenges with CZT(S,Se).....	5
1.3.1	Understanding Defects and Motivation for Single Crystals.....	8
1.4	Approach of This Work.....	9
2	FABRICATION OF SINGLE CRYSTALS	11
2.1	Abstract.....	11
2.2	Overview of Crystal Growth	12
2.2.1	Literature and Overview of Methods	13
2.2.1.1	Overview of Flux Growth Methods	18
2.3	Fabrication Methods	20
2.3.1	Summary of Below Melt Procedure	22
2.3.2	Summary of Above Melt Procedure.....	22
2.3.3	Comparison of Crystal Size.....	24
2.4	Growth Dynamics Above T_m	25
2.4.1	Crystals Above T_m	28
2.5	Growth Dynamics Below T_m	29

2.5.1	Summary of Growth Above and Below Melt.....	33
2.6	Variables and Optimization.....	34
2.6.1	Effect of Time.....	35
2.6.2	Effect of Temperature.....	37
2.6.3	Effect of Reaction Precursors.....	41
2.6.3.1	Form Factor of Elemental Precursors.....	41
2.6.3.2	ZnSe and Cu ₂ SnSe ₃ Precursors.....	42
2.6.4	Effect of Composition.....	43
2.6.4.1	Effect of Cu.....	44
2.6.4.2	Effect of Se.....	45
2.6.5	Achieved Compositions.....	47
2.6.6	Other Growth Variables.....	50
2.7	Summary.....	53
3	MODIFICATION OF DEFECTS IN Cu ₂ ZnSnSe ₄ SINGLE CRYSTALS.....	55
3.1	Abstract.....	55
3.2	Overview.....	55
3.2.1	Photoluminescence Background.....	60
3.3	Passivation.....	62
3.3.1	Natural Crystal Growth Surfaces.....	63
3.3.2	Polishing.....	65
3.3.3	Br Etching.....	66
3.3.4	Air Annealing.....	70
3.3.5	Alternative Passivation Methods: ZnSe Passivation Layer.....	74
3.3.6	Effects of CdS.....	76
3.3.7	Summary of Passivation.....	78
3.4	Stoichiometry.....	80
3.4.1	Overview.....	80
3.4.2	CZTSe Phase Diagram and Secondary Phases.....	81
3.4.3	Optimal Compositions and the Role of Defect Compensation in Multinary Solar Cells.....	82
3.4.4	Effect of Se Composition.....	84

3.4.5	Effect of Cu Composition.....	85
3.4.5.1	Hall Effect Measurements	85
3.4.5.2	Majority Carrier Transport	87
3.4.5.3	Effects of Cu Composition on PL	88
3.4.6	Conclusions and Summary of Stoichiometry	90
3.5	Dopants and Substitutions	91
3.5.1	Na	92
3.5.1.1	Na Solubility and Diffusion in Bulk CZTSe	92
3.6	Temperature Equilibria.....	95
3.6.1	Abstract.....	95
3.6.2	Introduction	96
3.6.3	Experimental Setup	99
3.6.4	Results	101
3.6.5	Discussion.....	108
3.6.5.1	Position of PL Peak	109
3.6.5.2	Shifting of PL Spectra	110
3.6.5.3	Peak Width and Peak Shape	110
3.6.6	Electrostatic Potential Fluctuations vs E_g -fluctuations.....	111
3.6.7	Conclusion.....	116
3.7	Progress in Single Crystal CZTSe Devices	118
3.8	Summary of Control of Defects	123
4	MODIFICATION OF DEFECTS IN THIN FILMS.....	126
4.1	Abstract.....	126
4.2	Overview	126
4.3	Fabrication Overview for IBM Thin Films	127
4.4	Passivation:.....	128
4.4.1	Effect of Br on Thin Films	128
4.4.2	Effect of CdS on Thin Films	131
4.5	Stoichiometry	133
4.5.1	Effect of Cu on Thin Films.....	133

4.5.2	Minority Carrier Lifetimes	137
4.5.2.1	Nature of PL Detector Saturation	137
4.5.2.2	Lifetime of Cu-poor and Stoichiometric Samples	141
4.5.3	Devices	142
4.5.4	Summary of Stoichiometry	143
4.6	Dopants and Substitutions in Thin Films	145
4.6.1	Effect of Na on Sub- E_g States	146
4.6.2	Ag Substitution	149
4.6.2.1	XRD of (Ag-Cu) ₂ ZnSnSe ₄ Alloy	149
4.6.2.2	Modeled XRD of Ag-Zn Anti-site	150
4.6.2.3	PL of (Ag-Cu) ₂ ZnSnSe ₄ Alloy	153
4.7	Temperature Equilibria Applied to Thin Films	155
4.7.1	Overview	155
4.7.2	Fabrication Methods	156
4.7.3	Photoluminescence	157
4.7.4	Capacitance-voltage	160
4.7.5	Device Results	162
4.7.6	Conclusions for Low-Temperature Annealed Devices	165
4.8	Single Crystal Champion Device Analysis and Comparison to Thin Films	166
4.8.1.1	Fill Factor and Series Resistance	167
4.8.1.2	Current and EQE	168
4.8.1.3	Capacitance-voltage and JV-Temperature Analysis ..	172
4.8.2	Conclusions and Paths Forward	175
5	THIN FILM FABRICATION BY CO-EVAPORATION: EFFECTS OF GROWTH CONDITIONS ON SECONDARY PHASES IN CZTSe	178
5.1	Overview of Work	178
5.2	Abstract	179
5.3	Introduction	180
5.4	Experimental	181
5.5	Results and Discussion	182
5.5.1	Decomposition during Film Cool-down	184

5.5.2	Decomposition at the Back Contact	186
5.6	Conclusions	190
5.7	Acknowledgements for thin film fabrication work	191
6	SUMMARY OF CONTRIBUTIONS	192
REFERENCES		195
Appendix		
A	SUMMARY OF PUBLICATIONS	211
B	CRYSTAL GROWTH	213
B.1	Decomposition of $\text{Cu}_2\text{ZnSnSe}_4$ and Cu_2SnSe_3 By Thermogravimetric Analysis (TGA)	213
B.2	Growth with $\text{ZnSe} + \text{Cu}_2\text{SnSe}_3$ Precursors.....	217
C	CHARACTERIZATION DETAILS	218
C.1	Summary of Characterization Equipment	218
C.2	Photoluminescence Spectra Power Calibrations	222
C.3	Photoluminescence Imaging.....	223
D	CALCULATION OF EQUILBRIUM DEFECT CONCENTRATIONS FOR QUENCH / SLOW-COOL CZTSe	225
E	MODELING PL EMISSION	228
E.1	Effects of E_g -Fluctuations on PL.....	228
E.1.1	Code for Modeling Bandgap Fluctuations:	230
E.2	Other PL Models	232
E.2.1	Change in PL Intensity with Temperature for Defect-related Transitions	232
E.2.2	PL Intensity for Band-Band Emission as a Function of Temperature.....	232
E.3	PL Intensities for Cu-poor and Near-Stoichiometric Thin Films	234
F	MODELING XRD OF AZTSe	235
F.1	Crystal structure of AZTSe	235

F.1.1	Separating Stannite and Kesterite in AZTSe by XRD	237
F.1.2	Identifying Ag-Zn Antisites in AZTSe by XRD	240
G	MODELING XRD OF V_{Cu} IN CZTSe	243
G.1	Cu-vacancies in CZTSe determined by XRD	243
H	THIN FILM DEPOSITION	247
H.1	Zn Source Design and Effusion Modeling	247
H.2	Substrate Temperature Uniformity	250
I	Permission, Copyright, and Reuse.....	252

LIST OF TABLES

Table 2-1: Solid state diffusivity of materials near the melt	13
Table 2-2: List of melting point and decomposition temperatures for relevant compounds.....	18
Table 2-3: Summary of growth variables	54
Table 3-1: Device parameters as a function of etch time	70
Table 3-2: Composition measurements of quenched and slow-cooled by XRF	102
Table 3-3: Hall measurements and device results on single crystals	106
Table 3-4: Device parameters for champion cells and improvements from processing.....	120
Table 4-1: Device results for Br etched films	131
Table 4-2: PL peak position and E_g extracted from QE for Cu-poor and stoichiometric thin films and single crystals	135
Table 4-3: Sample matrix for low temperature annealed thin films.....	156
Table 4-4: Composition of low-temperature annealed films.....	157
Table 4-5: Comparison of champion thin film and champion single crystal device..	166
Table 4-6: Series resistance contribution due to absorber thickness for single crystals and thin films.....	168
Table B-1: Summary of Decomposition Temperatures Measured by TGA.....	214
Table D-1: Modeled PL peak energy and PL rate from band to band emission	233

LIST OF FIGURES

Figure 1-1: Growth of solar and cost of solar panels	2
Figure 1-2: Potential solar energy from raw materials for common thin films.....	4
Figure 1-3: History of CZTS related publications and efficiency	5
Figure 1-4: Champion CZT(S,Se) IV curve and deficit to theoretical limit	7
Figure 1-5: Depiction of potential complexities in thin films	9
Figure 2-1: Schematic overview of select common bulk single crystal growth methods	15
Figure 2-2: Phase diagram of CZTSe.....	17
Figure 2-3: Vapor pressure curve for elements and relevant phases.....	17
Figure 2-4: Summary of steps in obtaining single crystal CZTSe.	22
Figure 2-5: Photos and XRF profile of boules fabricated above and below the melt.....	23
Figure 2-6: Distribution of crystal size above and below the melt.....	25
Figure 2-7: Temperature profile of samples quenched during above-melt growth....	26
Figure 2-8: Schematic of above melt growth dynamics.	27
Figure 2-9: Example of crystal obtained above the melt.....	29
Figure 2-10: Schematic of growth dynamics below melt.....	30
Figure 2-11: SEM image of crystal growth dynamics $<T_m$ showing role of CTSe.....	33
Figure 2-12: SEM image of typical single crystals and poly-crystals grown below the melt.	34
Figure 2-13: Crystal size as a function of time and resulting polycrystalline boules...	36

Figure 2-14: Temperature profile for temperature series and resulting polycrystalline boules	38
Figure 2-15: Effect of temperature on crystal size	39
Figure 2-16: Effect of temperature on crystal composition.....	40
Figure 2-17: Comparison of Zn precursors	42
Figure 2-18: Photos of ZnSe (A) and Cu ₂ SnSe ₃ (B) precursor ampoule, three mixed ZnSe/CTSe ampoules before CZTSe growth (C), and achieved CZTSe boule and composition profile by XRF.	43
Figure 2-19: Median crystal weight and distribution of crystal sizes as a function of Cu composition.....	44
Figure 2-20: Effect of excess Se on boules and phase distribution.	46
Figure 2-21: Crystal size as function of Se.	47
Figure 2-22: Summary of ampoule compositions explored by loaded elemental ratios	48
Figure 2-23: Composition of polished crystals by XRF compared to loaded elemental ratio	50
Figure 2-24: Photo of quenched ampoule and histogram of crystal size	52
Figure 2-25: Photos comparing ampoule size for 10 and 15 mm ampoules both with 10g of loaded elements.....	53
Figure 3-1: Depiction of defects in ideal solar cell and more complex conceptual picture facing multinary semiconductors such as CZTSe	58
Figure 3-2: Raman and optical and SEM images of as extracted crystals surfaces ...	63
Figure 3-3: PL image for various as-grown crystals	64
Figure 3-4: Photo of polished crystals mounted on polishing chuck after 0.03 μm alumina	66
Figure 3-5: Etch rate of Br-methanol for CZTSe and secondary phases.	67
Figure 3-6: Composition of crystal surface by XPS before and after Br-etch. Right: Raman signal of crystal before and after etching.	68

Figure 3-7: PL intensity as a function of Br etch time.	68
Figure 3-8: Effect of air anneal on PL intensity and energy.	72
Figure 3-9: Varied effects of AA on PL intensity	73
Figure 3-10: PL image and intensity of ZnSe/CZTSe.....	74
Figure 3-11: PL image of CdS coated crystal	78
Figure 3-12: Chemical potential single phase window for CZTS and CZTSe based on first principle calculations.	81
Figure 3-13: Defect energy level for V_{Cu} , Zn_{Cu} and $[V_{Cu}+Zn_{Cu}]$ compensated defect pair.....	84
Figure 3-14: Effect of low Se on PL intensity. PL image on right with four low Se crystals (top) and two reference crystals (bottom)	85
Figure 3-15: Effect of Cu on carrier concentration and mobility.....	87
Figure 3-16: Conductivity as a function of temperature for Cu-poor CZTSe single crystal with $Cu/(Zn+Sn) = 0.90$, and near-stoichiometric with $Cu/(Zn+Sn) = 0.99$ CZTSe single crystal.....	88
Figure 3-17: PL image and PL pseudo-spectra of Cu-poor and near stoichiometric single crystals.	89
Figure 3-18: Diffusion profile of Na in CZTSe single crystal after 6 hours annealing at $420^{\circ}C$	94
Figure 3-19: Raman spectra of slow-cooled and fully quenched CZTSe crystals.	103
Figure 3-20: XRD of powder from single crystals slow-cooled or quenched at $300^{\circ}C$ or $500^{\circ}C$ at the $[400]$, $[008]$ peaks.	104
Figure 3-21: PL intensity for samples quenched $500^{\circ}C$, $300^{\circ}C$ and slow-cooled to room temperature.	107
Figure 3-22: PL spectra at 5K for Set 1 of quenched and slow-cooled crystals. A) slow-cooled crystal, B) quenched crystal, C) normalized peak width and FWHM at full laser intensity, D) Position of peak as function of laser intensity for crystals.....	108

Figure 3-23: Depiction of defects and potential recombination for different cases of CZTSe.	114
Figure 3-24: History of single crystal champion device efficiency and key concepts enabling improvements	119
Figure 3-25: JV curve for champion 7.8% single crystal device and photo of other device for area correction	121
Figure 3-26: EQE curves for current champion single crystal and older devices.	123
Figure 4-1: PL intensity of Br-etched films..	129
Figure 4-2: SEM images of Br-etched films (in-lens detector).....	130
Figure 4-3: Effect of CdS on PL intensity. PL intensity of bare CZTS films after AA and the same films after CdS deposition.	132
Figure 4-4: Effect of Cu on PL image intensity and PL spectra	134
Figure 4-5: PL emission at 4K for stoichiometric and Cu-poor samples	136
Figure 4-6: PL spectra and lifetime in log scale as a function of wavelength showing correlation of lifetime with detector saturation.....	138
Figure 4-7: PL spectra of AZTSe sample with fixed laser intensity but changing neutral density filters in front of the detector.	139
Figure 4-8: Schematic showing effects of detector saturation for low-lifetime and high lifetime areas.	140
Figure 4-9: PL at 4K for Cu-poor and stoichiometric films for high laser intensities with effects from detector saturation.....	141
Figure 4-10: Devices from Cu-poor and stoichiometric films	143
Figure 4-11: 4K intensity-dependent PL spectra of CZTSe with different amounts of Na. (a) CZTSe film with 8 nm NaF, (b) 15nm NaF, and (c) 30nm NaF, (d) Single-crystal CZTSe sample grown without sodium	148
Figure 4-12: Shift in (112) XRD peak of ACZTSe samples (Ag/(Ag+Cu) ratio indicated above each curve) and (b) a and c lattice constants of ACZTSe samples as a function of Ag/(Ag+Cu) ratio	150

Figure 4-13: Simulated XRD profiles for kesterite AZTSe as a function of Ag-Zn cation disorder	152
Figure 4-14: (a) Room temperature PL and band gap from absorption measurements for AZTSe, CZSe and Ag-Cu alloy. (b) The difference between bandgap and PL peak position	154
Figure 4-15: PL at 4K for films annealed at low temperatures. A) Near-stoichiometric films. B) Cu-poor films.	158
Figure 4-16: PL peak position and E_g as extracted from QE of low-temperature annealed films.....	159
Figure 4-17: Lifetimes of low-temperature annealed films taken at room temperature	160
Figure 4-18: N_{CV} from carrier capacitance-voltage measurements	161
Figure 4-19: Device parameters for Cu-poor low temperature annealed films, average of 4 devices	162
Figure 4-20: Comparison of JV curves of best device from low-temperature annealed films.....	163
Figure 4-21: (A) EQE spectrum of as-made “None” and 150°C x 1 day annealed sample showing increase in long wavelength response. (B) Log plot of EQE for all annealed samples	165
Figure 4-22: EQE comparison of champion single crystal from this work and champion 11.6% CZTSe thin film device	169
Figure 4-23: Light-bias and reverse-bias EQE ratio.....	171
Figure 4-24: Defect densities from DLCP and CV for 6% single crystal and current champion 11.6% thin film [31]	173
Figure 4-25: V_{OC} -T measurements for 6.4% cell	174
Figure 5-1: Source and substrate temperature during deposition. A) Method 1 with no effusion during substrate cool-down. B) Method 2 with effusion of Sn and Se during cool-down	185
Figure 5-2: SEM images of CZTSe surface with different deposition methods. A) Method 1 with no effusion during cool-down showing. B) Method 2 with effusion during cool-down showing more faceted grains.	186

Figure 5-3: Cross-section of CZTSe absorber layer created by FIB and EDS depth profile.	186
Figure 5-4: Source and substrate temperature during deposition for Method 3. Deposition began with lower substrate temperature to minimize Sn loss.	188
Figure 5-5: SEM images of CZTSe deposited with different conditions. A) SEM scratch cross section of CZTSe deposited at 500°C (Method 2) B) SEM FIB cross-section deposited beginning at 300°C (Method 3).	188
Figure 5-6: Corresponding cell results for CZTSe films deposited at A) constant 500°C substrate (Method 2), and B) deposited beginning at 300°C (Method 3).	189
Figure B-1: TGA curve for CZTSe thin film and CZTSe powder	215
Figure B-2: TGA curve for Cu ₂ SnSe ₃ powder	216
Figure B-3: TGA curve for SnSe ₂ powder	216
Figure C-1: Repeatability of XRF measurement for thin films over 200 seconds.	219
Figure C-2: Power calibration for PL spectra tool. Incident laser power and calculated max e-h pair density as a function of neutral density filter wheel position for PL spectra.	223
Figure D-1: Calculated equilibrium defect concentrations for non-interacting defects with assumption listed above.	226
Figure D-2: Modeled PL spectra of a semiconductor with $E_g = 1$ eV such as CZTSe with varying degrees of bandgap fluctuations at room temperature	229
Figure D-3: Calculated PL peak position and FWHM for a semiconductor of 1 eV such as CZTSe with varying degrees of E_g fluctuations at room temperature	229
Figure D-4: PL intensity quenching for defect related PL emission as a function of temperature.	232
Figure D-5: PL spectra and shape as a function of temperature for band-band emission in ideal semiconductor with $E_g = 1$ eV.....	233

Figure F-1: Atomic models of AZTSe. Top to bottom: kesterite, stannite, and disordered kesterite (random occupancy of 2a and 2c site)	236
Figure F-2: Simulated XRD profiles of kesterite (red) and stannite (green).....	239
Figure F-3: Modeled XRD pattern for AZTSe as a function of Ag-Zn order. Bottom panels highlights the critical regions of differentiation.....	241
Figure G-1: Modeled XRD pattern for CZTSe as function of V_{Cu} concentration located equally at 2a and 2c sites.	244
Figure G-2: Modeled XRD pattern for CZTSe as function of V_{Cu} position for fixed 20% V_{Cu}	245
Figure G-3: Key peak changes for modeled XRD pattern for CZTSe as function of V_{Cu} position for fixed 20% V_{Cu}	245
Figure H-1: Source design for Zn bottle and new modification to allow operation above Zn melt	248
Figure H-2: Modeled Zn effusion rates for normal source and proposed rate-restricting source designs	248
Figure H-3: Depiction of thermocouple position for measuring substrate temperatures.	251
Figure H-4: Temperature uniformity mapped across thin film substrates and resulting composition	251

LIST OF ABBREVIATIONS

AA	Air anneal (typically $\sim 300^{\circ}\text{C}$ on hot plate in lab air)
AZTSe	$\text{Ag}_2\text{ZnSnSe}_4$
Br-Methanol, Br-MeOH	Bromine solution in methanol
CTSe	Copper Tin Selenide (Cu_2SnSe_3)
CV	Capacitance-voltage measurement
CZTS	Copper Zinc Tin Sulfide ($\text{Cu}_2\text{ZnSnS}_4$)
CZTSe	Copper Zinc Tin Sulfide ($\text{Cu}_2\text{ZnSnSe}_4$)* <i>*used as default throughout this work but also includes literature from sulfide</i>
DFT	density functional theory calculations
DLCF	Drive-level capacitance profiling
EDX	Energy dispersive spectroscopy
E_g	Bandgap
e-h pair	Electron-hole pair
EQE	External Quantum Efficiency
FF	Fill Factor
ITO	Indium Tin Oxide
J_{sc}	Current at short circuit
JV	Current density vs. applied voltage test
JVT	Current density-voltage vs. temperature test
μ	mobility
N_{CV} , N_{DLCF}	carrier concentration extracted from CV and DLCF measurements - in this case hole concentration (with limits for interpretation of CV measurement)
PL	Photoluminescence
QE	Quantum efficiency
R_s	Series resistance
SEM	Scanning Electron Microscope
SRV	Surface recombination velocity
T_m	Melt temperature
V_{oc}	Voltage at open circuit
V_{oc} -deficit	Deficit between bandgap/ q and V_o
V_{oc} -T	Open circuit voltage vs. temperature measurement
XPS	X-ray photoelectron spectroscopy
XRD	X-ray diffraction
XRF	X-ray fluorescence

ABSTRACT

Solar energy has dropped in cost and grown faster than all other energy technologies in the past 15 years, and as costs reach new lows, and installations reach new heights, raw material costs and availability become increasingly important. $\text{Cu}_2\text{ZnSn}(\text{S},\text{Se})_4$ has achieved the highest efficiency among earth-abundant thin film materials, however a significant voltage deficit caused by band tailing and high levels of poorly understood defects bottleneck commercial relevance. Understanding and controlling the complex defect chemistry of the quaternary material is further inhibited by the complexities inherent in polycrystalline thin films.

In this work, single crystals are used as a model system to better understand the challenging defects in $\text{Cu}_2\text{ZnSnSe}_4$. New methods are developed for fabrication of single crystals and thin films, and the defect properties are examined by photoluminescence and other techniques. Both bulk and surface defects for single crystals and films are investigated and manipulated to reduce recombination and improve V_{OC} . For the surface, new passivation methods are developed. For the bulk, variations in stoichiometry, dopants, and temperature equilibria are explored. From stoichiometry, additional insights into reasons why bulk compositions are found to be Cu-poor and Zn rich are demonstrated. Bulk incorporation of the critical dopant Na is measured for the first time and the effects on sub- E_g states are demonstrated. Further manipulation of defect populations by temperature equilibria are shown to change sub- E_g defects critical for band-tailing.

Single crystal devices are demonstrated for the first time, and based on optimized methods for improving surface and bulk defects, a 7.8% efficient single crystal device is demonstrated with a voltage deficit equal to record thin film devices. The challenges of thin film fabrication are also discussed, and improved devices are demonstrated for a modified single-step co-evaporation, which remains the 2nd highest device efficiency for CZTSe by similar methods.

Chapter 1

INTRODUCTION

1.1 Motivation

One of the largest challenges for the current generation will be to sustainably provide for the world's growing energy needs. Energy demand is expected to rise by more than one-third by 2035 as developing nations grow in size and affluence [1]. Solar technology is uniquely positioned to meet the dual mandate of providing for vast and diverse energy needs while concurrently enabling the world to reach its climate and environmental goals. Factors driving the growth of solar include: environmental benefits and reduced health care costs, widespread abundance and geographic availability, as well as strong political and societal support. Ultimately however, the success of solar rests on the economics. The cost of energy from solar will determine its long term growth. Luckily, the solar cost forecast looks bright.

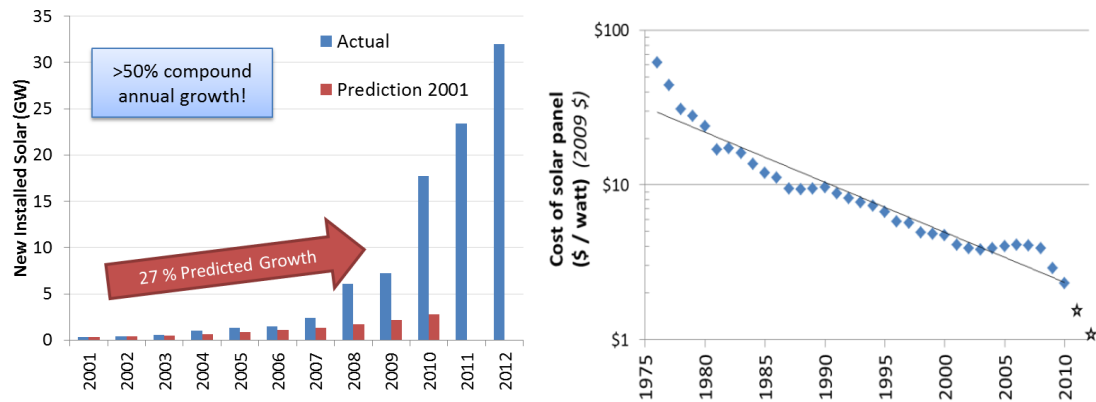


Figure 1-1: Growth of solar and cost of solar panels (raw data taken from [2]–[4])

Due to a rapid learning curve and government support, solar has grown faster and dropped in cost more quickly than even optimistic forecasts from a decade ago as seen in Figure 1-1. Compound annual growth rates of greater than 50% for the past decade have lifted solar from 330 MW installed in 2001 to 32,000 MW installed in 2012 while costs have fallen from >\$4/watt to under \$0.70/watt today [2], [5]. While crystalline silicon continues to dominate the photovoltaic market, polycrystalline thin films offer a number of attractive properties including: improved light absorption, defect tolerance, and a shorter, simpler fabrication process. First Solar has been the dominant thin film provider and demonstrated the cost potential by being first to achieve production costs less than \$1/watt in 2009 and has delivered more than 10GW since their founding [6]. Although thin films have traditionally claimed lower costs with lower efficiencies, recent improvements have shown high efficiencies are possible in both lab and production. Cu(InGa)Se₂ holds the thin film efficiency record at 22.3% in the lab

[7], [8], while the CdTe champion cell has improved 16.7 to 21.5% over the past five years after not improving for a decade from 2001-2011 [9]. Similarly, in modules in production, First Solar has improved CdTe from 11.2% module efficiency in Q2 2011 up to 16.2% for the lead lines in Q2 2015 and has also demonstrated a champion module of 18.6% [6], [10]. The efficiency improvements demonstrated by First Solar are the first time a thin film module has been competitive with or surpassed polycrystalline silicon in efficiency. While the number of companies exploring thin films has decreased in the past decade, recent technological and production progress has shown a promising path for a few key players to expand the thin film market.

Despite the continuing improvements in CIGS and CdTe thin-films, the record growth of solar has raised questions about the long term viability of solar energy dependent on rare elements or scarce materials. Indium in CIGS, and tellurium in CdTe are both potentially supply constrained materials that may prove limiting in the future. While raw materials prices currently represent a fraction of thin film solar production costs, continued thin film growth may tax supply and demand, raising material costs and limiting future cost reduction. Different estimates in the literature predict that raw material availability may be a limiting factor if thin film production reaches between 20 GW/year for conservative estimates, to greater than 100 GW/year for more optimistic estimates [4, 5].¹ Given current solar growth trends –the current industry will produce more than 50 GW of panels in 2015 [4]– and the current world energy demand of 18,000 GW, even the higher limits of thin film production could potentially be reached well before mid-century. A new material, $\text{Cu}_2\text{ZnSnS}_4$ (CZTS) and related compounds

¹ Recent evaluations of the In and Te markets are given in Ref [172]–[174]

including the selenide², have become leading candidates in the search for earth abundant alternative thin films. In fact, enough raw materials (copper, zinc, tin and sulfur) are produced in one month to create solar panels capable of powering the entire world (Figure 1-2).

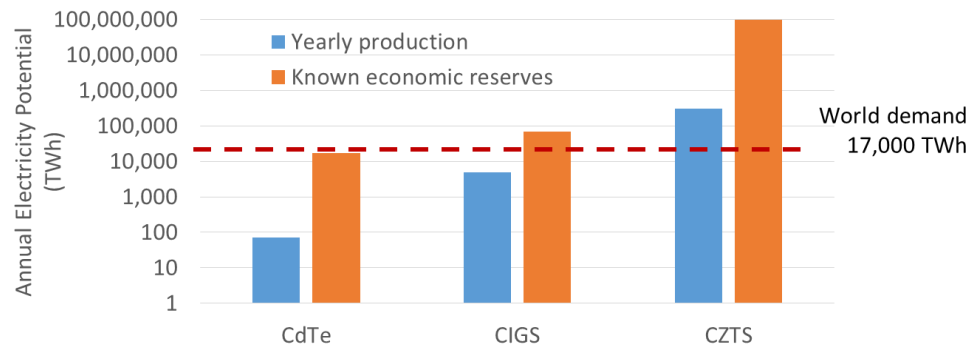


Figure 1-2: Potential solar energy from raw materials for common thin films (raw data from [13])

1.2 Introduction to CZT(S,Se)

CZT(S,Se) is a compound semiconductor that crystallizes in the kesterite structure derived from the zinc blende structure. It has many similarities to CIGS including an optical band gap that is optimally suited for capturing the solar spectrum and that can be tuned linearly by substituting selenium for sulfur, from 1.0 eV for the

² Se is less abundant than sulfur, but the raw material availability is not expected to be constrained in the near term as discussed in Ref. [175]

pure selenide to 1.5 eV for the pure sulfide³. The semiconductor is p-type and direct gap with high absorption coefficient ($>10^4/\text{cm}$) which allows most light to be captured in a one micron thin film. Interest in the material has grown significantly in the past five years as seen by the large increase in number of and journal publications, while lab efficiencies have risen from 6.7% in 2007 to 12.6% in 2015 (Figure 1-3).

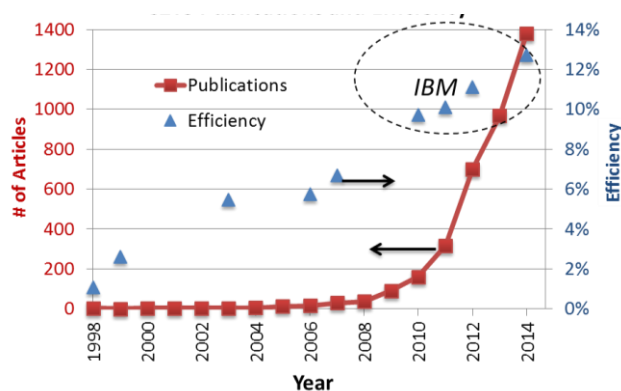


Figure 1-3: History of CZTS related publications and efficiency (Google Scholar search term: (CZTS, CZTSe, $\text{Cu}_2\text{ZnSnSe}_4$, $\text{Cu}_2\text{ZnSnS}_4$, Kesterite) AND (solar or photovoltaic))

1.3 Challenges with CZT(S,Se)

Despite the recent improvements in efficiency, a number of challenges have slowed further efficiency improvements and may threaten future prospects for the CZT(S,Se) material system. The primary long-term barrier is controlling the complex defect chemistry of the material system which is discussed at the heart of this work. The

³ This investigation is primarily focused on $\text{Cu}_2\text{ZnSnSe}_4$ so the term CZTSe will generally be adopted, however remarks frequently pertain to $\text{Cu}_2\text{ZnSnS}_4$ (CZTS) as well as the alloy, $\text{Cu}_2\text{ZnSn(S,Se)}_4$.

complex chemistry of the quaternary phase also leads to challenging fabrication and difficult characterization of CZTSe and secondary phases. These challenges are addressed in more detail in Part II of this work.

The current-voltage (JV) output curve under one-sun illumination of the current champion device can be seen in Figure 1-4. Interestingly the bandgap of 1.13 eV (achieved at ~75% Se:S) is comparable to current champion CIGS devices, however the efficiency, and specifically the voltage, is severely lacking. The JV curve based on the Shockley-Queisser (SQ) limit is also plotted as an upper theoretical bound for voltage and current and the deficit to this limit can be a useful metric to measure progress. In the case of CZT(S,Se), the current is 84% of the SQ limit while the voltage for the champion cell is only ~54% of the theoretical bound. The open-circuit voltage (VOC) at a given band gap is ultimately controlled by recombination through defects –either in the bulk or at surfaces/grain boundaries. Therefore the origin, understanding, and control of defects is of primary importance for future progress of CZT(S,Se). The understanding and origin of defects is discussed briefly in Chapter 1.3.1 and is the focus of Part 1 of this work.

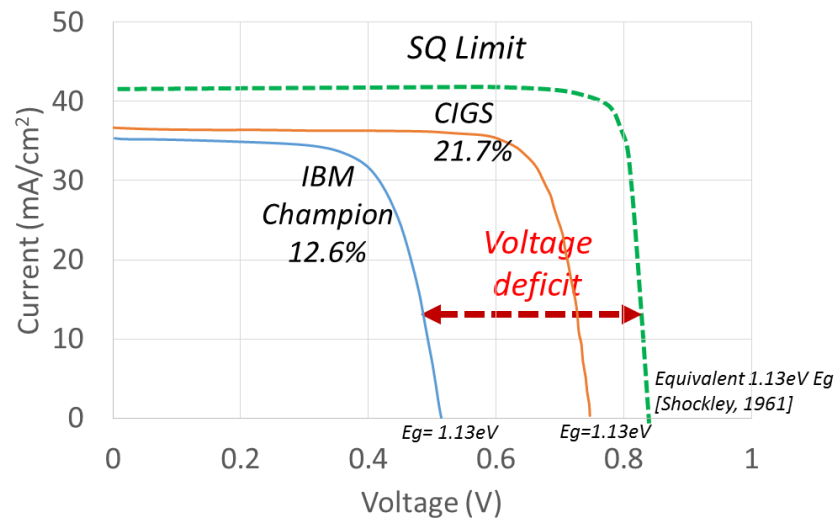


Figure 1-4: Champion CZT(S,Se) IV curve and deficit to theoretical limit (data taken from [7], [14], [15])

Beyond the lack of understanding of fundamental defects, challenging fabrication and characterization of CZT(S,Se) are a continued barrier to progress. Compared to CIGS, CZT(S,Se) contains more volatile phases, is less thermodynamically stable, has a smaller single phase regime, and has a larger range of native defects and defect complexes. In addition, secondary phases possess related crystallographic structure with similar lattice constants and are therefore difficult to discern via techniques such as XRD. The similar lattice also allows low-energy epitaxy between CZT(S,Se) and secondary phases which exist at surfaces, grain boundaries or even as inclusions within a grain. Strategies for formation of thin films and control of secondary phases are discussed in Part II of this work.

1.3.1 Understanding Defects and Motivation for Single Crystals

Open circuit voltage in thin film heterojunction solar cells is ultimately controlled by defects and recombination in the space charge region of the device, arising from a combination of bulk and interface defect states. Unfortunately the understanding of bulk and surface defects in CZT(S,Se), as well as their control is severely lacking. First principle studies have shed light on the expected defect depths and formation energies however rigorous experimental verification can be very difficult. A number of measurements such as low-temperature PL provide insight into the depth of sub- E_g defects, yet the physical origins of these transitions are hard to discern.

Polycrystalline thin film-based devices are a particularly complex system to study. Thin films often deviate from equilibrium bulk materials predicted in first principle experiments, and instead are metastable and can be inhomogeneous on both nano- and micron-scale. These fluctuations of composition and defect levels are particularly significant at grain boundaries and interfaces in which secondary phases or ordered defect compounds are commonly reported [16]–[18] as depicted in Figure 1-5. In most research, device measurements are made on isolated areas of approximately 1 cm² and therefore contain an amalgamation on the order of 100 million grains and resulting grain boundaries. Similarly, the vast majority of electrical and defect measurements, such as PL, probe areas measured in millimeters, and therefore ultimately probe a combination of grain boundaries and bulk, as well as any secondary phases in the thin film material. It is worth noting despite the relatively small volume of a grain boundary or a secondary phase relative to the desired bulk material, they can still have an outsize impact on recombination or measured properties. Carriers will preferentially localize to phases of smaller band gap if they are generated within a diffusion length of said phase. In high efficiency devices, a diffusion length is larger

than the micron-sized grain dimension, making carrier localization all the more likely. Recombination, as well as carrier transport, can therefore be dominated by minority phases or deviations from the bulk, even at small volume percentages of the total material.

These complications can make the physical interpretation of measurements for polycrystalline thin films challenging to interpret. For this reason, bulk single crystal materials are needed to gain insight into the origin of defects and provide reduced ambiguity for interpretation.

Bulk single crystals provide: a controlled crystallographic orientation, large bulk volume to surface ratio, reduced effects of secondary phases, and bulk properties generally closer to equilibrium.

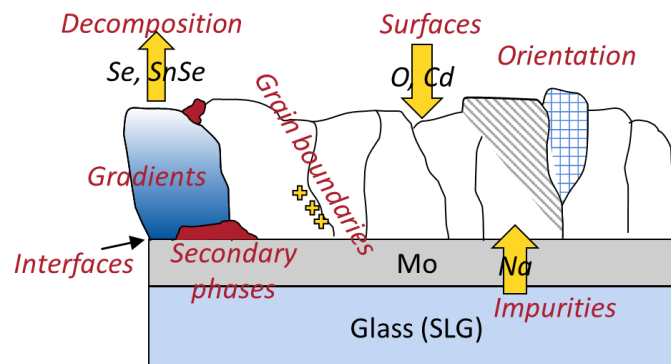


Figure 1-5: Depiction of potential complexities in thin films

1.4 Approach of This Work

The goal of this work is to provide insight into control of defects and secondary phases in both bulk single crystal and thin-film CZTSe. High quality CZTSe material and established methods for fabrication were not readily available for use, and therefore

in this work, we develop and optimize new fabrication methods for both single crystals and thin films. Recent collaboration with IBM has helped provide a comparison to state-of-the-art thin film devices. By studying and contrasting a single crystal system and champion thin films, we hope to improve understanding of the underlying CZTSe material.

This work is divided into two parts. In Part 1, we aim to examine defects in CZTSe through the use of single crystals. First, we develop methods of fabrication for millimeter-sized single crystals (Chapter 2) and then we examine four different levers to control defects: surface passivation, stoichiometry, dopants and substitutions, and temperature equilibria (Chapter 3). Using the aforementioned levers, we demonstrate efficient single crystal solar cell devices (Section 3.7).

In Part 2, we examine thin films. First we look at the same four levers for defect modification as applied to state-of-the-art thin films fabricated by IBM (Chapter 4). Champion thin film and single crystal devices are compared and future opportunities for the materials system are offered.

In the penultimate chapter we discuss challenges in thin film fabrication and improved co-evaporation methods which were developed at the IEC in 2011-2013. The challenges of element volatility and CZTS decomposition in high-temperature co-evaporation are demonstrated and an improved method for efficient devices is developed (Chapter 5). The final chapter briefly summarizes the highlights and significance of this work.

Chapter 2

FABRICATION OF SINGLE CRYSTALS

2.1 Abstract

Bulk CZTSe crystals are not available for purchase, nor are there established or well documented recipes for control of crystal size and boule homogeneity. For this reason, new methods were developed and key variables were established for bulk crystal growth of CZTSe.

Bulk crystal growth can generally be broadly categorized across three main variables: with or without a flux agent, above or below the compound melt, and with simple precursors –often elements, or compound precursors, through use of repeated ampoule growth. In this work, a non-flux method, below the compound melt was pursued, with a single stage ampoule growth from elemental precursors.

Flux agents were avoided to reduce potential contamination or composition pinning on the phase diagram. Both above and below melt were investigated, and their growth dynamics are discussed, but below-melt growth temperatures were found more reliable due to the challenging CZTSe peritectic phase decomposition. Growth from elemental precursors under a single stage was found to be necessary for large crystal size, likely due to liquid phase assisted growth-mechanisms. Repeated-stage growth (compactions) improved ampoule uniformity, and composition control, however grain growth was limited, and the simplicity, shorter times, and more flexible loading profile for utilizing precursor elements with a single growth stage was generally preferred for this work.

Single crystals⁴ with 4-5 mm grains were achieved with both above and below melt growth methods with no flux agent for the first time. Growth dynamics were studied in detail and more than a dozen key variables were identified and utilized to improve crystal size and properties.

This chapter starts with a brief theoretical background on approaches to crystal growth (Section 2.2) and related CZTSe specific literature, including thermodynamic data and phase diagrams for related phases (Section 2.2.1). The pursued fabrication methods are summarized in Section 2.3, and detailed growth dynamics for above and below melt growth are given in Section 2.4 and 2.5 respectively. Key growth variables and optimization are discussed in Section 2.6 and finally summarized briefly Section 2.7. Defects, optoelectronic properties and devices for the aforementioned single crystals are presented in Chapter 3.

2.2 Overview of Crystal Growth

Bulk crystal growth requires significant control of elemental diffusion and suppression of unwanted grain nucleation. The time scale required for solid state diffusion over desired length scales (multiple mm) shows why liquids and flux agents are often utilized. Table 2-1 compares the typical upper limits for diffusivities of

⁴ Single crystal is believed based on available forms of characterization. Secondary phases were examined by powder XRD, Raman, and EDS composition mapping. Laue-diffraction images were taken with spot size approximately equal to crystal diameter and a single orientation diffraction image was obtained among many tested crystals which suggests single-crystal nature. A bi-crystal would show a shifted orientation pattern in the Laue image. SEM imaging before and after etching was also used to search for grain boundaries. Proving the complete lack of grain boundaries is daunting task and beyond the scope of this work.

elements when diffusing in either a solid state crystal, at a grain boundary, or at a crystal surface. The listed diffusivities are surveyed near the melt of the given materials, and give a sense of the timescales needed for multi-mm diffusion [19].

Table 2-1: Solid state diffusivity of materials near the melt

	Diffusivity near melt (cm ² /s)	Time to diffuse ~1mm
Low (solid state)	10 ⁻¹⁴	7927 years
Med (solid state)	10 ⁻¹¹	7.9 years
High (solid state)	10 ⁻⁹	29 days
GB	10 ⁻⁶	42 min
Surface	10 ⁻³	2.5 sec

Solid state diffusion, even in optimistic cases, requires ~ 1 month for diffusion of 1 mm in the solid state. It is likely then, that grain boundaries and surfaces play a large role in the solid state, confirms one reason why liquids and gas phase are can be very helpful for large crystal growth.

The second major challenge in large crystal growth is the suppression of grain nucleation. Uncontrolled grain nucleation leads to smaller polycrystalline regions which compete for grain size via Ostwald ripening. Although diffusion can occur on polycrystalline grain boundaries, the driving force for increased grain size –reduced interfacial area– is relatively small and therefore large single crystals are unlikely to be obtained [20].

2.2.1 Literature and Overview of Methods

Bridgman-Stockbarger technique is one of the most common bulk crystal growth techniques. The method involves heating a polycrystalline charge in a sealed

ampoule above the melting point of the material. Crystallization is then induced by a slow cool of the charge from one end to allow for directed solidification into a crystalline ingot (Figure 2-1). The liquid phase allows for increased mass transfer agent which significantly reduces the diffusion problems noted above. Often a seed crystal of a desired orientation is used to provide starting point for crystal growth. A polycrystalline boule can also be grown through the same technique when it is desired or when crystal growth proves to be challenging.

Other variations based on similar principles include vertical gradient freezing seen in Figure 2-1. Instead of translating the charge through a temperature gradient, this method utilizes furnace controls to translate the temperature gradient through a stationary ampoule. In this way, the material is brought above its melting point and directionally cooled. This method has increased in popularity due to the wide availability of temperature-programmable furnaces without the need for the relatively less common stepper motor for crystal translation. Horizontal gradient freezing (Figure 2-1) works in a similar fashion, but the ampoule is held in the horizontal orientation and the temperature gradient is translated horizontally across the length of the ampoule. This typically results in a half-cylinder shaped crystalline boule, which has the advantage of decreased Z-height of melt material and a large free top surface area. The first characteristic is beneficial when buoyancy segregation is an issue, and the latter is useful to allow relaxation of strain which can be problematic across the crystal growth surface [20].

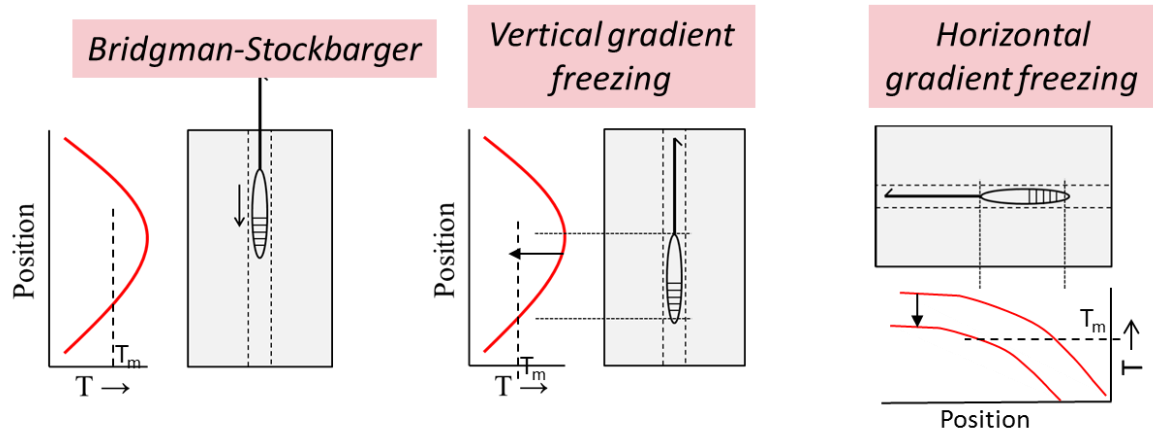


Figure 2-1: Schematic overview of select common bulk single crystal growth methods

CZTSe however is a peritectic system which significantly complicates liquid crystal growth. The $\text{Cu}_2\text{SnSe}_3\text{-ZnSe}$ cross-section of the phase diagram is shown below in Figure 2-2. When heated above the melt, CZTSe decomposes into a solid ZnSe phase and a liquid CTSe phase. On cooling below the peritectic temperature, regions of ZnSe reaction with liquid CTSe to form CZTSe however additional reaction now requires the diffusion of reactants –ZnSe and/or CTSe– through the growing product layer –CZTSe. This results in a diffusion limited growth process which slows as the formed CZTSe increases in thickness due to the increasing required diffusion distance for continued reaction. Solid state diffusion often becomes the limiting growth mechanism which in turn limits crystal growth in timescales of interest. For these reasons, crystal growth through the peritectic often results in limited crystal size and very slow reactions.⁵

⁵ Note: In this work, the terminology “ T_m ” or “above/below melt” will reference the incongruent melt/peritectic temperature of the quaternary CZTSe which occurs at 690°C . At much higher temperatures, $\sim 1100^\circ\text{C}$, $\text{L-Cu}_2\text{SnSe}_3 + \text{ZnSe}$ becomes (next pg)

The vapor pressure curves for the relevant phases are listed in Figure 2-3 and the melting points, decomposition temperature and vapor pressures at approximate crystal growth temperatures are listed in Table 2-2. At typical growth temperatures of 750°C, the phases with relevant vapor pressures are Se ($\sim 10^3$ Torr), Zn ($\sim 10^2$ Torr) and SnSe $\sim 10^{-1}$ Torr. Note these elements and phases typically react during the temperature ramp up and therefore the listed vapor pressures are likely not achieved. Additionally, the high Se secondary phases CuSe and SnSe₂ typically decompose at $\sim 387^\circ\text{C}$ and 647°C although decomposition is likely delayed due to the high expected Se partial pressures. This decomposition leads to Se vapor pressures over the binary compounds as shown in dotted lines in Figure 2-3 where the curve stops at the literature decomposition temperature. Data on vapor pressures and decomposition curves for CTSe and Cu₂SnSe₃ are not available in the literature however TGA experiments performed in this work suggest decomposition of CTSe into Cu₂Se + SnSe at $\sim 627^\circ\text{C}$, and decomposition of CZTSe at $\sim 670^\circ\text{C}$ under flowing N₂ atmosphere through the loss of Se in the gas phase. The actual decomposition temperatures during crystal growth will again be higher due to the high partial pressures of Se and other components in the sealed ampoules. The TGA curves and details are listed in the Appendix **Error! Reference source not found.**

a homogenous melt. This point is less relevant for the growth approaches of this work. Any other melt points for related phases, such as the ternary, will be specified.

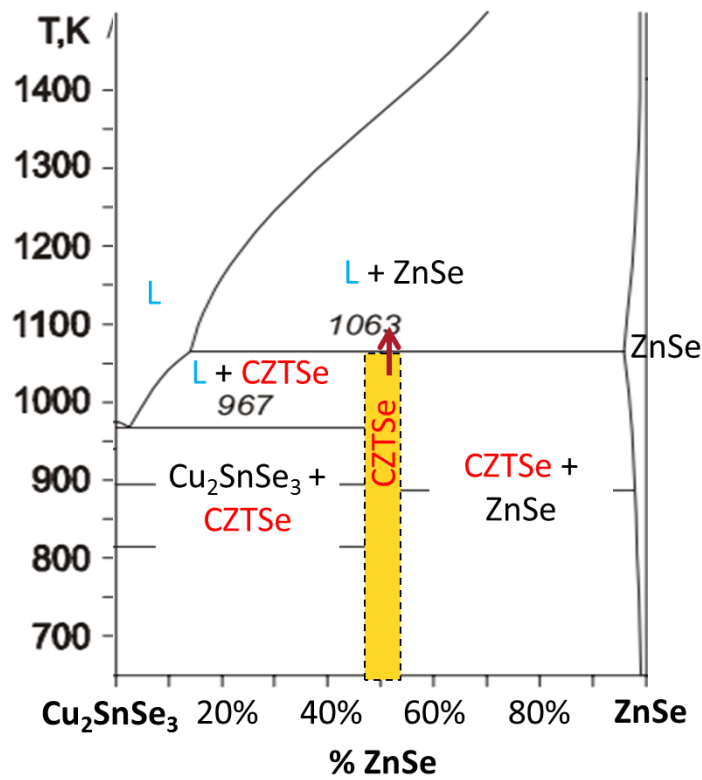


Figure 2-2: Phase diagram of CZTSe (modified from [21]). Temperature in Kelvin.
 Note: CZTSe region width is not to scale.

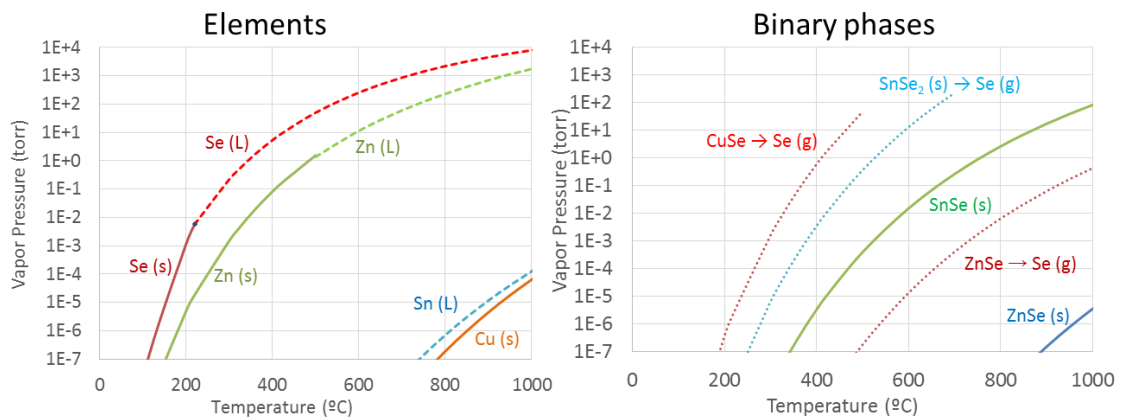


Figure 2-3: Vapor pressure curve for elements and relevant phases. Data taken from Knacke [22]

Table 2-2: List of melting point and decomposition temperatures for relevant compounds

	T_M / T_D	Notes	$P_{self} @ 750^\circ C$	$P_{se} @ T_d$	Source
CZTSe	789°C	Peritectic: Cu_2SnSe_3 (L) + ZnSe (s). Decomposes at $\sim 670^\circ C$ in N_2 from TGA experiments	-	-	[21] + this work
Cu_2SnSe_3	687°C	Decomposition at $\sim 627^\circ C$ in N_2 from TGA experiments	-	-	[Appendix]
SnSe	873°C	Melt but Sublimes easily.	8×10^{-1}		Knacke [22]
SnSe ₂	647°C	Decomposes to SnSe + Se (g)	-	6.2×10^1	
CuSe	387°C	Decomposes to Cu_2Se + Se (g)	-	3.1×10^{-1}	
Cu_2Se	1113°C	Melt	-	-	
ZnSe	1525°C	Melt	4.0×10^{-10}	1.8×10^{-3}	
Cu	1085°C	Melt	4.4×10^{-8}		
Zn	420°C	Melt	1.3×10^2		
Sn	232°C	Melt, Sublimes easily	1.4×10^7		
Se	221°C	Melt. Gas phase Se_x chains. Se_2 dominant at $750^\circ C$.	1.5×10^3		

2.2.1.1 Overview of Flux Growth Methods

An alternative to the above methods involves adding external flux agents to enable mass transport and control crystal growth. Chemical vapor transport is one such method where a flux agent, such as iodine, is added to a sealed ampoule. This method often involves formation of a CZTSe precursor through solid state reaction, followed by loading of CZTSe powder into a sealed ampoule with the iodine flux agent. The ampoule is put in a strong temperature gradient where the precursor solubility with the flux agent is high in the hot end, but low in the cold end. This results in the transport of CZTSe to the cold end of the ampoule. The gradient is then reversed and reduced to decrease the driving force for nucleation and the flux agent transfers the precursor again to the cold end of the ampoule where single crystals are grown. There are a number of

challenges with this technique including control of final crystalline dimensions. For example the most successful early result of this growth technique was crystalline needles 20 x 0.1 x 0.1 mm [23], more recent groups have achieved 5 x 1.5 x 1 mm [24]. Despite the operational challenges, the main drawback is potential for unintentional contamination of crystals with the flux agent which can alter electronic properties even at low concentrations. Since the goals of this work included the study of defects in equilibrium states, external flux techniques were avoided.

The largest single crystals yet obtained for CZTSe were grown with a traveling heater method with a liquid Sn flux. Nagaoka et al pioneered the method for CZTSe and have achieved single crystals up to 20 mm in size (although complete lack of grain boundaries is hard to demonstrably prove) [25]–[27]. This technique uses excess Sn as a solvent to dissolve the solid CZTSe phase at 900°C. A heater transferred along the length of the ampoule with a narrow hot zone at 900°C moving at a rate of 4-5 mm per day. Similar to other liquid techniques, CZTSe in liquid Sn at the cold end of the ampoule is selectively precipitated at the growth interface. The main drawback to this technique is the additional liquid Sn may limit the stoichiometric control of the growing crystal and could lead to compositional pinning of the crystal along the Sn-edge of the phase boundary. There is ample evidence that Sn-rich crystals do not make good solar cells. In fact $[2\text{Cu}_{\text{Zn}}+\text{Sn}_{\text{Zn}}]$ defect complexes are predicted to be the most abundant deep defects in CZTS and CZTSe [28]. Experimental support for this idea has been well demonstrated by Halem et al. with time-resolved-photoluminescence (TRPL) lifetimes as a function of Cu/Sn concentration [29]. Additional empirical evidence shows the best performing CZTSe devices are rich in Zn relative to Sn ($\text{Zn} / \text{Sn} = 1.1\text{-}1.2$) [30]. For this reason, a Sn flux was avoided in this work. Similar pinning of the phase diagram

may result from a Zn flux method (Zn melts at the 420°C but the Zn-CZTSe liquidus curve is not known). The one element in CZTSe for which excess may not be detrimental is selenium. In fact many successful thin film growth methods use significant excess Se including the current champion device [31]. For this reason, crystal growth with excess Se intended to provide a liquid flux was investigated and is discussed in Section 2.6.4.2 .

It is worth noting that despite the excess Sn flux used during growth, Nagaoka et al. has reported Cu-poor and Zn rich crystals as desired for solar cells [27]. Due to the success of the traveling heater method in the last two years, we are in process of developing similar tools and growth processes at the IEC.

Variations on all aforementioned non-flux methods were examined (Bridgman, VGF, HGF) as well as solid state synthesis which avoids the peritectic phase decomposition. Both strategies, above CZTSe melt growth and growth below CZTSe melt will be discussed in more detail in the section below.

2.3 Fabrication Methods

Many variables were investigated including: variations on temperature profile (max temperature, duration of annealing, ramp rate, rate of cooldown, and temperature gradient), variations in precursors (quantity, precursor form factor (powder vs. pellet), elements vs binary + ternary phases) and variations in ampoules (size and dimension, as well as carbon-lined and bare quartz). The effects of these variations are discussed in latter sections. However the most general procedure is listed below and variations to that procedure will be specified.

The standard process is depicted in Figure 2-4. First, 8-60 g of high purity Cu, Zn, Sn, and Se elements⁶ were weighed to the desired stoichiometry and loaded into a cleaned and etched⁷ quartz ampoule ~1 cm inner diameter. The ampoule was sealed under dynamical pumping at a base pressure $\sim 1 \times 10^{-6}$ Torr and the ampoule was placed in a vertical furnace and heated, held and cooled according to a desire temperature profile. After cooldown, the quartz ampoule was broken to extract the solid polycrystalline boule. The characteristics of the outer edge of the boule were investigated via optical photographs, XRF composition profiles, and Raman spectra. Crystals were found to cleave naturally along growth planes with the application of pressure to the boule. Chunks often separated as polycrystals which required additional, more deliberate separation. In certain cases, the boule was instead cut into wafers with a diamond-coated wire saw. This allows for vertical cross sections of the boule growth and easier handling. Despite this benefit, individual crystal extraction method was used more frequently due to the ability to interrogate natural crystal growth facets, provide crystal orientation in an arbitrary direction, and obtain single crystals in the absence of grain boundaries.

⁶ 6N Cu, Zn, Sn and 5N Se elements were purchased from Alfa Aesar. Millimeter-sized shot were used for Cu, Sn and Se, however Zn precursor morphology varied between Zn shot and Zn powder depending on the growth. The effects of variation in Zn precursor morphology are discussed in Section 2.6.3 **Error! Reference source not found.** To mitigate oxidation, Cu shot was etched in ~5% nitric acid for 15 seconds prior to ampoule loading.

⁷ Quartz ampoules were etched 30 min in aqua-regia to remove impurities and flame-polished to reduce surface defects

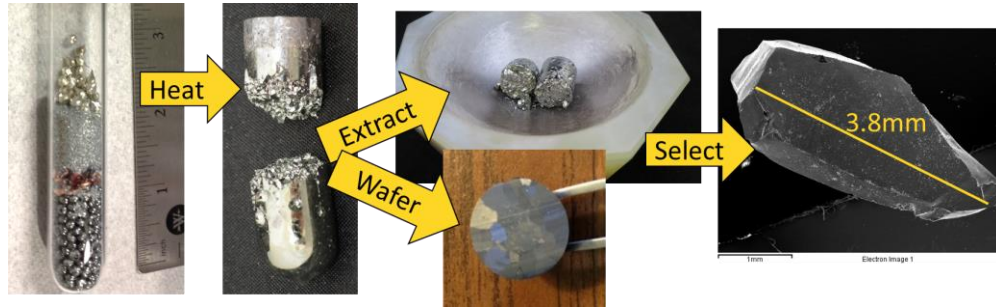


Figure 2-4: Summary of steps in obtaining single crystal CZTSe.

2.3.1 Summary of Below Melt Procedure

The furnace was ramped over 24 hours to a max temperature of 760°C defined (~29°C below the melt temperature) at the top of the elemental charge and held for 20 days under a temperature gradient of ~25°C/inch with the top of the ampoule at the highest temperatures to avoid preferential condensation of gas phases. After 20 days at the set point temperature, the ampoule was cooled naturally over 12 hours to ambient.

2.3.2 Summary of Above Melt Procedure

Crystals were grown above the melt using the vertical gradient freezing method. The procedure was very similar to that used for the crystals fabricated below the melt, described above, however the max temperature was set to 840°C at the coldest point in the ampoule, leaving all of the ampoule above the peritectic decomposition temperature of CZTSe 789°C. The temperature was then lowered slowly at 1°C/hr until the bottom of the ampoule reached 740°C at which point the entire boule is in the solid state. Speed of cool-down increased to 4°C/hr for an additional 50 hours until the bottom of the ampoule achieved 540°C at which point the ampoules were let naturally cool over ~12 hours.

A representative boule from growth temperatures both above and below the peritectic temperature can be seen in Figure 2-5. Raman was used to confirm the phases present along the outer length of the boule as listed in the Figure.

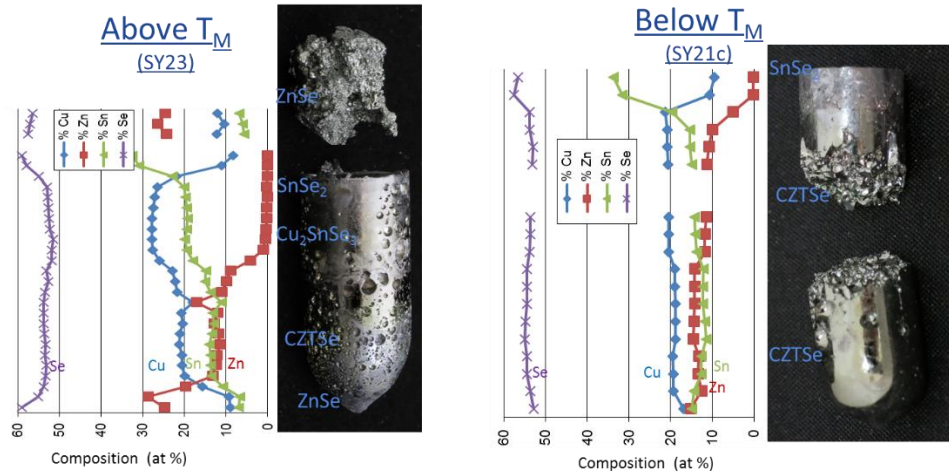


Figure 2-5: Photos and XRF profile of boules fabricated above and below the melt.

The boule grown above the melt showed clear segregation of phases ZnSe and Zn-rich CZTSe spanning at the bottom of the boule located at the coldest end of the ampoule and CTSe with a thin layer of SnSe₂ at the top of the boule. The middle region of the boule contained CZTSe with large grains, while a small porous highly Zn-rich portion remained adhered to the quartz above and physically separated from the boule.

The boule grown below the melt exhibited a significantly more uniform composition close to that of CZTSe throughout its length.. The bottom of the boule still exhibits a very slight increase in Zn-composition while the top of the boule similarly contains a small region of CTSe followed by SnSe₂. Raman confirmed the edges of the boule were almost entirely CZTSe along the area of uniform composition. The phase

homogeneity was found to increase with increasing temperatures below the CZTSe melt.

2.3.3 Comparison of Crystal Size

CZTSe crystals were found to be identifiable by naked eye by from distinct shiny facets and a golden hue under the reflected light. This was confirmed by Raman, powder XRD, SEM/EDS and XRF as well as Laue diffraction patterns. Only crystals of notable size, typically greater than 1 mm were chosen for further characterization while in most growths significant quantities of small grained material was not analyzed further.

The distribution of crystal sizes above and below the melt is seen in Figure 2-6. Crystal growth above the melt resulted in less than a dozen crystals, however the crystal sizes ranged up to ~5 mm when conditions were optimal. In contrast $<T_m$ crystal growth resulted in dozens of crystals although only a handful of large crystals were obtained per batch. An explanation for the main features of the above and below melt are explored in more detail below.

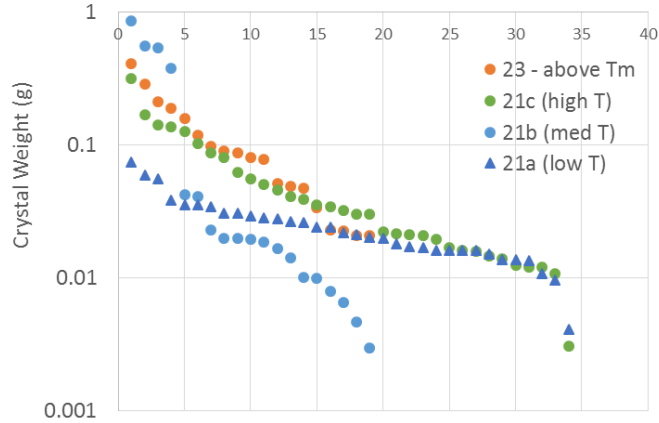


Figure 2-6: Distribution of crystal size above and below the melt. X-axis is crystal count. Temperatures at the midpoint of each ampoule for below melt samples were 735, 755, and 775°C.

2.4 Growth Dynamics Above T_m

To investigate the phase formation dynamics above the melt, additional samples were prepared for growth according to a similar vertical gradient freezing method and then quenched at desired points during the crystal growth. The temperature profile is shown in Figure 2-7.

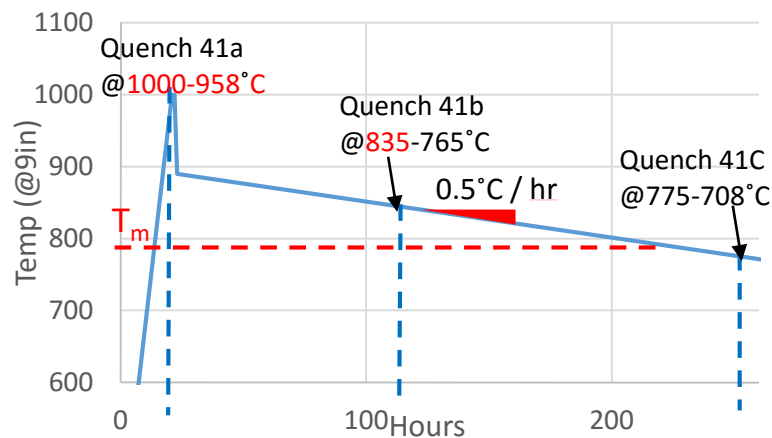


Figure 2-7: Temperature profile of samples quenched during above-melt growth. The temperature at the top and bottom of the boule are listed as a range. Temperatures in red are above the melt.

Three ampoules, SY41A, B and C, were prepared in parallel with elemental precursors. All ampoules were heated to 1000°C for 1 hr to promote homogenization and then cooled quickly to 890°C (remaining above the melt) before slowly cooling to 775°C. The growth interface occurs at T_m , 790°C, and moves slowly up the ampoule at ~0.5 mm/hr as the boule cools. The first ampoule (SY41A), was quenched from the max temperature of 1000°C where the entire ampoule should be above the CZTSe melt. Ampoule B was quenched at the midpoint (835-765°C) such that the top of the ampoule would remain liquid while the bottom would be solid. Ampoule C was quenched after the growth interface had passed above the top of the ampoule and the entire ampoule is expected to be below T_m (as depicted in Figure 2-7).⁸

⁸ The cooldown was slowed further (compared to earlier $>T_m$ growth) to promote crystal growth. The rate of crystal growth can be calculated based on the temperature gradient of (~25°C/in) and cooling rate (0.5°C/hr) to be ~0.5 mm/hr. ⁸

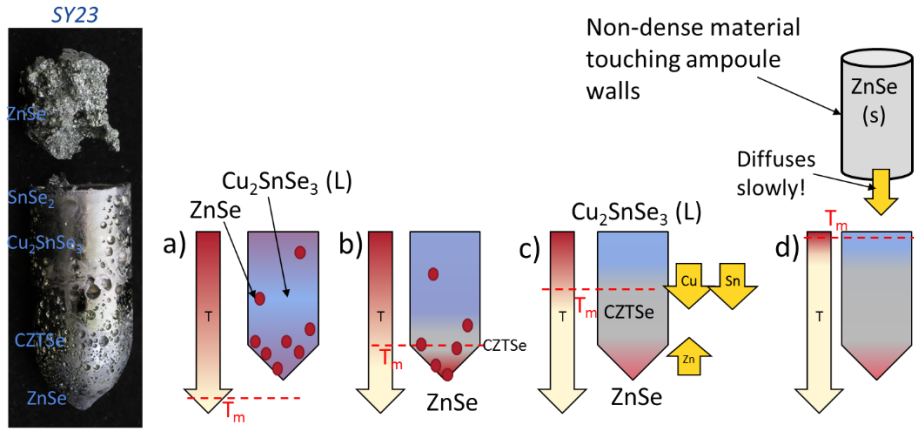


Figure 2-8: Schematic of above melt growth dynamics.

Based on XRF, Raman maps and powder XRD analysis of the aforementioned samples the following key steps were determined and depicted in the Figure above.

- 1) During ramp, elements melt and react to form binary, followed by ternary, and finally quaternary phases. If enough Zn adheres to ampoule above boule, ZnSe forms and remains separate from liquid phases and growth process.
- 2) Above the peritectic decomposition temperature, only liquid CTSe and ZnSe phases are favored (with small amounts of Zn dissolved in CTSe) – depicted in Figure 2-8-a.
- 3) ZnSe solid phase segregates to the bottom of the ampoule due to buoyancy effects and the heavier density relative to the liquid CTSe phase.
- 4) During cooldown CZTSe begins to form when the bottom of the ampoule goes below peritectic decomposition temperature. The growth interface for CZTSe

occurs between the ZnSe phase at the bottom of the ampoule with the liquid CTSe phase above and moves up as the ampoule cools.

- 5) CZTSe crystal growth occurs at 0.5 mm/hour until the diffusion of the reactants cannot supply the necessary elements to the reaction interface which requires diffusion through the increasingly thick CZTSe layer.

Zn-rich regions are sometimes found adhered to the ampoule wall above and physically separated from a dense boule (as depicted in Figure 2-8). If enough Zn reacts above the region of the boule early in the reaction, the resulting ZnSe can bridge across the quartz ampoule. Similar Cu and Sn rich phases will melt with CTSe or at the peritectic decomposition temperature and are then condensed in the bottom boule. ZnSe however, will stay solid throughout the entire growth and even above the peritectic temperature since the melting point 1525°C, far above reaction temperatures. Thus, ZnSe formed above the boule will remain for the duration of the growth with small reduction over time due to slow solid state diffusion.

2.4.1 Crystals Above T_m

While crystal sizes were found to be large, they were more frequently found to border regions of secondary phases with growth above the melt. Individual crystals were sometimes observed to span the entire vertical CZTSe region, bordering Cu_2SnSe_3 on the top, and regions of ZnSe on the bottom. An example of this is depicted in Figure 2-9.

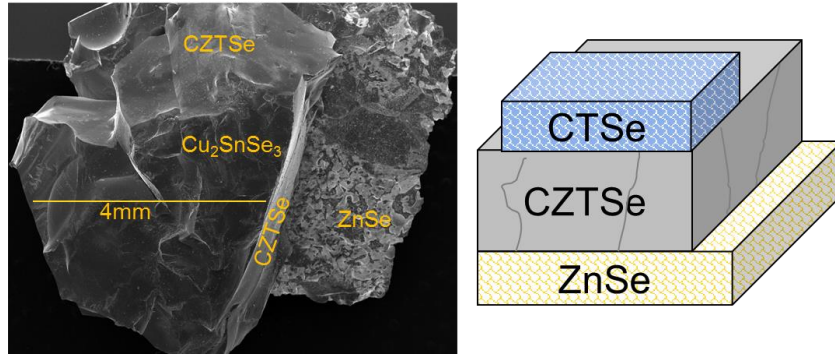


Figure 2-9: Example of crystal obtained above the melt. a) Top view of crystal by SEM extracted in between top layer of Cu_2SnSe_3 and bottom layer of ZnSe. b) Schematic representation of phases

2.5 Growth Dynamics Below T_m

To optimize growth below melt, similar to the aforementioned experiments, a series of ampoules were quenched during the typical growth process to gain better understanding of growth dynamics.

The temperature ramp procedure was empirically found to be critical for final phase formation for samples grown below the melt, and was therefore studied in more detail. Five ampoules were quenched at strategic points above elemental melting and reaction temperatures. Ampoules were quenched at set points of 260°C, 418°C, 600°C, and 790°C, although temperatures at the bottom of boule were 40°C lower due to a temperature gradient. The sequence of reactions occurring during this growth is shown in Figure 2-10.

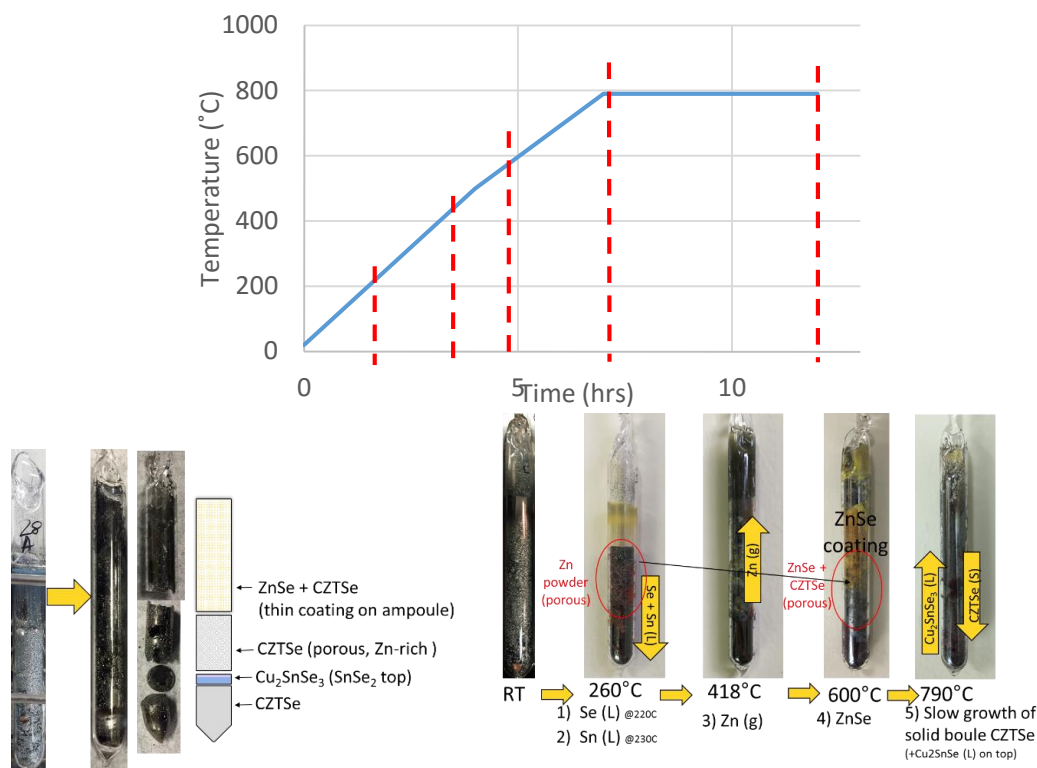


Figure 2-10: Schematic of growth dynamics below melt

The melting points of relevant phases are listed in Table 2-2 and the vapor pressures were given in Figure 2-3, however based on XRF, XRD and SEM/EDS measurements, the following critical points are summarized below:

- At 220°C Se melts, and 232°C Sn melts. Cu_{2-x}Se (s) and SnSe (s) formation occurs rapidly starting approximately at the Se melt temp.
- >400°C Zn has as significant vapor pressure ($8.5 \cdot 10^{-2}$ Torr at 400°C) and reacts with Se gas forming ZnSe coating on ampoule walls. This thin ZnSe coating often remains fixed for the duration of the anneal. CZTSe formation also begins. Above the Zn melt (420°C) ZnSe is formed which begins to diffuse and react with CZTSe

- $>690^{\circ}\text{C}$ CTSe melts and the liquid reacts with ZnSe to form CZTSe crystals.
- Crystals grow on the order of 1 mm / week depending on variables between 10-30 days (plotted in Figure 2-13)

In the literature, CZTSe sealed ampoule growth has been predominantly performed below the melt due to the challenges associated with peritectic decomposition [23], [25], [32]–[37]. However, in contrast to the mm-sized crystals in this work, only small grained sub-mm polycrystalline powders have been reported. In light of the failure to achieve large grain sizes in the literature, the $>4\text{mm}$ grain growth obtained in this work requires some explanation.

The published literature for CZTS and CZTSe single crystal growth has focused on characterization strictly limited to the single phase region of the growth, while ignoring wider questions uniformity or growth dynamics. Very few reports have shown photographs of crystals or boules, and generally have avoided the topic of grain size. Informal discussion with authors of aforementioned reports suggest minimal large grain material has been achieved. The focus of most reports on CZTSe fabricated by sealed ampoule growth has been powder XRD, in which small grain material does not present a problem [34], [38], [39].

There are a number of clues from our work that suggest that the ability to grow large grains below the melt point of CZTSe is supported by a liquid CTSe phase. Under this hypothesis, binary and ternary phases form as the temperature ramps up, but the reaction to form single phase CZTSe remains incomplete due to the slow reaction and solid state diffusion (see Table 2-1). CTSe is the lowest melting precursor of the system, so when the temperature ramps above $>690^{\circ}\text{C}$, a liquid CTSe phase forms. From the phase diagram (Figure 2-2, pg 17), $\sim 15\%$ ZnSe can dissolve in CTSe at the temperatures

of growth $>750^{\circ}\text{C}$. Large CZTSe crystals begin to form as ZnSe diffuses into liquid CTSe, pushing beyond the limits of Zn solubility and thus precipitating CZTSe. This crystal growth mechanism is similar to $>T_m$ growth described in Section 2.4, but avoids the peritectic decomposition and limits the effect of buoyancy segregation since only limited portions of the boule are liquid at one time.

Four main factors strengthen the case for the role of liquid CTSe during growth. First, ampoules that were ramped slowly to max temperature had generally smaller crystal size. These ampoules would have spent considerable time below the melt of CTSe and therefore may have limited liquid formation when the max temperature was finally reached. Second, compositions of CZTSe were found to be typically lower Zn than reported via other methods in the literature as well as fixed at Cu/Sn ~ 2.0 . These compositions persisted despite changing the loaded elemental ratios to high Zn and low Sn. This would be expected if CZTSe is precipitating out of a liquid Cu_2SnSe_3 phase since Zn is limited and the Cu/Sn ratio for the ternary is 2.0. Third, small amounts CTSe phases were found to dot the surface of many crystal surfaces, as would be expected for a condensed liquid flux. Fourth and finally, in certain ampoules grown, the boule morphology and crystal growth was similar to ampoules $>T_m$ despite never being above T_m . This is shown in Figure 2-11, where a large crystalline CZTSe is region is seen growing below a Cu_2SnSe_3 region. This morphology was previously explained as the precipitation of CZTSe out of a previously liquid CTSe phase. SnSe_2 noted on the surface is also liquid during growth and is expected in excess since the ampoules are loaded with a Cu-poor stoichiometry. The segregation of excess SnSe_2 also explains the relatively fixed Cu/Sn ratio found in the CZTSe growth. This fact, as will be discussed in Section 3.4 on stoichiometry, is a potential limitation of growth using the

single-chambered ampoule to synthesize crystals while attempting to control electronic properties.

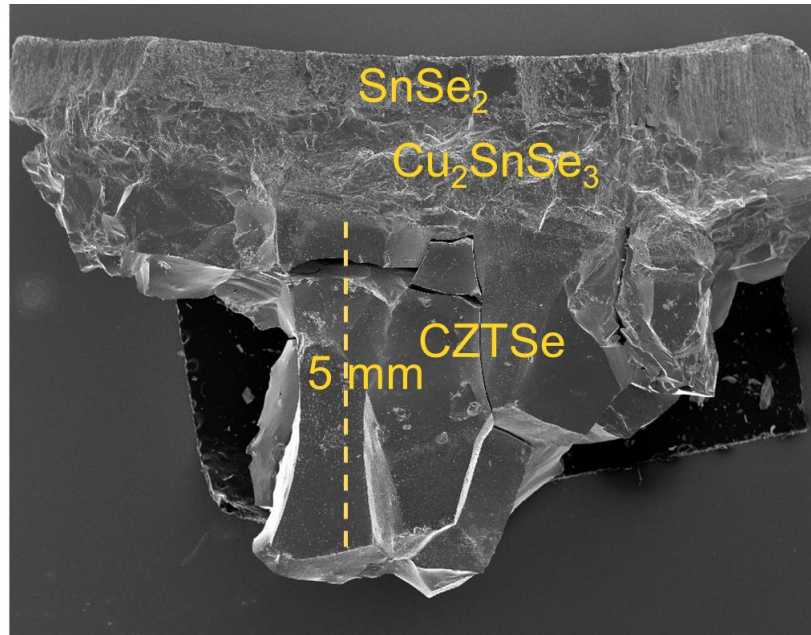


Figure 2-11: SEM image of crystal growth dynamics $<T_m$ showing role of CTSe.

2.5.1 Summary of Growth Above and Below Melt

Below melt growth was chosen as the dominant method for experiments outlined in this work due to more consistent results with more crystals and more uniform boule compositions. Throughout the lifetime of the project, a total of 11 ampoules were fabricated using $>T_m$ growth, while 90 syntheses were performed below the melt. To perform over 100 growths, often a month in length, two vertical furnaces and a horizontal 3-zone oven were setup and modified for the desired purpose of crystal growth and up to six ampoules were often grown in parallel in a furnace to increase throughput and allow multiple changes of a variable to be performed.

Crystal size, as well as shape and other metrics were found to be dependent on the controlled growth variables. In non-ideal growths, crystals were all below 1mm in size where in more optimized conditions, up to 60 crystals ranging from 1-5mm could be extracted. A typical crystal is seen in Figure 2-12. The variables affecting crystal growth are discussed in detail the next section.

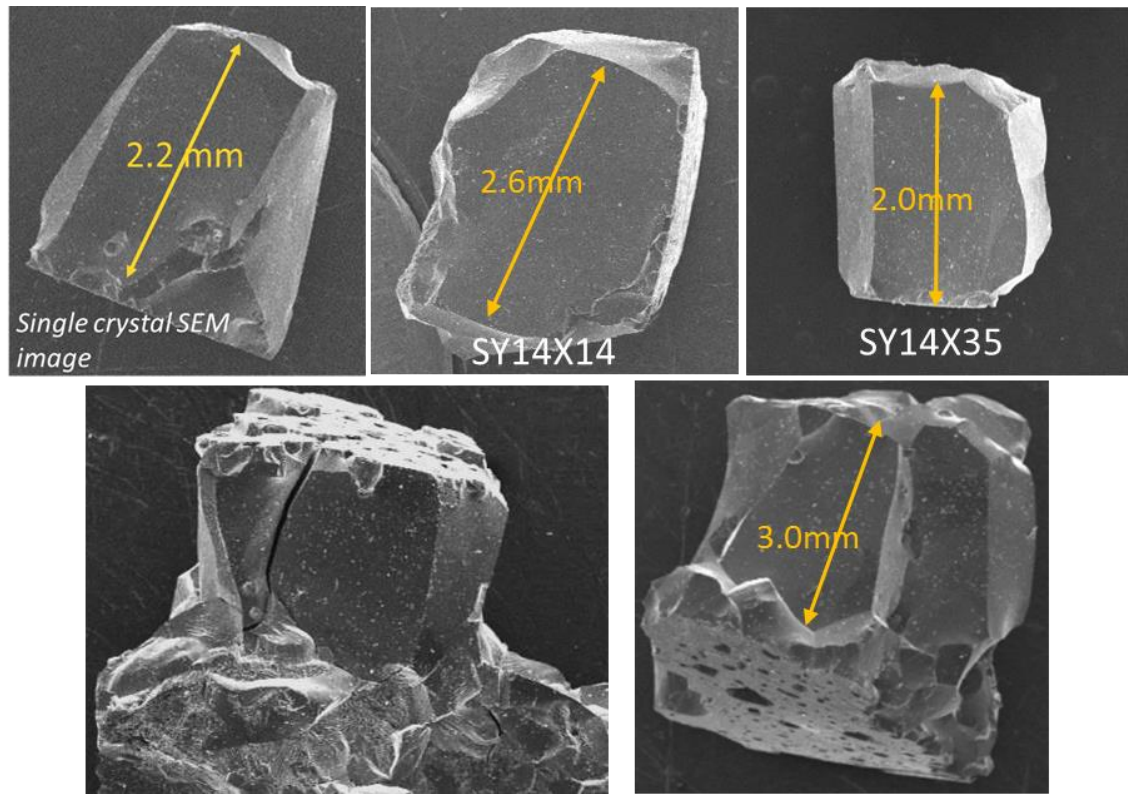


Figure 2-12: SEM image of typical single crystals (top row) and poly-crystals (bottom row) grown below the melt.

2.6 Variables and Optimization

Crystal growth includes equal measures science, art and optimization. Long process times that extend from 2 weeks to greater than a month make cycle times slow.

Unknown and uncontrolled variables or failed growths can cause significant time setback. To get meaningful results and multiple-mm sized crystals, many factors had to be optimized and controlled. They include temperature profile, precursors, ampoule size and preparation and oven geometry. The major effects of these variables are summarized below.

2.6.1 Effect of Time

Growth time at max temperature is a critical factor for optimizing growth size as well as understanding the dynamics of the growth process. As a test of this parameter, a series of equivalent ampoules were prepared and heated to a max temperature of 760°C for 11, 21 and 31 days. All of the ampoules were comprised of CZTSe precursor powder, compacted in a manner described below. All ampoules were allowed to cool naturally together over ~8 hours after 11 days. The remaining ampoules were reheated for an additional 10 days without opening the ampoule. The final ampoule was reheated a 3rd time for a total of 31 days at the max temperature.⁹

⁹ It is worth noting this series was performed as a compaction. This meant the precursor loaded into each ampoule was a CZTSe phase made from a previous synthesis. This precursor may affect the kinetics of the growth process and therefore additional experiments with elemental precursors may be warranted. In addition, 10% excess Se was loaded into the ampoule to provide a Se overpressure and act as a flux agent for diffusion and grain growth.

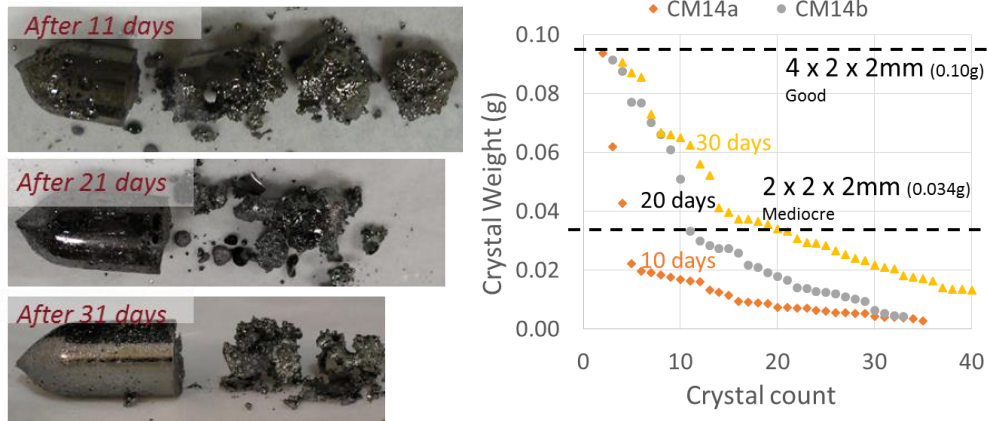


Figure 2-13: Crystal size as a function of time and resulting polycrystalline boules

The resulting boules (Figure 2-13) contained a compact dense boule and a less-dense region as was previously discussed in Figure 2-10. With time, the size of the denser region grew as the less-dense region slowly diffused into the boule driven by an intentional temperature gradient. The more important qualities and size of the resulting crystals were examined by weight. Weight provides a quick and quantitative way to gauge crystal size from a particular batch. It is worth noting however, that although most polycrystals were broken apart, some were left together either intentionally (to evaluate growth dynamics or grain boundary properties) or overlooked. This makes the weight count a non-exact measure of single crystal size, however trends between ampoules are still meaningful.

A histogram of crystal weights is shown in Figure 2-13. Crystal weight increased approximately linearly time from a median of 0.01g after 11 days, to 0.024g after 21 and 0.037g after 31 days. Additional time beyond 31 days may continue to increase median crystal size, however it appears that the largest crystals had more limited growth beyond 20 days. This decrease in growth rate for large crystals may be due to the

surrounding grains competing for growth in the solid-state rather than assisted by liquid phases, or it may stem from the lack of available material of the correct composition. Regions lacking the proper stoichiometry could lead to the presence of second phase precipitates which have been shown in the literature to significantly decrease grain growth through a process known as solute drag [40].

Given the slowing growth of the largest crystals, 20 days at max temperature (plus ramp and cooldown) was generally chosen as the compromise between time and crystal size in most growths.

2.6.2 Effect of Temperature

Equivalent ampoules were fabricated and grown for 20 days at varying temperatures below the melt. The ampoules were loaded at the same time into a furnace with a temperature gradient at different heights. This allowed the same ramp rate and growth conditions. The growth temperatures as a function of ampoule position and photos of the resulting boules can be seen in Figure 2-14.

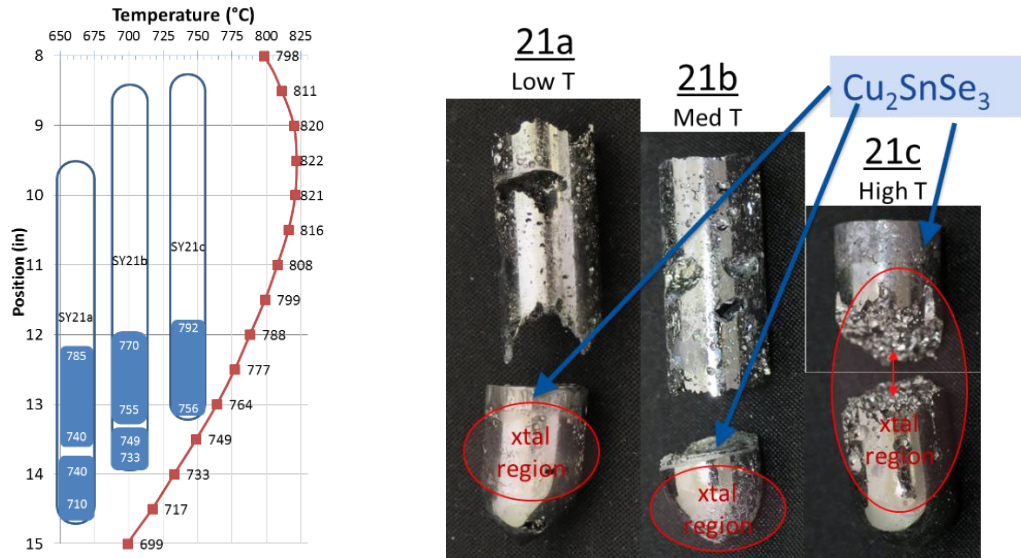


Figure 2-14: Temperature profile for temperature series and resulting polycrystalline boules

The coldest temperature at the base of each ampoule was $\sim 710^{\circ}\text{C}$, $\sim 733^{\circ}\text{C}$, and $\sim 756^{\circ}\text{C}$ for ampoules 21a, 21b and 21c respectively. Due to a temperature gradient of $\sim 25\text{C/in}$, the higher parts of the boules were exposed to higher temperatures. At 1.5in above the bottom of the ampoule, which is expected to be the height of a dense boule, temperatures were 756°C , 777°C and 792°C – slightly below the melt point).

Similar to previous descriptions, a compact dense boule was noted at the bottom of each ampoule, followed by a less-dense region that remained physically separated from the boule and adhered to the quartz glass. Notably, the highest temperature ampoule, 21C was completely dense without physical segregation noted in the other boules. Temperatures were above the CZTSe melting temperature at the surface of the boule which meant any CZTS which formed above the boule would decompose and join the boule below. This observation may explain the lack of material accumulation above the boule.

Examination of the edge of the boule via Raman showed the higher temperature ampoules had fewer secondary phases throughout the dense boule region than the lower temperature growths. At the top of the dense boule, where crystal growth was observed, a thin Cu_2SnSe_3 layer was noted. Above the dense boule, the less-dense region was noted to be mainly CZTSe, although no grain growth of significance was noted (sub-mm). This supports the concept that a CTSe liquid phase mediates crystal growth.

As depicted in the histogram in Figure 2-15, crystal size was found to increase with increasing temperature although the largest four crystals were from SY21b at middle temperature. These 4 crystals were all found in the dense lower region of the ampoule which was the smallest dense boule in the series. It is not clear if the temperature range experienced (733-749°C) was optimal, or if the small volume of the boule in SY21b meant that fewer areas occurred to initiate grain growth leading to larger crystals. Since the largest 4 crystals made up the majority of the volume of the small dense region, the remaining crystals were found to be insignificant in size.

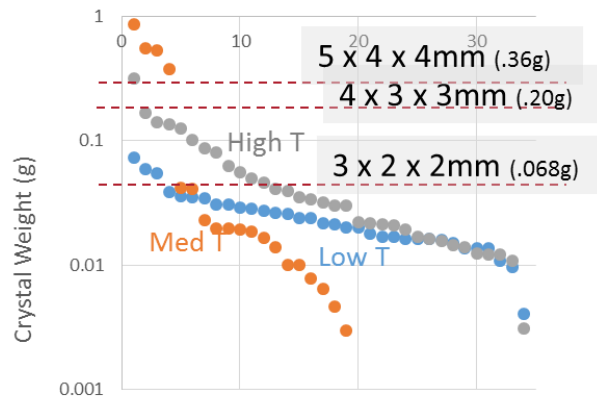


Figure 2-15: Effect of temperature on crystal size

Temperature was found to affect the stoichiometry of the grown CZTSe as well. Within each ampoule, as well as between ampoules, higher temperatures resulted in an enhanced Zn incorporation into the CZTSe phases. SY21C was found to have the highest Zn content in crystals while lower temperature SY21B and SY21A had less. The same trends applied within ampoules, crystals from the lower regions of ampoules were grown at lower temperatures and had lower Zn content. This is opposite of the trend expected from buoyancy segregation of ZnSe which has been discussed in samples above the CZTSe melt. It is likely that the increased Zn is related to increased solubility of Zn in the liquid CTSe phase, as well as additional Zn diffusion allowed by higher temperatures although further verification is necessary.

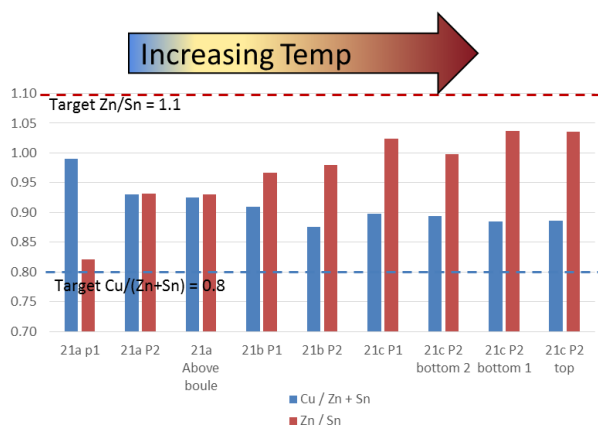


Figure 2-16: Effect of temperature on crystal composition

The increasing Zn-content of crystals also showed lower hole densities which were found to be a critical parameter for well performing solar cells [41]. Increasing Zn content, and thus decreasing conductivity, was a critical interest as will be discussed in later chapters. For this reason, high temperature approaches near the melt were pursued.

2.6.3 Effect of Reaction Precursors

2.6.3.1 Form Factor of Elemental Precursors

Various forms of elemental precursors were explored. Of particular concern was the relatively large form factor of the elemental nuggets of Zn (3-4mm). Achieving homogenous distribution of Zn throughout the polycrystalline boule has been particularly challenging and this may be related to the slow diffusion of Zn once reacted with ZnSe. Indeed, recent attempts to fabricate ZnSe in ampoules has demonstrated that Zn remains unevenly reacted after 7 days at 760°C. A Zn powder (5N, 20 mesh) was obtained as a countermeasure to improve Zn distribution and reduce required diffusion. Zn powder was found to generally increase composition uniformity in the boule, although there are trade-offs with increasing potential for oxidation due to high surface area, Zn evaporation during evaporation during ramp, and the potential for ZnSe to form above the boule adhered to the quartz and remain physically separated from the boule for the entirety of growth. See Figure 2-8 and 2-14, both of which used Zn powder.

A Zn wire was also tried in effort to obtain a more uniform Zn profile across the height of the boule. The Zn wire was cut to a length similar to the boule as shown in Figure 2-17, but after annealing for 20 days the form factor of the Zn wire was retained in the form ZnSe.

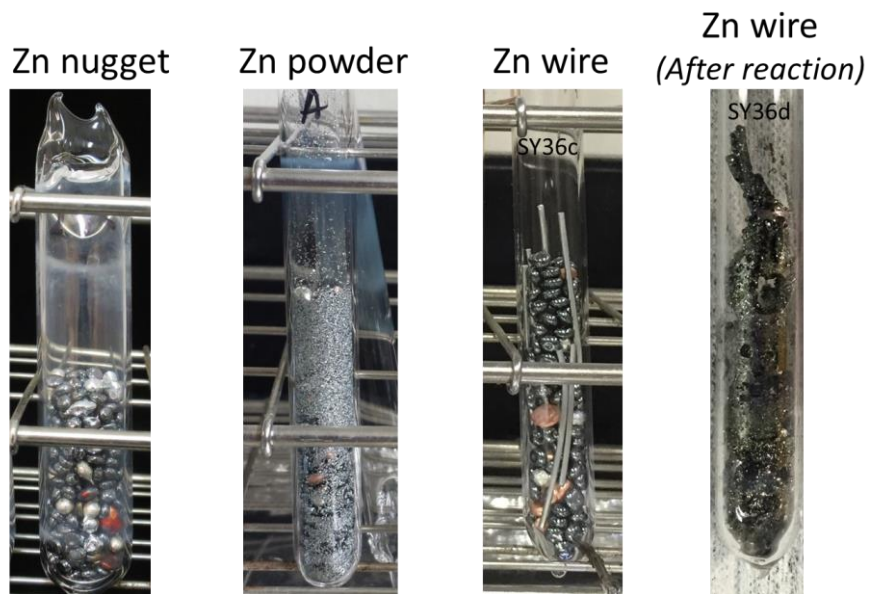


Figure 2-17: Comparison of Zn precursors

Towards the same goal of improving uniformity, a Sn powder was also tried. Unfortunately, the resulting boules showed significant amounts of oxide and poor grain growth. Attempts to remove the oxide skin of the pure Sn nuggets was pursued with chemical etches in various acids however these trials were not successful.

2.6.3.2 ZnSe and Cu₂SnSe₃ Precursors

Precursors made from ZnSe and Cu₂SnSe₃ were also investigated. These precursors were grown in-house in sealed ampoules and then powdered with mortar before being mixed in the desired ratio and sealed in a second ampoule for growth of CZTSe. Details of each method can be found in the Appendix Pg. 217. The goal of this process is two-fold. First, the reaction path is simplified to a single step which may help reduce secondary phases in the resulting boule. Second, because the precursor is an

intimately mixed powder from the previous ampoules, the starting homogeneity and necessary diffusion lengths can be reduced.

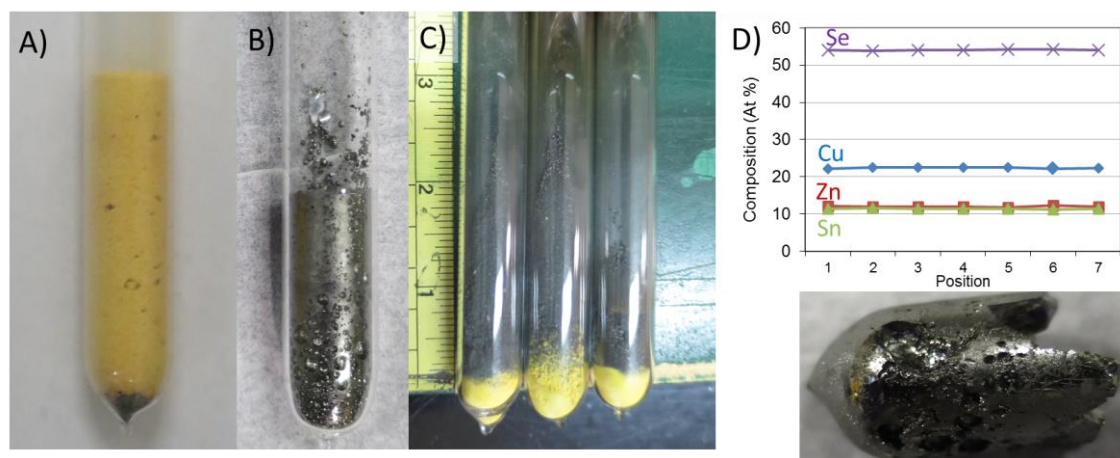


Figure 2-18: Photos of ZnSe (A) and Cu_2SnSe_3 (B) precursor ampoule, three mixed ZnSe/CTSe ampoules before CZTSe growth (C), and achieved CZTSe boule and composition profile by XRF.

The precursors ampoules as well as the mixed ampoule and final boule and XRF profile can be seen in Figure 2-18. Although and boule uniformity obtained from this method is promising, definitive comparisons with elemental precursors cannot be made because the reference elemental ampoule broke during heating. Additional experiments and comparisons are currently being explored by coworkers.

2.6.4 Effect of Composition

The starting weighed elemental composition of a synthesis was varied to obtain a range of final stoichiometries and the effects on crystal growth, second phases and electrical properties were explored. The changes are explored more detail in Chapter 3.

2.6.4.1 Effect of Cu

Ampoules were weighed with different target Cu stoichiometries (SY24A-E) and the resulting crystal properties as well as crystal sizes were compared (Figure 2-19). Crystal size was found to increase as Cu concentration was decreased from Cu/(Zn+Sn) = 1.0 to 0.7. Se was kept at a fixed 8% atomic excess in all growth in order to provide a charge balance of cations and anions for the samples with the lowest Cu¹⁰. An additional ampoule with stoichiometric Cu and no additional Se was also prepared for comparison and is discussed in the next section.

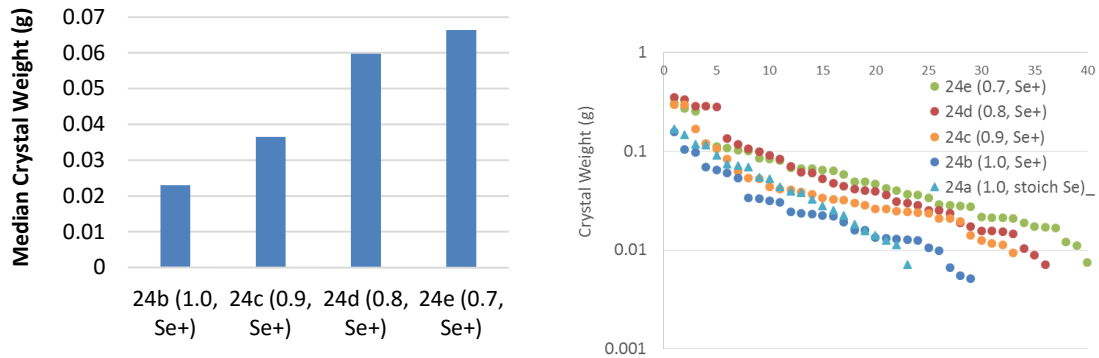


Figure 2-19: Median crystal weight and distribution of crystal sizes as a function of Cu composition

¹⁰ Atomic balance of cations and anions in $\text{Cu}_2\text{ZnSnSe}_4$ is achieved with Se/cation ratio = 1, with the elements taking the valence of Cu = +1, Zn = +2, Sn = +4, and Se = -2, therefore the charge is balanced as well ($[2*1] + [1*2] + [1*4] + [4*-2] = 0$). However, when samples are made off-stoichiometry, either the atomic balance or charge balance is altered. For instance, it is thought that champion solar cells should be targeted with charge balance and therefore excess Se. Therefore ideal composition is expected at $\text{Cu}_{1.7}\text{Zn}_{1.15}\text{SnSe}_4 \rightarrow$ charge balance: $([1.7*1] + [1.15*2] + [1*4] + [4*-2]) = 0$ while (Se/cation) = 1.039.

2.6.4.2 Effect of Se

Se vacancies are predicted to be deep defects in CZTSe [42], and due to high vapor pressures, most thin film growth processes utilize very high overpressures of Se to ensure stoichiometry is not deficient in Se. In sealed ampoule growth, excess Se has another potential benefit in that it could potentially provide a flux agent for improving element diffusion due to the low melt temperature. A liquid Sn flux has been demonstrated to grow large crystals in the literature [26], however as noted previously, excess Sn is a particular concern for electronic properties of CZTSe. In theory, Se is the one element in the CZTSe system where detrimental electronic effects are not predicted from its presence in excess, and therefore Se would be an ideal flux agent, if it could work. This concept was explored on multiple occasions however the potential benefits noted above did not bear out. In fact, high quantities of excess Se were found to increase phase segregation and decrease crystal size (Figure 2-20 and Figure 2-21). For the highest quantities of Se (33% excess), all of the Zn was observed at the bottom of the ampoule followed by a thin layer of CZTSe with Cu, Sn and Se rich phases found on top. The kinetics as well as the thermodynamics of growth are likely changed by excess Se and it likely that Se rich secondary phases are lower free energy compared to the desired CZTSe + Se. In fact EDS noted regions consistent with Cu_2SnSe_8 and $\text{Cu}_4\text{Sn}_3\text{Se}_8$, as well as SnSe_2 all of which have higher Se/cation ratios than CZTSe. Cu_2SnSe_3 has been known to have many similar off-stoichiometric and high Se phases and therefore the above phase are not unsurprising. The thermodynamics of such phases are not available.

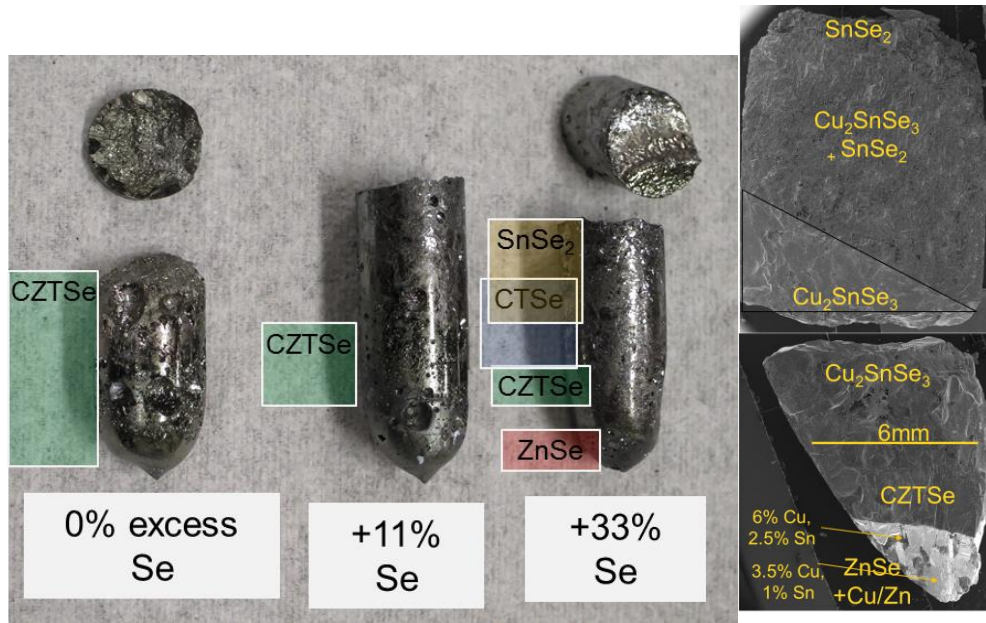


Figure 2-20: Effect of excess Se on boules and phase distribution.

In addition to increasing phase segregation, CZTSe crystal size was also suppressed. In a separate synthesis, 8% excess Se was added to a stoichiometric growth. This was found to result in reduced crystal size as noted in Figure 2-21. A low Se growth, at Se/cation ratio = 0.96, was also tried, however crystal size appeared slightly reduced compared to stoichiometric and low PL intensities were observed which match with the theoretical prediction of deep defects for Se vacancies. Based on the above data, valance balanced amounts of Se are thought to be best for growth size, while re-annealing CZTSe in excess Se post-crystal growth may be an additional tool for reducing Se vacancies and improving electronic properties without favoring secondary phases.

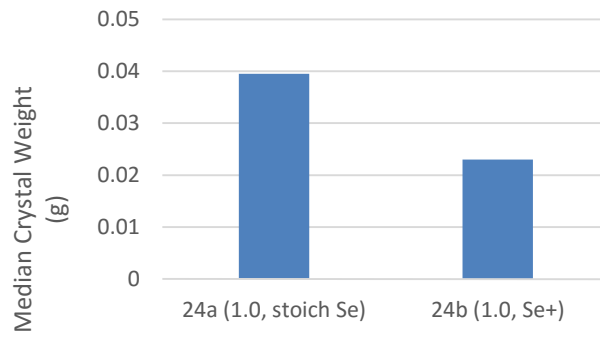


Figure 2-21: Crystal size as function of Se.

2.6.5 Achieved Compositions

Over 100 ampoules of a variety of compositions were created during this work (Figure 2-22: Summary of ampoule compositions explored by loaded elemental ratios 2-22). Effort focused on the Cu-poor, Zn rich region ($\text{Cu}/\text{ZnSn} = 0.8$, $\text{Zn}/\text{Sn} = 1.2$) which is found to be optimal for devices, however additional ampoules of other stoichiometries were fabricated to better understand the effect of bulk composition on electronic properties (explored in Chapter 3).

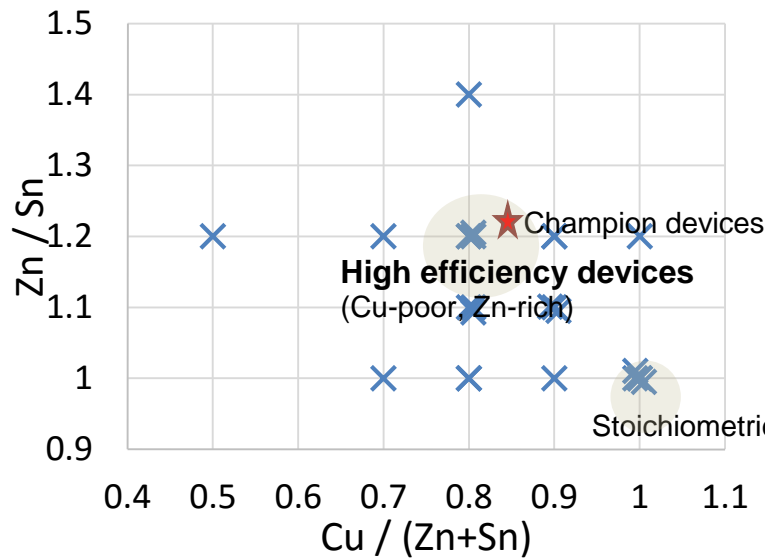


Figure 2-22: Summary of ampoule compositions explored by loaded elemental ratios

Stoichiometric control was achieved by changing the elemental ratios loaded into an ampoule before growth, however the final bulk crystal composition did not always equal the loaded ratio of elements. As seen in Figure 2-23, stoichiometric ampoules generally gave near-stoichiometric crystals, and Cu-poor ampoules generally gave Cu-poor crystals, however there were limits and exceptions to this trend. When excess Se was added to otherwise stoichiometric ampoules, the compositions were found to skew to low Cu and high Zn. As previously suggested in Section 2.6.4.2, Gibbs Free Energies of excess Se may favor reactions with Sn and $\text{Cu}_2\text{SnSe}_{3+x}$, which would in effect make the remaining CZTSe Cu-poor and Zn rich.

Limits were also realized for low Cu concentrations. Ampoules loaded with $\text{Cu}/\text{Zn}+\text{Sn} = 0.8$ and 0.7 both achieved crystals $\text{Cu}/\text{Zn}+\text{Sn} \sim 0.85$. Further decreases in Cu were appeared difficult with the given growth methods however other methods such as compactions were found to help improve stoichiometric control and achieved crystal

stoichiometries as low as $\text{Cu}/\text{Zn}+\text{Sn} = 0.83$. Further decreasing Cu and achieving Cu/Sn ratios closer to 1.75 is likely an important step for further improving bulk qualities such as lifetime [29] and further improving devices. It may be that $\text{Cu}/\text{Zn}+\text{Sn} \sim 0.85$ is at the boundary of the CZTSe phase diagram at the growth temperatures of $\sim 750^\circ\text{C}$, however the achieved composition may speak more to the growth method relating to liquid Cu-Sn phase, rather than fundamental limits. Additional efforts to alter composition via post-annealing, compactions, or new growth techniques are being pursued and may prove fruitful.

Within one ampoule, compositions of different crystals had a variance of less than 5% as depicted from Figure 2-23. Although improved composition control continues to be an important goal, the method of this work allowed for dozens of crystals to be fabricated at the same time and then quickly screened for the desired properties (composition, conductivity and size), and then further down-selected for detailed characterization or fabrication of single crystal devices.

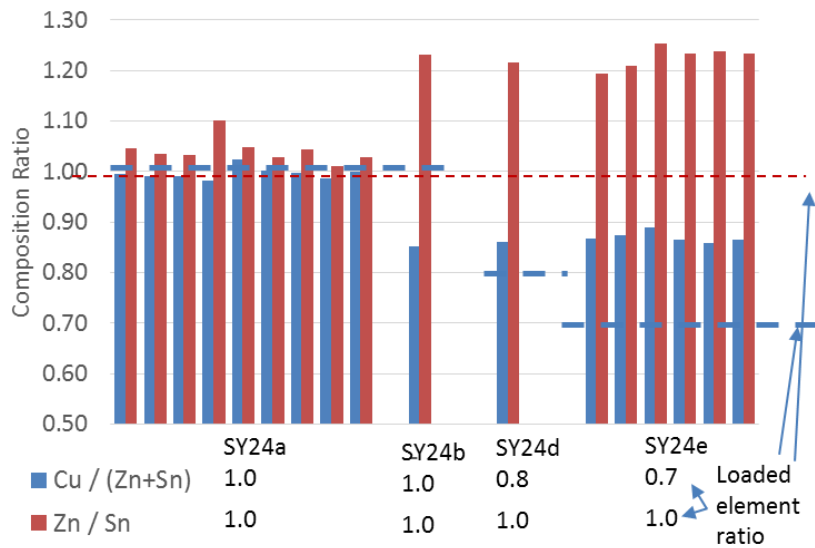


Figure 2-23: Composition of polished crystals by XRF compared to loaded elemental ratio

2.6.6 Other Growth Variables

A number of other variables were explored including: ramp-rate, rate of cool-down, quartz liners, ampoule size, and growth orientation. They are summarized in brief below.

A carbon liner can be added to ampoules for the dual purpose of getting oxygen with the unburned hydrocarbon while also providing protection reduced adhesion to the quartz ampoule wall. Liners from acetone and xylene were tried, but few significant differences were noted. In certain cases it appears the liner may have contained residual hydrocarbon increasing probability of ampoule explosion. The liner was found to be effective in preventing de-vitrification of quartz when Na was incorporated.

Ramp-rate has the potential to control early precursor reactions as well as affect the quantity of liquid phases achieved during growth. Ramp rate is limited by the potential for excess Se overpressure in the ampoule which can cause the ampoule to explode. Particular caution must be used when ampoules are made using sulfur instead of selenium since the vapor pressure of sulfur is 5-10x higher than Se (at 750°C $P_{Se}=2.2$ atm while $P_S=14$ atm). In addition, it was found when ampoules were ramped too quickly that violent reactions within the ampoule can occur resulting in vibrating and dislodging the ampoules from their desired growth positions. There is evidence that the reaction, which occurs between 400-600°C, relates to a Cu, Sn or Se reaction since it was observed when in an ampoule containing Cu, Sn and Se, while it was not observed in ampoules containing only Zn and Se. The most commonly used ramp rate was 500°C in 1 hr followed by max temperature in 24 hrs. This was optimized empirically so that it is slow enough to avoid violent reactions while being fast enough to avoid substantial segregation of liquid phases such as Se ($T_m=220^\circ\text{C}$), Sn ($T_m=232^\circ\text{C}$), and Zn ($T_m=420^\circ\text{C}$).

Rate of cool-down appeared to have a small effect on crystal growth, however Se was noted on the sides of quenched ampoules from the residual Se overpressure at the quench temperature. This resulted in a dramatic red color for quenched ampoules. Additional effects of the rate of cool-down are discussed in the next chapter.

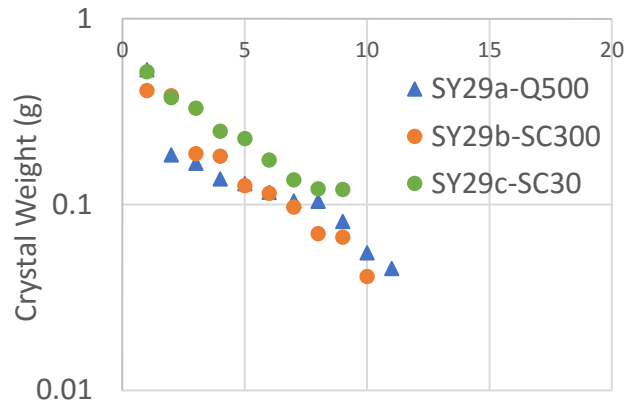


Figure 2-24: Photo of quenched ampoule and histogram of crystal size

Ampoules sizes of 10, 12.5 or 15 mm inner diameter were utilized as seen in Figure 2-25, depending on quantity of desired precursor. A balance between ampoule size and elemental quantity was found to be important for uniformity. As discussed, a significant portion of the elemental segregation is a result of buoyancy effects. When the height of the boule can be kept to a minimum by choosing large diameter ampoules relative to the precursor quantity the extent of the segregation can be reduced. Smaller ampoules and thus tall boules were used for the majority of growths due to their ease of handling and sealing however current and future work has focused on wider ampoules and thus shorter boules to address concerns of phase segregation.



Figure 2-25: Photos comparing ampoule size for 10 and 15 mm ampoules both with 10g of loaded elements.

Most ampoules were grown in the vertical orientation, hung from a quartz rod welded to the top of the ampoule. However, the horizontal growth configuration was utilized in a subset of growth processes. In the latter configuration, the ampoules were laid at a ~30 degree incline to promote the condensation of material in the lower portion of the ampoule. Vertical orientations promoted cylindrically dense boules, however element segregation related to density differences were more frequently problematic. Multi-mm crystal growth was achieved in both methods however the majority of crystal growths were performed in the vertical orientation due to both availability of equipment (two dedicated vertical furnaces), as well as the compact and dense resulting boules.

2.7 Summary

CZTSe crystals in excess of 4 mm were achieved for the first time both above and below the melt without an external flux agent. The reaction kinetics of both methods were explored and optimized for crystal growth and phase purity. For above melt growth the limiting step is likely diffusion of Cu and Sn through the solid CZTSe product layer and the key variable is a slow cool down as the melt point moves through the ampoule. For below melt growth, slow diffusion in solid state and control of nucleation are the

key challenges. A liquid Cu_2SnSe_3 phase is suspected to play a role in enabling mm-sized crystal growth which hasn't been achieved in literature.

While simple in premise, crystal growth requires patience, understanding and significant optimization. The effects of numerous variables were tested and the optimal conditions are summarized below.

Table 2-3: Summary of growth variables

Variable	Optimal	Explanation
Time	>20 days	Crystal growth continues with increasing time beyond 20 days, however growth of largest crystal may slow possibly due to competition of grains or depletion of Zn and increasing diffusion distances.
Temperature	>750-780°C	Higher temperatures below the melt gave generally larger crystals and more phase pure boule.
Cu stoichiometry	Cu/Zn+Sn = 0.7 or less	Low Cu in starting boule increased crystal size. Availability of Zn may be limiting element to continued crystal growth.
Se stoichiometry	Stoichiometric by valence balance	Excess Se decrease crystal size and 33% excess Se resulted in extreme phase segregation. Thermo may favor Se rich phases over CZTSe such as SnSe_2 $\text{Cu}_2\text{SnSe}_{3+x}$. Low Se also gives poor crystals and poor electronic properties.
Zn-precursor	Zn powder or small nuggets	Zn is slow to diffuse → Zn powders provide improved Zn uniformity however potential for evaporation of Zn and formation of ZnSe above boule.
Ramp rate	1hr to 500°C, followed by 23hr to max temp	Very slow ramp may allow excess element segregation before reaction. However, need to be slow enough to avoid rapid violent reactions that occur between 400-600°C and avoid excess overpressure of unreacted anion.

Chapter 3

MODIFICATION OF DEFECTS IN $\text{Cu}_2\text{ZnSnSe}_4$ SINGLE CRYSTALS

3.1 Abstract

Understanding and controlling the complex defect chemistry in CZTSe is the number one issue contributing to the V_{OC} deficit. In this chapter, single crystals are examined through photoluminescence and hall measurements to give new insights into defects carrier concentration and bulk properties of CZTSe. New passivation methods are developed for surfaces, and bulk defects are explored by variations in stoichiometry and dopants. Additional insights into reasons why bulk compositions are found to be Cu-poor and Zn rich are demonstrated. The bulk incorporation of Na, which is a critical dopant, is measured for the first time. Further manipulation of defect populations by temperature equilibria are demonstrated to change sub- E_g defects critical for band-tailing. Single crystal devices are demonstrated for the first time, and based on modification of surface and bulk defects as discussed throughout the chapter, a 7.8% efficient single crystal is demonstrated with a voltage deficit equal to record thin film devices.

3.2 Overview

Overcoming the V_{OC} deficit in CZTSe heterojunction solar cells requires first identifying and then controlling both cell-based and materials-based limitations of the device. At the cell level the heteropartner choice and interface issues are key. At the materials level, the defect landscape of the semiconductors is key, in particular bulk

defects in CZTSe which govern doping, carrier recombination, band edges and surface termination.

In an ideal homojunction cell the maximum open circuit voltage that can be maintained across the device at room temperature is the semiconductor band gap energy minus a few kT . In a heterojunction cell in which the entire space charge region is located within the p-type material, in which all of the photocurrent is generated, the maximum voltage is the band gap minus the electron affinity difference, minus the Fermi energies in each semiconductor. Therefore, with no electron affinity mismatch and high doping –Fermi energies located near the valence band in the p-type and conduction band in the n-type material– the maximum voltage is the band gap minus a few kT of the p-type semiconductor. Real heterojunction solar cells must contend with some degree of electron affinity mismatch, interface states, and bulk recombination. In this work, we will focus on understanding and modifying both bulk and surface/interface states. We utilize CdS as a junction partner which has been shown to have acceptable band alignment [43].

In the 4-element CZTSe compound semiconductor, the native defect population is complex as depicted in Figure 3-1. While many CZTSe devices have been fabricated and many electrical measurements have been performed, the location, identity, and effect of the defects controlling CZTSe are not fully understood. A few key messages are clear from hundreds of experimental results. Cu-poor and Zn rich solar cells work best, deep defects of unclear origin limit lifetimes to <10 ns, and high levels of cation disorder appear to cause significant fluctuations of the band edges and the resulting band-tailing further limits V_{OC} [14], [29], [44], [45].

Many of the physical insights into the origins of the defects has been provided by Density Functional Theory (DFT) calculations. The key conclusions are: Cu_{Zn} and V_{Cu} acceptors are expected to be the dominant defects explaining the p-type behavior and trends in majority carrier concentrations. These defects, among others, are very highly compensated by other intrinsic defects forming neutral complexes –of which the most prominent is $[\text{Cu}_{\text{Zn}}+\text{Zn}_{\text{Cu}}]$. Significant cation disorder, particularly due to Cu-Zn antisite formation, as depicted by the aforementioned complex, is favorable and may result in shallow states or local areas of reduced E_g which may explain the aforementioned band tails. Lastly, the origin of deep defects is not fully clear but Se vacancies and Sn-related defects are predicted to be deep [28], [42], [46]–[49].¹¹

Confirming the aforementioned defect origins and controlling the resulting defects in a predictable fashion has proven difficult. This is in part due to complexities in thin films such as grain boundaries and metastable phases, as discussed in Section 1.3.1. Single crystalline materials offer one way to reduce ambiguity as we study the CZTSe system.

¹¹ Shi-you Chen and Su-Huai Wei at NREL have performed the most detailed DFT calculations for CZTSe-related materials compared to dozens of other groups in the literature, and their calculations are cited as the default throughout this work. NREL calculations have been performed with the more rigorous HSE method and utilize a larger 128 atom super-cell while most of the literature base cites 64 atoms. The NREL theory group has pioneered DFT calculations for optoelectronic materials over the last 25 year including calculation of phase diagrams [176], band offsets [177], bulk defects [178], [179] and surfaces [57]. The best review of DFT calculations for CZTSe is Ref. [42] and is cited frequently throughout this work.

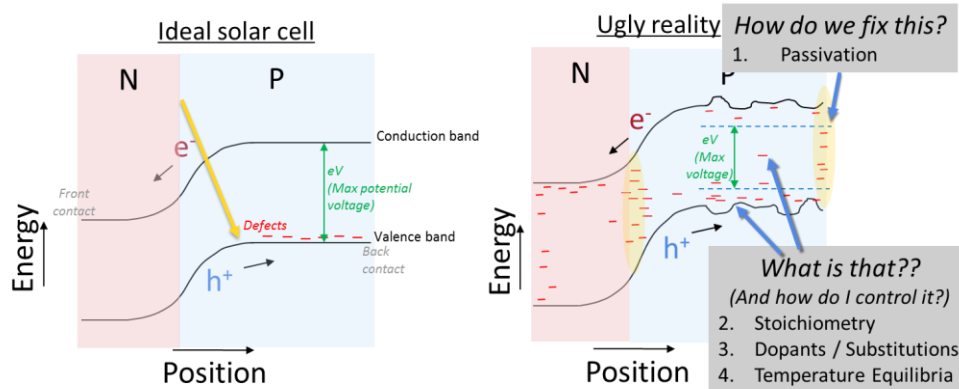


Figure 3-1: Depiction of defects in ideal solar cell and more complex conceptual picture facing multinary semiconductors such as CZTSe. Real band alignment for CZTSe/CdS hetero junction is Type I with ~ 0.4 eV spike due to large E_g of n-type window layer (not drawn).

A critical goal of this work –to demonstrate reduced V_{OC} deficit– was undertaken as part of a collaboration between IBM, UCSD and Harvard under a DOE Sunshot award. To achieve the goal, thermodynamic insights offered by DFT modeling at UCSD combined with device fabrication experiences at IBM revealed a series of device performance bottlenecks. For single crystals, improving surface passivation was found to be the first bottleneck that needed to be addressed. As with our eyes, with many measurements, one cannot “see” the bulk properties without first “seeing” the surface. Section 3.3 discusses crystal surfaces and methods for surface passivation. The following sections address understanding and improving bulk defects.

The most basic method for manipulating the bulk defects in multinary systems is altering composition. Solar cells are typically made Cu-poor, with deviations in excess of 15% from stoichiometric $Cu_2ZnSnSe_4$ and while there are some theories underlying our understanding of the optimal composition, it is primarily based on empirical device results. In Section 3.4, we provide additional insight into the optimal

stoichiometry region by measuring carrier concentrations, and sub- E_g defects of single crystals.

Dopants and substitutions offer a related method of manipulating bulk defects and passivating surfaces. Na is the most common dopant in this system and appears to play a critical role in highly efficient devices. Despite the importance, the relative role of Na at grain boundaries vs. Na in the bulk lattice incorporation is not clear. In Section 3.5, Na incorporation into the bulk is measured for the first time from a diffusion profile into a bulk CZTSe single crystal. A further investigation of the effects of Na on sub- E_g states is discussed in Chapter 4 on thin films.

Temperature processing also plays a key role in manipulating defects. Heat treatment processes are critical in phase formation, growth and manipulating defect quantity. Section 3.5 details a less frequently considered aspect of temperature processing: temperature equilibria. Quenched and slow-cooled single crystals provide a path to examining snapshots of defect pseudo-equilibria at different temperatures. Through fundamental relation between temperature and point defect concentrations, reduced defect densities can be achieved. The potential for reduction of Cu-Zn antisites which may be controlling band-tailing in this system is of particular importance, and therefore this investigation was pursued in the most depth. These concepts are further applied to thin films by low temperature annealing in the following chapter.

A comprehensive investigation of all defect manipulation is not possible in the scope of a single work. Therefore this work highlights the key variables for achieving high V_{OC} for single crystals and tries to explain the findings through comparison to calculations from first principles and the broader available literature. The final section of this chapter (Section 3.7), involves the summation of all of the learning from

passivation, stoichiometry and temperature equilibration and highlights current champion efficiency single crystal solar cells.

In the next chapter, Chapter 4, the same concepts –passivation, stoichiometry, doping, and temperature equilibria– are applied and investigated in thin films, and differences are compared and future directions are suggested.

3.2.1 Photoluminescence Background

Photoluminescence is used frequently in the course of this work and the critical aspects of interpretation necessary for this work are briefly highlighted. More detailed derivation of the physics can be found in references [50]–[52] but are left out of the body of the text for length. Additional details of the equipment, and brief modeling of PL spectra for related phenomenon are given in the Appendix Pg. 222. The appendix includes measurements of PL injection conditions, as well as modeling of PL spectra as a function of E_g fluctuations, and PL intensity as a function of temperature among other aspects (Pg. 228).

The interpretation of PL has two aspects: total integrated PL intensity and PL spectral distributions. The total integrated intensity is proportional to radiative efficiency, and is governed by competing non-radiative processes such as defect related Shockley-Read-Hall (SRH) recombination and surface recombination. By reducing these SRH or other non-radiative recombination (increasing $\tau_{non-rad}$), the radiative efficiency, η , improves as seen in Equation 1.

$$\eta = \frac{1}{1 + \tau_{rad}/\tau_{non-rad}} \quad \text{Equation 1}$$

τ_{rad} is the radiative lifetime, which is governed by recombination type and energy [52]. Therefore reducing non-radiative defects and surface recombination will

often not affect τ_{rad} . This means the radiative efficiency and therefore PL intensity will correlate with minority carrier lifetimes. This fact –PL intensity as a metric for material quality– is used throughout this work, and the expected relationship between PL yield, minority carrier lifetimes, and V_{OC} for this material has been confirmed in the literature [53]. In certain cases, where treatments change the radiative recombination type or energy, the radiative lifetime can also change. These cases are discussed in more detail for discussion of air annealing.

PL intensities were most frequently measured with a PL imaging tool with an diffuse 808 nm laser (1.53 eV) due to the ability to create repeatable uniform imaging conditions. Calculations using the laser setup suggest an upper bound of 10^{16} electron-hole pairs/cm³ are created, which is on the border of low-high injection conditions. The details of the setup and the calculations can be found in the Appendix.

The spectral PL distribution expresses the distribution and density of states near the band edges. At room temperature the PL spectra should give the $E_g + kT/2$ however significant band-tailing and potential fluctuations, as will be shown in this work, result in lower energy emission [54]. Band tailing and sub- E_g states can be most readily seen at low temperatures, where the thermal energy, kT , is small and therefore carriers are localized to the band tails and sub- E_g states.

A pseudo-PL spectra was obtained with the 808 nm PL image tool by inserting a series of bandpass filters in front of the detector. This allowed rough determination of PL peak energy and PL shape. A dedicated PL spectra tool with no imaging capability but with a monochromator and pulsed spot laser, were utilized for more accurate PL spectra measurements discussed in Section 3.6 and Chapter 4.

The PL spectra were measured using a Hamamatsu time-correlated single photon counting (TCSPC) system equipped with an InGaAs PMT detector cooled to -80°C . A 532 nm (2.33 eV) pulsed laser was used for excitation. The laser repetition rate was 15 kHz with a 1 ns pulse width and a ~ 170 micron spot size. A helium cryostat was used for low temperature measurements, and intensity dependent measurements were achieved by passing the laser through a variable neutral density filter. Based on measured power, the upper bound for e-h pair density was calculated to be between 10^{18} - 10^{20} depending on neutral density filter position. This translates to high injection for the duration of the laser pulse. More details of the setup and calculations can be seen in the appendix Pg. 222.

Both PL intensity, which relates to carrier lifetimes, and PL spectral distribution, which relates to the distribution of sub- E_g states, will be discussed through the remainder of the work.

3.3 Passivation

In device fabrication the electrical junction is formed on the CZTSe crystal or film surface. The chemical, structural, and electronic state of this surface region prior to junction formation influences the interface obtained after junction formation. The objective is to minimize interface states that produce high recombination currents, or conduction band spikes that prevent electron minority carrier collection. The processes used to prepare a surface with low recombination are collectively referred as “passivation”, and a junction having low recombination current is said to be “passivated”. Passivating processes can be generally intrinsic, such as cleans, chemical etches, and surface reconstruction in vacuum, or extrinsic such as doping, oxidation, or passivation layers. A metric for assessing the relative degree of passivation is

photoluminescence intensity. At 532 nm, 90% of the light will be absorbed in the top 140 nm of CZTSe, and therefore the vast majority of carriers are within one diffusion length of the surface and therefore PL intensity is found to be very sensitive to the surface condition [55], [56].

3.3.1 Natural Crystal Growth Surfaces

After extraction, surfaces of crystals were examined by optical microscope, SEM, and Raman to investigate uniformity and phase homogeneity. Cu_2SnSe_3 (CTSe) and SnSe_2 were found to decorate some crystal facets, while other facets appeared to be single phase CZTSe. As seen in Figure 3-2, secondary surface phases were seen most easily in optical microscope images and can be clearly identified in Raman spectra.

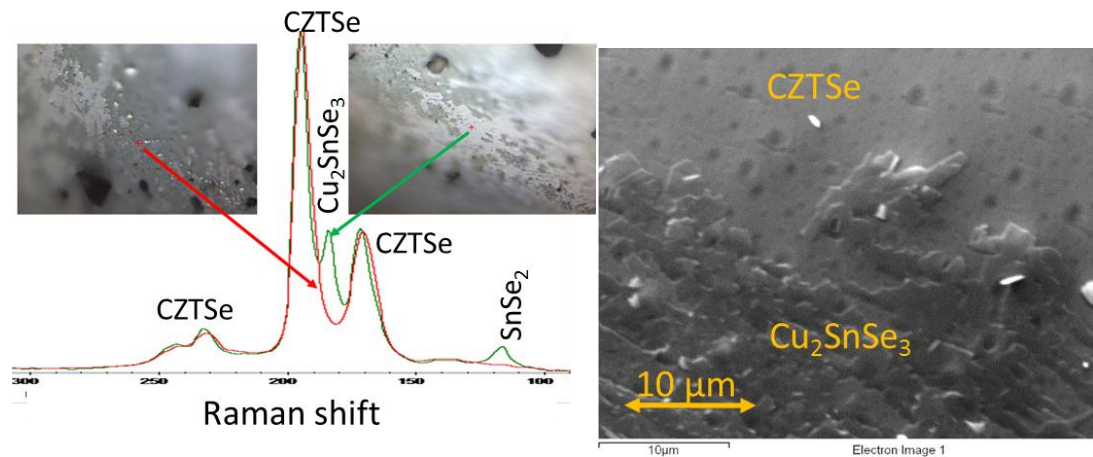


Figure 3-2: Raman and optical and SEM images of as extracted crystals surfaces

The origin of the secondary phases fits the concept that crystal growth is assisted by a CTSe liquid phase as described in Chapter 2. SnSe_2 is also expected to be liquid at

growth temperatures and since crystal growth were typically performed with Cu-poor target stoichiometry, SnSe_2 is likely to be present during growth.

Unfortunately, the as-grown crystal surfaces do not provide suitable electronic properties for devices. CTSe is a lower bandgap phase and will therefore localize carriers and increase recombination. In certain stoichiometries, CTSe can be degenerate and therefore can potentially shunt solar cells. Even after removal of Cu_2SnSe_3 secondary phases, first principle calculations suggest that CZTSe facets that are Cu and Sn-rich are likely to increase recombination [57]. Measurements of PL intensity on a variety of as grown crystals appears to validate this prediction. PL images of crystal surfaces are generally low PL intensity and non-uniform, consistent with high recombination and a non-uniform distribution of secondary phases.

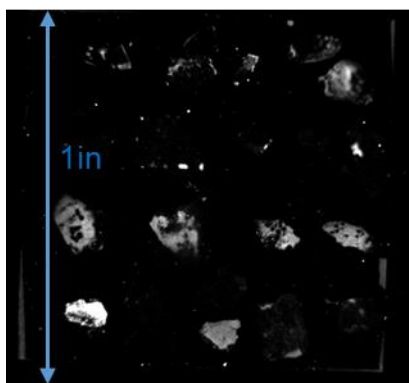


Figure 3-3: PL image for various as-grown crystals. (SY16, SY22, taken at 30Ax10sec, 1300nm bandpass, 10K max white)

To avoid the second phases and Cu and Sn-rich terminating surfaces, polishing and etching were pursued and are discussed in more detail the following sections.

3.3.2 Polishing

Polishing allows for the removal of the detrimental effects and phases at growth surfaces and provides a better representation of the crystal bulk. In addition, flat and parallel surfaces of controlled thickness can be obtained which is critical for many methods of characterization.

Crystals were attached to a polishing chuck glycol-phthalate thermal adhesive and then dry-polished with a series of fine SiC sand papers (minimum 2400 grit), followed by a series of wet-polishes with an alumina solution with 0.5 and 0.03 micron particle size. A final polish of dilute 0.1% Br-methanol on lens paper was used for later crystals. The crystals can be removed from the polishing chuck after heating to $\sim 45^{\circ}\text{C}$ in a hot plate and then are rinsed in 50% toluene-acetone solution with agitation for ~ 5 minutes to remove excess glycol-phthalate. The crystals are finally rinsed in methanol and then DI water. When needed, both sides of the crystal were subsequently polished. Crystal thickness can be controlled in ~ 25 micron increments with the polishing chuck although limited to the mechanical stability of the crystal. Crystals were typically polished to final thickness between 0.7 - 1 mm.

The as-polished crystal surfaces often have lower but more uniform PL intensity than the natural crystal facets, suggesting additional damage is done to the crystal surface. Chemical etching and annealing were investigated to remove surface damage and passivate the crystal surface.



Figure 3-4: Photo of polished crystals mounted on polishing chuck after 0.03 μm alumina polish

3.3.3 Br Etching

Br-methanol etching has been used to thin both CIGS [58]–[62] and CdTe [63], [64], and more recently has been investigated for CZTSe [65]–[67], however the final surface condition and the electronic effects of the etch are not well known for CZTSe. In addition, the selectivity and etch rate for CZTSe secondary phases are not reported.

Etching calibrations were performed on thin films –grown by co-evaporation as discussed in the next chapter– for CZTSe and additional films of CTSe, ZnSe and SnSe secondary phases to confirm the etch-rates as a function of Br concentration. Linear rates were found with concentration and secondary phases were found to etch more quickly than CZTSe.

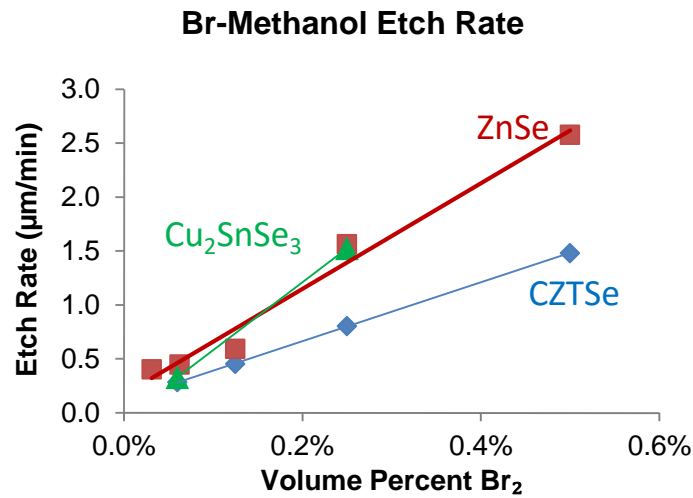


Figure 3-5: Etch rate of Br-methanol for CZTSe and secondary phases.

Prior to etching, surface composition as determined by XPS was found to be an exaggerated version of the bulk stoichiometry. Cu-poor samples had significant Cu-depletion of the surface, while near stoichiometric samples appeared to have Cu-rich surfaces. For samples with bulk composition pinned at the edge of the phase diagram, such behavior would be expected, with further deviations in stoichiometry segregating as surface layers or secondary phases. After etching, surfaces were found to be Se-rich and cation ratios shifted slightly closer to the expected bulk cation ratios (Figure 3-6). No traces of Br or Br-related compounds could be detected on the terminating surface via XPS scans. A anion terminated surface is also noted in CIGS and CdTe [58], [64], which for CZTSe, is predicted to reduce recombination [57]. The FWHM for Raman spectra is found to broaden from polishing, likely due to the mechanical damage, and is restored to a narrow peak after Br-etching. This can be seen in the Raman spectra on the right in Figure 3-6.

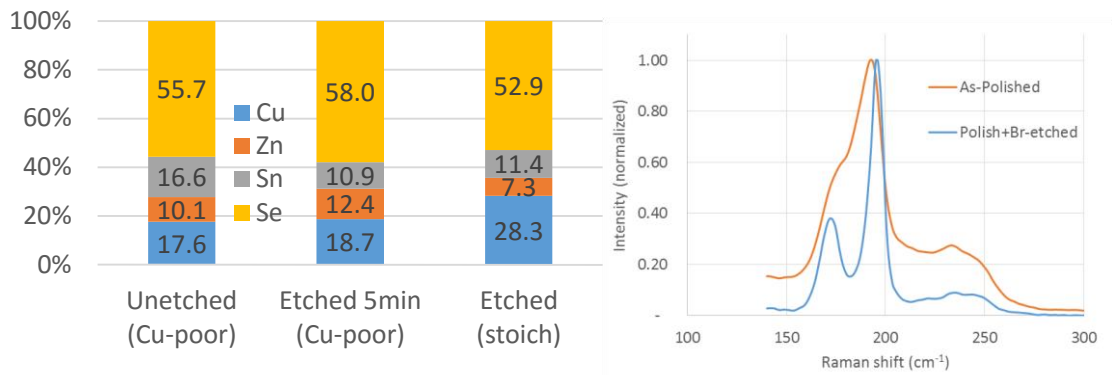


Figure 3-6: Composition of crystal surface by XPS before and after Br-etch. Right: Raman signal of crystal before and after etching.

Br-etching was found to be critical part of the surface passivation process when making a successful device. As shown in Figure 3-7, PL intensity increases strongly as a function of etch time suggesting a large decrease in surface recombination velocity. PL peak energy does not change which suggests the increase in PL intensity is explained by a reduction in non-radiative defects rather than a change in radiative emission pathway.

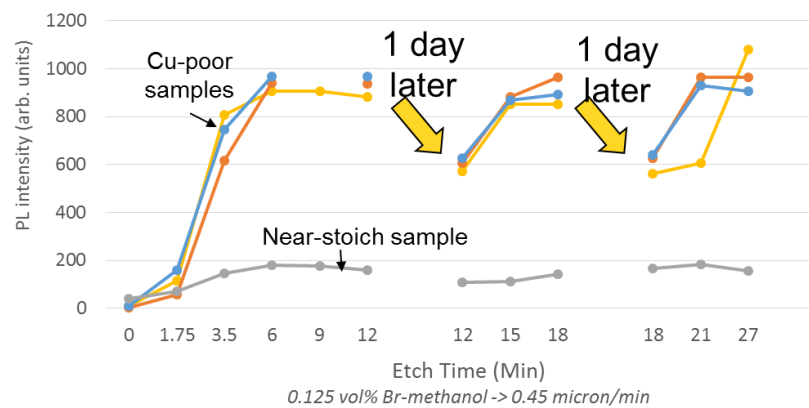


Figure 3-7: PL intensity as a function of Br etch time.

After approximately 6 minutes of etch time on polished crystals, the PL intensity plateaus suggesting the surface recombination is no longer significantly changing. The origin of the PL improvement continues for long etch times, as multiple microns of the crystal surface is etched away. This suggests that in addition to modifying the terminating surface, removal of the top surface layer may in-part explain the change in PL intensity. A damaged surface layer is expected in mechanically polished crystals and the change in surface quality confirmed by a decrease in Raman peak width with increasing etching. Based on the plateau in PL after 6 minutes and calibrated etch rates as shown in Figure 3-5, this layer appears to be ~3 microns thick. In addition to removal of a damaged surface layer, ultraviolet photoelectron spectroscopic (UPS) measurements of Br-etched films performed at IBM, suggest that an additional origin of passivation may be due to upward band-bending which will repel electrons and lower recombination [68].

The results additionally suggest there is no significant degradation of the surface after long etch times, although the surface is found to degrade by 30-40% in PL intensity after 24 hours of storage in a N₂ desiccator with limited air exposure. The surface can be restored by ~3 minutes of further Br etching. The mechanism of the degradation with time or atmospheric exposure requires further understanding since in certain samples, no changes were noted with days or even weeks of atmospheric exposure.

Further confirmation of the improvements and importance of surface passivation can be seen in device results. Devices were made on similar composition single crystals from the same ampoule with varying Br-etch time. Similar to PL results, V_{OC} improved with increasing etch time which would be expected as surface recombination is reduced.

Table 3-1: Device parameters as a function of etch time. The J_{SC} values were not measured with precision due to the small device area and difficulty accounting for probe shading losses.

Br-etch time	Voc	Jsc
1 min	179 mV	>20
5 min	244 mV	>20
10 min	277 mV	>20
10min +AA	372 mV	>25

Despite dramatic improvements in PL and V_{OC} , further optimization of the terminating surface after etching is likely needed. Champion efficiency thin films, after significant optimization, use an air-anneal before the CdS bath [14]. The effects of this anneal on single crystals are explored below.

3.3.4 Air Annealing

Champion IBM films are annealed on a hot plate set at 375°C x 10 minutes in lab air, although measured film surface temperatures are ~275°C. This is found to increase PL intensity up to 100x which is presumed to be due to passivation at the exposed surface and at the grain boundaries. A SnO_x phase has been shown to form at the grain boundaries from air annealing, and it has been hypothesized that this high bandgap phase contributes to passivation of the grain boundaries by confining electrons [69], [70]. Techniques such as cathodeluminescence are needed to evaluate this further. The oxide is expected to be removed from the film surface during the CdS deposition in the reducing chemical bath deposition, eliminating the insulating barrier while leaving passive grain boundaries intact. The nature of the CdS interface and offsets may passivate the surface further.

Single crystals provide an interesting comparison, since only surface and bulk can be affected by air annealing. The lack of grain boundaries suggests that the air anneal would have less effect on crystals. In addition, air annealing may affect prepared single crystals in a different way due to differences in the terminating surface as compared to thin films. Annealing a crystal may allow surface reconstruction from either a mechanically damaged, or Br-etched surface. Interestingly, despite the drop in PL due to increasing exposure to atmosphere, oxygen is reported to be a beneficial part of the annealing atmosphere [69], [71].

Unfortunately determining changes in surface recombination from annealing is more complex than etching. While PL intensity from Br-etching provides a very strong correlation with V_{OC} , air annealing has a more varied effect. It is expected that etching only affects the top nanometer in a single crystal, however given sufficient treatment time, air annealing could change both surface and bulk properties.¹² In fact, the PL energy after annealing is found to shift, which is likely to alter the radiative transition probability which in turn changes the PL intensity. This may explain the more nuanced correlation between V_{OC} and PL intensity for annealed films. A shift of the PL emission to higher energy is generally considered to be beneficial (move to shallower defects or increasing bandgap), yet other things being equal, the PL intensity will likely decline

¹² It is unlikely that diffusion from the surface will have much effect on the bulk of the crystal in the temperatures (below 500°C) and timescales of interest (minutes), however local diffusion, on the order of multiple unit cells can manipulate intrinsic defects during annealing by creating or removing antisites, interstitials and vacancies. Additional diffusion of defects to form more stable defect complexes is also likely. A rough estimate for the characteristic diffusion distances over the 10 min anneal at moderate temperatures can be calculated to between ~1 nm to ~1 micron for a range of assumed diffusivities.

due to the reduction of radiative transition probability for higher energy transitions [52], Pg. 147.

The highest achieved increases in PL intensity with air annealing of single crystals are shown in Figure 3-8. Up to 10x increases in PL intensity are noted in single crystals, which although significant, is less than the 100x improvement sometimes found for thin films. The larger improvement noted for thin films is likely related to the large surface area of grain boundaries, which have been shown to be modified by the anneal [69]. For samples subjected to polishing only, where a damaged surface was expected, PL intensity increased by a factor of 20, although PL intensities were still far lower than those achieved by Br-etched crystals. PL peak energy was also noted to shift to lower energies as shown in Figure 3-8B. This shift to lower energy transition may in part explain the PL intensity increase. The origin of the shift in PL energy is believed to be related to a change in Cu-Zn cation ordering discussed in more detail in Section 3.5.

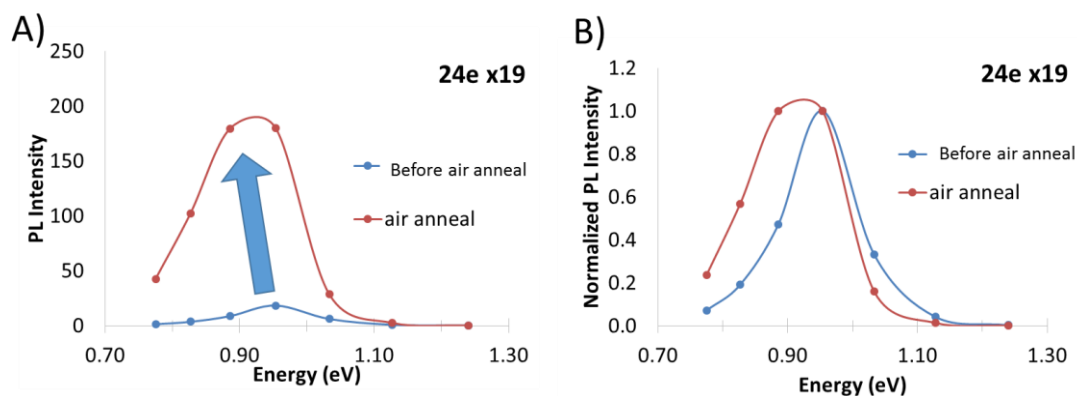


Figure 3-8: Effect of air anneal on PL intensity and energy. A) PL intensity increase (SY24E x19). B) Normalized PL intensity showing shift of PL peak for the same sample.

In other single crystals, only modest increase or significant decrease in PL intensity was noted. PL intensity was found to drop by a factor of 3 in certain cases. The causes of the variations in PL with air annealing are not yet clear, however investigation is ongoing. A selection of results performed at the IEC, under controlled flowing 20% O₂ atmosphere can be seen in Figure 3-9. Interestingly, the highest PL improvements were noted using the 375°C hot plate setup at IBM under ambient atmosphere, and the more controlled 20% O₂/N₂ atmosphere at IEC has, thus far, not shown similar PL intensity improvements. This raises questions about the effect of H₂O however a controlled study of the effect of humidity has not been performed. Initial sample composition, as well as whether samples were originally quenched or slow-cooled, also appear to explain some of the variations noted with air annealing, however more direct comparisons are needed.

Despite the mixed story for PL intensity, improved device operation was generally noted for crystals that were air annealed prior to CdS deposition. Device results for air annealed samples are discussed in Section 3.7.

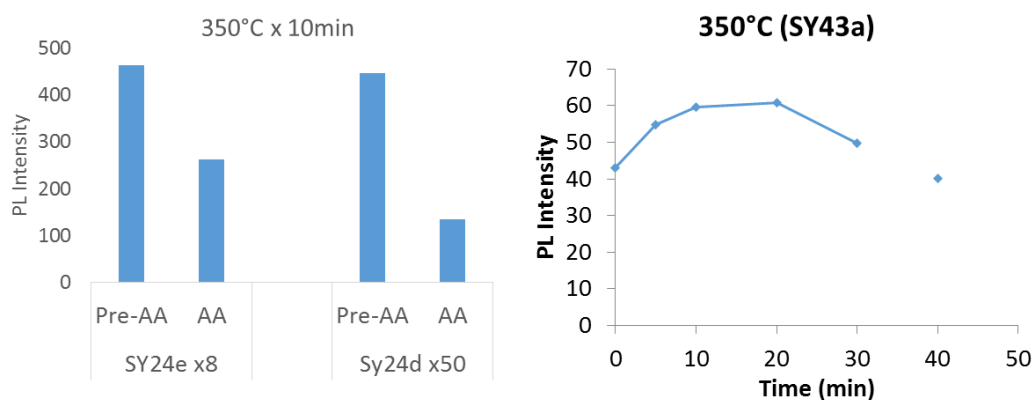


Figure 3-9: Varied effects of AA on PL intensity. [SY43a measurements conducted by Mike Lloyd]

3.3.5 Alternative Passivation Methods: ZnSe Passivation Layer

A separate method for passivation involves depositing a capping layer on exposed surfaces to reduce surface/interface defect density by lattice matching, and further reduce recombination through band bending. This has been strikingly demonstrated with CdTe epitaxial single crystals which have been grown as a double heterostructure with thin layers of (MgCd)Te to passivate the surfaces. With this technique, CdTe/MgCdTe has achieved PL radiative efficiencies comparable to the best GaAs/AlGaAs DH structures, and carrier lifetimes have been raised to 0.83 μs , an improvement of $>10^5$ compared to non-passivated single crystals [72].

For similar reasons, ZnSe was investigated as a passivating layer for CZTSe surfaces taking advantage of the close match in lattice constant and the ability of ZnSe to form a Type I heteroface: $\chi_{e\text{ZnSe}} = 4.09$ eV ($E_G = 2.67$ eV, $\chi_h = 6.76$ eV), $\chi_{e\text{CZTSe}} = 4.56$ eV ($E_G = 0.98$ eV, $\chi_h = 5.54$ eV). ZnSe was deposited through a 1.5 mm mask on to single crystals surfaces by co-evaporation. The whole crystal surface was etched with Br-methanol prior to loading and was held at 300°C during deposition for an expected layer thickness of ~ 125 nm. A PL image of the structure is shown in Figure 3-10.

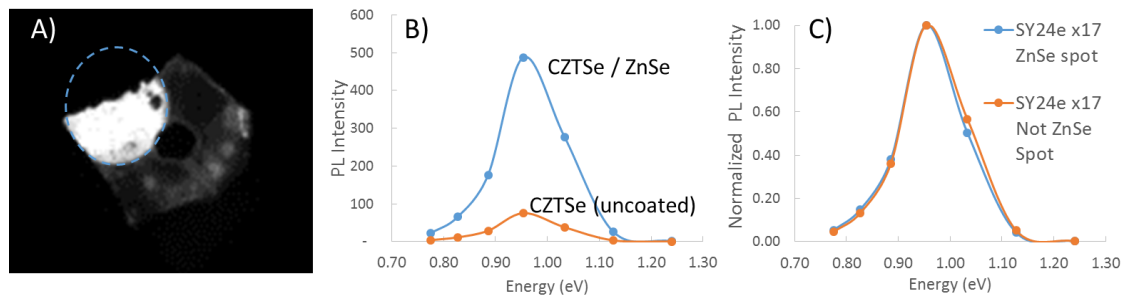


Figure 3-10: PL image and intensity of ZnSe/CZTSe. A) PL image (Note mask was not centered during deposition), B) PL intensity, C) normalized PL intensity

Greater than 10x increase in PL intensity was noted for regions of ZnSe deposition. Similar to Br-etching, no change in PL energy is found which confirms the reduction in surface recombination velocity. Three aspects may contribute to the reduction in surface recombination velocity (SRV). First, the similar lattice constants of CZTSe and ZnSe allows for improved interface quality with reduced defect density. The lattice mismatch = 0.4% and 0.1% for a_0 and c_0 axes respectively [36], [73]. Second, the wider 2.7 eV E_g of ZnSe creates a type I band alignment between the absorber and the passivation layer [74]. This alignment confines carriers away from the CZTSe surface further reducing interface recombination. And lastly, theoretical predictions suggest additional Zn-enriched CZTSe surface –which may occur by diffusion as a result of the 300°C ZnSe deposition– increases the E_g slightly by reducing the valence band which further pushes carriers away from the interface to reduce SRV [71].

Separate attempts to create Zn-enriched surfaces without ZnSe were not successful due to decomposition of the surface and loss of Se during annealing. Further optimizing annealing conditions to enrich surfaces in Zn are a promising path for future improvements in passivation. Interestingly, despite the large conduction band spike expected for the interface, ZnS has been used with moderate success as a buffer layer for CZTS [75]–[78]. Additionally in co-evaporated CZTSe/CdS films, V_{OC} has been shown to be positively correlated with Zn-content at the surface of the CZTSe. XPS confirmed the highest achieved V_{OC} (400 mV) was achieved when only Zn and Se were detected at the surface [71]. The above results help explain the previously noted improvements.

The low interface recombination for ZnSe in CZTSe helps explain why films with very high quantities of Zn, and considerable quantities of ZnSe, can still achieve

relatively high efficiency. ZnSe is found to segregate towards grain boundaries and surfaces during thin film growth [79], and while thicker layers on the surface or back contact can potentially block current [80], ZnSe segregated at grain boundaries may in fact improve passivation. Excess ZnSe at grain boundaries has been noted in Auger nanoprobe measurements performed by collaborators at the University of California at San Diego of high-efficiency CZTSe thin films fabricated from the baseline process for current world record CZTSe devices [81].

3.3.6 Effects of CdS

The most critical surface for a solar cell is likely the interface with n-type junction since high concentrations of photo-excited holes and electrons will be generated near this junction, and all of the minority carriers are required to cross this interface. The interface partner must provide transparency, proper band alignment, and ideally strong surface passivation.¹³ CdS is the most common n-type layer used in the literature and in this work. The band alignment of CdS/CZTSe has been measured to be a spike of ~ 0.4 eV, however downward bending noted at the CZTSe surface suggests that traps at the surface could lead to problematic interface recombination [43]. These are competing mechanisms. As previously discussed, PL intensity measurements provide a means of gaining insight into carrier lifetimes, however due to the presence of a PN junction and resulting space charge region, additional understanding is needed.

¹³ A sub-surface induced homo-junction has been reported for CIGS however first principle calculations suggest this may not be possible due to fermi level pinning in CZTSe [42].¹³

The space charge region is expected to extend mainly into the CZTSe absorber with a width of ~50-200 nm [31]. Using Beer's law, 90% of photon absorption can be calculated to occur in the top ~600 nm given the absorption coefficient for CZTSe for the 808 nm laser used for PL images in this work [82]. This suggests, a non-trivial portion of photo-excited carriers will be created in the space charge region, and since charge separation is typically much faster than the radiative lifetime of photo-excited carriers, PL intensity can be quenched [83], [84]. This quenching is balanced by increasing passivation, with some similarities to ZnSe. The lattice match for CZTSe with CdS in the meta-stable zinc-blende crystal structure is +2.2 to 2.6% compared to -0.1 to 0.4% for ZnSe depending on orientation [36], [73]. Generally, wurtzite is the preferred crystal structure for CdS where no lattice match is found under the primary (100), (001) axes. A form of epitaxy may still be possible through arrangement across similar anion sub-lattices which can be found off the central crystal axis (i.e. (112), etc...) [85]. However due to the chemical bath deposition at low temperatures, as deposited CdS is found to have low levels of crystallinity which improve with annealing [86]. Interestingly, large improvements in V_{OC} have been recently noted in this work after annealing the completed device at temperatures below 200°C. Improvements in the latest champion single crystal device of >0.5% absolute were noted with annealing potentially attributable to improved CdS/CZTSe interface although more follow-up investigation is needed. This is discussed in more detail in the Device section (3.7).

For single crystals, PL intensity was frequently found to be highest when coated with CdS, however additional before and after comparisons are required to confirm the findings. As seen in Figure 3-11, PL laser intensities had to be decreased to avoid overexposing the PL image. The increase in PL intensity suggests CdS, similar to ZnSe,

is passivating the surface region of CZTSe. CdS coats the entire crystal surface in the samples below and the dark circle in the middle of the crystal sample is coincides with the area of the ZnO/ITO. Absorption of the incident laser is unlikely to explain the decrease in PL intensity noted, since the ZnO/ITO have E_g much higher than the 808 nm (1.53 eV) laser. Literature results suggest this decrease is due to an increase in strength of the CdS junction with ZnO deposition, which increases the number of carriers quenched by charge separation [83]. The opposite behavior, a decrease in PL intensity with CdS, is exhibited by thin films and is discussed in the thin film Passivation section in Ch. 4.

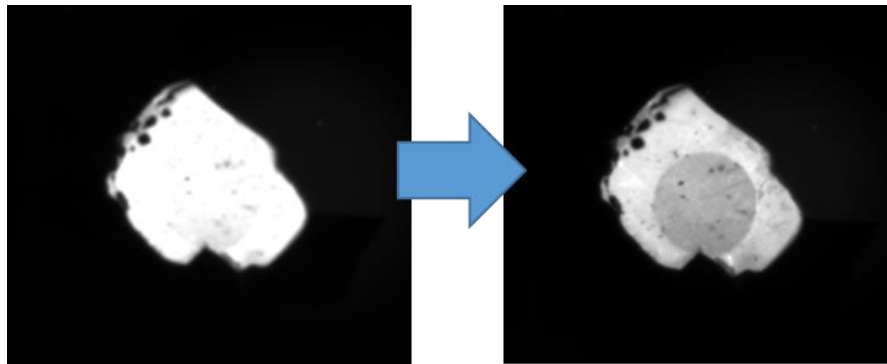


Figure 3-11: PL image of CdS coated crystal. Laser fluence had to be reduced (30w, Left) to avoid saturation (15 W, Right). CdS covers the entire crystal surface, and the dark circle represents ZnO/ITO layer.

3.3.7 Summary of Passivation

Passivation was found to be critical for single crystal optoelectronic properties. Growth surfaces are found to have high recombination due to high Cu and Sn and polished surface are found to be mechanically damaged. Br-etching is shown remove the damaged surface layer and improve both PL intensity and device V_{OC} . Air annealing,

which is used on champion thin films devices, is also found to be helpful for single crystal devices although the effects on PL intensity and passivation are not clear. For films, air annealing has been shown to passivate grain boundaries and results in an increase 10-100x increase in PL intensity, while for crystals high PL intensities are obtained without air annealing and the effects of the anneal appear to be more muted and mixed –likely due to the absence of grain boundary recombination. Passivation layers such as ZnSe and the effects of the CdS junction are also discussed, but as discussed throughout the text, further optimization of single crystal surfaces is still needed.

3.4 Stoichiometry

The existence region of a compound semiconductor presents two challenges: the role of bulk defects created by off-stoichiometric composition, and the compounds or secondary phases formed on the bulk surface comprising the terminating surfaces.

3.4.1 Overview

Control of stoichiometry is critical in multinary systems. Variations of bulk stoichiometry are a primary variable for control of defects in CZTSe, since variations in bulk stoichiometry are only possible through the formation of anti-site defects, interstitials and vacancies. In addition, the presence of secondary phases, particularly at thermodynamic equilibrium, are determined by the local composition.

In this work we wanted to provide insight into the ideal bulk composition of for CZTSe solar cells. Single crystals provide a less ambiguous way of comparing bulk composition and basic electrical properties. In addition, due to the long, high temperature pseudo-equilibrium fabrication methods, composition measurements of bulk single crystals can provide additional data points for the phase diagram.

The phase diagram and a brief description of the tolerance of CZTSe to accommodate and even require stoichiometric variations are reviewed in Section 3.4.2 and 3.4.3 respectively. The detrimental effect of low Se are briefly discussed in Section 3.4.4. For cations, the effects of Cu concentration were found to be the most critical variable for solar cell performance, and therefore variations in Cu stoichiometry were examined in the most detail in Section 3.4.5. Sub-sections focus on carrier concentration and intra-grain mobility (3.4.5.1), carrier transport (3.4.5.2), and radiative defect energies and recombination via PL (3.4.5.3).

3.4.2 CZTSe Phase Diagram and Secondary Phases

The calculated single phase regime is shown in Figure 3-12. The chemical potential window for single phase CZTSe is predicted to be narrow and due to strong deviations from stoichiometry found for ideal films, the presence of coexisting secondary phases is likely.

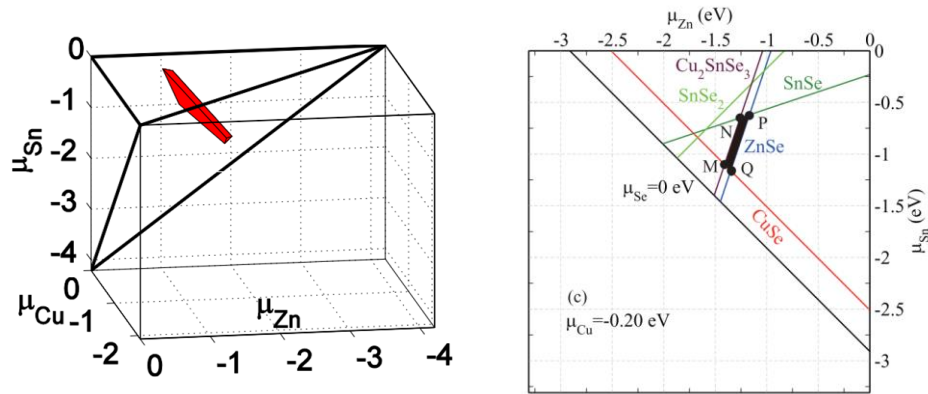


Figure 3-12: Chemical potential single phase window for CZTS (in 3D, Left) [87], and CZTSe (2D, right) based on first principle calculations [88].

In CZTSe, the expected secondary phases are Cu_2Se , $SnSe_x$, Cu_2SnSe_3 , and $ZnSe$. In thin films, the low E_g and high conductivity of the Cu, and Sn-rich secondary phases provide paths for shunting and recombination [89]. Although Cu_2Se and $SnSe_x$ are found frequently, Cu_2SnSe_3 is not frequently reported in thin film literature, but is often found in single crystal formation [90], [91]. $ZnSe$ is the most common reported secondary phase in large part because target stoichiometries tend to be Zn-rich, and as noted in the phase diagram, the CZTSe single phase region has a narrow Zn chemical-potential width which encourages the precipitation of Zn-rich phases [42], [79]. Fortunately, $ZnSe$ appears to be less detrimental to solar cell performance, and is even

found in champion films [31], [79]. As previously discussed, ZnSe has a larger bandgap and therefore will not trap carriers and may provide passive interfaces with CZTSe due to band alignment and similar lattice constants.

3.4.3 Optimal Compositions and the Role of Defect Compensation in Multinary Solar Cells

The composition for optimal solar cells is approximately a 15% decrease in Cu and a 15% increase in Zn, equal to $\text{Cu}_{1.7}\text{Zn}_{1.15}\text{SnSe}_4$ [31], [92]–[94]. One important question is whether the ideal composition measured in thin films accurately reflects the bulk CZTSe stoichiometry, or whether the measured composition is biased heavily due to secondary phases or strong compositional deviations at grain boundaries and on the exposed surface. Calculated phase diagrams based on DFT models suggest that bulk composition in equilibrium should be pinned at the phase boundary with secondary phases after only a few percent deviation in stoichiometry [42]. Surprisingly however, reports from single crystals, as well as data from this work, suggest deviations greater than 10% from stoichiometry appear to be possible in the bulk [39], [95]. Non-modeled factors such as temperature and entropy may account for some of the discrepancy between the narrow theoretically calculated phase diagram and the wider observed phase boundary [96]. In addition, an important recent theoretical prediction suggest the wide breadth of the phase diagram may also be explained by significant interaction between compensating defects which form extended defect complexes [49]. By significantly lowering the formation energy of composition-changing compensated defects such as $[\text{V}_{\text{Cu}}+\text{Zn}_{\text{Cu}}]$, the achieved “single phase region is expanded.

This empirically determined optimal stoichiometry is equivalent to substitution of 15% $[\text{V}_{\text{Cu}}+\text{Zn}_{\text{Cu}}]$ compensated defect pairs. Despite an expected anti-site and vacancy

defect concentration of 1.5×10^{22} , the off-stoichiometric material is found to have lower hole concentrations –on the order of 10^{16} – and higher lifetimes compared to stoichiometric $\text{Cu}_2\text{ZnSnSe}_4$ [29]. The low carrier concentrations are evidence of significant compensation. This can be seen by calculating the number of free carriers expected using a modified fermi-distribution function for an acceptor state [97]. At room temperature, with an acceptor energy of 0.04 eV, as predicted for V_{Cu} , 5% of the states will be ionized and therefore only 2×10^{17} acceptors states (in this case V_{Cu}) would be necessary to provide the observed 10^{16} holes, a deviation of ~ 1 ppm from stoichiometry. Beyond reducing carrier densities, the existence of charge-balanced defects in close proximity has a second electrical consequence, shifting the isolated defect energy levels to shallower depths due to the coulomb interaction between the charged defects. The extent of the reduction in binding energy can be expressed by $\Delta E = \frac{q^2}{\epsilon r}$ where q is the charge of the defect, ϵ is the dielectric constant of the material and r is the distance between defects [52], Pg. 18. In the lowest energy configuration (closest proximity), this defect pair interaction shifts the shallow V_{Cu} and Cu_{Zn} defect states entirely inside the valance and conduction band respectively (depicted in Figure 3-13). This minimizes the electronic consequences for significantly Cu-poor, Zn-rich solar cells that would otherwise would be detrimental due to extremely high concentrations of sub- E_g defects.

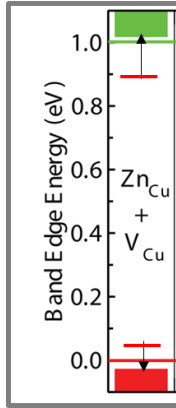


Figure 3-13: Defect energy level for V_{Cu} , Zn_{Cu} and $[V_{Cu}+Zn_{Cu}]$ compensated defect pair. Red dashes in gap represent isolated defect energy, while arrows to red and green bar represent the shift of defect energy level with complex formation: Figure modified from [42].

In addition to beneficial defect compensation and defect complex formation, Cu-poor and Zn rich solar will reduce the likelihood for detrimental second phases while favoring the relatively benign or propitious ZnSe phase [89], [98].

3.4.4 Effect of Se Composition

As mentioned in Section 2.6.4.2 (Pg. 45), single crystals were created from ampoules of both low and high Se. High Se was noted to suppress crystal growth but negative electronic effects were not seen. The effects of low Se are briefly shown below. Ampoules were loaded with the desired Cu-poor and Zn-rich cation ratios with a reference ampoule at the nominal Se (Se/cation=1.0) while a second “low Se” ampoule was loaded 3% deficient in Se (Se/cation=0.97). Despite typical passivation procedures including polishing and etching, PL intensity, as seen in Figure 3-14, drops dramatically for crystals grown in the Se deficient ampoule. The peak energy of the PL spectra could not be accurately obtained due to the low levels emission. The reduction in intensity is

supported by theoretical predictions that Se vacancies will form a deep double acceptor state at ~ 0.35 eV from the valence band [42]. Despite the 3% Se reduction in loaded ampoule elemental ratio, the measured Se/cation ratio in the resulting crystals had only small changes as detected by XRF, likely within the instrumental error (~ 0.15 at %, error bars detailed in the appendix, Pg. 218). Reductions in Se concentration in concentrations much smaller than the detection limits could still lead to the observed PL decrease.

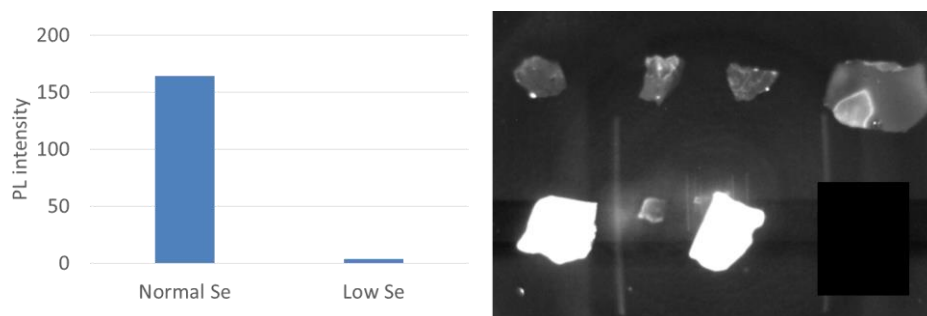


Figure 3-14: Effect of low Se on PL intensity. PL image on right with four low Se crystals (top) and two reference crystals (bottom)

3.4.5 Effect of Cu Composition

Crystals of a variety of Cu-compositions were achieved over the course of this work and found to be the best predictive variable of final device performance. Hall Effect, temperature-conductivity, and photoluminescence measurements are discussed.

3.4.5.1 Hall Effect Measurements

Individual crystals were contacted in Van der Pauw configuration for Hall measurements. Crystals were mounted on a glass substrate with a non-conductive adhesive and were contacted with silver paste attached to four gold wires, which were

routed to contact pads at the corners of the substrate. Crystals selected for hall were $\sim 3 \times 2 \times 1$ mm or larger.

Obtained electrical properties represent bulk values where transport is not impeded by grain boundaries. Mobility varied between 50-150 $\text{cm}^2/\text{V}\cdot\text{s}$ depending on crystal and synthesis conditions, although trends with composition or fabrication variables are not yet clear (Figure 3-15). This is much higher than previous studies of CZTS and CZTSe, which have reported majority carrier mobilities of 10-50 $\text{cm}^2/\text{V}\cdot\text{s}$ for single crystals [25], [26] and 0.1 – 10 $\text{cm}^2/\text{V}\cdot\text{s}$ for thin films [99], [100]. High mobilities can potentially help device performance by slightly decreasing series resistance therefore increasing fill factor, and by increasing diffusion length of generated carriers, which is proportional to the product of lifetime and mobility. The effects of mobility on total series resistance however are likely small and the measured film mobilities are likely understated due to the cross-grain nature of the measurement as will be discussed in Section 4.8.1.1. Increasing conductivity and improving carrier diffusion length have been highlighted as future opportunities to raise the efficiency of recent champion devices [14], [99].

All crystals exhibited p-type conduction based on hot probe Seebeck voltage measurements and carrier concentrations ranged from 5×10^{16} for the most Cu-poor crystals and 10^{19} cm^{-3} for near stoichiometric crystals, consistent with literature reports [101]. Resistivities decreased with increasing [Cu] reflecting the change in hole concentration, while carrier mobility had no apparent trend. Carrier densities and mobilities as a function of [Cu] is shown in Figure 3-15. Cu_{Zn} antisite has been identified to be the majority defect over most stoichiometries of CZTSe, which would be consistent with the correlation between copper concentration and number of carriers

[42]. High efficiency thin film devices have tended to be more Cu-poor than the compositions achieved in this work, and thus the lower range of carrier concentrations achieved (5×10^{16}), are still higher than those of record devices [31], [102].

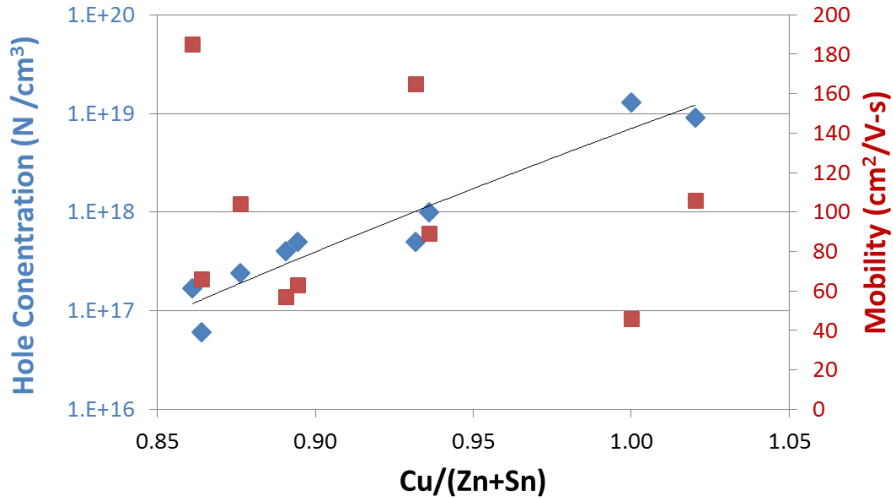


Figure 3-15: Effect of Cu on carrier concentration and mobility

3.4.5.2 Majority Carrier Transport

Temperature dependent conductivity measurements were performed on a range of with Cu/(Zn+Sn) from 0.90 to 0.99 encompassing both Cu poor and near stoichiometric samples to better understand defect structure and the nature of the high observed mobilities. A metal-insulator transition was seen as Cu concentration in CZTSe increased (Figure 3-16). Conductivities increased with increasing temperature for low Cu-samples, which can be attributed to increasing carriers contributing to conduction, while the opposite trend was seen for the near-stoichiometric sample. In this case the decreasing conductivity is similar to a metal, where increasing temperature

decreases mobility due increasing phonon scattering. This transition occurs above a critical defect concentration and has been calculated in CZTS to occur at $>8 \times 10^{18} \text{ cm}^{-3}$ [103], which is very close to the measured hole concentration of $9 \times 10^{18} \text{ cm}^{-3}$ for the near-stoichiometric CZTSe sample. The conductivity data for the Cu-poor sample is found to be consistent with Mott variable-range hopping, which is also found in CZTS and other disordered semiconductors [103].

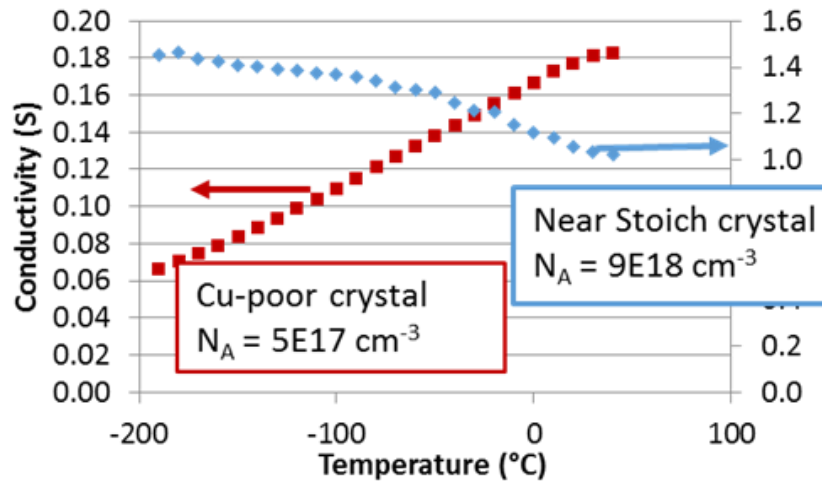


Figure 3-16: Conductivity as a function of temperature for Cu-poor CZTSe single crystal with $\text{Cu}/(\text{Zn}+\text{Sn}) = 0.90$, and near-stoichiometric with $\text{Cu}/(\text{Zn}+\text{Sn}) = 0.99$ CZTSe single crystal.

3.4.5.3 Effects of Cu Composition on PL

The electronic effects of Cu concentration were investigated on both crystals and thin films. Thin film measurements are presented in the following chapter.

PL images of Cu-poor and near stoichiometric single crystals are shown in Figure 3-17. The composition of the Cu-poor crystal was measured by XRF as

Cu/(Zn+Sn)=0.85, Zn/Sn=1.2 and the stoichiometric crystal measured Cu/(Zn+Sn)=0.99, Zn/Sn=1.02. All samples were polished and etched 2 min with 0.25 vol % Br-methanol.

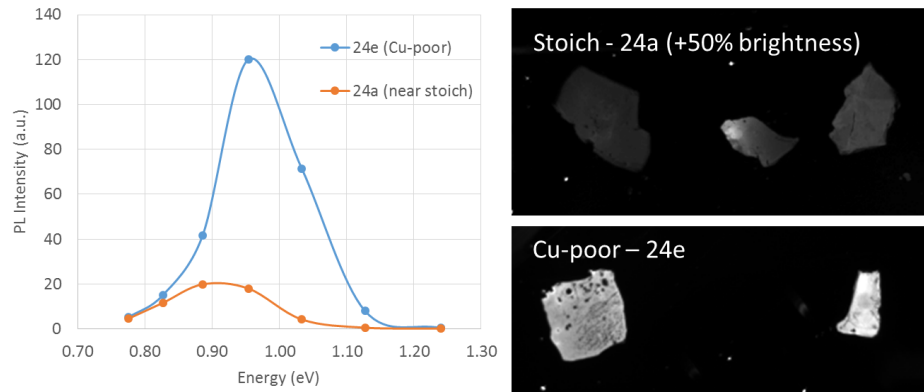


Figure 3-17: PL image and PL pseudo-spectra of Cu-poor and near stoichiometric single crystals.

The stoichiometric crystals were found to have lower PL intensity by a factor of 5 compared to the Cu-poor crystals. In addition, a lower energy PL peak emission of 0.91 eV was also noted for the stoichiometric sample while the Cu-poor sample had a PL peak \sim 0.96 eV. This compares to a bandgap of \sim 0.98 eV, which extracted from the inflection point of QE on Cu-poor SY24e crystals from the same batch. A bandgap from the stoichiometric sample could not be extracted due to shunted devices, however it is expected to be within \pm 0.01 eV from literature measurements. The distance between $E_g - E_{PL}$ suggests lower Cu-samples have shallower bulk defects. This concept will be discussed further in Chapter 4 for thin films.

3.4.6 Conclusions and Summary of Stoichiometry

The effects of stoichiometry critically effect defects and large deviations from the stoichiometric point ($>10\%$) can be achieved in the bulk as demonstrated by the compositions measured in this work. Theoretical predictions suggest the formation of compensated defect pair such as $[V_{Cu}+Zn_{Cu}]$ make this possible without creating $\sim 10^{22}$ states inside the bandgap.

The effect of Cu and Se were investigated on bulk single crystals. Small deficits in Se, lower than the detection limit of typical composition measurement, were found to extinguish the PL intensity of bulk crystals, suggesting high levels of recombination from predicted deep V_{Se} defects. Only p -type conductivity was found regardless of stoichiometry and *intra-grain* hole mobilities were measured to be from 40-200 cm^2/s , far in excess of thin films and with little correlation to composition. Carrier concentrations in bulk crystals are anti-correlated with Cu concentration, consistent with Cu_{Zn} as the dominant defect. Cu concentration was also found to critically change the electronic transport, as well as the recombination and sub-Eg defects. At high Cu concentrations single crystals are shown to cross the metal-insulator transition. PL measurements demonstrate shallower defects and improved PL intensities for Cu-poor samples. These factors help explain the Cu-poor stoichiometry found for highly efficient devices. The effects of Cu on thin film devices are further elaborated in Section 4.5.1.

3.5 Dopants and Substitutions

Na doping has been found to be an essential component for high efficiency devices. Collaborators at IBM have shown improvements in all device parameters with higher Na doping [104]. Other reports have demonstrated higher carrier concentration [105]–[107], improved grain growth [40], [108], [109], and empirically confirmed improved device efficiencies [105], [107]–[109]. Na has been shown to have higher concentrations at grain boundaries [110] and recent evidence suggests limited incorporation into the bulk of CZTSe [106], however both the extent of incorporation and the resulting effect on sub- E_g defect states has not been documented.¹⁴

In this section, the extent of Na incorporation into the bulk of a CZTSe single crystal was measured by SIMS. Na was diffused into a single crystal and the resulting diffusion profile was measured to obtain solubility limits and diffusion coefficient of Na in bulk CZTSe.

The effect of Na on sub- E_g states was further studied with collaborators at IBM and compared to single crystal photoluminescence measurements. This investigation is shown in Section 4.6.1 and was published [104].

¹⁴ Due to the Cu-poor stoichiometry for efficient devices, Na may sit on the V_{Cu} site creating a neutral Na_{Cu} defect but this hypothesis has yet to be confirmed directly. To what extent it is possible to incorporate a larger Na (atomic radius 190 pm) into the smaller cation sites (145, 142, and 145 pm for Cu, Zn and Sn) is still not clear.

3.5.1 Na

Growth of single crystals with Na was attempted but was only moderately successful. Sodium selenite, Na_2SeO_3 , precursors were first explored due to ease of handling, however due to the stability of metal oxides, non-oxygen containing precursors were preferred. Later ampoules were grown with pure Na (0.05 and 0.2% Na atomic %), however Na was found to react and devitrify the quartz ampoule wall which increased risk of the ampoule breaking during heating or cool-down. Limited Na runs were achieved, however grain sizes and compositions were not as desired. Na post-deposition may be a more promising method for future single crystal testing.

3.5.1.1 Na Solubility and Diffusion in Bulk CZTSe

Measuring the extent of Na doping in the bulk is difficult in thin films due to the presence of grain boundaries where high concentrations of Na are often noted [110], [111]. A single crystal was used to investigate Na solubility limits and diffusion in the bulk of the CZTSe. The crystal of $\sim 4 \times 4$ mm was polished to a mirror surface and etched with Br before being loaded into a chamber for NaF deposition. 100 nm of NaF was deposited on the surface of the crystal at room temperature, and without breaking vacuum, the crystal was heated to 420°C for 6 hours. After deposition, the crystal was sent to Evans Analytical Lab for measurement of a composition depth profile over the top 25 microns by SIMS. Before measurement, excess Na on the surface was rinsed with DI water.

Na diffusion was modeled with Fickian diffusion with a complementary error function and the diffusivity at 420°C was extracted. The equation and diffusion profile are shown in Figure 3-18. Due to the thick NaF layer, the Na source can be considered an “infinite well” for the course of the measurement which is confirmed by a NaF layer

still present on the crystal surface at end of the annealing step. The initial concentration of Na at the surface, $3.8 \times 10^{17} / \text{cm}^3$, represents the solid solubility of Na in the CZTSe lattice at 420°C which is equivalent to approximately 1ppm. The modeled diffusion appears to fit two regions with slightly faster diffusivity near the surface (Region 1: $D_1 = 1.75 \times 10^{-11} \text{ cm}^2/\text{s}$), and a lower diffusivity after ~ 15 microns (Region 2: $D_2 = 1.5 \times 10^{-12} \text{ cm}^2/\text{s}$). The plateau in concentration below $10^{16} / \text{cm}^3$ is due to the detection limits for the SIMS measurement.

The fitting in multiple regions is seen in other systems and can occur when high concentrations of a dopant in the lattice affect the activation energy for other dopant atoms to diffuse [19]. A second potential explanation could be the near surface remains damaged with micro-cracks. The crystal surface was prepared with the typical thinning/polishing procedure with a final polish with a wet 0.03 micron alumina polish followed by a Br-etch. Remaining cracks could potentially provide a faster diffusion path in the near surface, while the deeper surface beyond 15 microns may be less disturbed from the mechanical polishing. It's worth noting, Cu Zn, Sn and Se concentrations were unchanging after the 0.2 microns. Under both hypotheses, the lower diffusion coefficient of Region 2 is likely the undisturbed CZTSe bulk diffusivity although given the off-stoichiometric nature of the crystal, extended defect complexes may also contribute to diffusion.

This is one of the first data points directly confirming incorporation of Na in the CZTSe bulk [106], and is the first measurement of bulk solubility limits and diffusion of Na in this system. It's worth noting that measured diffusivities and solid solubility's may depend strongly on composition. The measured crystal was chosen to be Cu-poor ($\text{Cu}/\text{Zn}+\text{Sn} = 0.85$, $\text{Zn}/\text{Sn} = 1.2$), in order to be relevant to efficient devices. Cu-poor

crystals may be expected to have higher Na solubility limits and higher diffusivities given the significant concentration of V_{Cu} . Further diffusion profiles as a function of temperature are being considered for to enable extraction of activation energy and diffusion coefficient for Na diffusion in bulk CZTSe.

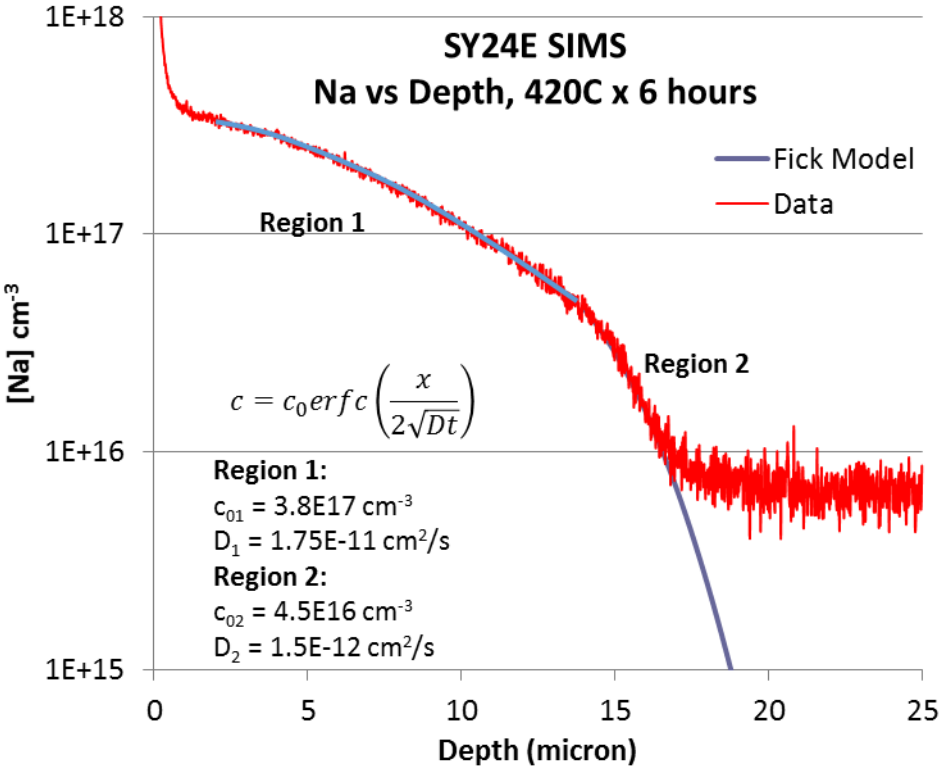


Figure 3-18: Diffusion profile of Na in CZTSe single crystal after 6 hours annealing at 420°C

3.6 Temperature Equilibria

Note: This work was prepared for submission to Journal of Applied Physics and is with reviewers currently. It is printed here with only minimal modification.

3.6.1 Abstract

Recent literature reports have shown the ability to manipulate Cu-Zn cation ordering for $\text{Cu}_2\text{ZnSnSe}_4$ (CZTSe) via low temperature treatments. Theoretical arguments suggest one of the major roadblocks to higher V_{OC} —significant band tailing—could be improved with increased cation order, however few direct measurements have been reported and significant device improvements have not yet been realized. This report investigates electrical properties, defects, and devices from quenched and slow-cooled single crystals of CZTSe. Disorder was characterized by Raman spectroscopy as well as x-ray diffraction (XRD), where the change in Cu-Zn order can be detected by a changing c/a ratio. Quenched samples show higher acceptor concentrations, lower hole mobilities and a lower-energy photoluminescence (PL) peak than crystals cooled at slower rates, consistent with a reduction in bandgap. In addition, samples quenched at the highest temperatures showed lower PL yield consistent with higher quantities of deep defects. Devices fabricated from slow-cooled CZTSe single crystals showed improved efficiencies, most notably with increased V_{OC} ; however low temperature intensity-dependent photoluminescence measurements continue to indicate the existence of potential fluctuations. We discuss the possibility that potential fluctuations in slow-cooled samples may be related to the inability to achieve long range order of the Cu-Zn sub-lattice resulting in local regions of high and low levels of cation order, and consequent local variations in bandgap. The presence of significant potential fluctuations, even after single crystals are slow-cooled, suggests the difficulty of

eliminating band-tailing in this system, and thus additional approaches may be needed for significant reduction of the V_{OC} deficit.

3.6.2 Introduction

$Cu_2ZnSn(S,Se)_4$ based materials have received considerable attention due to earth-abundant raw materials and attractive optoelectronic features for solar cells. The current champion cell has achieved 12.6% efficiency, however this is a significant deficit compared to comparable-bandgap (E_g) CIGS devices, which can be explained mainly by a shortfall in V_{OC} [7], [14]. The largest factors in this shortfall are believed to be deep defects and band tailing, since interface alignment is expected to be favorable in low E_g devices [43]. The presence of deep defects manifests in high recombination and short carrier lifetimes compared to CIGS [44]. Furthermore, significant band tailing from local potential fluctuations or E_g variations can be observed in CZTS-based materials from a shallow EQE curve near the band edge, as well as a PL peak which is typically found below the bandgap [45], [54].

The origins of the band tailing are predicted to arise from a high density of $[Cu_{Zn} + Zn_{Cu}]$ defect pairs [45], which in the case of high temperature processing ($T > 200^\circ C$), leads to a fully random cation occupancy on the Cu-Zn sub-lattice in the CZTS/Se kesterite structure [37]. The prevalence of this Cu-Zn cation disorder is promoted by their similar atomic size which leads to low formation energies of both antisite defects coupled with further reductions in formation energy due to the creation of charge-balanced defect pairs. At non-zero temperatures Cu-Zn cation disorder is promoted by entropic stability which outweighs the positive enthalpy of defect complex formation. Recent literature has found that Cu-Zn disorder can be reduced to a certain extent by

slow cooling from growth temperatures or post-growth low temperature annealing below the disorder-transition temperature ($\sim 200^\circ\text{C}$ for CZTSe and 260°C for the sulfide) [112], [113]. The ability to reduce Cu-Zn disorder could theoretically be a promising avenue to mitigate one of the major roadblocks for CZTSSe performance: significant detrimental band tailing.

Characterization of Cu-Zn disorder through common structural techniques, such as XRD, has been limited due to the similar scattering factors for Cu and Zn which makes changes in cation occupancy difficult to determine based on peak intensity alone. Raman spectroscopy has can discern qualitative changes linked to cation ordering but more quantitative measurements require more specialized tools such as neutron diffraction or NMR [37], [95], [114].

It is important to note that even after slow-cooling or long low-temperature annealing, the Cu-Zn lattice still contains extremely high levels of Cu-Zn antisites. Available experimental evidence suggests antisite occurrence decreases from 50% to 30% of Cu-2a lattice sites after the slow-cooling of poly-crystals. These reduced antisite densities are still extremely high, $\sim 1.7 \times 10^{21} / \text{cm}^3$ [37]. Therefore, the term “ordered” is inaccurate, and a transition from full disorder to “partial-disorder” is more accurate.

Literature reports have demonstrated significant changes in bandgap related to Cu-Zn ordering. The CZTSe band gap has been reported to range from $\sim 0.95 - 1.06\text{eV}$ for disordered and low-temperature annealed partial-disordered samples respectively [113], [115]. These variations in bandgap, as well as significant sub- E_g states, such as band tails, are critical to solar cell performance. Low temperature photoluminescence (PL) is a powerful method of looking at these sub- E_g states. The importance and origin of band tails was discussed by Gokmen et al. who highlighted the extended low-

temperature lifetimes in CZTSe films which may arise from electrostatic potential fluctuations. Recent experimental literature has suggested the E_g fluctuations may additionally be present in CZTSe due to the presence of high and low-order phases [47]. The detrimental effects of E_g fluctuations on efficiency and V_{OC} have been detailed elsewhere [116], [117] and may explain a portion of the V_{OC} deficit in this system. The ability to reduce aforementioned potential fluctuations through slow-cooling, low-temperature annealing or other techniques is therefore of particular importance. Grossberg et al. investigated low temperature PL as a function of function of cooling rate for CZTS monograins, [118], but limited reports exist for the effect of cation ordering on low-temperature PL in the case of the selenide. In addition, changes to electrical and transport properties have hitherto not been reported.

Despite the theoretical improvements that would be presumed for more “ordered” CZT(S,Se), few device results have been reported, and certain reports have shown a reduction in device efficiency when low-temperature ordering was attempted [119]. It is worth noting that the current champion devices are not fabricated in vacuum where cooling is expected to be slow, and do not use a low-temperature anneal to increase order [14]. The lack of device improvement with increasing ordering (so far) may be a consequence of a non-order-related phenomenon (surface oxides, back contact reactions, band alignment), or may be an intrinsic problem inherent to low-temperature bulk defect equilibria. More understanding is needed to determine if low-temperature treatments can be part of the solution to decreasing the V_{OC} deficit. To better address this question we investigate the electronic properties and sub- E_g defects of quenched and slow-cooled single crystals.

Single crystals have the benefit of having defect properties that are closer to equilibrium in comparison to thin films due to their long isothermal growth and large ratio of bulk to surface and grain boundary area. Theoretical predictions predominantly assume that defects exist in their thermodynamic equilibrium state, making single crystals an ideal experimental reference for theory. Furthermore, the presence of grain boundaries and interfaces in thin films often give rise to local deviations in composition as well as local secondary phases which can be more easily avoided in single crystals.

In this report, single crystals were fabricated in sealed ampoules and slow-cooled to room temperature, or quenched after a partial slow-cool, thus providing snapshot of the defect population at semi-equilibrium for the quench temperature [96]. The quench temperatures included: high growth temperature (750°C), film formation temperature (500°C), and a temperature just above the disorder transition (300°C). Structural changes are observed via Raman measurements, as has been previously seen in the literature, and we show that the disorder transition can also be observed via XRD analysis. Intra-grain electrical transport and carrier concentrations are extracted from individual quenched and slow-cooled crystals by Hall measurements and initial device results on individual single crystals are presented. Finally, the effects of quenching and slow cooling on sub- E_g states are demonstrated with low temperature PL and possible sources for observed potential fluctuations are discussed.

3.6.3 Experimental Setup

Crystals were fabricated via solid state synthesis of elements below the CZTSe melt as described elsewhere [104], [120]. High purity elements (5-6N) were loaded into quartz ampoules and sealed at a base pressure of 10^{-6} Torr. Each ampoule was ramped to 750°C over 24 hours and annealed for a total of 20 days in a temperature gradient of

25°C/in. The boules were slow-cooled to room temperature at 3°C/hr, or partially slow-cooled (also at 3°C/hr) to a temperature above the Cu-Zn disorder transition and then quenched into an ice water bath. Quench temperatures of 750°C, 500°C and 300°C were used to provide a snapshot of defects at crystal growth, film growth and temperatures slightly above the disorder transition. The resulting polycrystalline boule was broken and crystals larger than 3 X 3 mm were selected for analysis. A regular, smooth surface was obtained via mechanical polishing down to a 0.03 micron alumina slurry. After polishing, approximately 2 microns of the surface was etched away with a bromine-methanol solution (5 minutes at 0.125 vol % Br) to mitigate surface damage from the prior steps.

Composition measurements were performed via X-ray Florescence spectroscopy (XRF) calibrated by inductively coupled plasma mass spectroscopy (ICP). Raman spectra were taken with a 532-nm laser at low power settings to avoid sample heating in order to examine phase purity and crystalline order. Crystals analyzed via XRD were powdered in an agate crucible with 125-mesh per ASTM standards to investigate second phases and lattice changes. A digital Laue camera operated at 35 kV and 20 mA with a 1.5 mm beam diameter was used to obtain diffraction patterns confirming crystal orientation and monocrystalline nature.

PL measurements were recorded at 5K using a Hamamatsu single photon counting system equipped with a 532 nm pulsed laser and liquid He cryostat for sample cooling. Intensity dependent measurements were performed using a neutral density filter wheel to obtain a range of excitation densities from 1.5×10^{-3} J/cm²/pulse to 6.4×10^{-5} J/cm²/pulse. A separate room-temperature PL image setup with 808 nm laser and InGaAs camera were used to obtain comparisons of total PL intensity.

Hall measurements were performed in the Van der Pauw configuration on individual single crystals to obtain intra-grain mobilities and carrier concentrations above and below the disorder transition. Silver paste was used to attach gold wires to the corners of a 4x3x1mm crystal. A hot-probe measurement was used to obtain Seebeck coefficient and confirm conductivity type of each crystal. Devices were fabricated on individual single crystals using a traditional device structure although a metal top contact was avoided due to the small cell area. CdS was deposited by chemical bath deposition and ZnO/ITO layer was sputtered through a 3.14mm² circular mask. The crystals were mounted on Mo-coated glass with Ag paste and probes were contacted directly to the ITO as the front contact. Device area was confirmed via LBIC to be equal to ITO contact area.

3.6.4 Results

Raman and elemental composition measured across the surfaces of polished and etched crystals show no evidence of secondary phases. Additional powder XRD of selected crystals similarly lacked evidence of secondary phases, although the similar lattice structure for Cu₂SnSe₃ and ZnSe means their coexistence at low concentrations cannot be fully ruled out by this method. Laue images of individual crystals show sharp diffraction spots with no evidence of extraneous reflections confirming the single crystalline nature of the samples [120].

Sample compositions for quenched and slow-cooled crystals were slightly Cu-poor and Zn rich although closer to stoichiometric compared to typical for state-of-the-art devices and are listed in Table 3-2. Two sets of samples were fabricated and are compared separately due to slight variation of composition between sets. Within a set, crystals were within, ~0.2 at% absolute, which is approximately within the margins of

error of the measurement. Other crystals from each batch were found to have similar properties to the rest of the batch, despite small changes in XRF composition suggesting cooldown treatment, rather than composition, is the dominant factor in the variances discussed in more detail below.

Table 3-2: Composition measurements of quenched and slow-cooled by XRF

		Cu / Zn+Sn	Zn / Sn	Cu / Sn
Set 1	Quench (@750°C)	0.94	1.11	1.98
	Slow-cool	0.96	1.07	1.98
Set 2	Q500	0.97	1.07	2.00
	Q300	0.97	1.07	2.00
	Slow-cool-2	0.98	1.04	2.00

The Raman spectra for quenched and slow-cooled samples can be seen in Figure 3-19. Similar to literature results, a notable shift in the 196 cm^{-1} main peak (m_{1A}) can be seen in the quenched single crystal, as well as a broadening and decrease in the 168 cm^{-1} mode (m_{2A}). Although these peaks can be attributed to exclusively anion motion, changes in their behavior can be telling of Cu-Zn ordering [112], [121]. General broadening and shift to lower wave number observed in A-symmetry modes has been identified in literature to correspond with a reduction in phonon correlation lengths which occurs for disordered samples [112], [121].

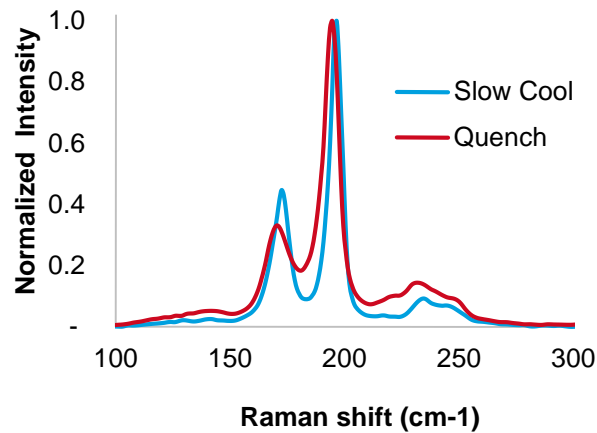


Figure 3-19: Raman spectra of slow-cooled and fully quenched CZTSe crystals.

As previously stated, the use of XRD as a metric for Cu-Zn ordering has been hindered by the similar scattering factors for Cu and Zn. In modeled kesterite XRD patterns, full-disorder on the Cu-Zn lattice (random occupation of the Zn lattice) changes normalized peak intensity by a maximum of only 0.01% relative to the highest (112) peak intensity. This is further complicated by the difficulty of comparing peak intensities in oriented thin films. Despite minimal differences in peak intensity and similar atomic radii, changes to lattice constants related to the Cu-Zn defect have been predicted by first principle calculations and detected by neutron diffraction. First principle calculations suggest an expansion of the c-axis will result from breaking of the octet rule which occurs when swapping Cu and Zn [122]. This is further confirmed by Neutron diffraction data which has demonstrated a changing c/a ratio above and below the disorder transition temperature [37]. We confirm this change in lattice constant via XRD measurements as shown in (Figure 3-20).

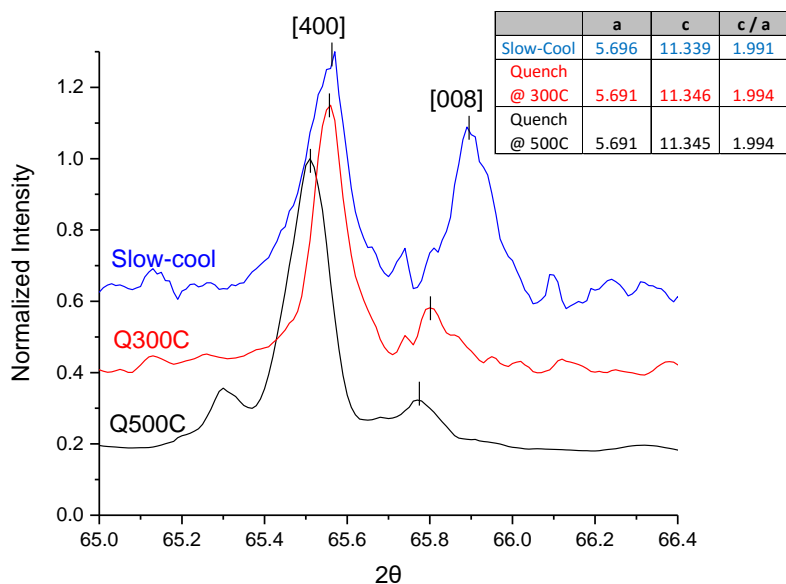


Figure 3-20: XRD of powder from single crystals slow-cooled or quenched at 300°C or 500°C at the [400], [008] peaks. $k\text{-}\alpha_2$ has been removed and smoothed with Savitzky-Golay filter for clarity.

The c/a ratio can most easily be visualized at the [400], [008] peaks at 2θ of ~ 65.5 degrees which shows clear splitting and allows complete separation of the c and a -axes. The expansion of the c -axis for samples quenched above the disorder temperature can be seen with the [008] peak at 65.89 for the slow cooled sample and 65.80 for the sample quenched at 300°C. Samples quenched at 500°C and above showed a slight additional expansion of both c and a possibly due to freezing of thermal expansion although the c/a is consistent with samples quenched at 300°C. The lattice constants for c and a , calculated by full pattern Rietveld refinement, as well as by hand for just the [400] and [008] peaks, show consistent changes as found by neutron diffraction data for quenched and slow-cooled powders [37]. It is worth noting the overlapping $k\text{-}\alpha_2$ peaks must be removed by the Rachinger correction to properly

visualize the separation of c and a-axis or must be accounted for in refinements. Standard error in all refinements was in the 4th decimal point, far less than observed differences between samples.

Intra-grain hole mobilities and carrier concentrations for individual single crystals, as measured by Hall Effect, can be seen in Table 2. Seebeck coefficients were positive confirming strong p-type character for all samples. Hole mobilities increased from 50 cm²/(V·s) to 180 cm²/(V·s) for slow-cooled crystals consistent with increasing crystalline order. Carrier concentrations decreased from 10¹⁸/cm³ for quenched samples to 10¹⁶ /cm³ for slow-cooled crystals. The mobilities in the slow-cooled samples reported here are among the highest values reported for CZTSe, however literature reports for single crystals and intra-grain measurements, in general, have been shown to be 10-100x higher than thin film measurements [25].

Literature reports for carrier concentrations for thin film CZTSe of similar composition are closer to the range of the quenched crystals, however carrier concentration has not previously been investigated as a function of cation ordering [90], [123]. Increasing point defects, including vacancies such as V_{Cu} are expected at the higher temperature equilibrium for quenched samples, however Cu_{Zn} is predicted to be the dominant defect for typical samples near stoichiometry (similar to crystal composition) due to significantly lower formation energies. Based on ΔH_f of non-interacting defects, a lower bound estimate of defect concentration at the highest quench temperature suggests $\sim 10^{19}$ and 10^{20} V_{Cu} and Cu_{Zn} defects per cm³ are expected respectively. This is far in excess of measured hole concentration which confirms the system is highly compensated (see supplementary info).

Table 3-3: Hall measurements and device results on single crystals

Sample	# of Carriers (N_a)	Hole Mobility (μ)	V_{OC}
Quenched	$3 \times 10^{18} \text{ cm}^{-3}$	$22 \text{ cm}^2/\text{v-s}$	286 mV
Slow-cooled	10^{16} cm^{-3}	$180 \text{ cm}^2/\text{v-s}$	354 mV

Table 3-3 shows the best V_{OC} among 6 devices fabricated on quenched and slow-cooled single crystals. Slow-cooled crystals demonstrated consistently higher V_{OC} by over ~ 50 mV. The improvements in V_{OC} are likely due to changes in bandgap for more ordered samples as has been noted in the literature, as well as changes in recombination as evidenced by the PL results discussed below. Additionally, increased collection is seen for samples with lower carrier concentration which is consistent with an extension of the space charge region further into the device.

Changes in non-radiative deep states that may influence V_{OC} can be inferred from changes in PL yield, which has been shown to correlate well with minority carrier lifetime [53]. Deep defects will reduce PL yield due to increased Shockley-Read-Hall recombination. PL yields were measured at room temperature with a photoluminescence imaging tool. PL yields were found to be highest for slow-cooled samples as seen in Figure 3-21. PL yields decreased by 15% for samples quenched above the disorder temperature at 300°C , and were reduced by 54% for samples quenched at 500°C compared to slow-cooled samples. The relatively small change in PL intensity above and below the disorder temperature suggests Cu-Zn ordering does not have drastic effects on recombination rates. In addition, it is likely that other deep defect states promoted by higher energy and entropy are responsible for the larger reduction in PL intensity for samples quenched at 500°C (relative to samples quenched at 300°C), since both samples are quenched above the disorder temperature and are anticipated to have similar fully disordered Cu-Zn lattice [42]. For instance, the most

abundant deep defect predicted in this system is the $[2\text{Cu}_{\text{Zn}} + \text{Sn}_{\text{Zn}}]$ complex, which is expected to increase by 10x for samples in equilibrium at 500°C compared to samples equilibrated at 300°C (detailed calculation shown in supplemental).

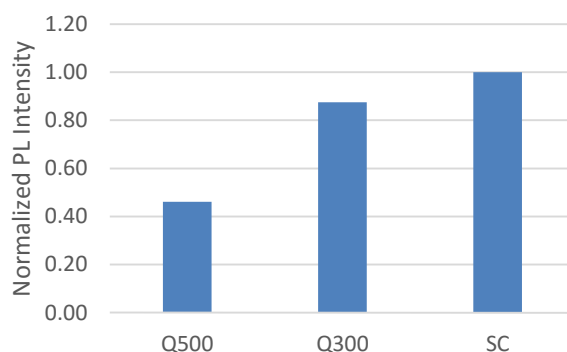


Figure 3-21: PL intensity for samples quenched 500°C, 300°C and slow-cooled to room temperature.

PL spectra taken at 5K show large differences in sub- E_g defect states as seen in Figure 3-22. Three particular observations are worth noting. First, at high laser intensities, the PL peak for quenched samples occurs at much lower energy, 0.93 eV, compared to 1.04 eV for slow-cooled samples. Second, with increasing laser intensity, the PL peak position demonstrates a small blueshift for the quenched sample, but a much more severe blueshift for slow-cooled sample. Third, the spectra are highly asymmetric for the quenched sample, but are both more symmetric, and significantly broader for the slow-cooled sample. The first observation of a higher PL peak energy for the slow-cooled sample matches literature reports of higher E_g correlating with less disordered samples [113]. The other observations – shifting peak position and a wider FWHM for slow-cooled samples – require more explanation, and at first glance might seem to

conflict with the assumed model of lower defects and lower disorder. Each observation will be discussed in more detail in the discussion.

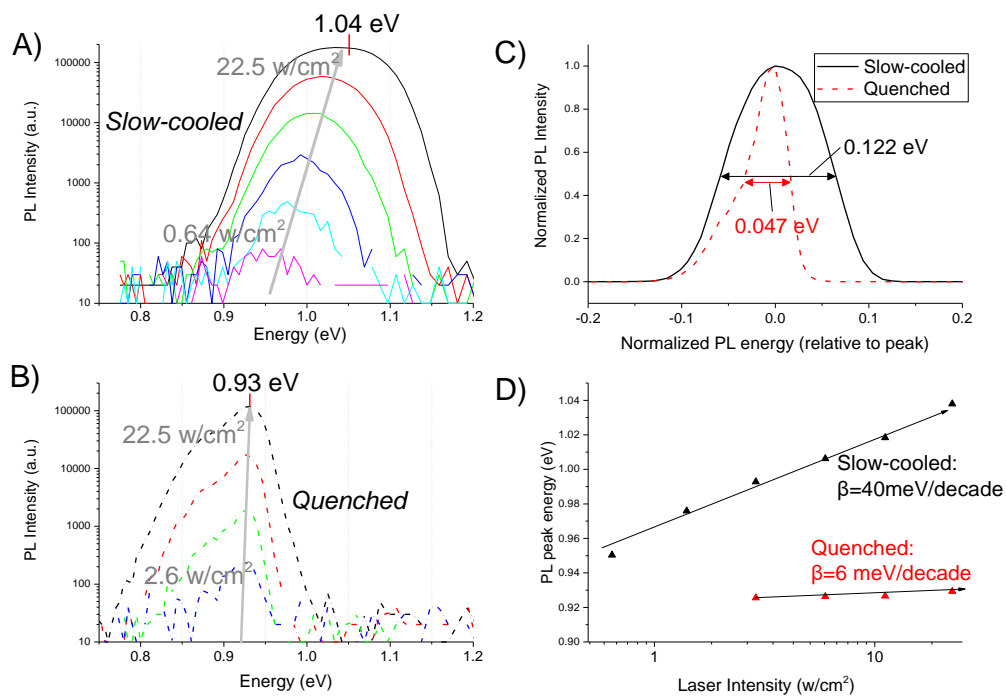


Figure 3-22: PL spectra at 5K for Set 1 of quenched and slow-cooled crystals. A) slow-cooled crystal, B) quenched crystal, C) normalized peak width and FWHM at full laser intensity, D) Position of peak as function of laser intensity for crystals

3.6.5 Discussion

The changes in PL are described in three sub-sections, 1) Position of PL peak, 2) shifting of PL spectra, and 3) Peak width and peak shape.

3.6.5.1 Position of PL Peak

From the literature, the E_g of the quenched sample is expected to be approximately 0.95 eV which is consistent with room temperature PL measurements for this sample. The description of the E_g is non-trivial in systems with high levels of defects and band tailing [54], but a reduction in E_g compared to the unperturbed system (1.0 eV) has been predicted for higher densities of Cu-Zn defects. While at low densities, Cu-Zn antisites are expected to create shallow localized states, however for a fully disordered Cu-Zn lattice with expected defect densities of 10^{22} cm^{-3} , the individual states can act as a delocalized band and can be described as a reduction in E_g . This is depicted in Figure 3-22. The extent of the E_g reduction have been predicted by first principle calculations to be between 24 meV and 300 meV depending on Cu-Zn cation arrangement as well as defect density [47]. The resulting 0.95 eV E_g fits expectation since cation arrangements with minimum reduction in E_g tend to have the lowest formation energy and therefore are expected to be most prevalent [47], [124]. For the quenched sample, the PL peak at 4K is at 0.93 eV with continued emission extending to 0.8 eV which suggests that both localized defect states inside of the gap and/or band tails give rise to the emission. It's interesting to note the lowest energy emission from the quenched sample is approximately equal to the emission expected from isolated non-interacting Cu_{Zn} and Zn_{Cu} (depicted in Figure 3-22a).

The PL transition energy of the slow-cooled sample is harder to interpret due to the strong dependence on intensity. At maximum laser intensity, the room temperature PL peak is 1.06 eV which is very similar to E_g reported for low-temperature annealed samples (also 1.06 eV) [113]. At low temperatures the PL emission peaks at ~0.95 eV at the lowest laser intensities (similar to the disordered kesterite), and then rises

smoothly and broadens with increasing laser intensity to 1.04 eV, slightly below the room-temperature PL peak.

3.6.5.2 Shifting of PL Spectra

The second observation, of shifting peak position with laser intensity is expressed by the parameter β (shown in Figure 3-22d). For quenched samples, the PL peak energy blue-shifts slightly, $\beta = 6$ meV/decade of laser intensity. The slow-cooled sample shows much larger peak shifts with laser intensity of 40 meV/decade. In donor-acceptor-pair (DAP) emission, increasing intensity leads to coulombic interaction between increasingly dense populations of charged carriers. This interaction blue-shifts the PL emission with increasing laser intensity, typically between 0-10 meV/decade. High levels of both donors and acceptors are expected in the quenched sample and the coulombic interaction of DAPs likely explains the blue-shift seen for the quenched sample.

The more severe shift seen for the slow-cooled sample is more typical of samples with significant local potential fluctuations. The physical origin of the potential fluctuations can be caused by electrostatic variations from high levels of charged defects, or from local E_g -fluctuations which in this case could be caused by deviations in composition or deviations in Cu-Zn ordering [45]. The role of these two sources of potential fluctuations is discussed further below.

3.6.5.3 Peak Width and Peak Shape

Differences of the peak shape and width can be easily seen in Figure 3-22c. The quenched sample has a highly asymmetric shape with a shallow low energy tail decaying more than 100 meV below the peak, and a sharp fall-off on the high energy

side of the peak. This asymmetric shape and low energy tail is typical of emission from band tails. The sharp fall-off on the high energy side is consistent with minimal thermal broadening of carrier energy expected at the low temperatures of the measurement. This level of tailing could potentially be explained by the presence of alternative cation arrangements which would be expected to be present in limited quantities due to the quenching from high temperatures [47].

The slow-cooled sample has a more symmetric shape which would be expected for a reduction in density of sub- E_g defects and band-tailing, however the FWHM of the PL spectra is more than twice that of the quenched sample. The increasing width for the slow-cooled sample is again consistent with increasing local potential fluctuations.

3.6.6 Electrostatic Potential Fluctuations vs E_g -fluctuations

The observed increase in potential fluctuations for the slow-cooled sample appears counter to the original motivation: “increasing Cu-Zn order will reduce band tailing and increased efficiency”. Therefore, it’s important to understand how the potential fluctuations arise, and if there may be routes to controlling them. In reality, both electrostatic potential fluctuations and E_g -fluctuations will be present to different degrees in highly disordered multinary systems such as chalcopyrites and kesterites [116].

For electrostatic potential fluctuations, the high densities of charged defects cause perturbation of the bands. At low laser intensities, electron-hole pairs find local minimum and max in the conduction and valence band respectively resulting in a low energy PL emission peak. As intensity increases, the local minimum in the valence and conduction bands become increasingly saturated resulting in higher energy emission. In addition, the potential fluctuations flatten under increasing excitation caused by

additional screening of defects from increasing density of photogenerated electron-hole pairs which further shifts the PL emission closer to the undistorted DAP or band edge.

Literature reports of doped semiconductors show that high levels of defects *and* high levels of defect compensation are needed to promote potential fluctuations [125]. This compensation creates high levels of charged defects which cause the band perturbations. The extent of fluctuations is related to total number of charged defects, $[N_t]^{2/3}$. On the other hand, high levels of free carriers provide screening for band edge perturbation, consequently decreasing the size of potential fluctuations with hole concentration, $[p]^{1/3}$ for p-type samples [126]. The lower carrier concentration for the slow-cooled sample suggests higher levels of compensation and less charge screening from free carriers are anticipated despite the expected reduction in Cu-Zn defect density.

There are a number of reasons however to believe that E_g -fluctuations may also, at least in part, explain the PL features noted in the slow-cooled sample. Although electrostatic potential fluctuations will result from any distribution of charged defects, the model assumes a random distribution of charged defects which have equal electrostatic interactions with both valence and conduction band resulting in no change in E_g . However theoretical results suggest the two basic assumptions are broken. First, the Cu-Zn defect complexes are expected to affect the band edges unequally resulting in changes in E_g depending on Cu-Zn order, as has been predicted and shown experimentally [46], [47], [124]. Second, the defect complexes will not be distributed randomly, and instead are predicted to cluster due to the reduction in energy from aggregations of Cu-Zn. If the defect complexes cluster, the energy cost of a 2nd $[\text{Cu}_{\text{Zn}} + \text{Zn}_{\text{Cu}}]$ can be $\frac{1}{4}$ of the cost of the first defect complex due to the reduced proportion of anions which must break the octet rule to accommodate the Cu-Zn anti-sites [46]. In

fact, recent literature has suggested CZTS unit cells will be at minimum energy cost with either full-order or full-disorder (1 defect complex / unit cell), while intermediate amounts of Cu-Zn defects (0.5 defect complexes/ unit cell) require the highest amount of energy [47]. This would suggest that when Cu-Zn anti-sites are reduced from fully random, material will prefer to create clusters of ordered and disordered areas. Experimental reports are beginning to find similar evidence of Cu-Zn clustering, and more severe composition clustering of regions of high and low Zn has also been observed [114], [127].

It is expected that by slow-cooling, we reduce but do not eliminate the Cu-Zn disorder. Similar slow-cooled powders were found to have 30% of Cu-Zn antisites on the Zn sub-lattice which still equates to 1.6×10^{21} defect complexes per cubic centimeter [37]. The slow-cool will encourage the formation of the lowest energy structures, which in the case of Cu-Zn will correspond to clusters of more ordered and disordered areas which will consequently lead to cluster of high and low E_g phases. This scenario is depicted in Figure 3-23d.

At low laser intensities, carriers localize and recombine from the low- E_g disordered phase, while at higher laser intensities the low- E_g phases will become increasingly saturated resulting in a broadening and blue-shifting of the PL peak. The length scale of the local bandgap fluctuations is not clear, but must be smaller than the minority carrier diffusion length or else the shift in PL peak would not be noted. Similar reports of shifting PL from E_g -fluctuations from clustering of ordered and disordered materials has been noted for GaInP [128].

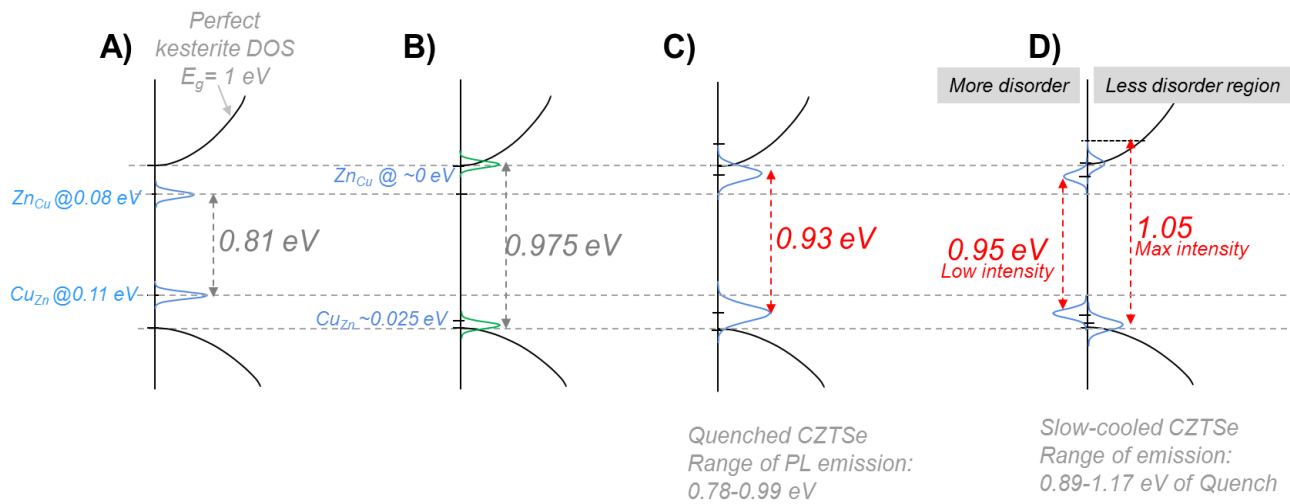


Figure 3-23: Depiction of defects and potential recombination for different cases of CZTSe. A) Isolated Cu_{Zn} and Zn_{Cu} defects. B) Ideal $[\text{Cu}_{\text{Zn}}+\text{Zn}_{\text{Cu}}]$ complex. C) High density of random Cu-Zn (similar to quenched). D) Regions of higher and lower Cu-Zn concentration (similar to slow-cooled). Defect energies from [42]

Notably, the quenched sample does not show significant signs of E_g -fluctuations. Although such fluctuations may occur, they could be masked by more consistent localization into the deeper defects or a lower E_g phase (hence consistent emission at 0.93 eV) (Figure 3-23c). Less clustering may also be expected at high temperatures since the small attractive forces which cause defect clustering will be swamped by thermal energy and entropy. In addition, at high temperatures before quenching, a very high percentage of the sample will be in the disordered low- E_g state, which could result in a smaller distribution of bandgaps. Thus, when samples are quenched, despite higher levels of defects, a more random defect distribution can result in both deeper defects and less defect clustering.

The presence of electrostatic potential fluctuations in CZTS-based samples was most clearly demonstrated by Gokmen et al. [45]. Low temperature TRPL measurements of thin films show significant extension of lifetimes attributed to localization of carriers in energy wells from the potential fluctuations and a resulting requirement for tunneling in recombination. In E_g -fluctuations, tunneling is not necessarily required for emission and therefore less improvement in lifetime is expected. It is worth noting that both quenched and slow-cooled single crystals did *not* show significant extension in lifetime at low temperatures which suggests the potential fluctuations are less significant in these samples. In reality, both E_g -fluctuations and potential fluctuations are likely present, however more detailed follow-up will be required to separate both phenomenon and more fully determine the interplay of low temperature treatments and potential fluctuations.

Regardless of cause, observations consistent with additional potential fluctuations noted for the “more ordered” samples have also been observed but not explained in the literature. Rey et al. observed a wider PL FWHM for room temperature PL of thin films annealed below the order transition [113]. Other reports on CZTS monograins showed the expected increase in PL peak position as cooling rate was slowed, followed by a notable decrease in PL peak position for the slowest cooling rates of 0.06K/hour [118]. Both observations support the idea that potential / E_g fluctuations may be encouraged by low-temperature equilibrium.

This may also explain the lack of champion cells with “order” annealing. The effects of slow-cooling are predicted to be either helpful or harmful depending on the modeled assumptions. Decreased carrier concentration may increase SCR length leading to better current collection, or decrease quasi-Fermi level splitting which could

limit V_{OC} . Similarly mobility can improve collection lengths but also increase recombination resulting in lower efficiency in certain models [44]. Slow-cooling increases the E_g and may reduce the number of sub- E_g states, but increases defect compensation and may also increase the extent of local E_g changes which could ultimately limit the potential for improvement with slow-cooled samples. It may be desirable to reduce Cu-Zn defects while discouraging defect clustering, however kinetics may impose practical limitations. Based on the neutron diffraction results of slow-cooled samples, an upper limit on Cu-Zn order likely contains multiple percent Cu-Zn anti-sites which would mean $>10^{20}$ defect pairs which could still provide significant E_g variations.

In the experiments above, slow-cooled single crystals offered better voltage and device performance than quenched crystals, however this only offers the outer bounds of what is to be expected for thin film devices. Quenched samples were cooled from higher temperatures (750°C) and cooled faster ($>50^\circ\text{C}/\text{sec}$) compared to traditional thin film samples (500-600°C max and cooldown at 0.1-10°C/sec depending on vacuum or ambient environment). Most literature reports still don't pay diligence to controlling or reporting cool-down times during fabrication, but it is likely that most thin films samples fall somewhere between the quenched and slow-cooled extremes demonstrated in this report. More work is needed to determine if there is an optimal post-annealing or slow-cooling procedure which can allow for some of the benefits of slow-cooling without defect clustering which can lead to detrimental E_g fluctuations.

3.6.7 Conclusion

We have shown that in addition to Raman, XRD is useful for determining the presence of cation disorder in CZTSe. In addition we have shown that single crystals

subject to a slow-cool exhibit improved intra-grain mobilities and reduced carrier concentrations.

Low temperature PL measurements show reduced peak energies for quenched samples and recombination likely dominated by DAP with a tail of states below the emission peak. Although fewer Cu-Zn defects are expected for slow-cooled or low-T annealed samples, the PL behavior appears less ideal. We observe a broad PL peak with large peak shifts with intensity suggesting significant potential fluctuations are present. The origin the fluctuations may include both E_g fluctuations and local electrostatic potential fluctuations due to a highly compensated sample with fewer free carriers to screen band edge perturbations. The inability to completely “order” the samples are predicted to lead to local clustering of more ordered (high E_g) and more disordered (low E_g) phases due to the reduction in energy by clustering of local Cu-Zn defects. The resulting E_g -fluctuations may therefore be larger in samples where slow-cooling or low temperature annealing is used and may explain why “order” annealing has not yet led to improved champion devices. Additional research will be needed to determine if an intermediate level of annealing or cooling can provide some of the benefits of slow-cooled samples without promoting detrimental defect clustering or if additional techniques may be required to reduce band-tailing.

3.7 Progress in Single Crystal CZTSe Devices

Devices were fabricated on individual single crystals using a traditional device structure although a metal top contact was avoided due to the small cell area. CdS was deposited by chemical bath deposition and ZnO/ITO layer was sputtered through a 3.14mm² circular mask. The crystals were mounted on Mo-coated glass with Ag paste and probes were contacted directly to the ITO as the front contact. Device area was confirmed via LBIC to be equal to ITO contact area although shading from the front probe accounted for ~10% area coverage.

Dozens of devices were made over the last 2.5 years and the improvements in V_{OC} and efficiency have come from new improvements in understanding and optimization of crystal growth, surface passivation, and stoichiometry. The most recent champion cells were enabled by improving the CdS interface through low temperature annealing of the completed device. The history of progress in device efficiency and key enabling concepts are shown in Figure 3-24.

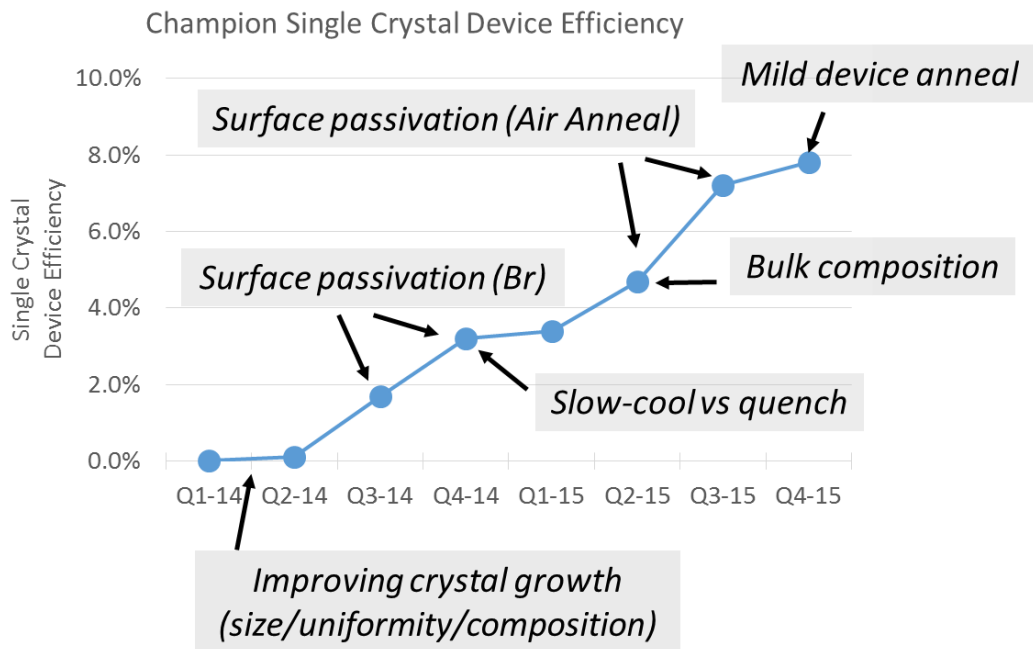


Figure 3-24: History of single crystal champion device efficiency and key concepts enabling improvements¹⁵

After the initial device trial period, surface passivation via Br-etching was the first breakthrough. The extent and depth of the damaged surface layer was recognized and etching was optimized. Slight improvements came with slowing the cool-down to moderate cooling rates, and further improvements were noted as crystal growth achieved lower Cu-concentrations. In the last year air annealing brought champion device efficiencies above 7%, and most recently, a mild device anneal further increased efficiencies to 7.8%.

¹⁵ This give little mention of the groundwork of more than 9 months of crystal growth and trial devices before an efficiency >1% and voltage >100mV was achieved. Special thanks to Brian McCandless whom without, we may still be stuck at <1%. He was the device making-wizard and performed much of the precise cell making labor.

The key parameters and JV curve for the champion device can be seen in Table 3-4 and Figure 3-25. In the table, the improvements with recent process steps can also be seen with iterative tests on the same cell. Cell re-processing was often used to re-examine promising cells with new surface treatments. This involved stripping off the CdS layer, redoing the Br-methanol etch (to remove the top 1+ micron), and re-passivating with a new treatment before re-applying the CdS and ZnO layers. This is noted in the table below.

Table 3-4: Device parameters for champion cells and improvements from processing

	Step	Treatment	V _{OC} (mV)	J _{SC} (mA/cm ²)	FF (%)	Efficiency (%)	Area adj Efficiency (%)	E _g from QE (mV)	V _{OC} Deficit E _g -qV _{OC} (mV)
SY24E-D20	1	Original	306	5.2	22.4	0.6	0.7		
	2	Re-process + re-passivate + AA 350°C x 6'	385	22.8	63.0	5.5	6.1		
	3	+ 100°C x 4'	382	27.8	64.2	6.7	7.4		
	4	+ 150°C x 4'	400	26.9	66.4	7.1	7.8	0.98	580
SY24E-D4	1	Re-process	341	30.4	40.3	4.7	5.1		
	2	+ 100°C x 4'	385	30.7	51.1	6.0	6.4	0.98	595

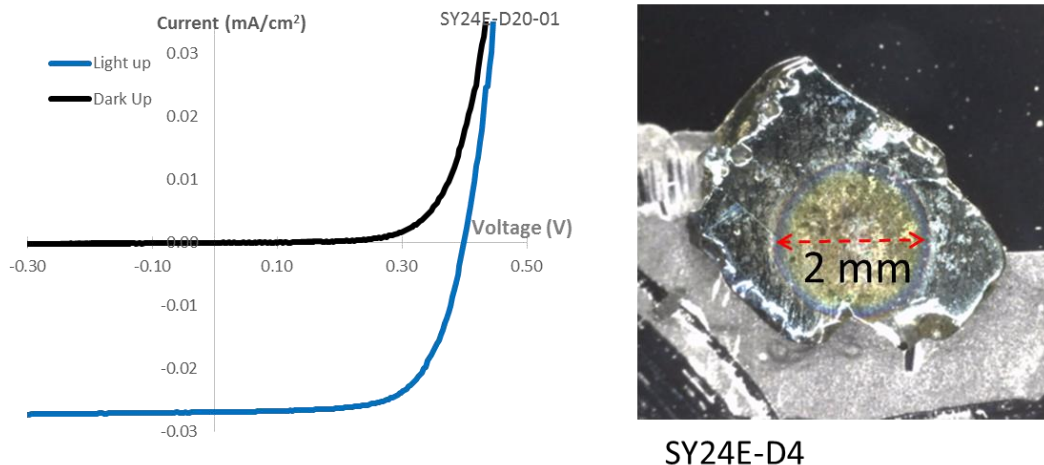


Figure 3-25: JV curve for champion 7.8% single crystal device and photo of other device for area correction

SY24E-D20 device was first tested in “Original” condition after 10’ of Br etching. It was later reprocessed with a more optimized Br etch and air anneal which brought cell efficiency up to ~6.1%. Further mild annealing of the CdS junction in air at 100°C improved efficiency to 7.4%, and finally re-annealing at 150°C for an additional 4 minutes brought the efficiency to 7.8% as seen in Figure 3-25.

A previous champion cell, SY24E-D4 listed at the bottom of the table, similarly showed an improvement in efficiency with mild device annealing, mainly through increased V_{OC} . The mechanism of the improvement likely arises from enhanced interface quality between device layers, the most critical of which is the CdS junction. A conduction band spike of ~0.4 eV has been measured at the junction to the CdS [43], which should reduce surface recombination by inducing band bending in the CZTSe layer to keep holes away from the junction [18]. A mild spike can be effective in reducing SRV regardless of interface defect density as shown in models for CIGS [129],

and CZTSe [44]. It's worth noting, the damaged surface region of single crystals, and the passivation discussed in Section 3.3, potentially extend more than 1 micron into the crystal surface and therefore would not be significantly improved by interface band bending which is only expected in the top tens of nanometers. Other literature reports have recently confirmed V_{OC} and efficiency improvements with mild device annealing and also cited improved CdS quality [130]. The most recent champion devices in this work, and the benefits of post device annealing were only noted in the last ~2 month of this work and therefore additional investigation to improve understanding and optimize the noted improvements is ongoing.

The progression of EQE curves over the last two years can be seen in Figure 3-26. The improvements in both passivation and bulk lifetimes and diffusion lengths can be seen leading to our current champion device. Surface recombination will generally shift the EQE curve down across all wavelengths since the electron minority carriers have to cross the interface for collection regardless of where they are generated. Improvements in the bulk can be more easily seen in the long wavelength fall-off of the EQE curve. Defective bulk material, as seen in the earliest cells, show very low collection in longer wavelengths because carriers recombine before they can diffuse to the junction.

A more detailed device analysis of the current champion cell is given in Section 4.8: Single Crystal Champion Device Analysis and Comparison to Thin Films.

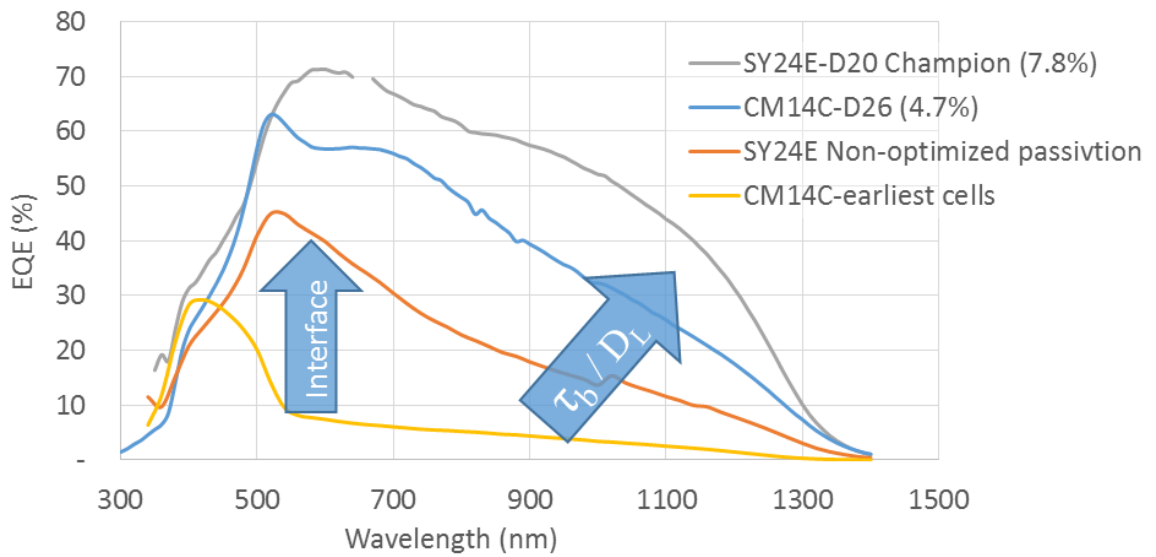


Figure 3-26: EQE curves for current champion single crystal and older devices.

3.8 Summary of Control of Defects

Passivation, stoichiometry, dopants, and temperature processing are all key aspects of controlling defects and achieving efficient devices. Single crystals can offer particular insight into each of these areas, and were investigated in order to explain the obstacles to efficient devices.

As grown, CZTSe crystal surfaces were found to have Cu and Sn rich surfaces not suitable for proper solar cells. Mechanical polishing was used to create parallel facets of controlled thickness away from growth surfaces. Furthermore, chemical etching in a bromine-methanol solution was demonstrated to improve passivation through the removal of a damaged surface layer as well as providing an anion terminated surface with upward band bending further reducing surface recombination. Additional passivation steps such as air annealing were found to change properties of both the surface and bulk and were essential for the best achieved devices.

Bulk properties of crystals were measured and Cu concentration was found to be the dominant controlling variable for the range of studied properties. Hole concentrations in bulk crystals are negatively correlated with Cu concentration, consistent with Cu_{Zn} as the dominant defect. Cu concentration was also found to critically change the electronic transport, as well as the recombination and sub- E_g defects. Shallower defects and higher PL intensities suggest bulk defect properties are improved for Cu-poor samples.

Alkali dopants such as Na are critical for high-efficiency thin films and have been shown to passivate grain boundaries but their role in the bulk of CZTSe is not yet clear. Direct measurements of Na incorporation into a bulk single crystals are demonstrated for the first time suggesting a solid solubility on the order of $\sim 10^{18}$ and high diffusivity at 420°C.

Thermodynamics principles can be used to predict the temperature dependence of point defect populations in equilibrium, and therefore temperature equilibria offers a unique way to control defect populations. This was found to be particularly critical for CZTSe where Cu-Zn anti-site formation has been shown to be dependent on cool-down speed. Theoretical arguments suggest one of the major roadblocks to higher V_{OC} – significant band tailing— could be improved with increased cation order, however few direct measurements have been reported and significant device improvements have not yet been realized. We report electrical properties, defects, and devices from quenched and slow-cooled single crystals of CZTSe. Disorder was characterized by Raman spectroscopy as well as x-ray diffraction (XRD), where the change in Cu-Zn order can be detected by a changing c/a ratio. Quenched samples show higher acceptor concentrations, lower hole mobilities and a lower-energy photoluminescence (PL) peak

than crystals cooled at slower rates, consistent with a reduction in bandgap. In addition, samples quenched at the highest temperatures showed lower PL yield consistent with higher quantities of deep defects. Devices fabricated from slow-cooled CZTSe single crystals showed improved efficiencies, most notably with increased V_{OC} ; however low temperature intensity-dependent photoluminescence measurements continue to indicate the existence of potential fluctuations. We discuss the possibility that potential fluctuations in slow-cooled samples may be related to the inability to achieve long range order of the Cu-Zn sub-lattice resulting in local regions of high and low levels of cation order, and consequent local variations in bandgap.

Improved devices are demonstrated attributable to improvements in passivation, stoichiometry and temperature processing discussed throughout the chapter. A 7.8% single crystal device was achieved with V_{OC} deficits competitive with current champion thin films.

The differences between the single crystal and thin films, as well a comparison of champion crystal and champion thin film devices and future opportunities are discussed in the next chapter.

**Chapter 4 - PART II: Thin Films:
MODIFICATION OF DEFECTS IN THIN FILMS**

4.1 Abstract

Passivation, Stoichiometry, Dopants and Substitutions and Temperature Equilibria are applied to thin films and comparisons to single crystals are discussed. This analysis focuses on device measurements and PL spectra including a significant reinterpretation of previous thin film PL results. Champion devices for thin films and single crystals are compared and opportunities for future improvements are highlighted.

4.2 Overview

This work has been performed as a collaboration with IBM, and other universities over the past 2 years. The collaboration has given us access to both analytical equipment such as PL discussed in this work, as well as champion efficiency thin films which have been developed at IBM and optimized over the last ~ 8 years. IBM currently holds the world record for device efficiency for both the pure selenide CZTSe at 11.6%, and the mixed sulfur-selenide, CZT(SSe) at 12.6%. The motivation of this work is to improve the ability to understand CZTSe and ultimately create more efficient polycrystalline thin film devices and therefore the comparison of single crystals and cutting-edge thin films is important.

In addition to contrasting to single crystals, the analysis of thin films had a number of benefits including: faster fabrication (1-day vs 1-month), a wider range of

achieved compositions and Na dopings, and less time-consuming characterization for PL spectra due to ease of alignment which proved difficult for single crystals.

This chapter is parallel to Chapter 3 with sections on Passivation (4.3), Stoichiometry (4.4), Dopants and Substitutions (4.5) and Temperature Equilibria (4.6) however the analysis will be focused on thin films made at IBM. Comparisons with single crystals are discussed throughout.

Characterization will focus on device measurements as well as sub- E_g states via PL spectra, Section 4.5.2.1 details new interpretations of PL measurements due to detector saturation which revises the previous understanding as described in five previous publications. At the end of the chapter, in Section 4.8, the champion single crystal and thin film devices are compared, and the device analysis of the single crystal is utilized to explain the deficits and differences. Finally, in Section 4.8.2, future opportunities for single crystals and film are compared based on the current champion devices.

To begin, the fabrication method of IBM films is briefly summarized.

4.3 Fabrication Overview for IBM Thin Films

IBM has developed co-evaporation and a solution-growth method, each of which involve deposition at low temperatures followed by very similar rapid selenization. In the solution method, hydrazine is used to dissolve constituent elements which are then spin-coated onto the substrate in layers before annealing. Details of the method are not examined in this work and are described in [14], [131]–[134]. For co-evaporation, the film is deposited at 100°C to avoid the challenging decomposition and volatile elements discussed in Chapter 5. The details of the methods can be found in ref. [31], [135], but both methods achieve a uniformly distributed Cu-Sn-Zn-Se mixed-

phase precursor which are then annealed by a rapid thermal process at $\sim 600^{\circ}\text{C}$ for a few minutes in the presence of excess S/Se. After selenization, an air anneal on a hotplate at 375°C is performed to improve passivation as described in ref. [69] before CdS deposition. A traditional device stack is used SLG/Mo/CZTSe/CdS/ZnO/ITO/grid with optimized thickness to minimize reflection and absorption as described in ref. [136]. A MgF_2 anti-reflective layer is used only in champion cells.

4.4 Passivation:

Thin films are likely to have a very different surface termination compared to single crystals due to vast differences in growth procedure, and therefore passivation procedures may not fully translate between single crystals and films. Contrasting the same passivation procedures on state-of-the-art films which are able to achieve $>10\%$ efficiency provides insights into continued surface optimization.

4.4.1 Effect of Br on Thin Films

Bromine etching was found to be a critical part of passivation for single crystals however the results for films were mixed. In hydrazine processed films, the PL intensity was found to increase with Br etching as depicted in Figure 4-1. However for films created by co-evaporation, PL intensity was found to drop and plateaued between 1-2.5 minutes of Br etching. At the tested etch concentration (0.1 vol %), films were likely to have etched less than 0.1 microns for the 15 second etch and ~ 1 micron for the 2.5 minutes of etching.

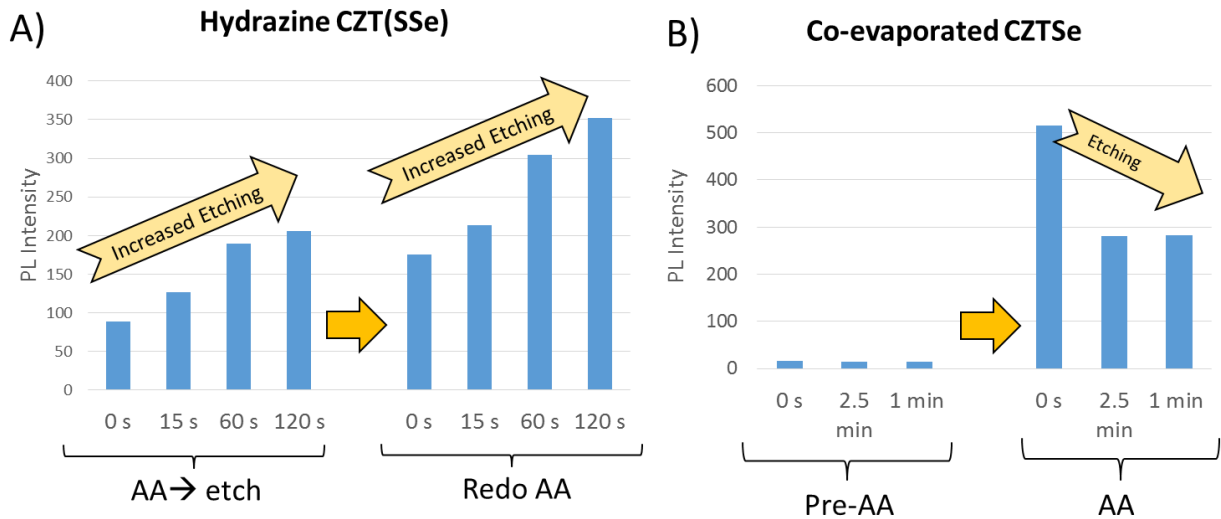


Figure 4-1: PL intensity of Br-etched films. In A) hydrazine fabricated films were AA first, and then etched for PL. The AA was then redone on the same samples. In B) samples were *etched prior to AA* and measured. Then samples were AA and re-measured with PL.

SEM images of the film surface, Figure 4-2, show the grain boundaries become more pronounced from Br-etching, however pinholes are not observed and shunting was not found to be a problem for the duration of the etch. The original 2 micron film is expected to be etched to ~ 1.2 microns over the course of the 2 minute etch.

Devices were made for the hydrazine processed films which increased PL intensity, however modest declines were noted in most device parameters summarized in Table 4-1. The origin of the decline, despite the increase in PL, requires additional explanation. Literature reports from CIGS suggest the Se rich layer left by the Br-etch can decrease device performance. This layer can be removed by a brief KCN etch or an annealing step, which has been shown to restore device performance [137].

This insight may be particularly important to the single crystal devices since much longer etching durations are utilized (upwards of 8 minutes). This may leave a problematic Se layer as noted in the literature and may explain observed device improvements for single crystals after air annealing through evaporation of the Se layer. Additional testing with KCN is warranted.

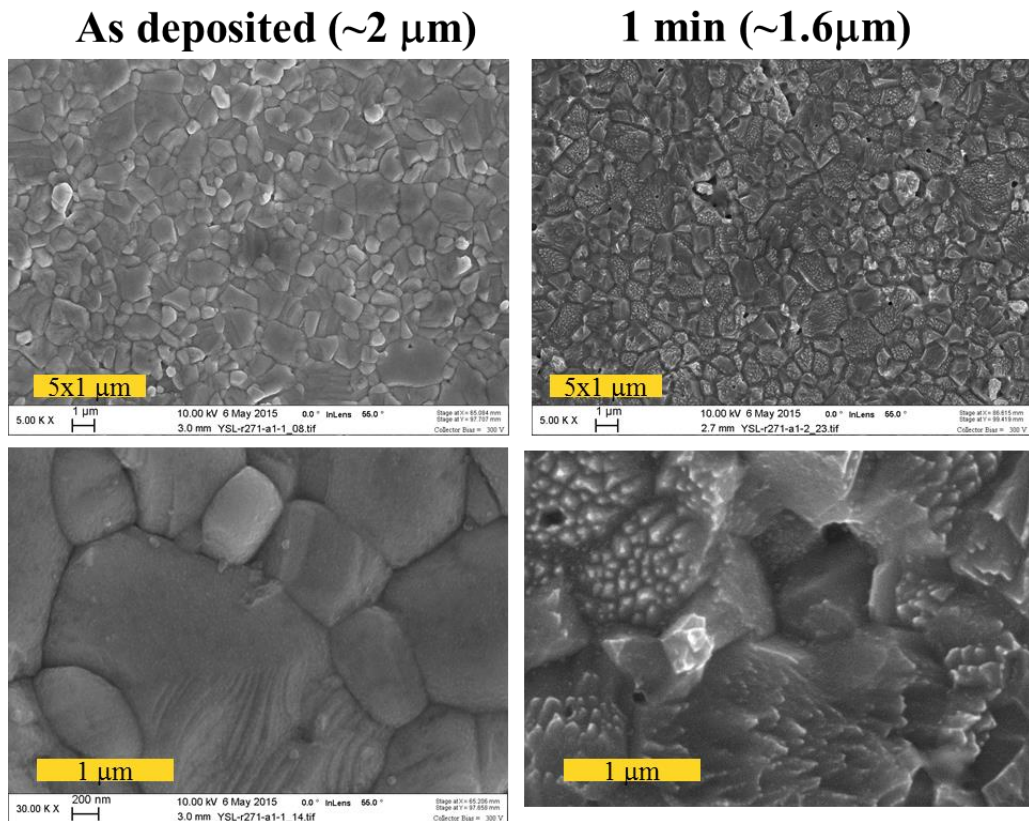


Figure 4-2: SEM images of Br-etched films (in-lens detector)

Table 4-1: Device results for Br etched films

	Eff	FF	V _{oc}	J _{sc}
	%	%	mV	mA/cm ²
Control	9.2	65.5	453.9	31.1
15 Sec	8.4	65.0	450.0	28.7
60 Sec	7.7	61.5	427.7	29.1
Control 2	8.7	65	447	29.9
120 Sec	8.4	64	445	29.6

4.4.2 Effect of CdS on Thin Films

For CZTS films, PL intensities were found to generally decrease after CdS deposition (Figure 4-3). This is the opposite of what was generally found for single crystal samples discussed previously (Pg 76). It is believed that the air anneal process provides passivation of grain boundaries and therefore the effects of carrier separation dominate over any further changes in grain passivation. No change in PL peak energy was noted.

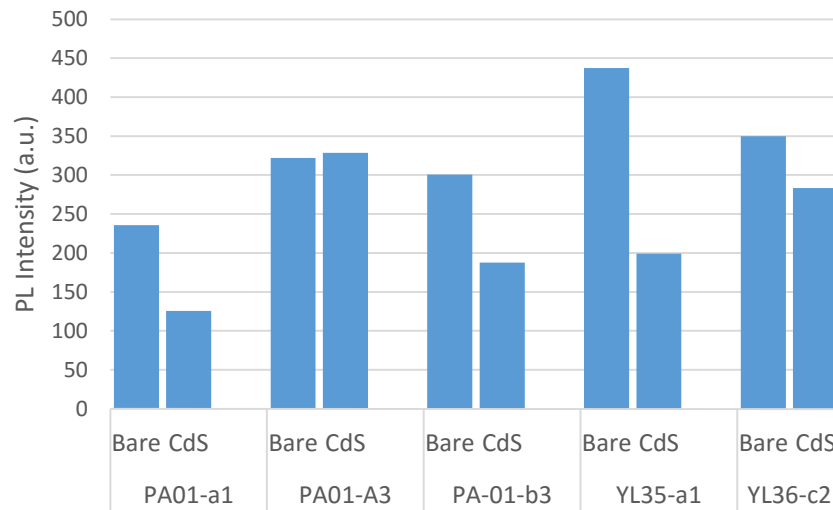


Figure 4-3: Effect of CdS on PL intensity. PL intensity of bare CZTS films after AA and the same films after CdS deposition.

The difference in behavior exhibited by thin films may be explained by differences in carrier concentrations, which are 5-10 times lower than are found in single crystals. This would result in a wider space charge region for films and therefore a higher percent of e-h pairs will be separated by the electric field in the space charge region, rather than recombining radiatively as discussed in 3.3.6. In addition, the improvement in PL through CdS passivation may be higher in single crystals if the uncoated crystal surface contained significant dangling bonds or other factors which otherwise increase SRV.

4.5 Stoichiometry

The effects of stoichiometry on sub- E_g defect states were also examined in thin films. Effects such as secondary phases are expected to have a larger impact due to their ability to form and segregate at grain boundaries. This section will be parallel to Section 3.4 on single crystals, and will focus on the effect of Cu on sub- E_g states in thin films.

One of the largest impacts of this work is a significant reinterpretation of PL measurements in the literature due to detector saturation which is discussed in 4.5.2. The new interpretation allows estimates of minority carrier lifetime. Finally, devices for Cu-poor and stoichiometric films are shown in Section 4.5.3.

4.5.1 Effect of Cu on Thin Films

Completed thin films devices (including CdS) of Cu-poor and near-stoichiometric compositions, similar to the aforementioned single crystal samples, were also examined by PL. The full compositions for Cu-poor and near stoichiometric samples are given in Table 4-4, Pg. 157. Similar to the single crystal results, the PL measurements for near stoichiometric samples had lower PL peak energy (0.87 eV), and lower PL intensity when measured with a 532 nm laser. The apparently brighter PL image for the Cu sample can be explained by the presence of the CdS junction. A more detailed description of the discrepancy in PL intensity is given in the appendix Pg. 234. As will be shown, Cu-poor samples appear to have longer minority carrier lifetimes. Interestingly PL uniformity also improves significantly in the near stoichiometric sample. This may be related to improved composition uniformity for stoichiometric samples or possibly fewer deviations in the CdS junction, but further investigation is necessary. The effects of aging may also play a role since the PL images were taken on samples that had been stored in a dry-box for multiple months. Despite the non-uniform

PL images, the Cu-poor devices achieved >9% efficiency while stoichiometric samples were shunted (device results discussed in Section 4.5.3, Pg. 142).

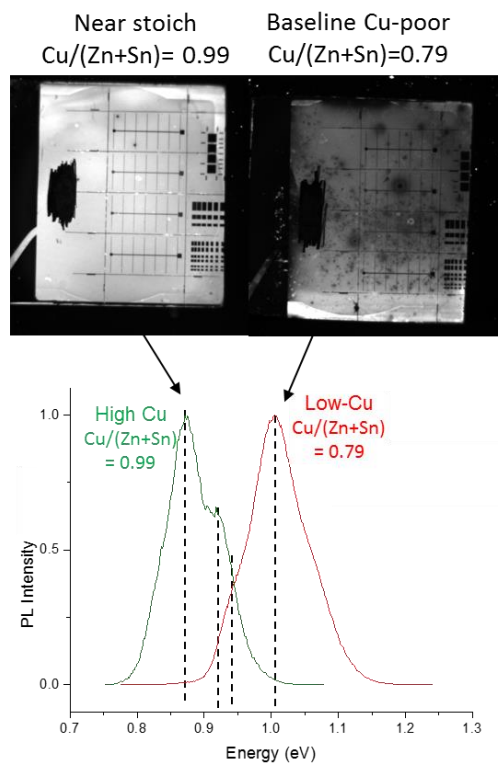


Figure 4-4: Effect of Cu on PL image intensity and PL spectra

Bandgaps and PL emission energy for both single crystals and films are compared in Table 4-2. The bandgaps were extracted from the inflection point of the QE for the depicted thin film devices as well as for single crystal devices discussed in Chapter 3.

Relative to the E_g , the PL emission was found to be shallower for Cu-poor samples, and was shallower still for Cu-poor single crystal samples. In well behaved

semiconductors, the PL emission peak at room temperature will be equal to the E_g , however a significant deficit from E_g are noted in CZTS-related films [138]. The increasing E_g-E_{PL} for near-stoichiometric samples represents increasing quantity and/or depth of the dominant sub- E_g defect states.

Table 4-2: PL peak position and E_g extracted from QE for Cu-poor and stoichiometric thin films and single crystals¹⁶

	$Cu / (Zn+Sn)$	E_{PL} @ RT (eV)	E_g from QE (eV)	Difference $E_{g-QE}-E_{PL}$ (eV)
Sy24e - Cu-poor xtal	0.85	0.96	0.98	0.02
SY24a - stoich xtal	0.99	0.91	NA	NA
119 - Cu-poor film	0.79	1.01	1.07	0.06
120 - Stoich film	0.99	0.87	1.03	0.17

The sub- E_g states and band tails can be best seen by low temperature PL since non-radiative recombination is reduced, and lacking thermal energy, photo-excited carriers relax to the lowest states before radiative emission. PL measurements taken at 4K are shown in Figure 4-5. Initial measurements at high laser intensity were found to saturate the detector and therefore only unsaturated PL spectra are shown in the Figure 4-5. Five previous publications discuss and offer explanations for the nature of the PL shape at high laser intensities prior to the recent recognition that the PL detector saturation can explain the noted PL spectra [40], [104], [138]–[140]. The origin and new interpretations from fixing this artifact are discussed in Section 4.5.2.1.

¹⁶ QE from the stoichiometric single crystal was not obtained due to shunted devices. Similarly, stoichiometric films were shunted and had poor long wavelength collection adding to potential error in determining E_g .

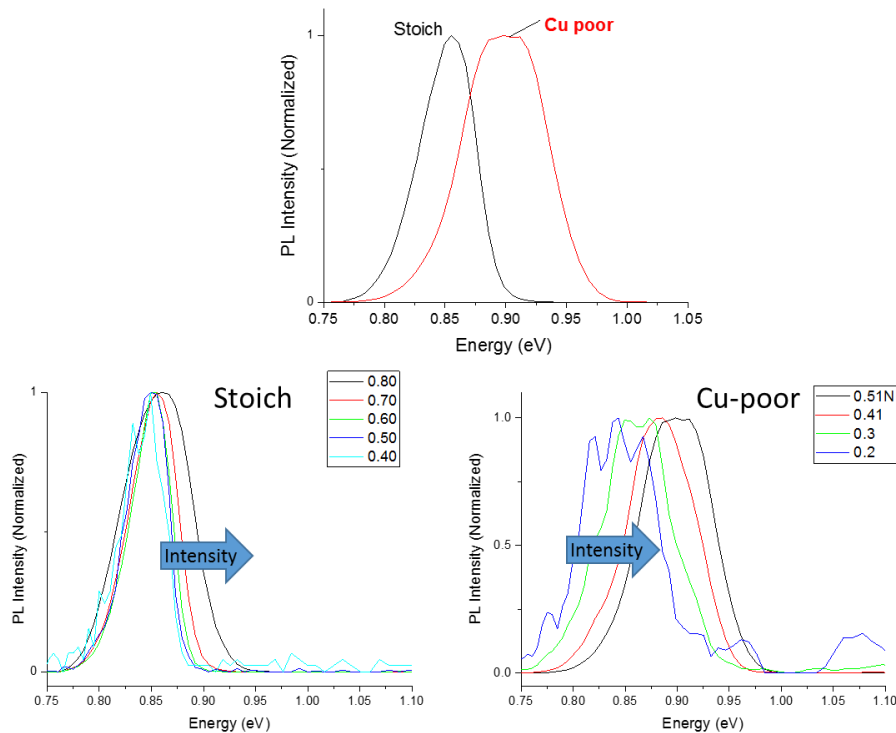


Figure 4-5: PL emission at 4K for stoichiometric and Cu-poor samples (laser intensities = 0.64 - 11.1 w/cm^2 for stoichiometric samples and 0.15 - 1.4 w/cm^2 for Cu-poor samples. Noise due to low signal accounts for the fluctuations noted at the lowest intensities.

At low temperatures, the peak position for stoichiometric CZTSe samples is ~ 0.85 eV and blue shifts ~ 13 meV / decade with increasing laser intensity. The low energy edge of the PL remains approximately unchanged, while the width of the PL emission increases slightly for high laser intensities. This can be attributed to filling of local density of states for the sub- E_g defects.

For Cu-poor samples, the PL peak position blue shifts strongly with intensity, ~ 59 meV per decade, from 0.85 eV to 0.90 eV over the range of tested laser intensities. The Cu-poor sample had much higher PL intensity at a given laser power and therefore

only lower laser power settings, below 1.5 w/cm^2 , could be used before the PL detector was found to saturate. The large blue-shift noted for the Cu-poor sample is likely explained by potential fluctuations. As laser intensity increases, electrostatic fluctuations become increasingly screened due to higher numbers of photo-excited carriers. These concepts are discussed in more detail in Section 3.6.4

4.5.2 Minority Carrier Lifetimes

An inadvertent discovery due to the realization of PL detector saturation was a new method of qualitatively obtaining lifetimes of semiconductors as a function of wavelength. From the PL curves taken with a saturated detector, the lifetimes can be estimated. To explore carrier lifetime for Cu-poor and stoichiometric samples, a brief explanation for the detector saturation must be first provided.

4.5.2.1 Nature of PL Detector Saturation

The PL spectra tool uses a pulsed laser with 1 ns pulse width and 15 kHz repetition rate to provide both PL spectra data and TRPL at a chosen wavelength. The PL signal is passed through a monochromator and measured by a time correlated single photon counting system with InGaAs PMT detector cooled to -80°C as described in Appendix, Pg. 222. Due to the pulsed nature of the laser, very high electron-hole pair densities can be generated during the duration of the laser pulse. At full intensity, each pulse generates $1.5 \times 10^{-3} \text{ J/cm}^2$ according to calibration measurements, which translates to $\sim 4 \times 10^{20} \text{ e-h pairs/cm}^3$ under a calculated absorption depth of 100 nm [138]. In previous investigations of CZTSSe with this tool, the PL spectra shape seen in Figure 4-6 was found. At low temperatures in high efficiency samples, a plateau is noted at high energies (often near and above the E_g). This region was shown to correlate with

low PL lifetimes as shown in the right-hand y-axis. The region that extends above the plateau height is found to have increasing lifetimes for lower wavelengths.

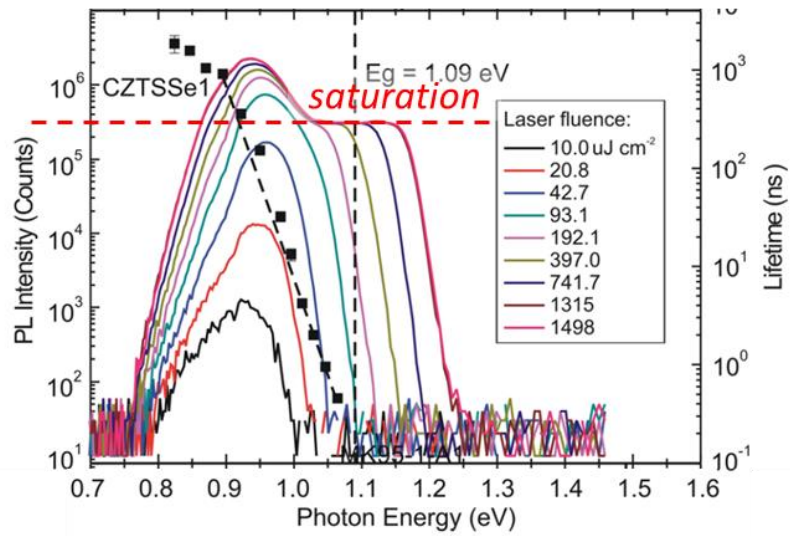


Figure 4-6: PL spectra and lifetime in log scale as a function of wavelength showing correlation of lifetime with detector saturation. Modified from [138].

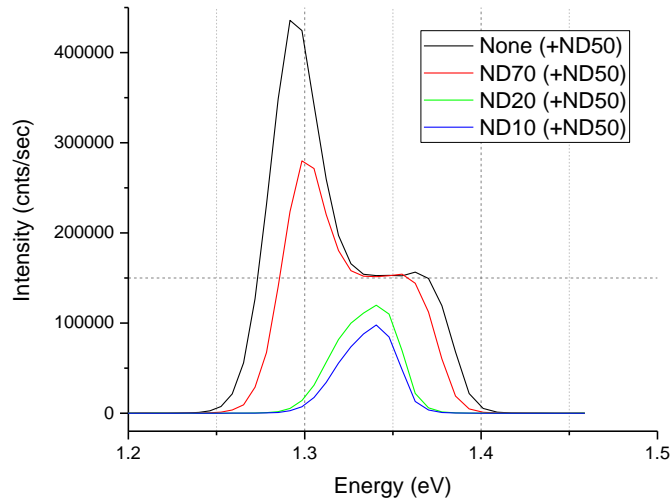


Figure 4-7: PL spectra of AZTSe sample with fixed laser intensity but changing neutral density filters in front of the detector.

The previous hypothesized explanation suggested the flat plateau at high energy was due to a physical phenomenon with the sample; saturation of radiative recombination occurring for higher energy e-h pairs near the E_g [40], [104], [138]–[140]. Further testing with a series of neutral density filters in front of the detector, demonstrated the PL shaped changed and the plateau disappeared when intensity at the detector was reduced as shown in Figure 4-7. This was the case regardless of the laser fluence hitting the sample surface, and confirmed that detector saturation is the cause of the noted shape. While saturation explains the noted plateau, the peak above the “saturated” plateau (exceeding 400,000 in Figure 4-7), requires further explanation.

For samples with high PL yield (high quality samples, high laser intensities, low temperatures), the PL detector saturates with each ns pulse as depicted in Figure 4-8. If a sample has PL emission only during the 1 ns laser pulse, the limit of ~ 150,000

counts/second is reached.¹⁷ This would be the case for regions of low lifetime (less than 1 ns). If samples continue emitting after the 1 ns laser pulse duration, which is true for samples with long lifetime, then the detector can reach above the 150,000 count saturation since the detector can continue to count photons over longer periods of time. From this knowledge, the PL spectra above the saturation plateau can be translated to estimations of lifetime. A more exact prediction of the lifetime from the measured PL intensity would require more detailed modeling accounting for detector refresh rate.

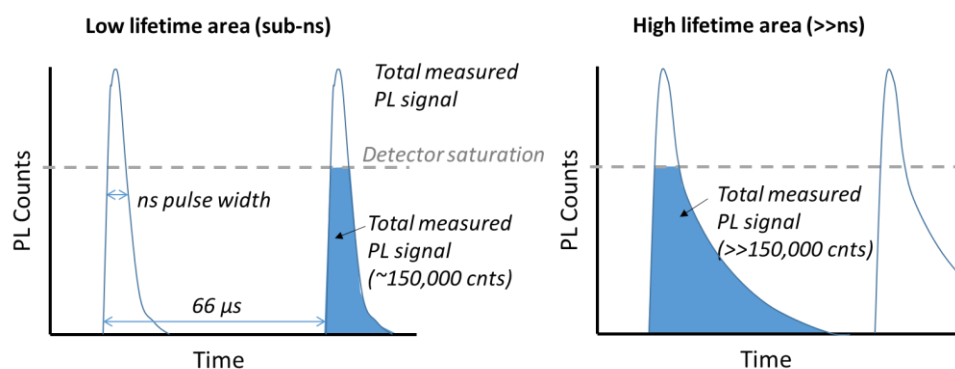


Figure 4-8: Schematic showing effects of detector saturation for low-lifetime and high lifetime areas. Laser pulse width is 1ns and laser repetition rate is 15khz therefore 66 μ s between pulses.

This qualitative method for lifetime assessment is limited to high quality samples, and/or low temperatures where PL saturation occurs and lifetimes are >1 ns,

¹⁷ The laser frequency is 15 khz and therefore it can be calculated: 150,000 counts/sec /15,000 pulses = 10 counts / ns pulse.

although in theory, with modification of detector settings, this concept could provide a helpful concept for screening lifetime.

4.5.2.2 Lifetime of Cu-poor and Stoichiometric Samples

The PL spectra for stoichiometric and Cu-poor thin films measured at 4K is shown in Figure 4-9 for all laser intensities. A dotted line at 150,000 counts/second depicts where PL saturation begins to effect the spectra. From the interpretation discussed above, the PL signal above this line is related lifetimes in excess of 1 ns. This suggests that stoichiometric samples, despite the low measurement temperatures, have very short lifetimes. The Cu-poor sample shows similarly short lifetimes at high energies above ~ 0.97 eV where the PL spectra is plateaued at the saturated limit, but lifetimes increase significantly for shorter wavelengths. Similar samples show lifetimes increasing to 100-1000 ns at 4K for PL energies below the peak seen at ~ 0.89 eV.

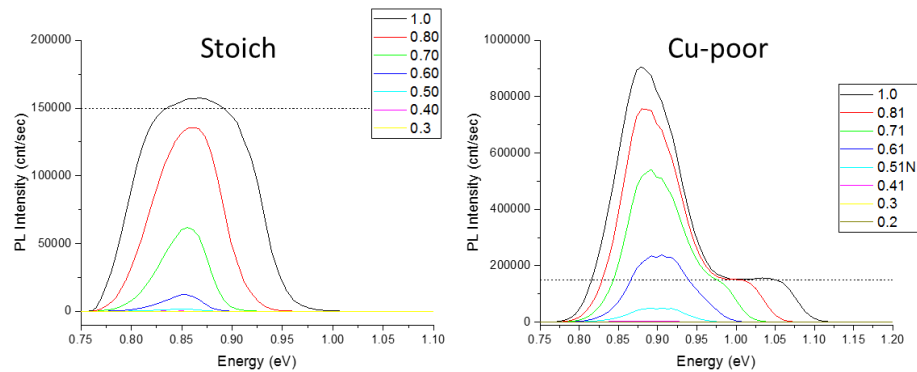


Figure 4-9: PL at 4K for Cu-poor and stoichiometric films for high laser intensities with effects from detector saturation.

This change in lifetime with energy has two likely contributions. Carriers in high energy states are expected to relax to lower energy states in time scales much faster than PL emission [52], Ch. 6. This leads to the low observed lifetimes at high energies. The origin of any PL emission at high energies, in some cases above the E_g , is likely explained by the high e-h pair densities achieved at full laser power ($\sim 10^{20}$ /cm³) which saturates the lower potential fluctuations and lower energy band states [139].

Extended lifetimes are expected at low temperatures due to reduced rates of SRH recombination [51], however an additional contribution can occur for samples with significant carrier localization. At low temperatures, carriers can become trapped in local potential minima, which reduces the likelihood of diffusing to a defect where SRH recombination is possible. In addition, in samples with high levels of charged defects, electrostatic potential fluctuations, can result in local potential minima and maxima occurring in neighboring regions, thus requiring tunneling for radiative recombination. This requirement for tunneling can similarly increase PL lifetimes at low temperatures and has been reported for CZTSSe [45].

4.5.3 Devices

The best device made from the aforementioned Cu-poor and stoichiometric films are shown in Figure 4-10. Efficiencies from 9 - 9.5% were achieved for Cu-poor films, while all stoichiometric samples were found to be significantly shunted. The origin of the shunting may be Cu and Sn-rich secondary phases, however the results of bulk measurements on thin films and single crystals in Chapter 3 demonstrate that stoichiometric samples have additional detrimental factors in the bulk which are likely to lead to poor devices results – even in the absence of secondary phases.

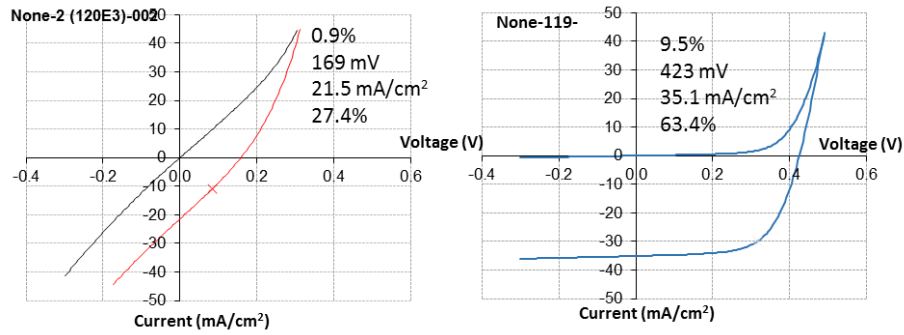


Figure 4-10: Devices from Cu-poor and stoichiometric films

4.5.4 Summary of Stoichiometry

The poor performance of stoichiometric samples has been frequently ascribed to shunting caused by Cu-rich secondary phases [90], [141]–[143]. Theoretical calculations have further suggested Cu-poor samples have bulk defects more suitable for solar cells however significant experimental confirmation is lacking. This work supports the theoretical calculations by showing a number of detrimental bulk changes for films and crystals with near the stoichiometric composition. These factors include carrier concentration, sub- E_g defects, and minority carrier lifetimes.

Cu-poor CZTSe has lower carrier concentration, explained by reduced Cu_{Zn} acceptors, which extends the depletion region further into the absorber layer. This can improve current collection, particularly for defective material with poor lifetime. This effect has been notable for CZTS-based materials, which typically have effective electron lifetimes of 1-10 ns and diffusion lengths of less than 1 micron even in highly efficient devices [14], [44]. Low carrier concentration can however also limit open circuit voltage. The maximum theoretical open circuit voltage is controlled by the difference in quasi fermi-levels in the PN junction. High carrier concentrations move the fermi-level closer to the band edges, therefore enabling higher V_{OC} . Modeling work

has detailed the potential efficiency improvements with increasing carrier density as well as maintaining or improving lifetimes [44]

Cu-poor samples also show shallower sub- E_g defect states as measured by PL. This can be explained by the promotion of V_{Cu} -related defects and complexes, which are predicted to be shallower than Cu_{Zn} -related defects. Related charge balanced defect complexes are expected to exist in larger concentrations than isolated defects due to lower formation energies and while $[Cu_{Zn}+Zn_{Cu}]$ is predicted to have shallow states inside the E_g , $[V_{Cu}+Zn_{Cu}]$, which would be favored for Cu-poor Zn-rich solar cells, does not [42], [46].

Finally, higher PL intensities and higher minority carrier lifetimes are observed in Cu-poor single crystals and thin films. The expected lack of secondary phases or grain boundaries in the single crystals suggests that bulk defects contribute to the low lifetimes. In fact, theoretical predictions suggest that the defect pairs $[2Cu_{Zn}+Sn_{Zn}]$ and $[Cu_{Zn}+Sn_{Zn}]^+$ are the most likely bulk defects to affect minority carrier lifetime [28], [42]. Both defects are predicted to exist in high concentrations and will be minimized for Cu-poor and Zn-rich stoichiometry which accounts for the observations in this chapter.

4.6 Dopants and Substitutions in Thin Films

As previously discussed in Section 3.5.1, Na is critical to high efficiency thin film performance. Literature shows high concentrations in grain boundaries [110], [111] and from the single crystal SIMS results in work, bulk incorporation on the order of $10^{18} / \text{cm}^3$ can also be expected. With collaborators at IBM, the impact of Na on sub- E_g states was studied and is discussed in Section 4.6.1. Low-temperature PL was performed on thin films with different Na-doping concentrations and compared to a Na-free single crystal. Na is shown to reduce deeper sub- E_g radiative recombination while also increasing total PL intensity.

In Section 4.6.2, the substitution of Ag for Cu is discussed. Under the hypothesis that band-tailing is directly related to the ease of Cu-Zn antisite formation, one method of ameliorating band tailing would be to replace Cu with an element that is not predicted to swap with Zn. Na is one such element, although as discussed, due to the atomic size, only substitution of ppm level appear possible. Ag is a second potential substitution for Cu and related (Ag-Cu)(In-Ga)Se₂ compounds have proven to be successful solar absorber candidates and have recently achieve 19.9% [144]. If Cu-Zn antisite formation is indeed the cause of band tailing, Ag₂ZnSnSe₄ has the potential to significantly reduce this problem.¹⁸

¹⁸ Substitution of Ag clearly goes against the “abundant materials” motivation for CZTSe. Despite this, two points are worth noting: 1) Ag in Ag-alloyed thin films is not expected to make up a large portion of device costs at recent prices, 2) We can learn about CZTSe and band tailing related to Cu-Zn through the analogous system without Cu-Zn such as Ag₂ZnSnSe₄.

In Section 4.6.2, thin films from the (Ag-Cu)ZnSnSe₄ alloy series are made and the extent of band tailing is measured as a function of Ag substitution by comparisons of E_g and room temperature PL peak energy.

4.6.1 Effect of Na on Sub- E_g States

CZTSe thin films were fabricated by IBM's baseline process of co-evaporation [31]. CZTSe was deposited on Mo-coated CZTSe with a diffusion barrier. Prior to deposition, either 8, 15 or 30 nm of NaF was deposited on to the Mo/SLG substrate. Cu, Zn, Sn and Se were deposited at 150°C and then underwent a rapid selenization at ~600°C. Films were then air annealed as previously discussed (Section 3.3.4, pg 70) and bare films were examined by PL at 4K Figure 4-11. A single crystal (SY25A x1) was prepared below the melt and quenched at growth temperatures. The 4x4 mm crystal was polished and Br-etched prior to measurement.

Intensity dependent measurements are shown in Figure 4-11, with laser fluence from 0.29 - 44 w/cm² as listed in the legend. At the time of measurement, the artifacts stemming from detector saturation were not understood, and therefore the PL spectra taken above 3 w/cm² laser fluence is distorted. For the discussion, the focus will be on lower laser energies below 3 w/cm². PL intensities of the crystal were found to be significantly lower than thin films using the tested 532 nm laser and therefore detector saturation did not occur on that sample. The abrupt drop at 0.75 eV is due to the low energy cut-off of the detector and therefore is not representative of the samples.

A peak at ~0.86 and ~0.92 eV are found in all samples. For the low Na sample, the peak 0.86 eV peak is dominant throughout all ranges of laser intensities, and the 0.92 eV peak becomes notable only at high laser intensities (>3 w/cm²). As Na increases

to 15 and 30 nm of NaF thickness, three changes can be noted. First, the 0.92 eV peak becomes increasingly observable at lower laser fluences. This suggests more emission is occurring from shallower defect states. Second, the falloff of the PL spectra on the low energy side, from 0.86 – 0.80 eV, is steeper with increasing Na. The low energy tail of the PL spectra at low temperatures is a function of the density of states below the band-gap and therefore this steeper low energy tail suggests a shallower and/or less dense sub- E_g states. This is confirmed by admittance measurement in the literature [107]. Third, at all laser fluences, PL intensities are notably higher for high Na samples. This suggests a reduction in non-radiative recombination is occurring as Na increases. Increased minority carrier lifetime [145], as well as passivation of the surface and grain boundaries by Na has been previously reported in the literature in both CZTSe and CIGS [40], [146].

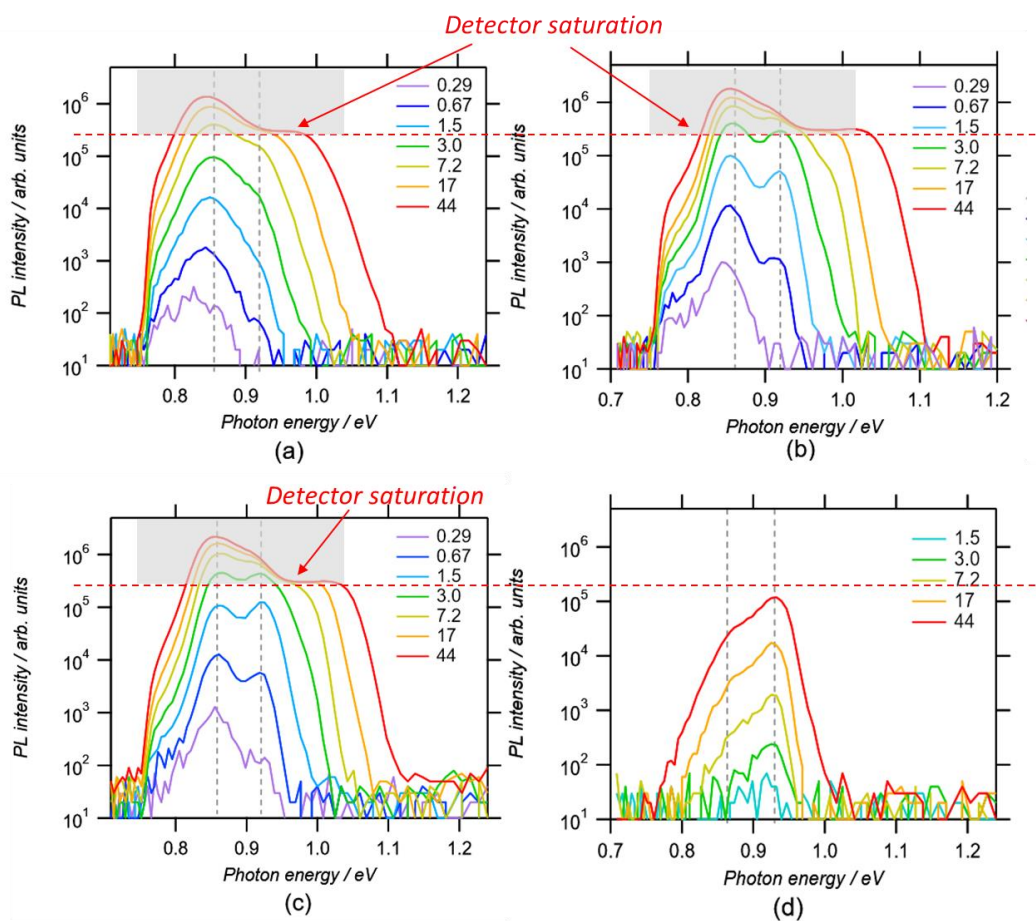


Figure 4-11: 4K intensity-dependent PL spectra of CZTSe with different amounts of Na. (a) CZTSe film with 8 nm NaF, (b) 15nm NaF, and (c) 30nm NaF, (d) Single-crystal CZTSe sample grown without sodium (Modified from [104])

Interestingly, the quenched single crystal with no Na appears to have PL emission which could be explained by the same two states at 0.86 and ~0.92 eV. This suggests that the two peaks are in fact related to intrinsic point defects in CZTSe (Cu, Sn, Zn or Se-related defects) which are modified by the presence of Na, rather than being new states contributed by Na-related point defects. This supports DFT

calculations which suggest Na-related defects are not predicted to have any states inside the bandgap [147], [148].

4.6.2 Ag Substitution

Note: The measurements reported here were part of a manuscript submitted to Advanced Energy Materials in December 2015.

A series of $(\text{Ag}_{1-x}\text{Cu}_x)\text{ZnSnSe}_4$ thin films were created by collaborators from 100% Cu, to 100% Ag. Films were created by co-evaporation as previously described but were selenized at different temperatures due to the reduced melting point as Ag is increased in the alloy. Fabrication details are provided in Ref. [149].

After fabrication the crystal structure was examined by XRD and full-pattern Rietveld refinement was performed to obtain lattice parameters as a function of Ag incorporation. An initial atomic model for the Rietveld refinement was generated for each sample by extrapolating from lattice parameters from references on the pure-Ag [150] and pure Cu [36] according to Vegard's law. The kesterite crystal structure has been reported for both compounds and was used in the modeling. The differences with the similar stannite crystal structure are modeled in detail in the Appendix, Pg. 235.

4.6.2.1 XRD of $(\text{Ag-Cu})_2\text{ZnSnSe}_4$ Alloy

The shift in the (112) peak and the derived lattice parameters can be seen in Figure 4-12. As the larger Ag atom is incorporated in to the lattice, the a-axis increases while the c-axis slightly decreases, increasing the tetragonal distortion of the lattice, in agreement with literature values, however we observe a slightly higher bowing for the

a-lattice parameter.¹⁹ The refinements for pure Ag and pure Cu matched the reference lattice parameters within +/- 2% [36], [150].

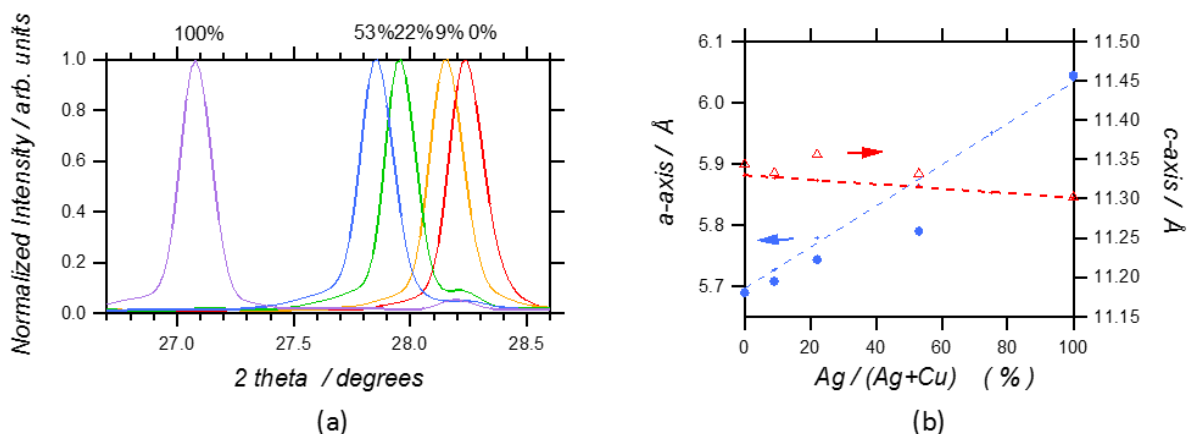


Figure 4-12: Shift in (112) XRD peak of ACZTSe samples (Ag/(Ag+Cu) ratio indicated above each curve) and (b) a and c lattice constants of ACZTSe samples as a function of Ag/(Ag+Cu) ratio

4.6.2.2 Modeled XRD of Ag-Zn Anti-site

One of the challenging aspects of Cu-Zn disorder in CZTSe is the difficulty characterizing it quantitatively with techniques such as XRD due to the similar scattering factors for Cu and Zn. The motivation for $\text{Ag}_2\text{ZnSnSe}_4$ derives from the hypothesized reduction in band tailing from reduced Ag-Zn anti-sites, however direct evidence for the presence or absence of Ag-Zn anti-sites is needed. In this work, the theoretical XRD profiles of $\text{Ag}_2\text{ZnSnSe}_4$ were simulated and it is shown that unlike

¹⁹ The bowing was particularly acute for the 53% Ag sample where excess MoSe_2 was also noted. It's not clear if stress related to the substrate may explain the larger extent of bowing.

CZTSe, Ag-Zn anti-sites can be measured by XRD. In the next section a reduction in band-tailing is demonstrated with increasing Ag.

Atomic models were generated based on the AZTSe reference lattice data by Gong [150] with the kesterite structure. The occupancy of Ag and Zn were altered on the 2c and 2d lattice sites from 100% Ag on 2c and 100% Zn on 2d (full ordered kesterite), to 50% Ag+50% Zn on both 2c and 2d (fully disordered kesterite). Three scenarios with intermediate amounts of disorder were also modeled (12.5, 25, and 37.5% Ag-Zn antisite pairs), and for all cases the total occupancy on each site (for Cu+Zn) added to one. Additional details including depiction of the physical model of the kesterite 2c and 2d atomic positions can be seen in the Appendix Pg. 235.

A related but distinct modification of cation order is the stannite crystal structure. In CZTSe, kesterite and stannite are extremely challenging to differentiate by XRD. An examination of the differences between kesterite and stannite in AZTSe is shown in the Appendix Pg. 235.

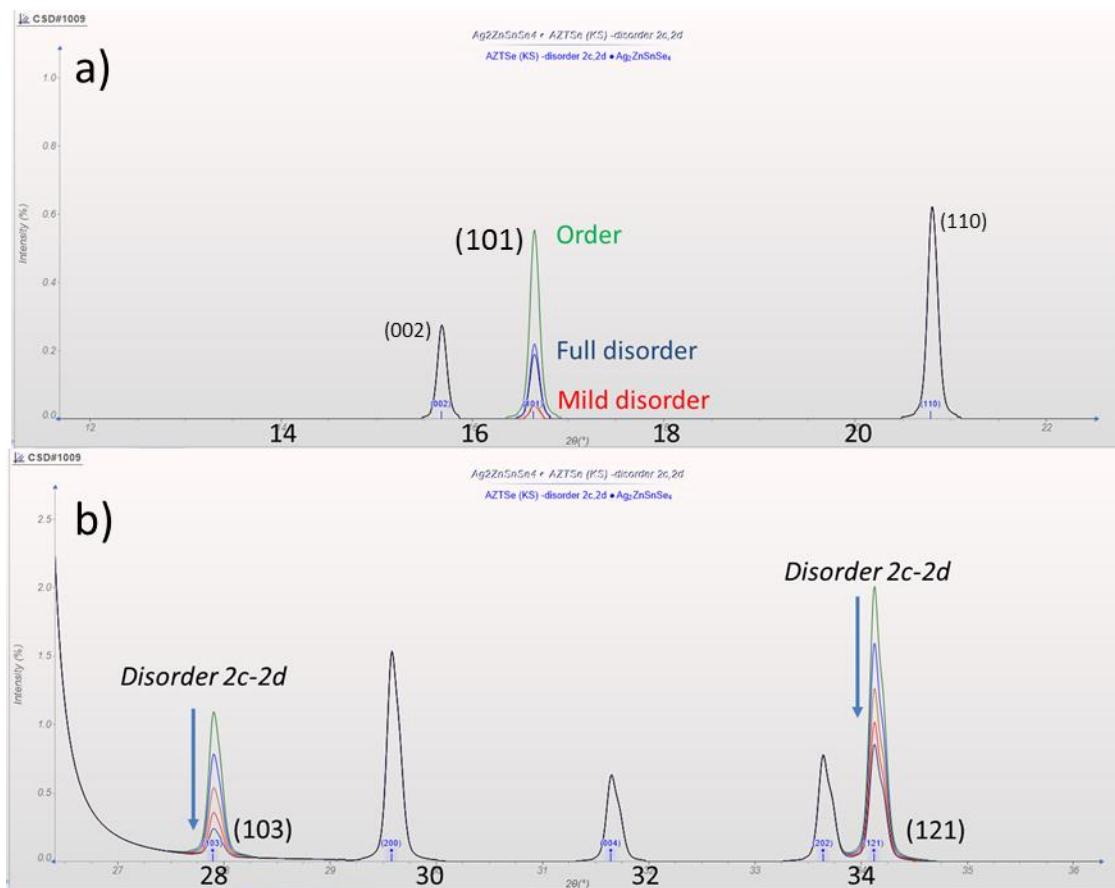


Figure 4-13: Simulated XRD profiles for kesterite AZTSe as a function of Ag-Zn cation disorder. Full order= 100% Ag on 2c, and 100% Zn on 2d-site. Full disorder = 50/50% Ag/Zn on 2c and 2d sites. Range of modeled Ag-Zn disorder: 0% (ordered), 12.5, 25, 37.5 and 50% (full disorder).

As seen in Figure 4-13, unlike CZTSe, Ag-Zn anti-sites can be seen by detailed XRD measurements however the modeled changes in intensity are quite small. The largest changes can be seen at low angle in the regions highlighted in Figure 4-13 from the (101), (103), and (121) peaks. Three key areas of differentiation are:

- 1) The 103 peak almost disappears from 1.2% absolute intensity for ordered, to ~0.2% absolute intensity for fully disordered –relative to nearby [200] peak which is fixed.
- 2) The 121 peak decreases from ~2.1% to ~0.9% absolute for the ordered and disordered case respectively while neighboring 202 peak is fixed.
- 3) The 101 peak reduces significantly with mild amounts of disorder from 0.6% to less than .06% between 25-37.5% antisites occupancy, and then increases to 0.25% for full disorder (50% antisites occupancy) which can be compared to neighboring 002 peak.

Large Ag-Zn order differences may be distinguishable through a qualitative description and the above points, however a more accurate assessment will require Rietveld refinement using the created references for initial refinement models.

4.6.2.3 PL of (Ag-Cu)₂ZnSnSe₄ Alloy

PL and absorption data are depicted for the aforementioned (Ag_{1-x}Cu_x)ZnSnSe₄ films in Figure 4-14. The E_g derived from the absorption curve can be seen to shift from ~1 eV up to 1.33 eV as Ag is incorporated to the lattice. The room temperature PL peak position is shown below the absorption data, and similarly, the PL peak position increases with Ag. Additionally, the gap $E_g - E_{PL}$ which is a metric of the extent of band tailing [54], shrinks from ~110 meV for the 100% Cu CZTSe sample, to ~0 meV for the pure Ag sample. In fact, Ag₂ZnSnSe₄ exhibits a PL peak 4 meV above the measured E_g , similar to the expectation of band-band emission energy, $E_g + KT/2$, for a semiconductor without band tailing [52]. The reduction in $E_g - E_{PL}$ for Ag substituted

films supports the hypothesis that Cu-Zn related anti-sites are related to the detrimental band tails in CZTSe and substitution of Ag for Cu may be a way to mitigate this problem.

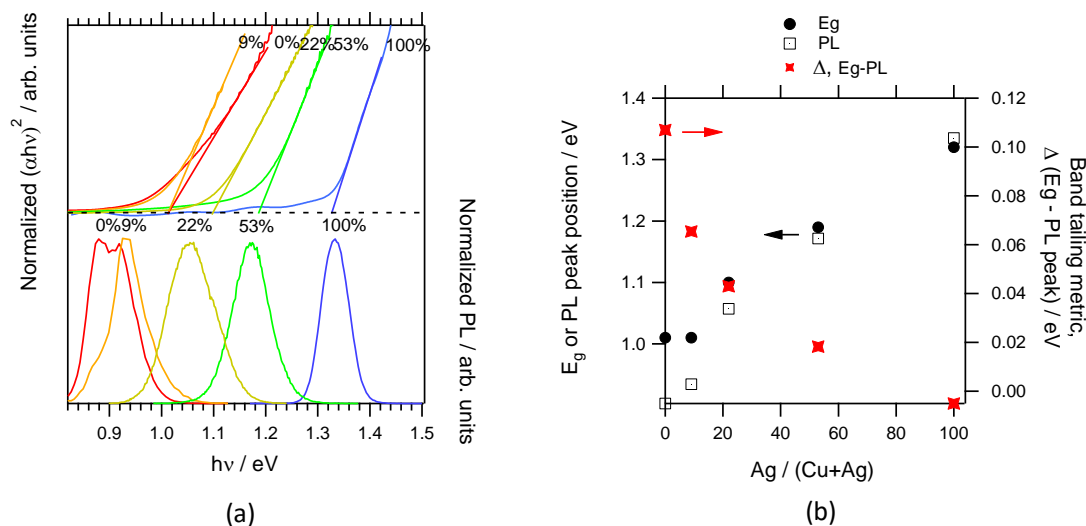


Figure 4-14: (a) Room temperature PL and band gap from absorption measurements for AZTSe, CZSe and Ag-Cu alloy. (b) The difference between bandgap and PL peak position. Submitted to [149]

Devices from collaborators demonstrated improved efficiencies, up to 10.2%, PCE with 10%-substitution of Ag in CZTSe. The boost in efficiency derived from a boost in V_{OC} and was attributed to the aforementioned reduction in $E_g - E_{PL}$. After an anti-reflective coating is added, the 10.2% device is expected to be close to the current world record CZTSe device of 11.6% [149].

4.7 Temperature Equilibria Applied to Thin Films

This investigation was started at IBM prior to my arrival, however after initial measurements were taken, it was not pursued further by IBM. Based on encouraging results from single crystals, I expressed interest in following up. I obtained the films (after annealing) and raw data for low-temperature PL (performed by Wei Wang at IBM). The interpretation, electrical and device measurements, as well as room temperature PL measurements are my own. A small subset of this work was published [151], although significant additional data and interpretation has been added.

4.7.1 Overview

To investigate application of the disorder-transition to thin films, samples were annealed low-temperature annealing for extended times above and below the expected transition. Long low-temperature annealing below the disorder-transition temperature should have similar effects to slow-cooling (although more limited by kinetics) and is a more feasible method for thin-films.

Both device-oriented Cu-poor, as well as near stoichiometric samples were fabricated and subject to annealing for 24 hrs at either 150, 200, or 250°C in a glove box. These anneals are expected to be below, at, and above the disorder transition respectively. A control set of samples was not annealed. One sample from each annealing condition was made into a device while a second sample was left bare for low-temperature PL measurements.

Table 4-3: Sample matrix for low temperature annealed thin films

Sample composition	Anneal time	Anneal Temp	Sample ID
Cu-poor	As-made	None	None
	1 day	150°C	150d
		200°C	200d
		250°C	250d
Near-stoichiometric	As-made	None	None
	1 day	150°C	150d
		200°C	200d
		250°C	250d

The sample annealed at 150°C (below the disorder transition) is expected to exhibit increased cation order and changes in defect properties as discussed in Section 3.6, Pg. 95. The 200 and 250°C anneals are expected to show fewer changes since the samples as-made are likely to already contain a fully disordered Cu-Zn lattice.

4.7.2 Fabrication Methods

Films were fabricated by IBM's baseline hydrazine process as described in the literature [14], [131]. After selenization, films were air annealed at ~300°C for 10 minutes and then cooled quickly. After air anneal, all films were transferred to a N₂ glovebox for low-temperature annealing. The glovebox was controlled at less than 0.1 ppm oxygen, however, oxygen is expected to be adsorbed on the films surface from air anneal and general exposure. After low-temperature annealing, the samples were removed from the glovebox and prepared with the traditional device stack. The compositions for the devices can be seen in Table 4-4. The samples contain low amounts of sulfur which slightly raises the E_g . Sulfur incorporation is an unavoidable byproduct from IBM hydrazine solution processed fabrication method and the films are similar in composition to the record 12.6% CZTSSe device [14].

Table 4-4: Composition of low-temperature annealed films

	Cu / (Zn+Sn)	Zn / Sn	Cu / Sn	Se+S / (Cu+Zn+Sn)	S / (Se+S)
Cu-poor	0.79	1.20	1.74	1.04	0.13
Near- Stoich	0.98	1.11	2.06	0.99	0.15

4.7.3 Photoluminescence

Low temperature PL spectra taken at 4K are shown in Figure 4-15. For both stoichiometric and Cu-poor samples, the 150°C low-temperature anneal was found to increase the PL peak energy, similar to the slow-cool. For the stoichiometric samples, annealing at 200 or 250°C showed minimal shift in PL peak position. The original sample, labeled “None,” was expected to be in a fully disordered state due a fast cool-down after air-annealing at 300°C, and therefore significant changes related to Cu-Zn ordering would not be expected for the higher temperature anneals.

For the Cu-poor samples, the low energy edge of the PL spectra shifted with annealing with the peak at 0.90, 0.925 and 0.94 eV for the 250, 200 and 150°C annealed samples respectively.

Interestingly, the deepest tail states exist for the 150°C samples, despite the expectation of increased cation order. The energy of the tail state for the 150°C sample is similar to the peak energy of the peak for the disordered samples and may be due to small regions of disorder in the ordered samples as discussed for slow-cooled single crystals.

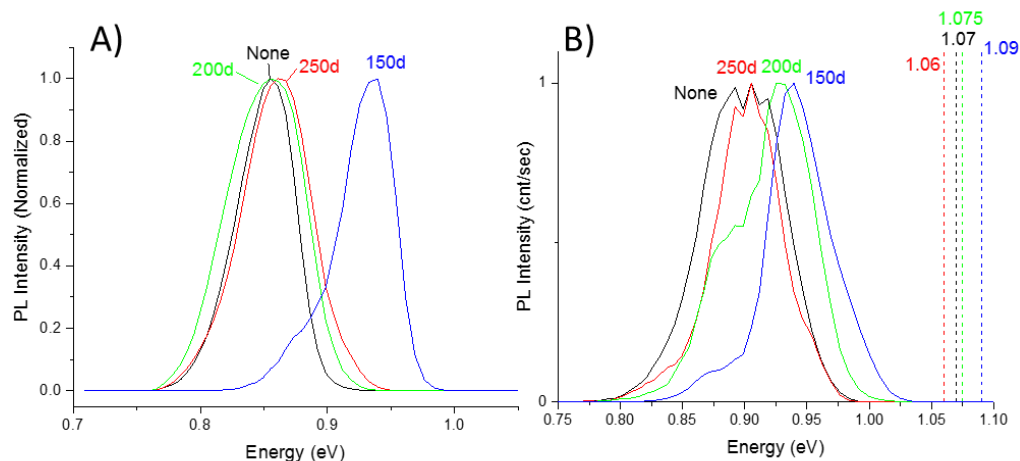


Figure 4-15: PL at 4K for films annealed at low temperatures. A) Near-stoichiometric films. B) Cu-poor films. Dotted line is E_g extracted from QE

Room temperature PL and QE spectra were also taken for Cu-poor samples. The E_g extracted from the inflection point of the QE, the PL peak at room temperature, and the PL peak at 4K are compared in Figure 4-16. The E_g extracted by QE also increase slightly with low temperature annealing at 150°C but no change is observed when annealing at higher temperatures.

The metric $E_{g-QE}-E_{PL-RT}$ decreases for the 150°C annealed sample however the onset of PL (i.e. the deepest tail states) are found to be ~250 meV below the E_g for all samples regardless of annealing condition. This suggests the deepest states are not removed by annealing. As previously found, near stoichiometric samples were found to have lower energy PL emission, however E_g were not extracted from QE since all stoichiometric films were shunted.

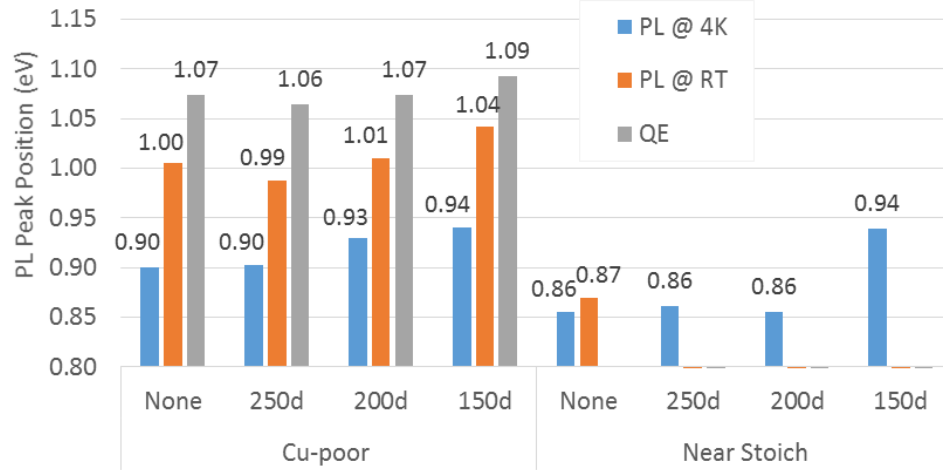


Figure 4-16: PL peak position and E_g as extracted from QE of low-temperature annealed films.

PL lifetimes measured at room temperature for the Cu-poor samples were also found to improve slightly for the low-temperature annealed samples as seen in Figure 4-17. The fast primary decay noted from the peak of the TRPL spectrum is convoluted with the fall-off of the 1 ns laser pulse width and is also often attributed to fast recombination mechanisms including the surface [152]. This region gives a lifetime of 0.2 ns. The slower decay region noted beyond 5 ns is attributed to slower recombination associated with the material quality. This region was fit with a single exponential decay and lifetimes of ~1.5 ns were extracted for the as-made 250°C annealed samples, while the 150°C annealed sample gave a lifetime of ~ 2 ns with the 200°C annealed sample falling in between. It's not clear if the origin of the increase in lifetime is related to Cu-Zn order, or other deeper defect states which might be expected to be reduced by lower temperature equilibria as discussed in Section 3.6.4.

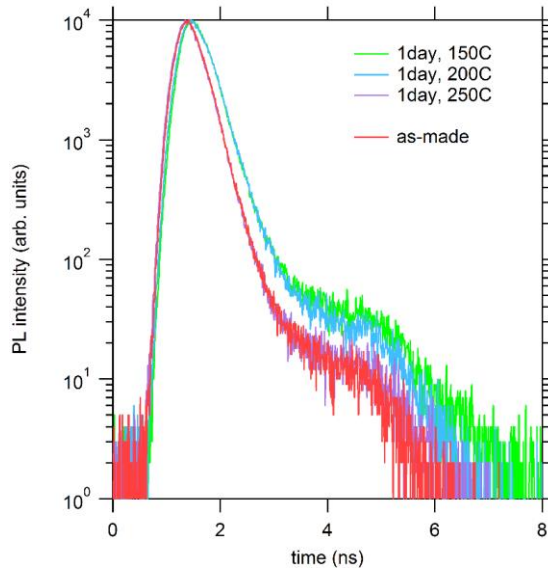


Figure 4-17: Lifetimes of low-temperature annealed films taken at room temperature

4.7.4 Capacitance-voltage

Capacitance voltage (CV) measurements can provide an upper bound for carrier concentration (N_{CV}) near the edge of the space charge region by measuring the change in capacitance under an applied AC bias. A DC bias can be further used to shift the edge of the depletion region and probe N_{CV} as a function of depth through the film. More details of the measurement are listed in appendix and a derivation and background on the method can be found in Ref. [153], [154]. Measurements were not found to vary significantly between 1 kHz to 1 MHz, and the data shown below were taken at 100 kHz.

As seen in Figure 4-18, carrier concentrations as measured by CV were found to decrease by a factor of $>2x$ after annealing for all temperatures. This is similar to the results reported for single crystal samples, where Hall measurements showed reduced carrier concentration for slow cooled samples. The origin of the slight changes in carrier

concentrations between 150, 200 and 250°C are not clear and are complicated by sub- E_g states and interface states which may respond and influence the CV measurements [153]. DLCP measurement, which give a more accurate estimation of carrier concentration typically show 2-10x lower carrier concentrations for similar CZTSe samples [31].

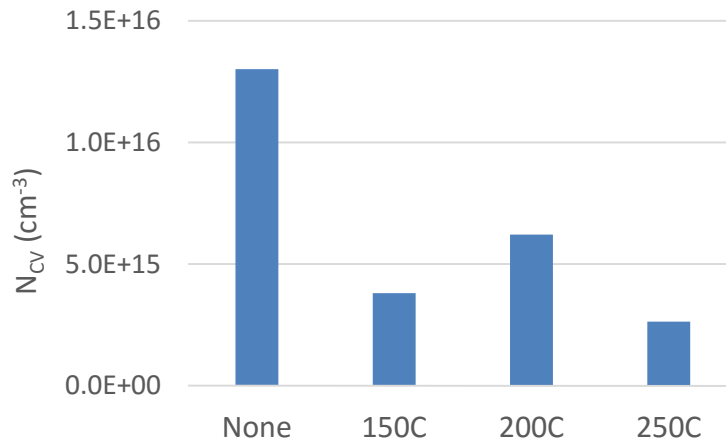


Figure 4-18: N_{CV} from carrier capacitance-voltage measurements

The trend of decreasing carrier concentration with annealing would have two primary impacts on devices. All other things being equal, a reduction in carrier concentration will reduce V_{OC} as shown in Equation 2:

$$\Delta V_{OC} = \frac{k_b T}{q} \ln\left(\frac{N_a}{N_{a0}^2}\right) \quad \text{Equation 2}$$

Where k_b is the Boltzman constant, T is temperature, q is electric charge, N_a is the hole concentration for a p-type material and N_{a0} is the initial hole concentration.

Second, the width of the space charge region (X_p), will be extended for lower carrier concentrations according to Equation 3.

$$X_p = w \left(\frac{N_D}{N_A + N_D} \right) \quad \text{Equation 3}$$

Where N_D and N_A are the electron and hole concentration of the n-type and p-type layers respectively and w is the total depletion region width.

4.7.5 Device Results

Devices made from samples annealed below the disorder transition temperature showed improved efficiency through in V_{OC} and current, while devices annealed at higher temperatures were found to decline in performance. The average of four devices for each annealing condition are shown in Figure 4-19, while the best device curve is shown in Figure 4-20.

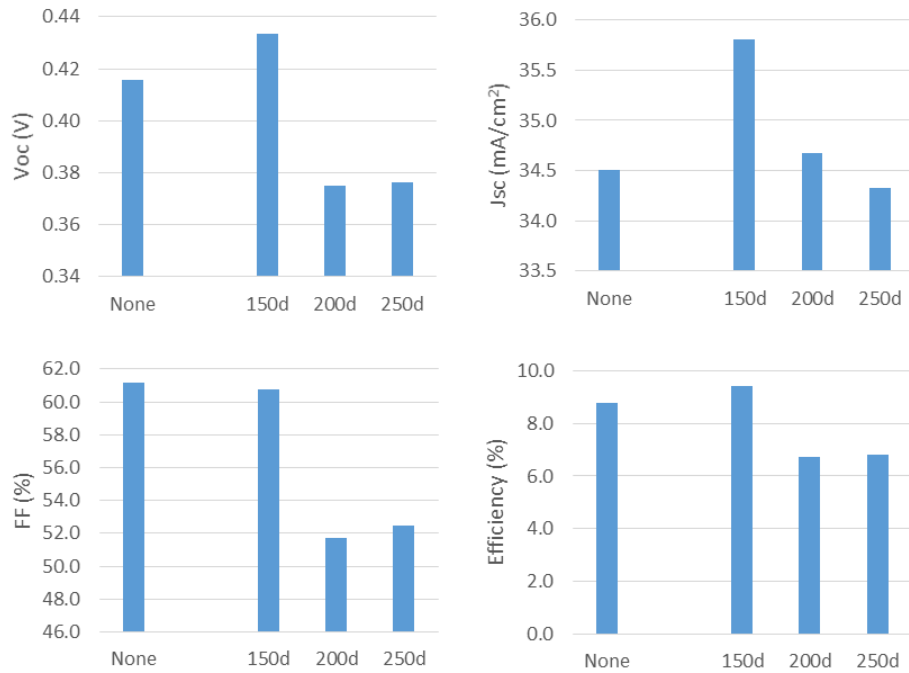


Figure 4-19: Device parameters for Cu-poor low temperature annealed films, average of 4 devices

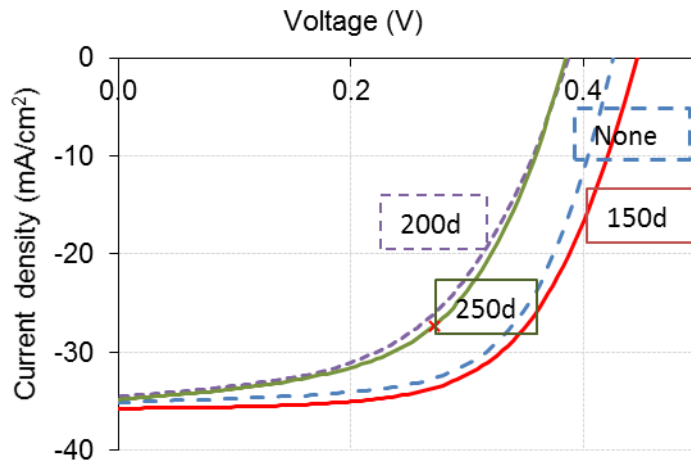


Figure 4-20: Comparison of JV curves of best device from low-temperature annealed films

The improvement in J_{SC} for the 150°C annealed sample can be attributed to improved long wavelength collection which is a function of both the extended depletion width, as expected from CV results, and the a slight improvement in minority carrier lifetime. This can be confirmed in the EQE spectrum shown in Figure 4-21. The increase in J_{SC} is noted despite a small increase in E_g . The origin of the improvements in V_{OC} for the sample annealed below the disorder-transition is less directly clear. The observed decrease in carrier concentration should slightly decrease V_{OC} , however the PL measurements may offer an explanation for the V_{OC} improvement. The reduction in $E_g - E_{PL}$ suggests optically active sub- E_g states are being reduced which would have a consequent reduction on band-tailing thus improving V_{OC} .

For samples annealed at 200 and 250°C, the V_{OC} is found to drop by 40 mV, the fill factor (FF) drops by 10% and the J_{SC} remains approximately unchanged. The samples as-made (“None”) are expected to be in the fully-disordered state on the Cu-Zn lattice due to the fast cool-down from the final 375°C air anneal step, and since the

annealing temperature is above the reported disorder temperature, Cu-Zn cations would be expected to remain fully-disordered. Consequently the E_g from EQE and PL spectra have only small changes. The decrease in V_{OC} predicted from the change in carrier concentration (Equation 2) is ~ 30 meV, which is close to the 40 meV observed decrease. In addition, the JV curves for the annealed samples show significant light/dark crossover and apparent EQE greater than 1 for short wavelengths under light bias. Both of these observations have been explained in the literature by changing photo-conductivity of CdS or a barrier at the interface [155]–[157].²⁰ This suggests change in the nature of the surface with annealing which may modulate the CdS deposition. Cu doping of the CdS has been explained as one potential source of the observed behaviors in literature reports [157]. The modified interface may explain the reduction in FF observed for these samples.

²⁰ Photoconductive CdS will result in a lower series resistance under light, thus causing the cross-over of the light and dark JV curves. In light-biased EQE, the bias light is expected to be a constant offset of collected current which is from a chopped light. For photoconductive layers, apparent EQE above 1 can be obtained when additional carriers are collected from the bias light due to changing photoconductivity CdS from the chopped light signal. More details are described in [155].

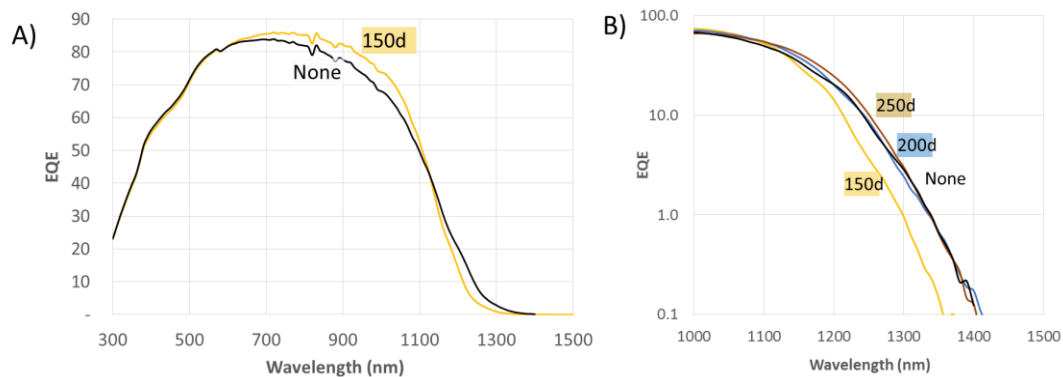


Figure 4-21: (A) EQE spectrum of as-made “None” and 150°C x 1 day annealed sample showing increase in long wavelength response. (B) Log plot of EQE for all annealed samples showing shift in E_g only for 150°C annealed sample.

4.7.6 Conclusions for Low-Temperature Annealed Devices

Annealing thin films for extended times below the disorder temperature may offer a promising way to improve device performance. Current champion thin films appear to be in fully disordered state as made, and often contain sub- E_g states significantly below the E_g as measured by PL.

Films annealed below the disorder temperature offer lower carrier concentrations, improved minority carrier lifetimes, and higher PL energy and higher E_g from QE. More importantly, band-tailing appears to be reduced as signaled by the reduction in deficit between the E_g and room temperature PL signal. These changes result in both improved V_{OC} and improved J_{SC} despite interface modification which proves detrimental for higher temperature annealing.

The changes in E_g and PL are smaller than observed in slow-cooled single crystals, likely due to the higher equilibrium disorder expected at 150°C. Further

increases in cation order and reduction in band-tailing may be achievable with annealing at temperatures below 150°C or with a slow-cool or step-down annealing procedure.

The slow cooled single crystal results suggest however that even with a very slow-cooling procedure, high levels of disorder (multiple % of the Cu-Zn) and potential fluctuations remain. Further techniques will be needed to completely eliminate band-tailing.

4.8 Single Crystal Champion Device Analysis and Comparison to Thin Films

The best achieved single crystal device parameters and the current record 11.6% CZTSe thin film device are compared in Table 4-5. The IV curve for the champion crystal can be found in

Table 4-5: Comparison of champion thin film and champion single crystal device

	V_{OC} (mV)	Area adj J_{SC} (mA/cm ²)	FF (%)	Area adj Efficiency (%)	E_g from QE (mV)	V_{OC} Deficit $E_g - qV_{OC}$ (mV)
Champion single xtal (SY24E-D20)	400	30	66.4	7.8	0.98	580
<i>IBM Record Film</i> [27]	423	40.6	67.3	11.6	1.0	578

The 33% deviation in efficiency is mostly explained by the 25% drop in current (J_{SC}), while the V_{OC} and fill factor (FF) are only 5% and 1% lower than the IBM champion device respectively. When adjusted for a slightly smaller bandgap measured in the single crystal, the V_{OC} deficit is almost equivalent to the record thin film device. A more detailed discussion of FF and J_{SC} are given below.

4.8.1.1 Fill Factor and Series Resistance

The small change in FF is also quite surprising given that the CZTSe layer in the single crystal is 1 mm, ~500x thicker than the 2 micron thin film. The series resistance component from the bulk absorber can be calculated by: $\frac{1}{q \rho \mu_p} * t$, where q is electric charge, ρ is hole density, μ_p is hole mobility in the through film direction and t is thickness. Min and max values for the R_S contribution of the absorber layer were calculated based on measured mobilities and carrier concentrations typical for films and crystals from Hall and DLCP. As seen in Table 4-6, in the worst case, the 1 mm CZTSe crystal contributes less than 25% of the measured series resistance of the device. For films, despite the lower carrier concentration and resistance, the absorber layer may contribute only a few percent of the total R_S .

A second conclusion from this analysis is improvements in R_S for the single crystals must target interfaces and other cell layers to reach similar values to thin films. It's also worth noting that in this case, only a small portion of FF is attributable to R_S and further improvement in FF will arise naturally from an increase in V_{OC} which is a more critical area for future improvements.

Table 4-6: Series resistance contribution due to absorber thickness for single crystals and thin films

		ρ	μ_p	Thickness	Calculated R_s from absorber	Measured R_s (for full device)
		/cm ³	cm ² /Vs	cm	Ω /cm ²	Ω /cm ²
Crystal	Min	1E+17	150	0.05	0.021	~1.2
	Max	5E+16	50	0.1	0.250	
Thin Film	Estimated	2E+15	50 ^{*21}	2E-04	0.013	0.325
	Max	2E+15	1 [*]	2E-04	0.625	

4.8.1.2 Current and EQE

The 25% lower current for the single crystal can be diagnosed from a comparison of the EQE curves as seen in Figure 4-22. The differences can be split into 3 regions with different attributions as noted by the arrows in the Figure.

²¹ The measured thin film $\mu_p \sim 1$ cm²/Vs, however the measurement is cross-grain. The expected through-grain mobility relevant for R_s is likely much higher and closer to the single crystal μ_p . In fact, the calculated R_s of the film is with the measured ~ 1 cm²/Vs mobility is 2x higher than the total device R_s which includes interface, contacts therefore confirming the measured mobility is too low.

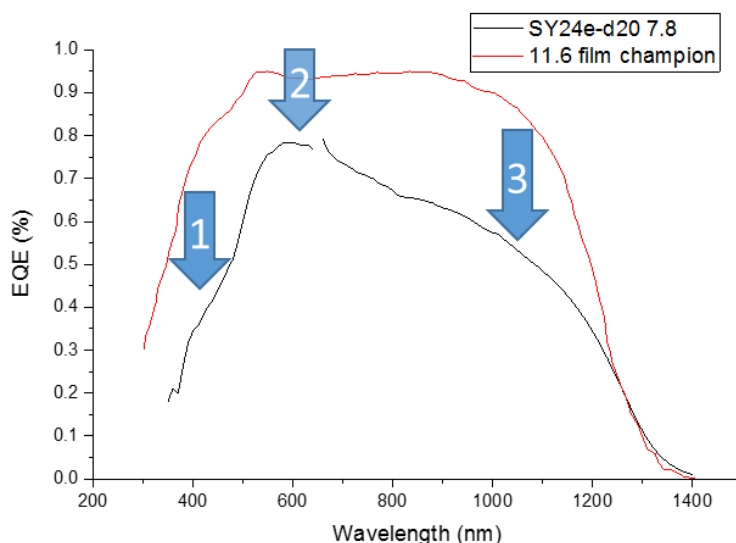


Figure 4-22: EQE comparison of champion single crystal from this work and champion 11.6% CZTSe thin film device (data extracted from [31])²²

For arrow (1) in the 300-500 nm high energy range, CdS as well as the TCO layer are expected to absorb a significant portion of the photons. IBM uses an optimized thin TCO/CdS stack as described [136], to reduce absorption and reflection in the low wavelength region and improves current by $\sim 3 \text{ mA/cm}^2$. Evidence for a thicker CdS layer for the single crystal sample is also noted in poor FF for the single crystal with under red illumination (not shown). The resistivity of CdS is reduced by photoexcitation above the E_g due to filling of trap states. Red light however is below the E_g and therefore does not reduce the resistivity. Consequently under red illumination,

²² Note: the EQE curves were taken on different setups and therefore small instrumental differences are expected but should not change the general conclusions.

or in the dark, thicker layers, or highly compensated CdS, can contribute significantly to series resistance [155].

Arrow (2) can be explained by improved reflection, as well potentially higher interface recombination in the single crystal sample. Interface recombination will shift the EQE down across the entire spectrum and due to the described surface challenges for single crystals, increased interface or near surface recombination may be expected. A MgF₂ anti-reflective coating is also used on the champion thin film in addition to a The aforementioned optimized CdS/TCO layer which is modeled to also reduce reflection.

Arrow (3) points to the long wavelength region where a fall off is seen for the single crystal sample. This suggest the inability to collect minority carriers absorbed deeper into the device away from the space region. The combination of both a narrower space charge region due to higher carrier concentrations and a shorter diffusion length from a shorter minority carrier lifetime explain this change. The minority carrier lifetime for the champion CZTSe film is on the order of 2 - 2.5 ns, and the best measured crystals were between 1-1.5 ns, although the current champion device has not yet been measured and may be slightly higher than past crystals as suggested by the improved EQE shape. Interestingly, despite the lack of grain boundaries, single crystals still appear to have lower minority carrier lifetimes compared to single crystals. This may be partially due to poor surface quality on single crystals compared to thin films. Calculations can show that the average e-h pair is generated >3x closer to the surface than it is to the closest

grain boundary using 532 nm excitation,²³ which suggests under the assumption of equal recombination velocities, surfaces will dominate over grain boundaries.

The EQE curve for the SY24E-D20 was also taken at reverse bias and under light bias and the ratios compared to the dark EQE are graphed in Figure 4-23. For both light and voltage bias, a slight improvement is noted beyond 1200 nm. The improvement is attributed to an extension of the space charge region which increases the field assisted collection and is typical in films with non-ideal collection. Although the improvement in long wavelength is mild, only a slight -0.3 V reverse bias voltage was applied.

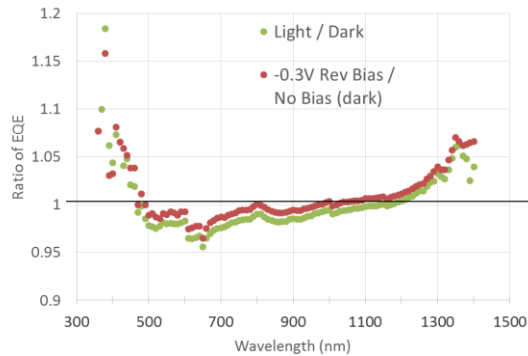


Figure 4-23: Light-bias and reverse-bias EQE ratio

²³ For CZTSe at 532 nm, 90% of light is absorbed in 150 nm, and an approximate average absorption depth of ~50 nm can be calculated. For a film with 1 micron grains (approximated as a 1x1 micron square), the average distance to the *closest* grain boundary can be calculated to be 142 nm. Champion devices have >2 micron grains and therefore average distance of a generated photon to a grain boundary is >280 nm, which is large compared to the average distance to the surface of ~50 nm. Therefore interaction with the surface is more probable. With 808 nm excitation, average surface and grain distances are closer to equal.

4.8.1.3 Capacitance-voltage and JV-Temperature Analysis

The defects around the edge of the space charge region were further studied by Capacitance-voltage (CV) and drive-level capacitance profiling (DLCP) as shown in Figure 4-24. An older 6% single crystal from the same synthesis, SY24E-D4, was used since the most recent champion was achieved only a month before this writing. The device parameters for this cell are listed in Figure 3-4. CV and DLCP measurements were taken at 100 kHz.

Both N_{CV} and N_{DLCP} are $>10x$ higher for the single crystal sample. N_{DLCP} should more accurately reflect the carrier concentration without interface states. The increase in carrier concentration is expected due to the higher Cu-composition of the single crystal sample ($Cu/(Zn+Sn) = 0.85$ vs 0.80). In addition, N_{DLCP} and N_{CV} for the single crystal sample increase strongly as the junction with a smaller space charge region. This could suggest changes affecting the surface of the crystal. The higher carrier concentration also results in a narrower depletion width which is depicted in the Figure with dotted lines from the measurements at zero bias. The depletion width for the single crystal is on the order of 100 nm which is less than half that of the thin film, which in part explains the EQE results shown above.

SY24E-D4-Charge density

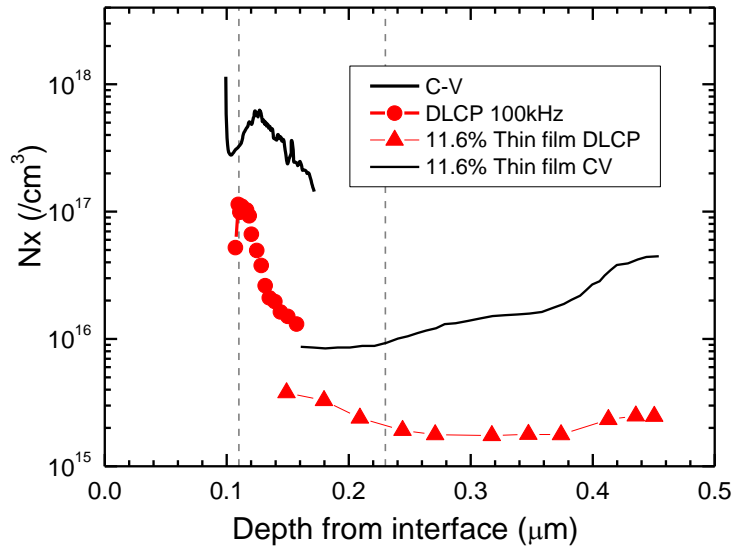


Figure 4-24: Defect densities from DLCP and CV for 6% single crystal and current champion 11.6% thin film [31]

Additional JV testing was performed as a function of temperature as shown in Figure 4-25. The V_{OC} as a function of temperature can be extrapolated at 0K to provide an activation energy for the main recombination process. In ideal solar cells this extrapolation is equal to the E_g , however band tailing and interface problems can lead to activation energies lower than the E_g [54], [158].

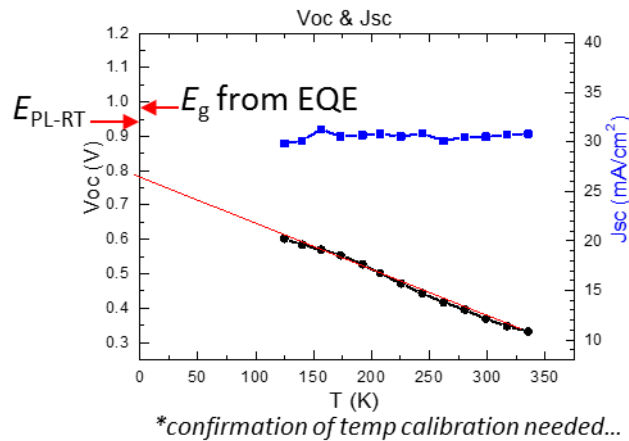


Figure 4-25: V_{OC} -T measurements for 6.4% cell (SY24E-D4).

As seen in the Figure, V_{OC} extrapolates to ~ 0.79 V which is significantly less than the observed 0.98 eV bandgap. It's worth noting however, the temperatures listed in the Figure are based on a monitor thermocouple mounted on a neighboring thin film. The samples are mounted on a cold block under low vacuum, however due to light exposure, the crystal surface may end up warmer than reference thermocouple due to thick nature of the crystal and distance from the cold block. This would offset the temperature and extrapolation closer to the E_g .

Although definite conclusions cannot be made due to the need for additional temperature calibration, the current record 12.6% CZT(SSe) extrapolates to ~ 100 meV below the E_g for the device which is similar to the PL peak at room temperature. This suggests that band tailing, rather than interface problems, may dominant recombination in these materials.

4.8.2 Conclusions and Paths Forward

Through the improvements noted in the course of this work, the V_{OC} deficit achieved for single crystals is now approximately equal to champion thin film devices. Despite progress, significant room for improvement remains.

In the bulk, Cu-concentrations and therefore carrier concentrations remain above that of high efficiency thin film devices. Higher carrier concentration directly relates to lower minority carrier lifetimes, and result in a shorter space charge region which limits collection in long wavelength. DFT calculations further suggest minority carrier lifetimes are reduced by $Cu_{Zn}+Sn_{Zn}$ defects which are minimized at Cu-poor and Sn-poor stoichiometries. This is supported by our lifetime measurements, as well as other TRPL measurement which suggest the optimal Cu/Sn ratio is ~ 1.75 (compared to ~ 1.95 achieved).

At the surface, further passivation or improved junction quality is needed. Annealing post-CdS deposition appears to be an easy to implement and promising opportunity. Removal of the damaged top surface layer has proven essential for current devices, and recent evidence, such as the ratio of PL at 1064 and 532 nm, suggests the surface is still a problematic region with high levels of recombination. Achieved minority carrier lifetime measurements appear to be dominated by the surface and are not reflective of the bulk material quality. Further improvements are expected with optimized air annealing and post-CdS annealing. Na incorporation via post-deposition is an additional area with large potential benefits for single crystals. All reported high efficiency thin film devices have incorporated Na which has been shown to passivate surfaces and improve all device parameters.

One method which may help both the bulk and surface is post-annealing in Zn and Se rich environments. In the near surface of 1-10 nm, a Zn-enrichment is thought

to create band bending which will improve passivation and CdS alignment. For changing bulk stoichiometry, only the top ~1 micron requires Zn-enrichment since this is the region of light absorption and therefore controls the space charge width and dominant recombination controlling V_{OC} and J_{SC} .

A third lesser challenge includes improving the device stack. Thinner CdS, optimized ZnO/ITO thickness, and an anti-reflective coating are likely to significantly reduce the noted deficit in current.

For thin films devices, band-tailing and deep defects appear to be the critical bottleneck. Defect states measured by PL were found to be deeper than quenched single crystal samples, and significantly deeper than slow-cooled single crystals. Further optimization of low-temperature annealing may prove fruitful. Although not discussed in this work, experiment performed while working at IBM suggest the reactions of CZTSe with the back contact appear to be correlated with the deep defect states observed by PL and are also the source of high recombination. Reducing this back contact reaction may help CZTSe achieve new record efficiencies.

Ag-substitution or other related strategies are an alternative method of achieving reduced band-tails, however, this further increases the complexity of the system in addition to diminishing the “earth-abundant” motivation for CZTSe.

Minority carrier lifetime also lags CIGS by 1-2 orders of magnitude and is an area for potential improvement [31], [44], [83]. The factors limiting the carrier lifetime are not yet clear – and single crystal may help elucidate these– but fast, sub-ns decay for 99% of the PL signal suggests further passivation of surfaces and grain boundaries may be necessary. Passivation techniques learned from single crystals prove helpful

here. Additional techniques borrowed from CIGS such as optimized Na and K post-deposition annealing may also prove beneficial.

Ultimately, the future of the CZTS material-system depends on our ability understand and control the bulk defects. Band-tailing from disorder in the cation lattice appears to be one of the most intractable thermodynamic problems due to the low formation energies of Cu-Zn anti-sites. Hopefully the future research can build off the steps and principles of this work to understand and control defects in CZTSe.

Chapter 5

THIN FILM FABRICATION BY CO-EVAPORATION: EFFECTS OF GROWTH CONDITIONS ON SECONDARY PHASES IN CZTSe

5.1 Overview of Work

Thin film fabrication was performed from 2011-2013, prior to collaboration with IBM. High temperature co-evaporation was utilized, and as will be discussed, the two primary areas for control of CZTSe formation are effusion rates, and the growth temperature throughout the duration of the growth. Efforts were made to improve control and repeatability in both areas.

In order to improve effusion repeatability, the Zn source design was modified to limit effusion through a rate controlling nozzle with effusion rates calculated by effusion model. This is not discussed in the body of the text but source design modifications and the source code for the effusion model are given in the Appendix Pg. 247.

Composition, and therefore electronic properties were found to be sensitive to growth temperature. Composition has an almost step-function change at critical temperatures of $\sim 520^{\circ}\text{C}$ for our depositions and therefore lower temperatures or strong temperature uniformity are required. The system was further modified so growth temperatures could be mapped and logged across the nine 1x1in substrates during growth. Improved uniformity and temperature control was investigated via modified substrate holders and the addition of heat-spreaders. Improved uniformities were ultimately achieved. This is discussed briefly in the appendix Pg. 250.

Additional modification of the evaporation chamber for fast cool-down, as well as computer programmed source control and temperature logging (with significant help from John and Shannon!), and an examination of the thermodynamics of phase formation through the use of the effective heat of formation model were explored but will not be covered in this work.

The work below focuses on decomposition at the front and back contact and was published in MRS Advances in 2013 and is re-printed here with minor modifications.

5.2 Abstract

High temperature multi-source co-evaporation has been the most successful approach to fabricate record efficiency Cu(InGa)Se₂ devices, yet many groups have been unable to replicate this success when transferring these methods to the Cu₂ZnSnSe₄ system. The difficulties stem from the dramatic differences in the thermochemical properties which result in decomposition and loss of volatile species, such as Zn and SnSe, at temperatures needed for growth. In co-evaporation, decomposition and element loss must be managed throughout the entire growth process, from the back contact interface to the final terminating surface of the film. The beginning and ending phases of deposition encompass different kinetic regimes suggesting a phased approach to growth may be helpful. A series of depositions with different effusion profiles were used to demonstrate the effects of decomposition during different stages of growth. Secondary phase detection can be challenging in CZTSe, but a combination of SEM imaging and thin cross-section depth profile by EDS were found to best identify and locate the secondary phases that occur during different phases of growth for co-evaporated Cu₂ZnSnSe₄ films.

Deposition with a uniform incident flux followed by shuttered vacuum cool-down yielded films with a ZnSe phase at the absorber/Mo interface and Cu-rich composition at the surface of the exposed film. Devices from these absorber layers never exceeded conversion efficiencies of 1%. Decomposition at the surface could be prevented by continuing effusion of Se and Sn during the cool-down of the substrate. Resulting films demonstrated more faceted grains as well as significantly improved device performance. Secondary phases that traditionally form at the back contact during the beginning of growth were minimized by decreasing the substrate temperature to 300°C during the initial stages of deposition which reduced the ZnSe formed at the Mo interface. The thermochemical origin of the secondary phases will be discussed and the performance of representative devices will be presented.

5.3 Introduction

$\text{Cu}_2\text{ZnSnS}_4$ and $\text{Cu}_2\text{ZnSnSe}_4$ (CZTS and CZTSe, respectively) have generated significant interest as earth abundant absorber materials for photovoltaic devices in the last half decade. The kesterite crystal structure can be derived from chalcopyrite structure, however, the thermochemical properties are quite different from $\text{Cu}(\text{InGa})\text{Se}_2$, leading to difficulties when growth and annealing strategies are translated directly to CZTSe [1-2]. In stark contrast to CIGS, record device efficiencies have often been achieved by solution-growth methods [134]. Research teams attempting high-temperature multi-source co-evaporation have reported mixed results with only one team (NREL) reporting >5% device efficiency without a separate controlled annealing process [161]. Co-evaporated films have often exhibited secondary phases at the front and rear of the film, which is a result of phase decomposition and element loss during different stages of growth [2, 5–7]. A key

advantage of co-evaporation at film formation temperatures is the potential to drive reaction chemistry towards desired compositions and properties by controlling the elemental incident fluxes throughout the deposition. Thus, despite the challenges in co-evaporation, with the proper understanding of the thermodynamics and kinetics, a procedure can be developed to avoid decomposition and manage element loss to obtain high efficiency CZTSe devices.

This paper highlights the thermodynamic challenges of the CZTSe system with a simple constant effusion deposition. Different time/temperature deposition profiles were used to control the location and presence of secondary phases at the front and back of the films.

5.4 Experimental

Films were deposited by multi-source co-evaporation from the elements on 1”x 1” SLG/Mo substrates held at 300-500°C depending on deposition. Base pressure was 1×10^{-6} Torr before growth. After deposition, devices were fabricated with the typical CIGS stack, SLG/Mo/CZTSe/CdS/ZnO/ITO and a Ni/Al grid on the front surface. Raman spectroscopy and x-ray diffraction (XRD) analysis showed only slight variations between films and little definitive evidence of secondary phases, but imaging the film surface and cross-section by scanning electron microscope (SEM) coupled with energy dispersive spectroscopy (EDS), were able to clearly illustrate decomposition and the presence of secondary phases. An Auriga 60 Crossbeam SEM was used. An in-lens secondary electron detector was used with 3kV beam voltage which was able to clearly distinguish the presence and location of ZnSe inclusions from scratch and focused ion beam (FIB) cross-sections. Film compositions were obtained using x-ray fluorescence (XRF).

5.5 Results and Discussion

As has been demonstrated in the literature, although Reaction 1 is spontaneous (Gibbs free energy < 0); the reverse reaction, decomposition of CZTSe, can still occur at an appreciable rate at temperatures needed for film processing. This is due to the distribution of energies and the relatively small difference in Gibbs free energy between CZTSe and binary reactants [163]–[165]



At solid state equilibrium, the products of decomposition would be quickly diminished by the more favorable forward reaction to create CZTSe, but in thin films with significant exposed surfaces, SnSe and Se can be lost due to high volatility, rendering the forward reaction to create CZTSe impossible. In this way, entire CZTSe films can decompose into Cu_2Se and ZnSe at temperatures above 500°C [9, 10]. This thermodynamic process occurs regardless of atmosphere, however a higher background pressure can slow the rate of SnSe loss by allowing some lost SnSe to re-adsorb. A SnSe-containing atmosphere, or effusion of Sn and Se in the case of co-evaporation, can also keep the surface at equilibrium by replacing species lost to volatility.

The vapor pressure of Zn is four orders of magnitude higher than SnSe at 500°C , and consequently Zn loss is also observed in many CZTSe deposition processes from elemental sources. However, Zn loss has not proven to be problematic. The reaction to form ZnSe , which occurs $>330^\circ\text{C}$, stabilizes any Zn from vaporization. In this case, the reverse reaction back to elemental Zn is extremely unfavorable due to the very low Gibbs free energy of ZnSe . Formation of Cu-Zn alloys can theoretically, also act to stabilize Zn, though the presence of Cu-Zn has not been detected in co-evaporated films.

From analysis of the final film, under our experimental conditions, 50% of the deposited Zn and 85% of the deposited Sn was lost during deposition at 500°C. A higher loss of Sn is observed despite the much lower vapor pressure of Sn/SnSe. This can be attributed to a combination of the rates of reaction to stabilize SnSe (by forming $\text{Cu}_2\text{ZnSnSe}_4$ or Cu_2SnSe_3) and also the aforementioned reverse reactions that can occur throughout the deposition.

The rate of SnSe loss changes during three growth regimes at the beginning, middle, and end of the growth process. During the first stage Sn and Se deposit on the Mo substrate with little CZTSe being formed. In this stage SnSe is formed quickly and lost very rapidly as the SnSe has not been stabilized by formation of CZTSe or Cu_2SnSe_3 [160]. The sticking coefficient also depends on lattice mismatch and bonding to the deposition surface, so it may be expected that the Mo substrate may also increase SnSe loss compared to later stages of film growth. In the second stage, during the majority of growth, Sn and Se are depositing on CZTSe and other binary intermediates. During this stage, SnSe is lost through either vaporization of the binary or decomposition of CZTSe, although SnSe is also somewhat stabilized through the formation of CZTSe. In the third stage, when growth has finished and the absorber layer is cooling, SnSe can only be lost through CZTSe decomposition. Since decomposition and the creation of secondary phases are directly related to SnSe loss, these regimes have a significant effect on the final absorber layer composition and the location of secondary phases.

The two main control variables during deposition include effusion rate and substrate temperature. Initial films were grown with a constant effusion onto a 500°C substrate with enough excess Sn and Se to achieve the desired Cu-poor, Zn rich CZTSe composition. In the control method (Method 1, see Figure 5-1), films were shuttered

immediately after growth, while in a second method, to replace lost SnSe and prevent CZTSe decomposition, effusion of volatile Sn and Se was continued but ramped down until films cooled below 350°C (Method 2, see Figure 5-2).

Since SnSe loss is particularly rapid in the first stage of growth, a lower substrate temperature was used to reduce volatility. For these depositions, elements were initially deposited at 300°C, before being ramped to 500°C in order to drive the reaction and promote grain growth (Method 3, see Figure 5-4).

5.5.1 Decomposition during Film Cool-down

The most apparent result of decomposition occurs on the surface of the film. During growth, excess effusion of volatile species compensates for SnSe loss, but after film growth has stopped, as the films cool down, decomposition and element loss continues unless further of Sn and Se are supplied.

In Method 1 (Figure 5-1A), a constant elemental effusion was used and substrates were shuttered after deposition and the substrate temperature cooled to room temperature before venting the chamber. Although this simple procedure can produce good quality films for CIGS, CZTSe films were found to be shunted, with a Cu₂Se secondary phase detected by XRD. The shunting and overall device performance were not fully restored with a KCN etch. Zn-rich regions were also found on the film surface through SEM and EDS mapping at low beam energies. The surface morphology from method 1 appears to be more rounded with facets, steps and islands on the surface which would be consistent with decomposition, as volatile species are removed more rapidly from corners and step edges (Figure 5-2A) [166].

In Method 2 (Figure 5-1B) the effusion of Sn and Se were ramped down during the cool-down of the film until the surface was below 350°C. The film morphology

exhibits a more faceted grain structure (Figure 5-2B) and produced devices that exhibited much less shunting (shunt conductance typically decreased by 2x-10x), and higher efficiencies (>4% compared with <1%), suggesting that CZTSe surface decomposition has not occurred. Zn was effused for 0-5 min during cool-down based on literature results observing improved cell results for slightly Zn rich termination [161].

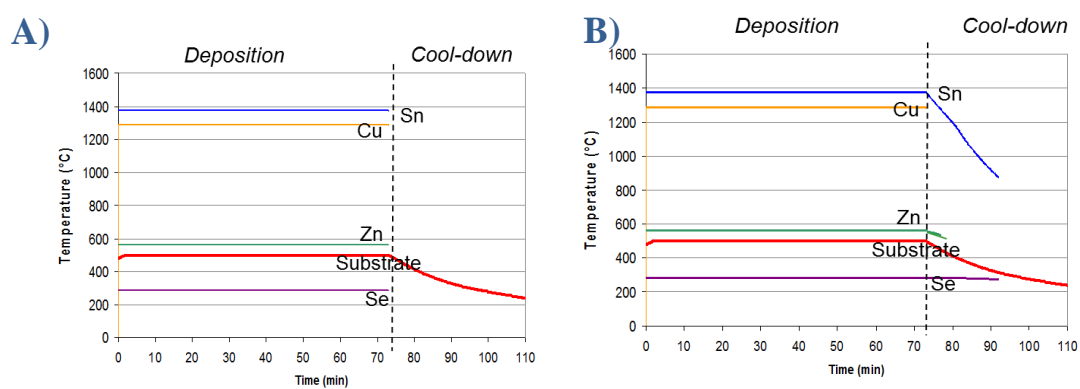


Figure 5-1: Source and substrate temperature during deposition. A) Method 1 with no effusion during substrate cool-down. B) Method 2 with effusion of Sn and Se during cool-down

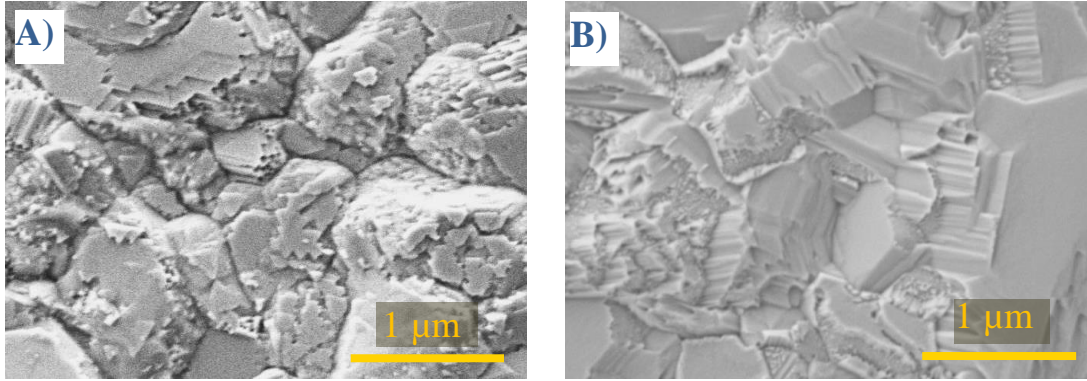


Figure 5-2: SEM images of CZTSe surface with different deposition methods. A) Method 1 with no effusion during cool-down showing. B) Method 2 with effusion during cool-down showing more faceted grains.

5.5.2 Decomposition at the Back Contact

Similar thermodynamic issues also present problems at the back side of the film during the beginning stages of film growth. For films deposited at 500°C, a layer of ZnSe is formed at the back contact as has been observed in the literature [5,6,12]. The ZnSe layer was confirmed by an EDS depth profile of a 100 nm thick cross-section created by a FIB (Figure 5-3).

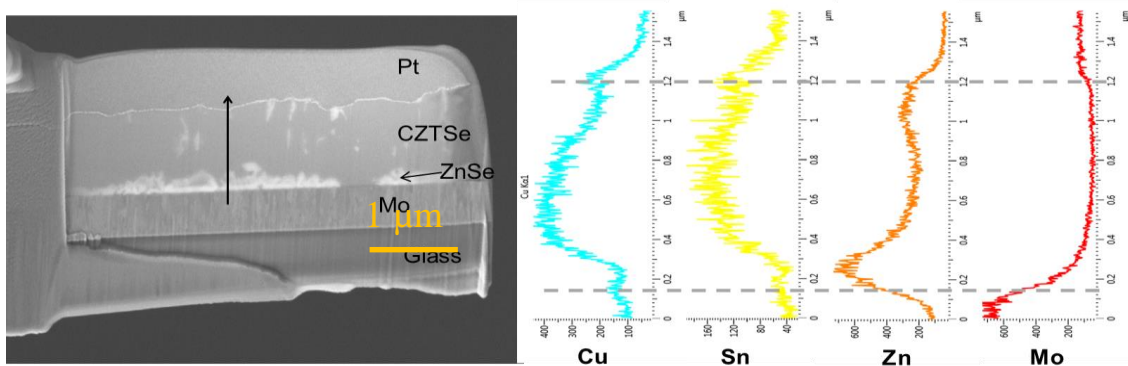


Figure 5-3: Cross-section of CZTSe absorber layer created by FIB and EDS depth profile.

ZnSe can be clearly illustrated by bright charging regions in secondary electron SEM images when in-lens secondary electron detection is used. The in-lens detector has better detector efficiency of low energy electrons and has higher signal-to-noise ratio allowing higher contrast for impurities and in this case, charging [167]. When the traditional secondary electron detector was used, the contrast elucidating ZnSe is not observed.

It is important to note that typical planar EDS measurements will often miss secondary phases at the back contact due to a sampling volume that highly weights the top micron of the film. For this reason all film compositions were measured by XRF which was calibrated by ICP.

The origin of the ZnSe layer is due to the higher volatility and loss of SnSe in the initial stages of deposition [2, 6]. A new deposition regime was developed to prevent SnSe loss particularly during the early stages of growth by beginning the deposition at a lower temperature (Method 3, Figure 5-4). The deposition was started with the substrate at 300°C and later ramped to 500°C for 20 minutes to drive the reaction and promote grain growth. Elemental source temperatures were correspondingly increased to accommodate the lower sticking at the higher substrate temperature. At 300°C, SnSe vapor pressure is three orders of magnitude lower than at 500°C, which allows Sn to incorporate into the growing film from the beginning of the deposition and decrease formation of the ZnSe layer.

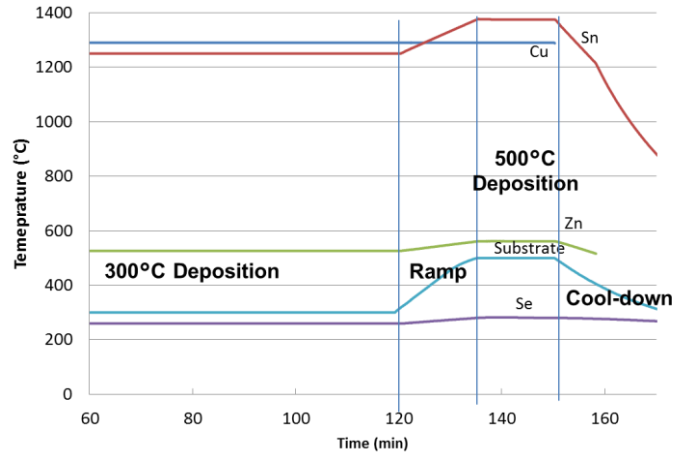


Figure 5-4: Source and substrate temperature during deposition for Method 3. Deposition began with lower substrate temperature to minimize Sn loss.

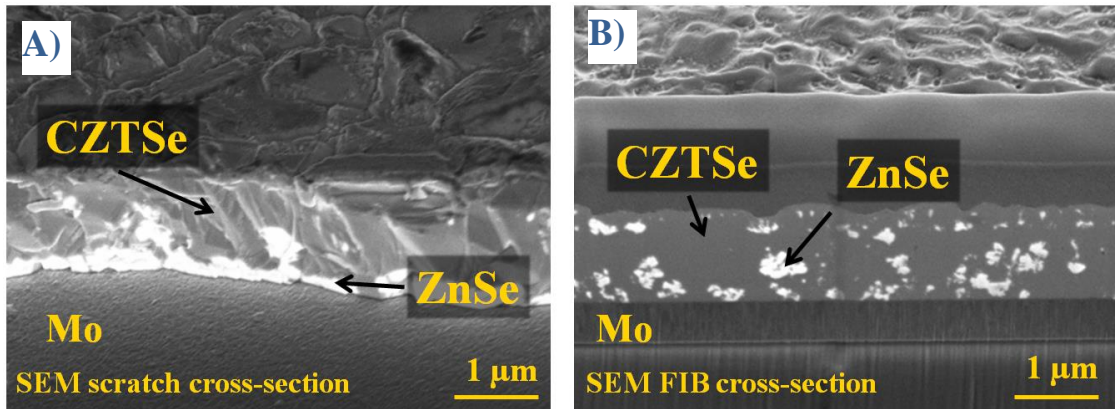


Figure 5-5: SEM images of CZTSe deposited with different conditions. A) SEM scratch cross section of CZTSe deposited at 500°C (Method 2) B) SEM FIB cross-section deposited beginning at 300°C (Method 3).

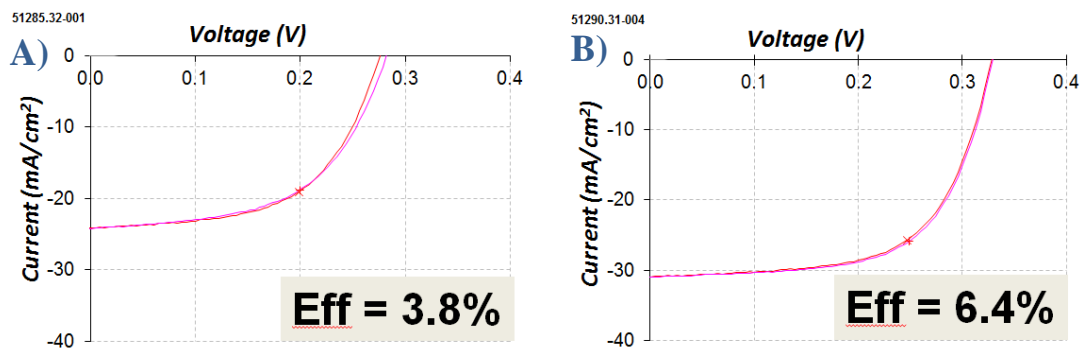


Figure 5-6: Corresponding cell results for CZTSe films deposited at A) constant 500°C substrate (Method 2), and B) deposited beginning at 300°C (Method 3).

Figure 5-5A and B shows cross-section SEM images of CZTSe films grown beginning at 500°C and beginning at 300°C respectively. Both films clearly contain ZnSe inclusions, however, in the deposition started at 300°C the precipitation occurred more evenly throughout the depth of the film and does not form a contiguous layer at the back contact. Previous reports in the literature have not observed ZnSe inclusions in the middle of the film, however this may be due to difficulty of detection [168]. The presence of ZnSe in the bulk is likely due to high Zn levels, beyond the tolerance of the narrow single phase region for CZTSe [41]. In depositions at 500°C, it is likely favorable for ZnSe to continue to grow from where it nucleated at the back contact, rather than forming precipitates in the middle of the film, in order to minimize interfacial energy.

Despite the similar compositions, Zn/Sn ratio of ~ 1.3 , and $\text{Cu}/(\text{Zn}+\text{Sn}) \sim 0.85$, substantial improvement in J_{SC} and V_{OC} is seen (Figure 5-6) with films deposited at 300°C. Previous literature reports have suggested ZnSe at the back contact has little effect on cell performance though the nearly contiguous ZnSe layer seen above appear

to decrease V_{OC} and J_{SC} . [41] . Given the low carrier lifetime in CZTSe, increasing the carrier distance to the back contact could lead to significant carrier recombination [161]. The ZnSe inclusions in the middle of the cell appear to have less effect on cell performance and may act mainly as “dark space” but do not block current as would be expected from a semi-contiguous ZnSe layer.

It is worth noting the “improved” devices still have not been fully optimized, as noted by the clear presence of 2nd phases. The record co-evaporated device (9.15%) used a Cu-rich growth (although similar high-performing devices were created from without Cu-rich growth) and also a number of additional steps including excess Na, air annealing, and an anti-reflective coating which may help explain part of the gaps in V_{OC} and J_{SC} [161].

5.6 Conclusions

Improved materials and devices have been demonstrated by modified deposition regimes that address the thermodynamic challenges of CZTSe multi-source evaporation. The use of in-lens SEM imaging has proven a useful tool for identifying the presence and location of ZnSe secondary phases.

Decomposition can be easily observed by the morphology on the surface of films cooled in a vacuum without continued supply of Sn and Se. The loss of SnSe must be addressed by effusion of volatile elements during all stages of growth and cool-down.

Different kinetics in the beginning phases of deposition can result in a ZnSe layer at the back contact which can block current. This layer, also related to loss of Sn, can be addressed by reducing SnSe volatility by lowering the substrate temperature at the beginning of growth. With an improved understanding of material

decomposition and chemistry throughout the film growth, deposition can be further optimized.

5.7 Acknowledgements for thin film fabrication work

The authors would like to acknowledge E. I. du Pont de Nemours and Company for partial funding of this work.

Chapter 6

SUMMARY OF CONTRIBUTIONS

In this work single crystals were studied to better understand the challenging defects in $\text{Cu}_2\text{ZnSnSe}_4$. New growth methods were developed and mm-sized crystals were achieved for the first time without a flux agent.

Both bulk and surface defects for single crystals and films were investigated and manipulated to reduce recombination and improve V_{OC} . The critical role of the surface was demonstrated and new passivation methods were shown to reduce surface recombination and improve V_{OC} . For the bulk, variations in stoichiometry, dopants/substitutions, and temperature equilibria were explored. In each area, variables were identified that reduce the observed sub- E_g defects and band-tailing which are critical bottlenecks in this system. This work has also revised the PL interpretation of five highly cited publications, and demonstrated a novel method for screening lifetime as a function of wavelength.

From stoichiometry, new insights into reasons why bulk compositions are found to be Cu-poor and Zn rich are demonstrated. In addition to lower carrier concentrations, Cu-poor CZTSe exhibits shallower defect states and higher lifetimes.

The critical role of Na was studied, and bulk incorporation and diffusion was measured for the first time. Na was shown to reduce non-radiative recombination and further reduce radiative sub- E_g states, therefore resulting in shallower PL emission. Substitutions of Ag were also shown to reduce the extent of band-tailing and pure $\text{Ag}_2\text{ZnSnSe}_4$ was demonstrated to have promising optoelectronic properties with band-

band emission without the effects band-tailing. These experiments further support the hypothesis of Cu-Zn anti-sites as the dominant origin of the band tails in the CZTSe system.

Further manipulation of defect populations by temperature equilibria are shown as a potential route to reducing sub- E_g defects critical for band-tailing. This concept has shown the potential to improve device performance in state-of-the-art thin films. The concepts and strategy of using cooling-rate or low-temperature annealing to intentionally manipulate defect populations is potentially valuable for applications to other multinary semiconductors.

Single crystal devices were demonstrated for the first time, and using the aforementioned insights, devices were optimized to achieve V_{OC} deficits competitive with the current champion thin film devices.

Contrasts with thin films have enabled new insights into the bottlenecks and role of grain boundaries of CZTSe. The contrasting effects of air annealing show the necessary role of grain boundary passivation in films. Despite improvements, single crystals have yet to obtain higher measured lifetimes compared to thin films and in fact are often lower, despite the lack of grain boundaries. The hypothesized explanation is that defective crystal surfaces are still limiting the measured lifetime of single crystals (despite etching) due to the surface sensitivity of 532 nm excitation. It is also possible that single crystal bulk compositions are less optimal (higher Cu and higher Sn) which contributing to lower lifetimes. Further experiments with a less surface sensitive 1064 nm laser are underway to better understand “bulk” lifetimes.

Additional PL comparisons have demonstrated that radiative defects appear shallower in single crystals when compared to state-of-the-art thin films. Reducing

defect depth either through slow-cooling or changes in composition may be promising avenues for improving champion thin films.

CZTSe is a complex and challenging absorber material and many questions of remain, however hopefully the insights in this work help provide new strategies to controlling the defects and improving performance for CZTSe and other multinary semiconductors.

REFERENCES

- [1] IEA, “WORLD ENERGY OUTLOOK 2012: Executive Summary,” 2012.
- [2] SolarPower Europe, “Global Market Outlook for Solar Power 2015-2019,” 2014.
- [3] EPIA, “Solar generation 6 Report,” 2011.
- [4] J. Jin, “Global PV Market Outlook,” 2014.
- [5] J. Trancik, “Technology improvement and emission reductions as mutually reinforcing efforts: observations from global development of solar and wind energy,” 2015.
- [6] “First Solar Q2 2015 Earnings Call,” 2015.
- [7] P. Jackson, D. Hariskos, R. Wuerz, O. Kiowski, A. Bauer, T. M. Friedlmeier, and M. Powalla, “Properties of Cu(In,Ga)Se₂ solar cells with new record efficiencies up to 21.7%,” *Phys. status solidi - Rapid Res. Lett.*, vol. 9, no. 1, pp. 28–31, 2015.
- [8] “Solar Frontier Achieves World Record Thin-Film Solar Cell Efficiency: 22.3%.” [Online]. Available: <http://www.solar-frontier.com/eng/news/2015/C051171.html>. [Accessed: 19-Jan-2016].
- [9] M. A. Green, K. Emery, Y. Hishikawa, W. Warta, and E. D. Dunlop, “Solar cell efficiency tables (version 46),” *Prog. Photovoltaics Res. Appl.*, vol. 23, no. 7, pp. 805–812, Jul. 2015.
- [10] R. J. Gillette, C. Executive, O. Bruce, P. J. Meyerhoff, C. F. Officer, U. Systems, G. Larry, V. President, and I. Relations, “First Solar Q2 2010 Earnings Call,” 2010.
- [11] V. M. Fthenakis, “Sustainability of photovoltaics: The case for thin-film solar cells,” *Renew. Sustain. Energy Rev.*, vol. 13, no. 9, pp. 2746–2750, Dec. 2009.
- [12] C. Candelise, M. Winkler, and R. Gross, “Implications for CdTe and CIGS technologies production costs of indium and tellurium scarcity,” 2012.
- [13] C. Wadia, A. P. Alivisatos, and D. M. Kammen, “Materials Availability Expands the Opportunity for Large-Scale Photovoltaics Deployment,” *Environ. Sci. Technol.*, vol. 43, no. 6, pp. 2072–7, Mar. 2009.
- [14] W. Wang, M. T. Winkler, O. Gunawan, T. Gokmen, T. K. Todorov, Y. Zhu,

- and D. B. Mitzi, "Device Characteristics of CZTS_{1-x}SSe Thin-Film Solar Cells with 12.6% Efficiency," *Adv. Energy Mater.*, vol. 4, no. 7, p. n/a–n/a, May 2014.
- [15] W. Shockley and H. J. Queisser, "Detailed Balance Limit of Efficiency of p-n Junction Solar Cells," *J. Appl. Phys.*, vol. 32, no. 3, p. 510, 1961.
- [16] S. . Wasmin, G. Marin, C. Rinco, P. Bocaranda, and G. Sanchez Perez, "Urbach's tail in the absorption spectra of the ordered vacancy compound CuGa₃Se₅," *J. Phys. Chem. Solids*, vol. 61, pp. 669–673, 2000.
- [17] A. Stokes, B. Gorman, D. Diercks, B. Egaas, and M. Al-jassim, "Direct Evidence of a Cu(In,Ga)₃Se₅ Phase in a Bulk, High-Efficiency Cu(In,Ga)Se₂ Device Using Atom Probe Tomography," in *IEEE PVSC 40*, 2014, pp. 3–5.
- [18] R. Klenk, "Characterisation and modelling of chalcopyrite solar cells," *Thin Solid Films*, vol. 387, no. 1–2, pp. 135–140, 2001.
- [19] R. Balluffi, S. Allen, and C. Carter, *Kinetics of Materials*. Hoboken: John Wiley & Sons, Inc., 2005.
- [20] G. Dhanaraj, K. Byrappa, V. Prasad, and M. Dudley, Eds., *Springer Handbook of Crystal Growth*. Berlin, Heidelberg: Springer Verlag, 2010.
- [21] I. D. Olekseyuk, I. V. Dudchak, and L. V. Piskach, "Фазові рівноваги в квазіпотрійній системі Cu₂Se-ZnSe-Cu₂SnSe₃," *Phys. Chem. Solid State*, vol. 2, pp. 195–200, 2001.
- [22] O. Knacke, O. Kubaschewski, and K. Hesselmann, *Thermochemical Properties of Inorganic Substances*, 2nd Ed. New York: Springer-Verlag, 1991.
- [23] R. Nitsche, D. F. Sargent, and P. Wild, "Crystal Growth of Quaternary I(2)II-IV-VI(4) Chalcogenides by Iodine Vapor Transport," *J. Cryst. Growth*, vol. 1, no. 1, pp. 52–53, 1967.
- [24] M. León, S. Levchenko, R. Serna, I. V. Bodnar, A. Nateprov, M. Guc, G. Guriyeva, N. Lopez, J. M. Merino, R. Caballero, S. Schorr, A. Perez-Rodriguez, and E. Arushanov, "Spectroscopic ellipsometry study of Cu₂ZnSnSe₄ bulk crystals," *Appl. Phys. Lett.*, vol. 105, no. 6, p. 061909, Aug. 2014.
- [25] A. Nagaoka, K. Yoshino, H. Taniguchi, T. Taniyama, and H. Miyake, "Growth of Cu₂ZnSnSe₄ single crystals from Sn solutions," *J. Cryst. Growth*, vol. 354, no. 1, pp. 147–151, Sep. 2012.
- [26] A. Nagaoka, K. Yoshino, H. Taniguchi, T. Taniyama, and H. Miyake, "Preparation of Cu₂ZnSnSe₄ single crystals from Sn solutions," *J. Cryst. Growth*, vol. 341, no. 1, pp. 38–41, Feb. 2012.
- [27] A. Nagaoka, R. Katsube, S. Nakatsuka, K. Yoshino, T. Taniyama, H. Miyake, K. Kakimoto, M. a. Scarpulla, and Y. Nose, "Growth and characterization of

- Cu₂ZnSn(S_xSe_{1-x})₄ single crystal grown by traveling heater method,” *J. Cryst. Growth*, vol. 423, pp. 9–15, 2015.
- [28] S. Chen, L.-W. Wang, A. Walsh, X. G. Gong, and S.-H. Wei, “Abundance of CuZn + SnZn and 2CuZn + SnZn defect clusters in kesterite solar cells,” *Appl. Phys. Lett.*, vol. 101, no. 22, p. 223901, 2012.
- [29] M. A. Halim, M. M. Islam, X. Luo, T. Sakurai, N. Sakai, T. Kato, H. Sugimoto, H. Tampo, H. Shibata, S. Niki, and K. Akimoto, “Study of time-resolved photoluminescence in Cu₂ZnSn(S,Se)₄ thin films with different Cu/Sn ratio,” *Jpn. J. Appl. Phys.*, vol. 54, no. 8S1, p. 08KC15, Aug. 2015.
- [30] D. Kuo, J. Hsu, A. D. Saragih, and T. Mo, “Effects of the metallic target compositions on the absorber properties and the performance of Cu₂ZnSnSe₄ solar cell devices fabricated on TiN-coated Mo/glass substrates,” *Mater. Sci. Eng. B*, vol. 186, pp. 94–100, Aug. 2014.
- [31] Y. S. Lee, T. Gershon, O. Gunawan, T. K. Todorov, T. Gokmen, Y. Virgus, and S. Guha, “Cu₂ZnSnSe₄ Thin-Film Solar Cells by Thermal Co-evaporation with 11.6% Efficiency and Improved Minority Carrier Diffusion Length,” *Adv. Energy Mater.*, p. n/a–n/a, Dec. 2014.
- [32] G. P. Bernardini, P. Bonazzi, M. Corazza, F. Corsini, G. Mazzetti, L. Poggi, and G. Tanelli, “New data on the Cu₂FeSnS₄-Cu₂ZnSnS₄ pseudobinary system at 750° and 550 °,” *Eur. J. Mineral.*, no. 14, pp. 219–225, 1990.
- [33] S. Das, R. M. Krishna, S. Ma, and K. C. Mandal, “Single phase polycrystalline Cu₂ZnSnS₄ grown by vertical gradient freeze technique,” *J. Cryst. Growth*, vol. 381, pp. 148–152, Oct. 2013.
- [34] M. Grossberg, T. Raadik, J. Raudoja, and J. Krustok, “Photoluminescence study of defect clusters in Cu₂ZnSnS₄ polycrystals,” *Curr. Appl. Phys.*, vol. 14, no. 3, pp. 447–450, Mar. 2014.
- [35] A. S. Ionkin, B. M. Fish, W. J. Marshall, and R. H. Senigo, “Use of inorganic fluxes to control morphology and purity of crystalline kesterite and related quaternary chalcogenides,” *Sol. Energy Mater. Sol. Cells*, vol. 104, pp. 23–31, 2012.
- [36] a. Nateprov, V. C. Kravtsov, G. Gurieva, and S. Schorr, “Single crystal X-ray structure investigation of Cu₂ZnSnSe₄,” *Surf. Eng. Appl. Electrochem.*, vol. 49, no. 5, pp. 423–426, Nov. 2013.
- [37] S. Schorr, “The crystal structure of kesterite type compounds: A neutron and X-ray diffraction study,” *Sol. Energy Mater. Sol. Cells*, vol. 95, no. 6, pp. 1482–1488, Jun. 2011.
- [38] S. Schorr, H.-J. Hoebler, and M. Tovar, “A neutron diffraction study of the

- stannite-kesterite solid solution series,” *Eur. J. Mineral.*, vol. 19, no. 1, pp. 65–73, Feb. 2007.
- [39] L. Choubrac, A. Lafond, C. Guillot-Deudon, Y. Moëlo, and S. Jobic, “Structure Flexibility of the Cu₂ZnSnS₄ Absorber in Low-Cost Photovoltaic Cells: From the Stoichiometric to the Copper-Poor Compounds,” *Inorg. Chem.*, pp. 2–4, Mar. 2012.
- [40] T. Gershon, B. Shin, N. Bojarczuk, M. Hopstaken, D. B. Mitzi, and S. Guha, “The Role of Sodium as a Surfactant and Suppressor of Non-Radiative Recombination at Internal Surfaces in Cu₂ZnSnS₄,” *Adv. Energy Mater.*, p. n/a–n/a, Aug. 2014.
- [41] W.-C. Hsu, I. L. Repins, C. Beall, C. DeHart, G. Teeter, B. To, Y. Yang, and R. Noufi, “The effect of Zn excess on kesterite solar cells,” *Sol. Energy Mater. Sol. Cells*, vol. 113, pp. 160–164, Jun. 2013.
- [42] S. Chen, A. Walsh, X.-G. Gong, and S.-H. Wei, “Classification of lattice defects in the kesterite Cu₂ZnSnS₄ and Cu₂ZnSnSe₄ earth-abundant solar cell absorbers,” *Adv. Mater.*, vol. 25, no. 11, pp. 1522–39, Mar. 2013.
- [43] R. Haight, A. R. Barkhouse, O. Gunawan, B. Shin, M. W. Copel, M. Hopstaken, and D. B. Mitzi, “Band alignment at the Cu₂ZnSnS_xSe_[1-x]₄/CdS interface,” *Appl. Phys. Lett.*, vol. 98, no. 25, p. 253502, 2011.
- [44] I. L. Repins, H. Moutinho, S. G. Choi, A. Kanevce, D. Kuciauskas, P. Dippo, C. L. Beall, J. Carapella, C. DeHart, B. Huang, and S.-H. Wei, “Indications of short minority-carrier lifetime in kesterite solar cells,” *J. Appl. Phys.*, vol. 114, no. 8, p. 084507, 2013.
- [45] T. Gokmen, O. Gunawan, T. K. Todorov, and D. B. Mitzi, “Band tailing and efficiency limitation in kesterite solar cells,” *Appl. Phys. Lett.*, vol. 103, no. 10, p. 103506, 2013.
- [46] D. Huang and C. Persson, “Band gap change induced by defect complexes in Cu₂ZnSnS₄,” *Thin Solid Films*, vol. 535, no. null, pp. 265–269, May 2013.
- [47] J. J. S. Scragg, J. K. Larsen, M. Kumar, C. Persson, J. Sandler, S. Siebentritt, and C. Platzer Björkman, “Cu-Zn disorder and band gap fluctuations in Cu₂ZnSn(S,Se)₄: Theoretical and experimental investigations,” *Phys. status solidi*, vol. 1–8, p. n/a–n/a, Sep. 2015.
- [48] P. Zawadzki, A. Zakutayev, and S. Lany, “Entropy-Driven Clustering in Tetrahedrally Bonded Multinary Materials,” *Phys. Rev. Appl.*, vol. 3, no. January, pp. 1–7, 2015.
- [49] P. Zawadzki, A. Zakutayev, and S. Lany, “Extended antisite defects in tetrahedrally bonded semiconductors,” *Phys. Rev. B*, vol. 92, no. 20, p. 201204,

2015.

- [50] T. Unold and L. Gutay, "Chapter 7 - Photoluminescence Analysis," in *Advanced Characterization Techniques for Thin Film Solar Cells*, D. Abou-Ras, T. Kirchartz, and U. Rau, Eds. Wiley VCH Verlag, 2011, pp. 151–175.
- [51] S. Siebentritt, "Shallow Defects in the Wide Gap Chalcopyrite," in *Wide-gap Chalcopyrites (Book Chapter)*, 2006.
- [52] J. I. Pankove, *Optical Processes in Semiconductors*. 1971.
- [53] H. Sugimoto, C. Liao, H. Hiroi, N. Sakai, and T. Kato, "Lifetime improvement for high efficiency Cu₂ZnSnS₄ submodules," in *2013 IEEE 39th Photovoltaic Specialists Conference (PVSC)*, 2013, no. c, pp. 3208–3211.
- [54] S. Siebentritt, G. Rey, A. Finger, D. Regesch, J. Sandler, T. P. Weiss, and T. Bertram, "What is the bandgap of kesterite?," *Sol. Energy Mater. Sol. Cells*, pp. 1–4, 2015.
- [55] D. Kuciauskas, A. Kanevce, P. Dippo, S. Seyedmohammadi, R. Malik, S. Member, and A. L. P. Emission, "Minority-Carrier Lifetime and Surface Recombination Velocity in Single-Crystal CdTe," *IEEE J. Photovoltaics*, vol. 5, no. 1, pp. 366–371, 2015.
- [56] C. H. Swartz, M. Edirisooriya, E. G. LeBlanc, O. C. Noriega, P. a. R. D. Jayathilaka, O. S. Ogedengbe, B. L. Hancock, M. Holtz, T. H. Myers, and K. N. Zaunbrecher, "Radiative and interfacial recombination in CdTe heterostructures," *Appl. Phys. Lett.*, vol. 105, no. 22, p. 222107, 2014.
- [57] P. Xu, S. Chen, B. Huang, H. J. Xiang, X.-G. Gong, and S.-H. Wei, "Stability and electronic structure of Cu₂ZnSnS₄ surfaces: First-principles study," *Phys. Rev. B*, vol. 88, no. 4, p. 045427, Jul. 2013.
- [58] M. Bouttemy, P. Tran-Van, I. Gerard, T. Hildebrandt, A. Causier, J. L. Pelouard, G. Dagher, Z. Jehl, N. Naghavi, G. Voorwinden, B. Dimmler, M. Powalla, J. F. Guillemoles, D. Lincot, and A. Etcheberry, "Thinning of CIGS solar cells: Part I: Chemical processing in acidic bromine solutions," *Thin Solid Films*, vol. 519, no. 21, pp. 7207–7211, Aug. 2011.
- [59] R. G. Wilks, M. A. Contreras, S. Lehmann, L. T. Bismaths, F. Kronast, R. Noufi, and M. Bär, "SURFACE MODIFICATION OF POLYCRYSTALLINE Cu(In,Ga)Se₂ THIN-FILM SOLAR CELL ABSORBER SURFACES FOR PEEM MEASUREMENTS," in *37th IEEE PVSC Conference*, 2011, pp. 1–4.
- [60] A. Darga, D. Mencaraglia, Z. Djebbour, A. Migan Dubois, J. F. Guillemoles, J. P. Connolly, O. Roussel, D. Lincot, B. Canava, and A. Etcheberry, "Two step wet surface treatment influence on the electronic properties of Cu(In,Ga)Se₂ solar cells," *Thin Solid Films*, vol. 517, no. 7, pp. 2550–2553, Feb. 2009.

- [61] Z. Jehl, M. Bouttemy, D. Lincot, J. F. Guillemoles, I. Gerard, a. Etcheberry, G. Voorwinden, M. Powalla, and N. Naghavi, "Insights on the influence of surface roughness on photovoltaic properties of state of the art copper indium gallium diselenide thin films solar cells," *J. Appl. Phys.*, vol. 111, no. 11, p. 114509, 2012.
- [62] Z. Jehl, F. Erfurth, N. Naghavi, L. Lombez, I. Gerard, M. Bouttemy, P. Tran-Van, a. Etcheberry, G. Voorwinden, B. Dimmler, W. Wischmann, M. Powalla, J. F. Guillemoles, and D. Lincot, "Thinning of CIGS solar cells: Part II: Cell characterizations," *Thin Solid Films*, vol. 519, no. 21, pp. 7212–7215, Aug. 2011.
- [63] M. O. Reese, C. L. Perkins, J. M. Burst, S. Farrell, T. M. Barnes, S. W. Johnston, D. Kuciauskas, T. A. Gessert, and W. K. Metzger, "Intrinsic surface passivation of CdTe," *J. Appl. Phys.*, vol. 155305, 2015.
- [64] S. Hegedus and B. E. McCandless, "CdTe contacts for CdTe/CdS solar cells: effect of Cu thickness, surface preparation and recontacting on device performance and stability," *Sol. Energy Mater. Sol. Cells*, vol. 88, no. 1, pp. 75–95, Jun. 2005.
- [65] M. Mousel, A. Redinger, R. Djemour, N. Valle, P. J. Dale, and S. Siebentritt, "HCl and Br₂-MeOH etching of Cu₂ZnSnSe₄ polycrystalline absorbers," pp. 6–9, 2012.
- [66] H. Miyazaki, M. Aono, H. Kishimura, and H. Katagiri, "Surface etching of CZTS absorber layer by Br-related solution," *Phys. Status Solidi*, vol. 4, p. n/a–n/a, 2015.
- [67] K. Timmo, M. Altosaar, J. Raudoja, M. Grossberg, M. Danilson, O. Volobujeva, and E. Mellikov, "CHEMICAL ETCHING OF Cu₂ZnSn(S,Se)₄ MONOGRAN POWDER," in *2010 35th IEEE Photovoltaic Specialists Conference*, 2010, pp. 1–4.
- [68] R. A. Haight, "UPS measurements, Unpublished." 2015.
- [69] R. Haight, X. Shao, W. Wang, and D. B. Mitzi, "Electronic and elemental properties of the Cu₂ZnSn(S,Se)₄ surface and grain boundaries," *Appl. Phys. Lett.*, vol. 104, no. 3, p. 033902, Jan. 2014.
- [70] K. Sardashti, R. Haight, T. Gokmen, W. Wang, L.-Y. Chang, D. B. Mitzi, and A. C. Kummel, "Impact of Nanoscale Elemental Distribution in High-Performance Kesterite Solar Cells," *Adv. Energy Mater.*, vol. 201402180, p. n/a–n/a, 2015.
- [71] I. L. Repins, J. V. Li, A. Kanevce, C. L. Perkins, K. X. Steirer, J. Pankow, G. Teeter, D. Kuciauskas, C. Beall, C. Dehart, J. Carapella, B. Bob, J.-S. Park, and S.-H. Wei, "Effects of deposition termination on Cu₂ZnSnSe₄ device

- characteristics,” *Thin Solid Films*, pp. 2–5, Sep. 2014.
- [72] S. Liu, X.-H. Zhao, C. M. Campbell, M. Lassise, Y. Zhao, and Y. Zhang, “Carrier lifetimes and interface recombination velocities in CdTe/MgxCd1-xTe double heterostructures with different Mg compositions grown by molecular beam epitaxy,” *Appl. Phys. Lett.*, vol. 041120, pp. 1–6, 2015.
- [73] J. Wang and M. Isshiki, “Wide-Bandgap II–VI Semiconductors: Growth and properties,” in *Springer Handbook of Electronic and Photonic Materials*, 2007, pp. 325–342.
- [74] O. Gunawan, T. Gokmen, C. W. Warren, D. Cohen, T. K. Todorov, A. R. Barkhouse, S. Bag, J. Tang, B. Shin, and D. B. Mitzi, “Electronic properties of the Cu₂ZnSn(Se,S)₄ absorber layer in solar cells as revealed by admittance spectroscopy and related methods,” *Appl. Phys. Lett.*, vol. 100, no. 25, p. 253905, 2012.
- [75] M. Nguyen, K. Ernits, K. F. Tai, C. F. Ng, S. S. Pramana, W. a. Sasangka, S. K. Batabyal, T. Holopainen, D. Meissner, A. Neisser, and L. H. Wong, “ZnS buffer layer for Cu₂ZnSn(SSe)₄ monograin layer solar cell,” *Sol. Energy*, vol. 111, pp. 344–349, Jan. 2015.
- [76] F. Haque, N. A. Khan, K. S. Rahman, M. A. Islam, M. M. Alam, K. Sopian, and N. Amin, “Prospects of Zinc Sulphide as an Alternative Buffer Layer for CZTS Solar Cells from Numerical Analysis,” in *8th International Conference on Electrical and Computer Engineering*, 2014, pp. 504–507.
- [77] A. I. Inamdar, K.-Y. Jeon, H. seok Woo, W. Jung, H. Im, and H. Kim, “Synthesis of a Cu₂ZnSnS₄ (CZTS) absorber layer and metal doped ZnS buffer layer for heterojunction solar cell applications,” in *Society*, 2011, vol. 41, no. 4, pp. 167–175.
- [78] J. Kim, C. Park, S. M. Pawar, A. I. Inamdar, Y. Jo, J. Han, J. Hong, Y. S. Park, D.-Y. Kim, W. Jung, H. Kim, and H. Im, “Optimization of sputtered ZnS buffer for Cu₂ZnSnS₄ thin film solar cells,” *Thin Solid Films*, vol. 566, pp. 88–92, Oct. 2014.
- [79] N. Vora, J. Blackburn, I. L. Repins, C. Beall, B. To, J. Pankow, G. Teeter, M. Young, and R. Noufi, “Phase identification and control of thin films deposited by co-evaporation of elemental Cu, Zn, Sn, and Se,” *J. Vac. Sci. Technol. A Vacuum, Surfaces, Film.*, vol. 30, no. 5, p. 051201, 2012.
- [80] J. Timo Wätjen, J. Engman, M. Edoff, and C. Platzer-Björkman, “Direct evidence of current blocking by ZnSe in Cu₂ZnSnSe₄ solar cells,” *Appl. Phys. Lett.*, vol. 100, no. 17, p. 173510, 2012.
- [81] K. Sardashti and A. C. Kummel, “Nano-auger Measurements, Unpublished.” 2015.

- [82] S. G. Choi, H. Y. Zhao, C. Persson, C. L. Perkins, a. L. Donohue, B. To, A. Norman, J. Li, and I. L. Repins, “Dielectric function spectra and critical-point energies of $\text{Cu}_2\text{ZnSnSe}_4$ from 0.5 to 9.0 eV,” *J. Appl. Phys.*, vol. 111, no. 3, p. 033506, 2012.
- [83] W. K. Metzger, I. L. Repins, and M. A. Contreras, “Long lifetimes in high-efficiency $\text{Cu}(\text{In}, \text{Ga})\text{Se}_2$ solar cells,” *Appl. Phys. Lett.*, vol. 93, p. 022110, 2008.
- [84] M. Maiberg and R. Scheer, “Theoretical study of time-resolved luminescence in semiconductors. I. Decay from the steady state,” *J. Appl. Phys.*, vol. 116, no. 12, p. 123710, 2014.
- [85] F. Hergert, “Chemical formation reactions for $\text{Cu}(\text{In}, \text{Ga})\text{Se}_2$ and other chalcopyrite compounds,” Universität Erlangen-Nürnberg, 2007.
- [86] M. Neuschitzer, Y. Sanchez, T. Olar, T. Thersleff, S. Lopez-Marino, F. Oliva, M. Espindola-Rodriguez, H. Xie, M. Placidi, V. Izquierdo-Roca, I. Lauermann, K. Leifer, A. Pérez-Rodríguez, and E. Saucedo, “The complex surface chemistry of kesterites: Cu/Zn re-ordering after low temperature post deposition annealing and its role in high performance devices,” *Chem. Mater.*, p. 150716105040008, 2015.
- [87] S. Chen, X.-G. Gong, A. Walsh, and S.-H. Wei, “Defect physics of the kesterite thin-film solar cell absorber $\text{Cu}_2\text{ZnSnS}_4$,” *Appl. Phys. Lett.*, vol. 96, no. 2, p. 021902, 2010.
- [88] F. Fan, L. Wu, M. Gong, G. Liu, Y. Wang, S. Yu, S. Chen, and F. A. N. E. T. Al, “Synthesis of Wurtzite-Derived Theoretical and Experimental Insights,” *ACS Nano*, no. Xx, 2013.
- [89] A. Kanevce, I. L. Repins, and S.-H. Wei, “Impact of bulk properties and local secondary phases on the $\text{Cu}_2(\text{Zn}, \text{Sn})\text{Se}_4$ solar cells open-circuit voltage,” *Sol. Energy Mater. Sol. Cells*, vol. 133, pp. 119–125, Feb. 2015.
- [90] T. Tanaka, T. Sueishi, K. Saito, Q. Guo, M. Nishio, K. M. Yu, and W. Walukiewicz, “Existence and removal of Cu_2Se second phase in coevaporated $\text{Cu}_2\text{ZnSnSe}_4$ thin films,” *J. Appl. Phys.*, vol. 111, no. 5, p. 053522, 2012.
- [91] S. Temgoua, R. Bodeux, N. Naghavi, and S. Delbos, “Effects of SnSe_2 secondary phases on the efficiency of $\text{Cu}_2\text{ZnSn}(\text{S}_x, \text{Se}_{1-x})_4$ based solar cells,” *Thin Solid Films*, pp. 2–6, Oct. 2014.
- [92] A. D. Collord, H. Xin, and H. W. Hillhouse, “Combinatorial Exploration of the Effects of Intrinsic and Extrinsic Defects in $\text{Cu}_2\text{ZnSn}(\text{S}, \text{Se})_4$,” *IEEE J. Photovoltaics*, vol. 5, no. 1, pp. 288–298, Jan. 2015.
- [93] G. Brammert, S. Oueslati, M. Buffi, J. Bekaert, H. El Anzeery, K. Ben

- Messaoud, S. Sahayaraj, T. Nuytten, K. Christine, M. Meuris, and J. Poortmans, "Investigation of Properties Limiting Efficiency in Cu₂ZnSnSe₄ -Based Solar Cells," *IEEE J. Photovoltaics*, vol. 1, pp. 1–7, 2014.
- [94] A. Fairbrother, M. Dimitrievska, Y. Sánchez, V. Izquierdo-Roca, A. Perez-Rodriguez, and E. Saucedo, "Compositional paradigms in multinary compound systems for photovoltaic applications: A case study of kesterites," *J. Mater. Chem. A*, 2015.
- [95] L. Choubrac, A. Lafond, M. Paris, C. Guillot-Deudon, and S. Jobic, "The stability domain of the selenide kesterite photovoltaic materials and NMR investigation of the Cu/Zn disorder in Cu₂ZnSnSe₄ (CZTSe)," *Phys. Chem. Chem. Phys.*, vol. 17, no. 23, pp. 15088–15092, 2015.
- [96] J.-H. Yang, J.-S. Park, J. Kang, W. Metzger, T. Barnes, and S.-H. Wei, "Tuning the Fermi level beyond the equilibrium doping limit through quenching: The case of CdTe," *Phys. Rev. B*, vol. 90, no. 24, p. 245202, 2014.
- [97] B. Van Zeghbroeck, "Semiconductor Fundamental: Carrier distribution functions," 2011. .
- [98] A. Redinger, K. Hönes, X. Fontané, V. Izquierdo-Roca, E. Saucedo, N. Valle, A. Pérez-Rodríguez, and S. Siebentritt, "Detection of a ZnSe secondary phase in coevaporated Cu₂ZnSnSe₄ thin films," *Appl. Phys. Lett.*, vol. 98, no. 10, p. 101907, 2011.
- [99] O. Gunawan, T. Gokmen, and D. B. Mitzi, "Suns-Voc characteristics of high performance kesterite solar cells," *arXiv [cond-mat.mtrl-sci]*, pp. 1–9, 2014.
- [100] J. C. González, G. M. Ribeiro, E. R. Viana, P. a Fernandes, P. M. P. Salomé, K. Gutiérrez, a. Abelenda, F. M. Matinaga, J. P. Leitão, and A. F. da Cunha, "Hopping conduction and persistent photoconductivity in Cu₂ZnSnS₄ thin films," *J. Phys. D: Appl. Phys.*, vol. 46, no. 15, p. 155107, Apr. 2013.
- [101] A. Nagaoka, H. Miyake, T. Taniyama, K. Kakimoto, and K. Yoshino, "Correlation between intrinsic defects and electrical properties in the high-quality Cu₂ZnSnS₄ single crystal," *Appl. Phys. Lett.*, vol. 103, no. 11, p. 112107, 2013.
- [102] O. Gunawan, W. Wang, T. Gokmen, T. K. Todorov, and D. B. Mitzi, "Impact of Cu Content in High Performance Cu₂ZnSn(Se,S)₄ Solar Cells," in *IEEE*.
- [103] K. G. Lisunov, M. Guk, A. Nateprov, S. Levchenko, V. E. Tezlevan, and E. Arushanov, "Features of the acceptor band and properties of localized carriers from studies of the variable-range hopping conduction in single crystals of p-Cu₂ZnSnS₄," *Sol. Energy Mater. Sol. Cells*, vol. 112, pp. 127–133, May 2013.
- [104] T. Gershon, Y. S. Lee, R. Mankad, O. Gunawan, T. Gokmen, D. M. Bishop, B.

- E. McCandless, and S. Guha, "The impact of sodium on the sub-bandgap states in CZTSe and CZTS," *Appl. Phys. Lett.*, vol. 106, no. 12, p. 123905, 2015.
- [105] T. Prabhakar and N. Jampana, "Effect of sodium diffusion on the structural and electrical properties of Cu₂ZnSnS₄ thin films," *Sol. Energy Mater. Sol. Cells*, vol. 95, no. 3, pp. 1001–1004, Mar. 2011.
- [106] A. Nagaoka, H. Miyake, T. Taniyama, K. Kakimoto, Y. Nose, M. a. Scarpulla, and K. Yoshino, "Effects of sodium on electrical properties in Cu₂ZnSnS₄ single crystal," *Appl. Phys. Lett.*, vol. 104, no. 15, p. 152101, Apr. 2014.
- [107] J. V. Li, D. Kuciauskas, M. R. Young, and I. L. Repins, "Effects of sodium incorporation in Co-evaporated Cu₂ZnSnSe₄ thin-film solar cells," *Appl. Phys. Lett.*, vol. 102, no. 16, p. 163905, 2013.
- [108] C. M. Sutter-Fella, J. A. Stückelberger, H. Hagendorfer, F. La Mattina, L. Kranz, S. Nishiwaki, A. R. Uhl, Y. E. Romanyuk, and A. N. Tiwari, "Sodium Assisted Sintering of Chalcogenides and Its Application to Solution Processed Cu₂ZnSn(S,Se)₄ Thin Film Solar Cells," *Chem. Mater.*, vol. 26, no. 3, pp. 1420–1425, Feb. 2014.
- [109] T. Ma, G. Jiang, W. Liu, and C. Zhu, "Sodium doping effects on the crystalline and electrical properties of Cu₂ZnSnSe₄ thin films," *Sol. Energy*, vol. 115, pp. 413–418, 2015.
- [110] S. Tajima, R. Asahi, D. Isheim, D. N. Seidman, T. Itoh, M. Hasegawa, and K. Ohishi, "Atom-probe tomographic study of interfaces of Cu₂ZnSnS₄ photovoltaic cells," *Appl. Phys. Lett.*, vol. 105, no. 9, p. 093901, Sep. 2014.
- [111] T. Schwarz, O. Cojocaru-Mirédin, P. Choi, M. Mousel, A. Redinger, S. Siebentritt, and D. Raabe, "Atom probe tomography study of internal interfaces in Cu₂ZnSnSe₄ thin-films," *J. Appl. Phys.*, vol. 118, no. 9, p. 095302, 2015.
- [112] J. J. Scragg, L. Choubrac, A. Lafond, T. Ericson, and C. Platzer-Björkman, "A low-temperature order-disorder transition in Cu₂ZnSnS₄ thin films," *Appl. Phys. Lett.*, vol. 104, no. 4, p. 041911, Jan. 2014.
- [113] G. Rey, A. Redinger, J. Sendler, T. P. Weiss, M. Thevenin, M. Guennou, B. El Adib, and S. Siebentritt, "The band gap of Cu₂ZnSnSe₄: Effect of order-disorder," *Appl. Phys. Lett.*, vol. 105, no. 11, p. 112106, Sep. 2014.
- [114] M. Paris, L. Choubrac, A. Lafond, C. Guillot-Deudon, and S. Jobic, "Solid-State NMR and Raman Spectroscopy To Address the Local Structure of Defects and the Tricky Issue of the Cu/Zn Disorder in Cu-Poor, Zn-Rich CZTS Materials.," *Inorg. Chem.*, Jul. 2014.
- [115] J. Krustok, T. Raadik, M. Grossberg, S. Giraldo, M. Neuschitzer, S. López-Marino, and E. Saucedo, "Temperature dependent electroreflectance study of

- Cu₂ZnSnSe₄ solar cells,” *Mater. Sci. Semicond. Process.*, vol. 39, no. 1, pp. 251–254, Nov. 2015.
- [116] J. H. Werner, J. Mattheis, and U. Rau, “Efficiency limitations of polycrystalline thin film solar cells: case of Cu(In,Ga)Se₂,” *Thin Solid Films*, vol. 480–481, pp. 399–409, 2005.
- [117] J. Mattheis, U. Rau, and J. H. Werner, “Light absorption and emission in semiconductors with band gap fluctuations—A study on Cu(In,Ga)Se₂ thin films,” *J. Appl. Phys.*, vol. 101, no. 11, p. 113519, 2007.
- [118] M. Grossberg, J. Krustok, T. Raadik, M. Kauk-Kuusik, and J. Raudoja, “Photoluminescence study of disordering in the cation sublattice of Cu₂ZnSnS₄,” *Curr. Appl. Phys.*, vol. 14, no. 11, pp. 1424–1427, Aug. 2014.
- [119] A. Redinger, J. Sandler, R. Djemour, T. Weiss, G. Rey, P. J. Dale, and S. Siebentritt, “Different Bandgaps in Cu₂ZnSnSe₄: A High Temperature Coevaporation Study,” *ieeexplore.ieee.org*, pp. 1–8, 2014.
- [120] D. M. Bishop, B. E. McCandless, R. Haight, D. B. Mitzi, and R. W. Birkmire, “Fabrication and Electronic Properties of CZTSe Single Crystals,” *IEEE J. Photovoltaics*, pp. 1–5, 2014.
- [121] M. Y. Valakh, O. F. Kolomys, S. S. Ponomaryov, V. O. Yukhymchuk, I. S. Babichuk, V. Izquierdo-Roca, E. Saucedo, A. Perez-Rodriguez, J. R. Morante, S. Schorr, and I. V. Bodnar, “Raman scattering and disorder effect in Cu₂ZnSnS₄,” *Phys. status solidi - Rapid Res. Lett.*, vol. 7, no. 4, pp. 258–261, Apr. 2013.
- [122] S. Chen, X.-G. Gong, A. Walsh, and S.-H. Wei, “Crystal and electronic band structure of Cu₂ZnSnX₄ (X=S and Se) photovoltaic absorbers: First-principles insights,” *Appl. Phys. Lett.*, vol. 94, no. 4, p. 041903, 2009.
- [123] D.-H. Kuo and M. Tsega, “The investigation of Cu_xZnSnSe₄ bulks with x=1.4–2.2 for debating the Cu excess and Cu deficiency used in thin-film solar cells,” *Mater. Res. Bull.*, vol. 49, pp. 608–613, Jan. 2014.
- [124] J.-S. Park, J.-H. Yang, A. Kanevce, S. Choi, I. L. Repins, and S.-H. Wei, “Ordering-induced direct-to-indirect band gap transition in multication semiconductor compounds,” *Phys. Rev. B*, vol. 91, no. November 2014, pp. 1–5, 2015.
- [125] P. Bäume, J. Gutowski, E. Kurtz, D. Hommel, and G. Landwehr, “Intensity-dependent energy and lineshape variation of donor-acceptor-pair bands in highly compensated ZnSe:N,” *J. Cryst. Growth*, vol. 159, no. 1–4, pp. 252–256, 1996.
- [126] S. Siebentritt, N. Papathanasiou, and M. C. Lux-Steiner, “Potential fluctuations

- in compensated chalcopyrites,” *Phys. B Condens. Matter*, vol. 376–377, pp. 831–833, 2006.
- [127] T. Schwarz, O. Cojocaru-Mirédin, P. Choi, M. Mousel, A. Redinger, S. Siebentritt, and D. Raabe, “Atom probe study of Cu₂ZnSnSe₄ thin-films prepared by co-evaporation and post-deposition annealing,” *Appl. Phys. Lett.*, vol. 102, no. 4, p. 042101, 2013.
- [128] M. C. DeLong, P. C. Taylor, and J. M. Olson, “Excitation intensity dependence of photoluminescence in Ga_{0.52}In_{0.48}P,” *Appl. Phys. Lett.*, vol. 57, no. 6, p. 620, 1990.
- [129] M. Gloeckler and J. R. Sites, “Efficiency limitations for wide-band-gap chalcopyrite solar cells,” *Thin Solid Films*, vol. 480–481, pp. 241–245, 2005.
- [130] M. Werner, D. Keller, S. G. Haass, C. Gretener, B. Bissig, P. Fuchs, F. La Mattina, R. Erni, Y. E. Romanyuk, and A. N. Tiwari, “Enhanced carrier collection from CdS passivated grains in solution processed Cu₂ZnSn(S,Se)₄ solar cells,” *ACS Appl. Mater. Interfaces*, p. 150518121124006, 2015.
- [131] T. K. Todorov, K. B. Reuter, and D. B. Mitzi, “High-Efficiency Solar Cell with Earth-Abundant Liquid-Processed Absorber,” *Adv. Mater.*, vol. 22, no. 20, pp. E156–E159, May 2010.
- [132] D. B. Mitzi, O. Gunawan, T. K. Todorov, K. Wang, and S. Guha, “The path towards a high-performance solution-processed kesterite solar cell,” *Sol. Energy Mater. Sol. Cells*, no. August 2010, pp. 1–16, Jan. 2011.
- [133] O. Gunawan, T. K. Todorov, and D. B. Mitzi, “Loss mechanisms in hydrazine-processed Cu₂ZnSn(Se,S)₄ solar cells,” *Appl. Phys. Lett.*, vol. 97, no. 23, p. 233506, 2010.
- [134] T. K. Todorov, J. Tang, S. Bag, O. Gunawan, T. Gokmen, Y. Zhu, and D. B. Mitzi, “Beyond 11% Efficiency: Characteristics of State-of-the-Art Cu₂ZnSn(S,Se)₄ Solar Cells,” *Adv. Energy Mater.*, p. n/a–n/a, Aug. 2012.
- [135] K. Wang, O. Gunawan, T. K. Todorov, B. Shin, S. J. Chey, N. A. Bojarczuk, D. B. Mitzi, and S. Guha, “Thermally evaporated Cu₂ZnSnS₄ solar cells,” *Appl. Phys. Lett.*, vol. 97, no. 14, p. 143508, 2010.
- [136] M. T. Winkler, W. Wang, O. Gunawan, H. J. Hovel, T. K. Todorov, and D. B. Mitzi, “Optical designs that improve the efficiency of Cu₂ZnSn(S,Se)₄ solar cells,” *Energy Environ. Sci.*, vol. 7, no. 3, p. 1029, 2014.
- [137] W. N. Shafarman, R. S. Huang, and S. H. Stephens, “CHARACTERIZATION OF Cu (InGa) Se 2 SOLAR CELLS USING ETCHED ABSORBER LAYERS,” in *IEEE Photovoltaic Energy Conversion Conference*, 2006, pp. 420–423.

- [138] K. F. Tai, T. Gershon, O. Gunawan, and C. H. A. Huan, "Examination of electronic structure differences between CIGSSe and CZTSSe by photoluminescence study," *J. Appl. Phys.*, vol. 117, no. 23, p. 235701, 2015.
- [139] T. Gershon, B. Shin, N. Bojarczuk, T. Gokmen, S. Lu, and S. Guha, "Photoluminescence characterization of a high-efficiency Cu₂ZnSnS₄ device," *J. Appl. Phys.*, vol. 114, no. 15, p. 154905, 2013.
- [140] T. Gershon, B. Shin, T. Gokmen, S. Lu, N. Bojarczuk, and S. Guha, "Relationship between Cu₂ZnSnS₄ quasi donor-acceptor pair density and solar cell efficiency," *Appl. Phys. Lett.*, vol. 103, no. 19, p. 193903, 2013.
- [141] H. Katagiri, K. Jimbo, M. Tahara, H. Araki, and K. Oishi, "The Influence of the Composition Ratio on CZTS-based Thin Film Solar Cells," in *Materials Research Society Symposium Proceedings*, 2009, vol. 1165.
- [142] T. Unold, S. Kretzschmar, J. Just, O. Zander, B.-A. Schubert, B. Marsen, and H. Schock, "CORRELATION BETWEEN COMPOSITION AND PHOTOVOLTAIC PROPERTIES OF Cu₂ZnSnS₄ THIN FILM SOLAR CELLS," in *37th IEEE PVSC Conference*, 2011, pp. 4–7.
- [143] G. Y. Kim, J. R. Kim, W. Jo, K. D. Lee, J. Y. Kim, T. T. T. Nguyen, and S. Yoon, "Effects of Cu_{2-x}S phase removal on surface potential of Cu₂ZnSnS₄ thin-films grown by electroplating," *Curr. Appl. Phys.*, vol. 14, no. 12, pp. 1665–1668, Dec. 2014.
- [144] C. P. Thompson, L. Chen, W. N. Shafarman, J. Lee, S. Fields, R. W. Birkmire, and A. N. Modeling, "Bandgap gradients in (Ag,Cu)(In,Ga)Se₂ thin film solar cells deposited by three-stage co-evaporation," 2015.
- [145] L. Q. Phuong, M. Okano, G. Yamashita, M. Nagai, M. Ashida, A. Nagaoka, K. Yoshino, and Y. Kanemitsu, "Photocarrier dynamics in undoped and Na-doped Cu₂ZnSnS₄ single crystals revealed by ultrafast time-resolved terahertz spectroscopy," *Appl. Phys. Express*, vol. 8, no. 6, p. 062303, Jun. 2015.
- [146] E. Jarzembowski, F. Syrowatka, K. Kaufmann, W. Fränzel, T. Hölscher, and R. Scheer, "The influence of sodium on the molybdenum/Cu(In,Ga)Se₂ interface recombination velocity, determined by time resolved photoluminescence," *Appl. Phys. Lett.*, vol. 107, no. 5, p. 051601, 2015.
- [147] E. Ghorbani, J. Kiss, H. Mirhosseini, T. D. Kühne, and C. Felser, "Hybrid Functional Calculations on the Na and K Impurities in Substitutional and Interstitial Positions in Cu₂ZnSnSe₄," *IEEE*, pp. 9–12, 2015.
- [148] W. Xiao, J. N. Wang, X. S. Zhao, J. W. Wang, G. J. Huang, L. Cheng, L. J. Jiang, and L. G. Wang, "Intrinsic defects and Na doping in Cu₂ZnSnS₄: A density-functional theory study," *Sol. Energy*, vol. 116, pp. 125–132, 2015.

- [149] T. S. Gershon and D. M. Bishop, “[Submitted] Photovoltaic Materials and Devices Based on the Alloyed Kesterite Absorber $(\text{Ag}_x\text{Cu}_{1-x})_2\text{ZnSnSe}_4$,” *Adv. Energy Mater.*, 2015.
- [150] W. Gong, T. Tabata, K. Takei, M. Morihama, T. Maeda, and T. Wada, “Crystallographic and optical properties of $(\text{Cu}, \text{Ag})_2\text{ZnSnS}_4$ and $(\text{Cu}, \text{Ag})_2\text{ZnSnSe}_4$ solid solutions,” *Phys. Status Solidi*, vol. 4, p. n/a–n/a, 2015.
- [151] T. Gershon, D. Bishop, B. E. McCandless, W. Wang, and R. Haight, “Capturing the effect of long low-temperature anneals on the sub-bandgap defect structure of CZTSSe,” *Proc. SPIE*, vol. 9552, p. 955209, 2015.
- [152] D. Kuciauskas, A. Kanevce, J. M. Burst, J. N. Duenow, R. Dhere, D. S. Albin, D. H. Levi, and R. K. Ahrenkiel, “Minority Carrier Lifetime Analysis in the Bulk of Thin-Film Absorbers Using Subbandgap (Two-Photon) Excitation,” *IEEE J. Photovoltaics*, vol. 3, no. 4, pp. 1319–1324, Oct. 2013.
- [153] J. T. Heath, D. Cohen, W. N. Shafarman, J. D. Cohen, and W. N. Shafarman, “Bulk and metastable defects in $\text{CuIn}[1-x]\text{Ga}[x]\text{Se}_2$ thin films using drive-level capacitance profiling,” *J. Appl. Phys.*, vol. 95, no. 3, p. 1000, 2004.
- [154] J. Heath and P. Zabierowski, “Capacitance Spectroscopy,” in *Advanced Characterization Techniques for Thin Film Solar Cells*, D. Abou-Ras, T. Kirchartz, and U. Rau, Eds. Wiley VCH Verlag, 2011, pp. 81–102.
- [155] S. Hegedus, D. Ryan, K. Dobson, B. E. McCandless, and D. Desai, “Photoconductive CdS: how does it affect CdTe/CdS solar cell performance?,” *Mater. Res.*, vol. 763, no. October, pp. 1–6, 2003.
- [156] T. Nagle, “Quantum Efficiency as a Device-Physics Interpretation Tool for Thin-Film Solar Cells,” p. 114, 2007.
- [157] G. Agostinelli, D. L. Bätzner, and M. Burgelman, “A theoretical model for the front region of cadmium telluride solar cells,” *Thin Solid Films*, vol. 431–432, no. 03, pp. 407–413, 2003.
- [158] S. Hegedus and W. N. Shafarman, “Thin-film solar cells: device measurements and analysis,” *Prog. Photovoltaics Res. Appl.*, vol. 12, no. 23, pp. 155–176, Mar. 2004.
- [159] B.-A. Schubert, B. Marsen, S. Cinque, T. Unold, R. Klenk, S. Schorr, and H.-W. Schock, “ $\text{Cu}_2\text{ZnSnS}_4$ thin film solar cells by fast coevaporation,” *Prog. Photovoltaics Res. Appl.*, vol. 19, no. May 2010, pp. 93–96, 2011.
- [160] A. Redinger and S. Siebentritt, “Coevaporation of $\text{Cu}_2\text{ZnSnSe}_4$ thin films,” *Appl. Phys. Lett.*, vol. 97, no. 9, p. 092111, 2010.
- [161] I. L. Repins, C. Beall, N. Vora, C. DeHart, D. Kuciauskas, P. Dippo, B. To, J. Mann, W.-C. Hsu, A. Goodrich, and R. Noufi, “Co-evaporated $\text{Cu}_2\text{ZnSnSe}_4$

- films and devices,” *Sol. Energy Mater. Sol. Cells*, pp. 1–6, Feb. 2012.
- [162] S. Ahn, S. Jung, J. Gwak, A. Cho, K. Shin, K. Yoon, D. Park, H. H. Cheong, and J. H. Yun, “Determination of band gap energy E_g of $\text{Cu}_2\text{ZnSnSe}_4$ thin films: On the discrepancies of reported band gap values,” *Appl. Phys. Lett.*, vol. 97, no. 2, p. 021905, 2010.
- [163] J. J. Scragg, P. J. Dale, D. Colombara, and L. M. Peter, “Thermodynamic Aspects of the Synthesis of Thin-Film Materials for Solar Cells,” *Chemphyschem*, pp. 3035–3046, Apr. 2012.
- [164] A. Redinger, D. M. Berg, P. J. Dale, and S. Siebentritt, “The consequences of kesterite equilibria for efficient solar cells,” *J. Am. Chem. Soc.*, vol. 133, no. 10, pp. 3320–3, Mar. 2011.
- [165] J. J. Scragg, T. Ericson, T. Kubart, M. Edoff, and C. Platzer-Björkman, “Chemical Insights into the Instability of $\text{Cu}_2\text{ZnSnS}_4$ Films during Annealing,” *Chem. Mater.*, vol. 23, no. 20, pp. 4625–4633, Oct. 2011.
- [166] R. C. Snyder and M. F. Doherty, “Faceted crystal shape evolution during dissolution or growth,” *AIChE J.*, vol. 53, no. 5, pp. 1337–1348, May 2007.
- [167] B. J. Griffin, “A comparison of conventional Everhart-Thornley style and in-lens secondary electron detectors: a further variable in scanning electron microscopy.,” *Scanning*, vol. 33, no. 3, pp. 162–73, 2011.
- [168] D. M. Berg, “KESTERITE EQUILIBRIUM REACTION AND THE DISCRIMINATION OF SECONDARY PHASES FROM $\text{Cu}_2\text{ZnSnS}_4$,” University of Luxembourg, 2012.
- [169] M. Klenk, O. Schenker, U. Probst, and E. Bucher, “X-ray fluorescence measurements of thin film chalcopyrite solar cells,” *Sol. Energy Mater. Sol. Cells*, vol. 58, no. 3, pp. 299–319, 1999.
- [170] M. Maiberg and R. Scheer, “Theoretical study of time-resolved luminescence in semiconductors. II. Pulsed excitation,” *J. Appl. Phys.*, vol. 116, no. 12, p. 123711, 2014.
- [171] S. Nakamura, T. Maeda, T. Tabata, and T. Wada, “FIRST-PRINCIPLES STUDY OF INDIUM-FREE PHOTOVOLTAIC COMPOUNDS $\text{Ag}_2\text{ZnSnSe}_4$ and $\text{Cu}_2\text{ZnSnSe}_4$,” in *37th IEEE PVSC Conference*, 2011, pp. 2–5.
- [172] T. T. Werner, G. M. Mudd, and S. M. Jowitt, “Indium: key issues in assessing mineral resources and long-term supply from recycling,” *Appl. Earth Sci.*, vol. 00, no. 0, p. 1743275815Y.000, Dec. 2015.
- [173] M. a. Green, “Rare materials for photovoltaics: Recent tellurium price fluctuations and availability from copper refining,” *Sol. Energy Mater. Sol. Cells*, vol. 119, pp. 256–260, 2013.

- [174] G. Kavlak and T. E. Graedel, "Global anthropogenic tellurium cycles for 1940-2010," *Resour. Conserv. Recycl.*, vol. 76, pp. 21–26, 2013.
- [175] N. A. Kul'chitskii and A. V. Naumov, "Modern state of markets of selenium and selenium-based compounds," *Russ. J. Non-Ferrous Met.*, vol. 56, no. 4, pp. 409–416, 2015.
- [176] S.-H. Wei, L. Ferreira, and A. Zunger, "First-principles calculation of temperature-composition phase diagrams of semiconductor alloys," *Physical Review B*, vol. 41, no. 12, pp. 8240–8269, Apr-1990.
- [177] S.-H. Wei, S. B. Zhang, and A. Zunger, "First-principles calculation of band offsets, optical bowings, and defects in CdS, CdSe, CdTe, and their alloys," *J. Appl. Phys.*, vol. 87, no. 3, p. 1304, 2000.
- [178] J.-H. Yang, W.-J. Yin, J.-S. Park, and S.-H. Wei, "Self-regulation of charged defect compensation and formation energy pinning in semiconductors," *Sci. Rep.*, vol. 5, p. 16977, 2015.
- [179] J. Ma, S.-H. Wei, T. Gessert, and K. Chin, "Carrier density and compensation in semiconductors with multiple dopants and multiple transition energy levels: Case of Cu impurities in CdTe," *Phys. Rev. B*, vol. 83, no. 24, pp. 1–7, 2011.

Appendix A

SUMMARY OF PUBLICATIONS

Publications Related to This Work

- **D. M. Bishop**, B. E. McCandless, R. Haight, D. B. Mitzi, and R. W. Birkmire, “Fabrication and Electronic Properties of CZTSe Single Crystals,” *IEEE J. Photovoltaics*, pp. 1–5, 2014.
- **D. M. Bishop**, B. E. McCandless, T. C. Mangan, K. Dobson, and R. Birkmire, “Effects of Growth Conditions on Secondary Phases in CZTSe Thin Films Deposited by Co-evaporation,” *MRS Proc.*, vol. 1538, no. 1, pp. 75–82, Jan. 2013.
- T. Gershon, Y. S. Lee, R. Mankad, O. Gunawan, T. Gokmen, **D. M. Bishop**, B. McCandless, and S. Guha, “The impact of sodium on the sub-bandgap states in CZTSe and CZTS,” *Appl. Phys. Lett.*, vol. 106, no. 12, p. 123905, 2015.
- T. Gershon, YS. Lee, P. Antunez, R. Mankad, S. Singh, **D. M. Bishop**, O. Gunawan, M. Hopstaken, R. Haight, “Photovoltaic Materials and Devices Based on the Alloyed Kesterite Absorber ($\text{Ag}_x\text{Cu}_{1-x}$) $_2\text{ZnSnSe}_4$,” *Adv. Energy Materials [Submitted]*
- **D. M. Bishop**, B. E. McCandless, R. Birkmire, “Modification of Defects and Potential Fluctuations in Slow-cooled and Quenched $\text{Cu}_2\text{ZnSnSe}_4$ Single Crystals,” *Adv. Energy Matl.*, [to be submitted Jan 2016]
- T. Gershon, **D. M. Bishop**, B. McCandless, W. Wang, R. Haight, “Capturing the effect of long low-temperature anneals on the subbandgap defect structure of CZTSSe,” *SPIE invited talk and proceedings, 2015*

Manuscripts In-Preparation

- **D. M. Bishop**, M. Lloyd, B. McCandless, R. W. Birkmire “Non-flux Growth of Single Crystal $\text{Cu}_2\text{ZnSnSe}_4$ Above and Below the Melt,” [In-preparation] *Journal of Crystal Growth*
- B. McCandless, **D. M. Bishop**, M. Lloyd, “Majority Carrier Properties of CZTSe Single Crystals” [In-preparation, *Appl. Phys. Lett*]

Other Publications

- P. Antunez, **D. M. Bishop**, K. Sardashti, O. Gunawan¹, R. Mankad¹, S. Singh, A. Kummel, B. McCandless, R. Haight, “Open Circuit Voltage Improvements in

CZTSSe Devices through High Work Function Back Contacts” *MRS Advances Fall 2015*

- P. Antunez, T. Gershon, O. Gunawan, Y. Lee, **D. M. Bishop**, R. Mankad, B. McCandless, R Haight “Solution-Based Deposition of Silver-Alloyed $\text{Cu}_2\text{ZnSn}(\text{S},\text{Se})_4$ Solar Cells”, *Submitted MRS Proceedings, Spring 2016*
- RR. Prabhakar, O. Gunawan, L. Woei, MA Hassan¹ **D. M. Bishop**, LH Wong, “Role of Na Incorporation in Improving Power Conversion Efficiencies in $\text{Cu}_2\text{MnSnS}_4$ Thin film solar cells” [*Submitted APL*]

Conference Oral Presentations

- “Fabrication and Electronic Properties of CZTSe Single Crystals,” *IEEE Photovoltaics Conference, June 2014*
- “Effects of Growth Conditions on Secondary Phases in CZTSe Thin Films Deposited by Co-evaporation,” *MRS Spring 2013*

Other Conferences

- **D. M. Bishop**, B. McCandless, Defect Changes in Quenched and Slow-cooled $\text{Cu}_2\text{ZnSnSe}_4$ Single Crystals, *IEEE Photovoltaics Conference, May 2015*
- M. Lloyd, **D. M. Bishop**, B. McCandless, “Surface passivation strategies for bulk single crystal $\text{Cu}_2\text{ZnSnSe}_4$ based solar cells” *Fall MRS 2015*

Appendix B

CRYSTAL GROWTH

B.1 Decomposition of $\text{Cu}_2\text{ZnSnSe}_4$ and Cu_2SnSe_3 By Thermogravimetric Analysis (TGA)

Link back to original text Pg. 17.

TGA was performed on CTSe and CZTSe phases formed by sealed ampoule synthesis as well SnSe₂ powder purchased from Alfa Aesar. The compositions and growth temperatures are given in the table, while the TGA curves are given below. Measurements were taken on a TA Instruments Q500 TGA with a ramp rate of 10°C/minute from 20-1000°C in flowing N₂. Prior to loading in the TGA, samples were powdered to XRD standard 200 mesh.

Decomposition temperature was found to depend on fabrication variables as shown in the table. The highest decomposition temperature obtained for CZTSe was 699°C, which was measured on the sample with the highest fabrication temperatures. A decomposition temperature of 637°C was measured for a thin film sample that was further from stoichiometric composition. Strong deviations from stoichiometry would be expected to increase defects and therefore raise the enthalpy of the material which would result in lower temperature decomposition.

The mass loss exhibited, up to 46%, suggests CZTSe lost almost all excess Se and SnSe which is volatile at high temperature, and therefore only Cu₂Se and ZnSe remain after the ramp to 1000°C. Decomposition curves for CZTSe, Cu₂SnSe₃ and SnSe₂ are shown in the Figures below.

The Cu_2SnSe_3 sample was found to decompose at 627°C through the loss of excess Se. Further decomposition occurs at $>770^\circ\text{C}$ due to the loss of SnSe.

SnSe_2 is shown in the bottom Figure. SnSe_2 decomposes through the loss of Se at 520°C and SnSe sublimation occurs at $\sim 750^\circ\text{C}$.

Table B-1: Summary of Decomposition Temperatures Measured by TGA

Sample type	Cu/ Zn+Sn	Zn / Sn	Growth Temp	Onset of Primary Decompos ition ($^\circ\text{C}$)	Mass Loss of Primary Peak	% Decomposition (% Loss Sn + Se)
Compaction powder	0.9	1.1	780°C	699	36.4%	79%
Compaction powder	0.9	1.2	780°C	683	36.2%	78%
Compaction powder	0.9	1.1	750°C	671	42.4%	92%
Thin film powder	0.9	1.2	500°C	637	46.6%	101%
Cu_2SnSe_3 ampoule powder	NA	NA	700°C (above melt)	627	8.4%	50%

CZTSe Decomposition Path

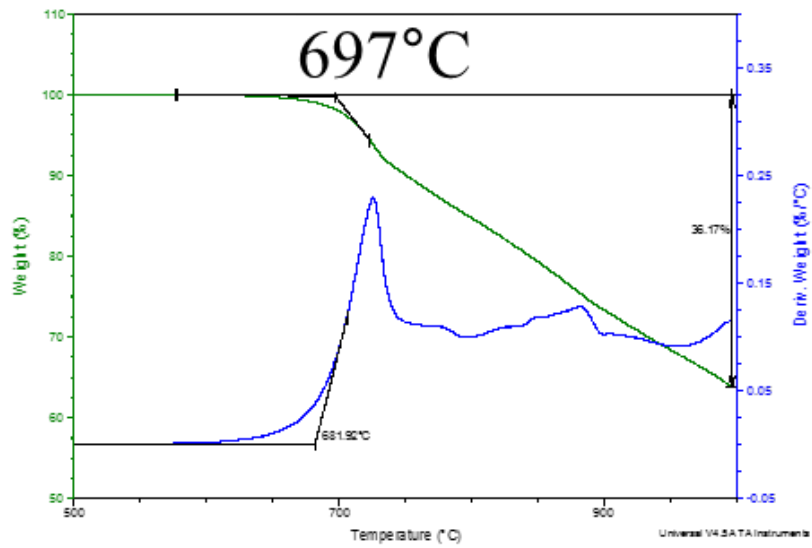
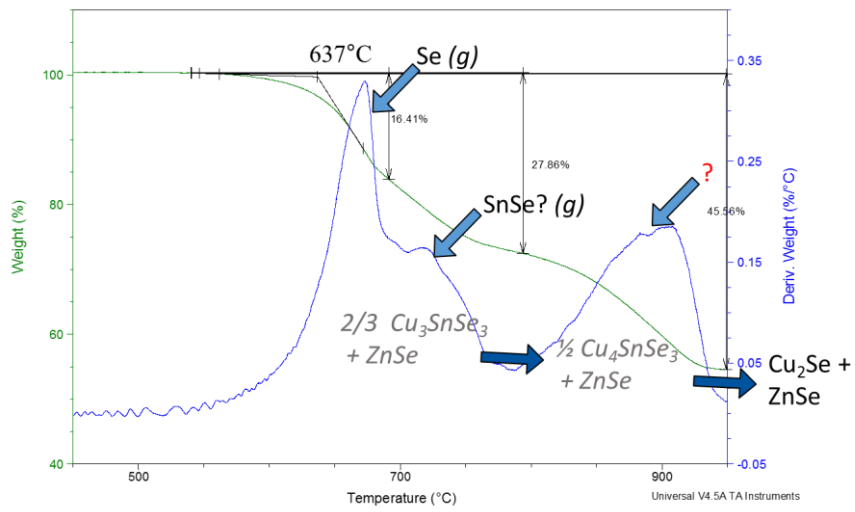


Figure B-1: TGA curve for CZTSe thin film and CZTSe powder

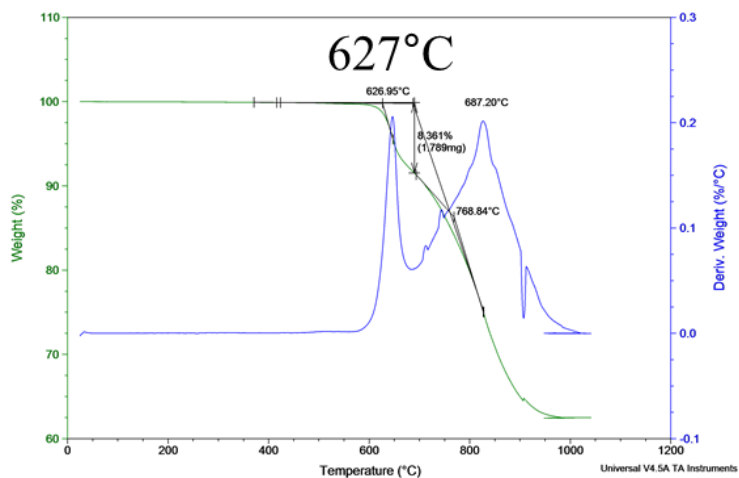
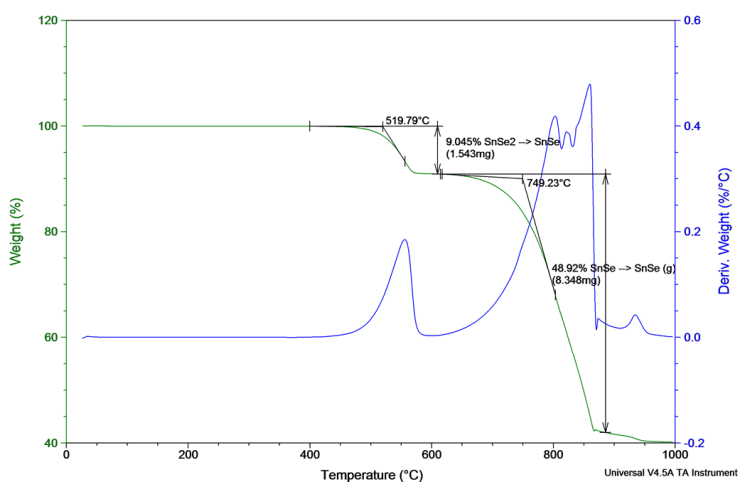


Figure B-2: TGA curve for Cu₂SnSe₃ powder



- SnSe₂ → SnSe + Se (*g*) at 520°C
- Possible SnSe evaporation at ~750°C

Figure B-3: TGA curve for SnSe₂ powder

B.2 Growth with ZnSe + Cu₂SnSe₃ Precursors

Link to original text Pg. 42.

Purchasing precursors from binary or ternary compounds (ZnSe, Cu₂SnSe₃, Cu₂Se, SnSe_x) were also investigated however finding acceptable precursors proved difficult. Commercial availability of the ternary CTSe was limited. For other binary precursors, purity was found to be significantly lower than elements (which were typically purchased at 6N). Phase purity was also problematic. Purchased samples of Cu₂Se and SnSe were found to contain significant phase impurities with large amounts of Cu_{1.8}Se and SnSe₂ detected by XRD. For ZnSe, significant absorption of water was found to be problematic, although additional dehydration steps are possible.

Consequently, precursors were made in-house via methods of sealed ampoule synthesis analogous to aforementioned methods described for CZTSe. Due to a high melting temperature, in excess of >1500°C, ZnSe was made below the melt at temperatures utilized for CZTSe formation. On the other hand, CTSe melts congruently at 687°C and was therefore made above the melt. For our purposes, the CTSe phase was made Cu-poor due to the target Cu/Sn ratios of less than 2 in the desired Cu-poor CZTSe.

CTSe and ZnSe precursor ampoules were grown at ~760°C, similar to the optimized CZTSe procedure. This temperature is not optimized for binary or ternary crystal growth (above CTSe melt and far below ZnSe melt), however the goal of ZnSe and CTSe growth was to provide a uniform powder as a precursor for CZTSe growth. Uniform powders were achieved over the course of ~ 1 week.

Appendix C

CHARACTERIZATION DETAILS

C.1 Summary of Characterization Equipment

1. Composition

- XRF – Oxford Instruments X-strata XRF was used. With x-ray tube energy of 45 kV and 0.8 mA with a 50 mil aperture for maximum signal. Separate application models and separate calibrations were performed for thin films and single crystals using samples measured by ICP as a standard. Measurement depth is ~200 microns depending on elemental transition. Therefore it measures composition evenly throughout a thin film, while also providing film thickness via total signal intensity. The application for films was calibrated with a Sn layer from the float glass as part of the model. For crystals the measurement was set to 1 mm which is equivalent to infinite thickness and should be accurate for samples far in excess of 200 microns. Separate calibrations had to be performed to account for matrix-related effects. Measurements were found to be much faster and smaller standard deviation compared to EDS. Ref. [169] provides a good review of the instrument technique. Standard error from counting statistics are shown in Figure C-1 for thin films.

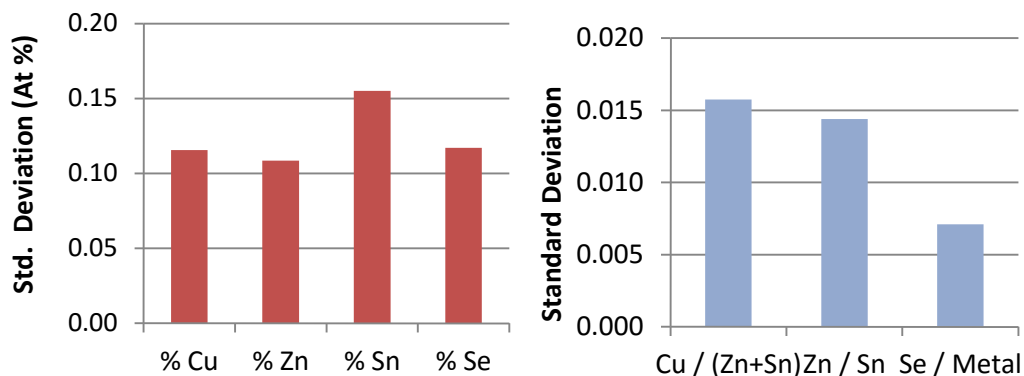


Figure C-1: Repeatability of XRF measurement for thin films over 200 seconds.

- EDS – An Oxford EDS detector with electron beam energies ranging from 7 - 20 keV were used depending on depth of information desired. The interaction depth of the electron beam varies from ~150 nm to 1.4 microns depending on elemental transition and electron beam energy. Interaction depth were modeled at different excitation energies as shown in xxx.
- XPS – was performed on Physical Electronics Model 5400, equipped with a multi-channel hemispherical analyzer, and a monochromatic Al K α x-ray excitation under the applied voltage of 20 kV. XPS lines for Cu 2p, Zn 2p, Sn 3d, and Se 3d were used for quantification with elemental corrections factor appropriate for the 54.7 angle between x-ray source and analyzer.

2. Phase analysis

- XRD – measurement were performed on both thin films and powders in symmetric Bragg-Bentano configuration. Cu k-alpha ration was used for the x-ray source operated at 35 kV and 20 mA. Quick scans were performed form 10-94 degrees 2theta with step of 0.04 and 2 second dwell, while fine

cans were performed over ~12 hrs with step of 0.01 and 5 second dwell. Powdered XRD was performed according to ASTM standards although the resulting pattern was found to change with air exposure and repeated measurement. Therefore samples were measured immediately after powdering. Detailed analysis of the effect of Cu-vacancies in modeled XRD patterns can be seen on Pg. 243.

- Laue – A Photonics Instruments digital Laue camera was used to obtain diffraction patterns confirming crystal orientation and monocrystalline nature. The X-ray tube was operated at 35 kV and 20 mA with a collimated beam diameter of approximately 1.5 mm, which is slightly smaller than crystal dimensions.
- Raman – Raman spectra were taken with a 532-nm laser at 0.3 mW and a 50- μm spot size to examine phases present on the surface. Raman spectra were calibrated using a Si wafer reference at 520 cm^{-1} . Interaction depth is limited to the top 150 nm for CZTSe.

3. Electrical

- Hall – performed in the Van der Pauw configuration on individual single crystals to obtain intra-grain mobilities and carrier concentrations. Silver paste was used to attach gold wires to the corners of a 4x3x1 mm crystal. For each crystal, three room temperature voltage measurements were made in the 10 to 15 kGauss range, using different applied currents to evaluate linearity.
- Seebeck – contacted individual crystals with home built hot probe setup at 225°C for carrier type and to extract Seebeck coefficient.

- Temp-Conductivity – Performed on bare crystals contacted by silver paste and gold wires. A Linkam cryostat and Keithley source were used for dark temperature-conductivity measurements in a 2-wire configuration.
- JV – Dark and light JV sweeps under AM1.5G were performed at both IBM and the IEC and both were calibrated to a silicon standard.
- V_{OC} -T – Performed on devices with a Linkam cryostat and Keithley source were used for dark and light measurements in 4-wire configuration with light intensity calibrated to the original J_{SC} of the device.
- EQE – Performed at both IBM and the IEC in the dark, and also in the light bias (at $\sim 50\%$ J_{SC}) and reverse bias. Measurements were performed out to 1400 nm and were calibrated to a certified Si-reference cell, however the calibration was not possible much beyond the Si E_g , ~ 1200 nm.

4. Defect

- Photoluminescence spectra – The PL spectra were measured using a Hamamatsu time-correlated single photon counting (TCSPC) system equipped with an InGaAs PMT detector cooled to -80°C . The detector response cut-off occurred at ~ 0.75 eV. The solid state laser excitation has a wavelength of 1064 nm (1.17 eV) although 532 nm (2.33 eV) was achieved by frequency doubling and was used as the default. The laser repetition rate was 15 kHz and had pulse duration of 1 ns. Intensity dependent measurements were performed using a neutral density filter wheel placed in front of the sample to obtain a range of excitation densities from 1.5×10^{-3} J/cm²/pulse to 6.4×10^{-5} J/cm²/pulse. A laser irradiation size was measured to be 170 microns at full laser fluence. Samples were mounted on a Cu heater

block and a liquid He cryostat was used for sample cooling. Small single crystal samples proved challenging to align due to the cryostat and blind alignment procedure. To avoid detector saturation, an adjustable aperture and neutral density filters were utilized in front of the detector. They are now standard procedure. Measurements of laser power were performed to find injection conditions. They are shown in section B2. Additional modeling of the effect of E_g are shown in in section B3.

- PL imaging – A separate room-temperature PL image setup with 808 nm laser (1.53 eV) and InGaAs camera were used to obtain comparisons of total PL intensity. Four 30W lasers with diffusers were used to evenly illuminate the samples.

C.2 Photoluminescence Spectra Power Calibrations

Link back to main text Pg. 60: Photoluminescence Background

Measurements of laser power were performed to find injection conditions when operated at the default 532 nm and 1064 nm. 90% absorption depth is 140 nm for the 532 nm excitation and ~680 nm for 1064 nm operation.

The laser had not been previously operated at 1064 nm and therefore a number modifications and calibrations were performed to allow consistent operation. Two 1100 nm long-pass filters were found to be needed to prevent 1064nm laser reflections and were installed right in front of the detector. Additional strong reflections were found at 1330 nm and were blocked by an 1100 short-pass filter installed in front of the laser (before the sample). The measured laser power numbers are shown in chart below.

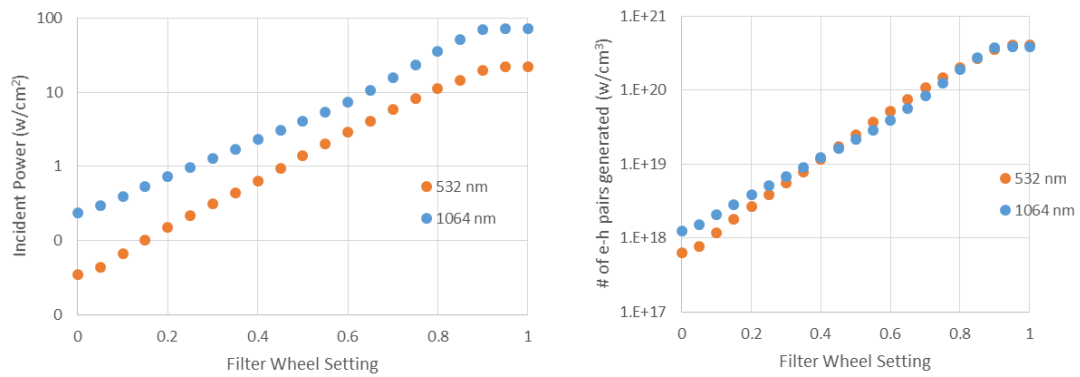


Figure C-2: Power calibration for PL spectra tool. Incident laser power and calculated max e-h pair density as a function of neutral density filter wheel position for PL spectra.

C.3 Photoluminescence Imaging

Link back to main text Pg. 60: Photoluminescence Background

A separate room-temperature PL image setup with an 808 nm laser (1.53 eV) and InGaAs camera were used to obtain comparisons of total PL intensity. Four 30W lasers with diffusers were used to evenly illuminate the samples.

Injection conditions had not been previously characterized so light intensities were characterized with a power meter as a function of distance and laser power. At full laser power using assumptions below, an e-h pair density of $\sim 3 \times 10^{16}$ was calculated.

Assumptions:

- Laser + diffuser 3 inches from the sample and at 45 degree angle
- Laser operated at 30 W (15 W operation used in much of the work is $\sim 1/2$ carrier e-h pairs)
- Carrier lifetimes of 10ns (this is upper limit)

- Light evenly absorbed in top 560 nm (~ point of 90% absorption for 808 nm)
- No other electronic losses (every photon creates a e-h pair)

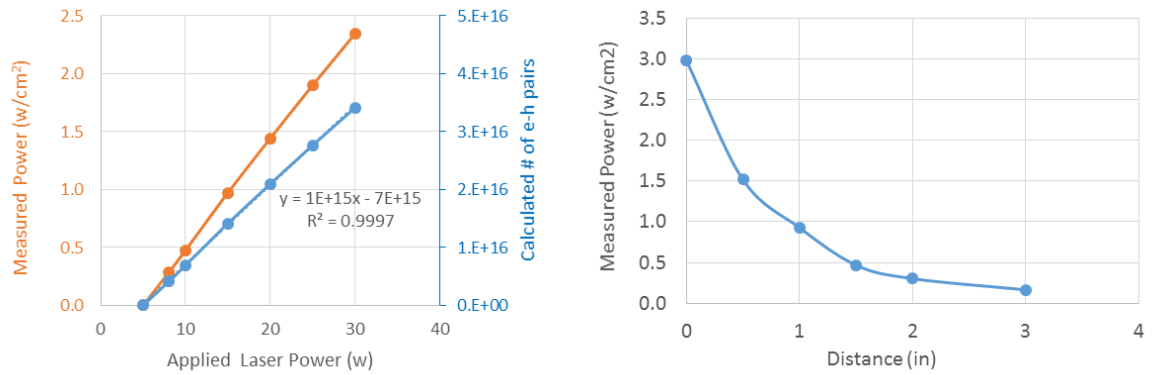


Figure C-3: Power calibrations for PL image tool. Measured power as a function of applied power for 1 laser at zero distance, and calculated e-h pairs for typical measurement (all 4 lasers, 45 degrees, 3 inches away)

Appendix D

CALCULATION OF EQUILBRIUM DEFECT CONCENTRATIONS FOR QUENCH / SLOW-COOL CZTSe

Link back to main text Section: Temperature Equilibria, Pg. 95

Concentration of point defects can be predicted from thermodynamics by Equation 4:

$$[Defect] = N_{sites} g e^{\left(\frac{-\Delta H_{defect}}{KT}\right)} \quad \text{Equation 4}$$

Where N_{sites} is the number of potential sites for the defect, g is the degeneracy factor which is related to the number of electronic configurations the defect can take and ΔH_{defect} is the formation energy of the defect. For Figure 1, the ΔH_{defect} values from Chen et al. were used, taken from the edge of the CZTSe phase diagram bordering ZnSe and SnSe. This should be similar to the area for efficient devices. However, four key assumptions are made in the graph below. First, vibrational entropy is ignored. Second, samples must be at equilibrium. Third, ΔH_{defect} is calculated with a fixed fermi-level position at the valence band edge. Lastly, and most importantly, ΔH_{defect} does not change with defect concentration which means defects are isolated and do not interact (beyond the listed complexes). Each of these assumptions will result in an understated defect concentration which serves as a lower bound.

An example of this understatement can be seen at 200°C where $[Cu_{Zn}+Zn_{Cu}]$ defect pair is calculated to have a concentration of $\sim 1 \times 10^{20} / \text{cm}^3$ although we expect a

random occupation which is equivalent to $2.75 \times 10^{22} / \text{cm}^3$. This may largely be explained by further defect clustering beyond the predicted charged balanced complex. One first principle calculations suggested the ΔH_{defect} of a 2nd $[\text{Cu}_{\text{Zn}} + \text{Zn}_{\text{Cu}}]$ arranged appropriately in a supercell will have $1/4$ of the cost of the first defect. Similarly, $[\text{V}_{\text{Cu}} + \text{Zn}_{\text{Cu}}]$ is suggested to interact and reduce energy costs for $[\text{Cu}_{\text{Zn}} + \text{Zn}_{\text{Cu}}]$ complexes.

Despite the understatement of defect concentrations, the calculation can be provide insight into the changing point defect populations as a function of temperature as well as the effects of quenching.

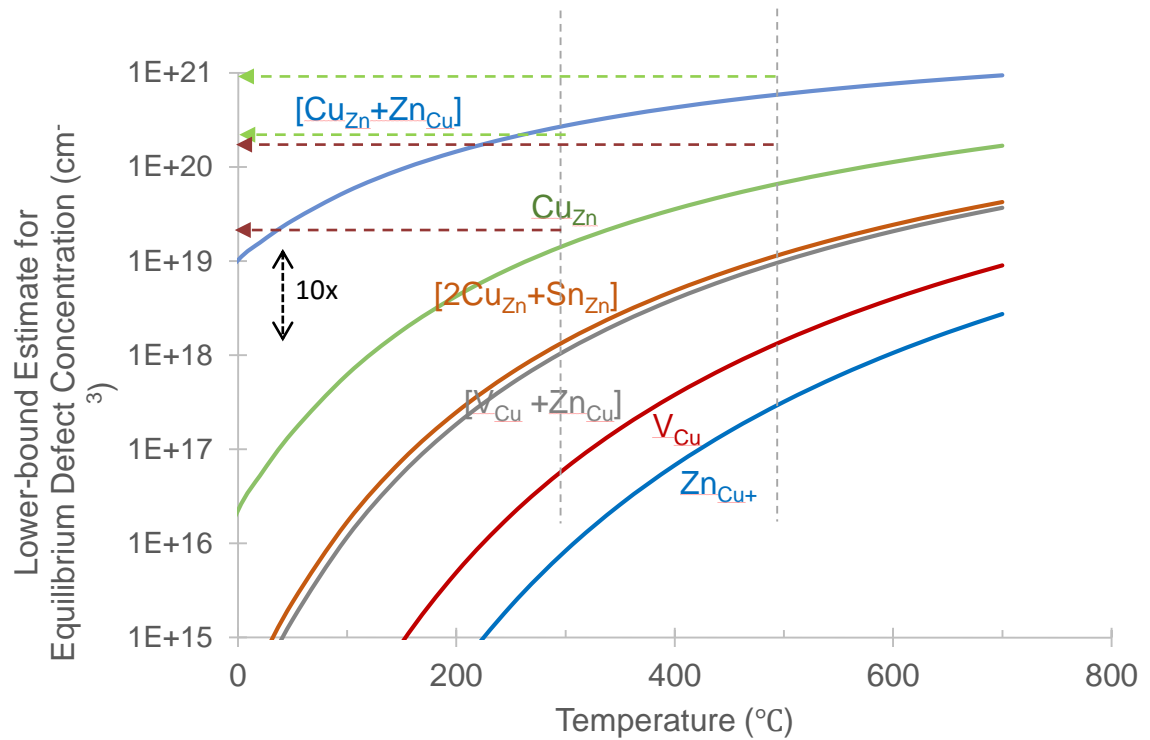


Figure D-1: Calculated equilibrium defect concentrations for non-interacting defects with assumption listed above.

Quenched crystals would expect to approximately freeze the defect concentrations of the quench temperature while slow-cooled crystals will reduce defect concentrations until kinetics limit further defect motion. As noted in the manuscript, the deep defect of highest predicted concentration in this system, $[2\text{Cu}_{\text{Zn}}+\text{Sn}_{\text{Zn}}]$, is predicted to be reduced by a factor of 10 when quenching at 300°C compared to formation temperatures of $\sim 500^{\circ}\text{C}$. Further low temperature annealing below 300°C may provide additional means of reducing this deep defect concentration –although limited by kinetics as well as stoichiometry.

Additional insights, like high ratio of charged balanced defect complexes compared to isolated defects can also be seen in the calculation. In addition, the p-type nature of conduction, from high levels of Cu_{Zn} and much lower levels of Zn_{Cu} can also be clearly seen. A more detailed calculation should self-consistently account for the fermi-level changes as a function of temperature and defect concentration. However moving the fermi-level away from the valence band edge will exaggerate the gap between predicted Cu_{Zn} and Zn_{Cu} by increasing the acceptor defect concentrations $[\text{Cu}_{\text{Zn}}]$, while decreasing donors $[\text{Zn}_{\text{Cu}}]$. Balanced defect complexes are not predicted to change.

Appendix E

MODELING PL EMISSION

E.1 Effects of E_g -Fluctuations on PL

Link back to main text Pg. 60: Photoluminescence Background

The effects of bandgap fluctuations on PL were modeled following the work of Matthies [117]. The model assumes a Gaussian distribution of bandgaps with standard deviation σ , laterally distributed in the film.

A second assumption is that *length-scale fluctuations in E_g is small* relative to diffusion length, therefore carrier localization into the smaller bandgaps will occur. The opposite case, of fluctuation on a large length-scale relative to diffusion length is rather trivial to model and involves simply a geometric average of PL from the distribution of bandgaps present. In the case of long-scale fluctuations or very small diffusion lengths, the peak energy of PL emission does not change, although the PL peak is similarly broadened.

The equation for emission with bandgap fluctuations can be seen here:

$$\phi_1 = \frac{\pi}{h^3 * c^2} * \text{Erfc}\left[\frac{\bar{E} - \epsilon}{\sqrt{2} * \sigma}\right] * \epsilon^2 * \text{Exp}\left[\frac{-(\epsilon - \mu)}{kb * T}\right];$$

ϕ_1 is the emission, ϵ is energy $E = \sigma = \mu$ is quasi fermi-level splitting and T =temperature The

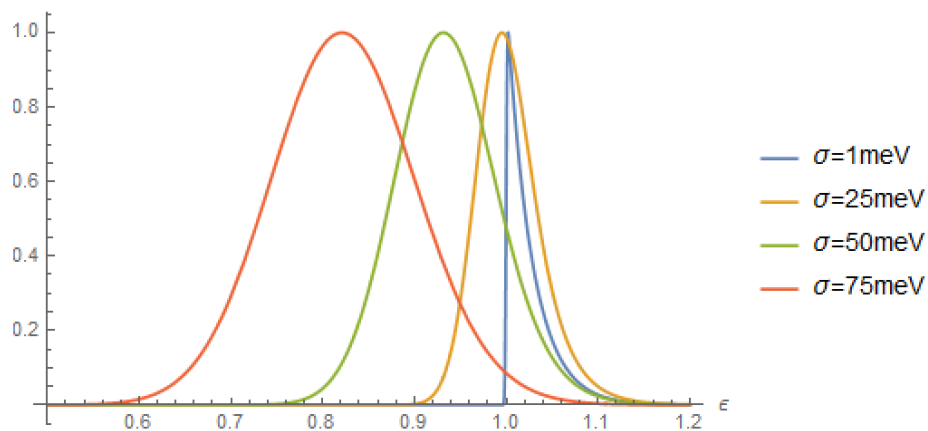


Figure D-2: Modeled PL spectra of a semiconductor with $E_g = 1$ eV such as CZTSe with varying degrees of bandgap fluctuations at room temperature

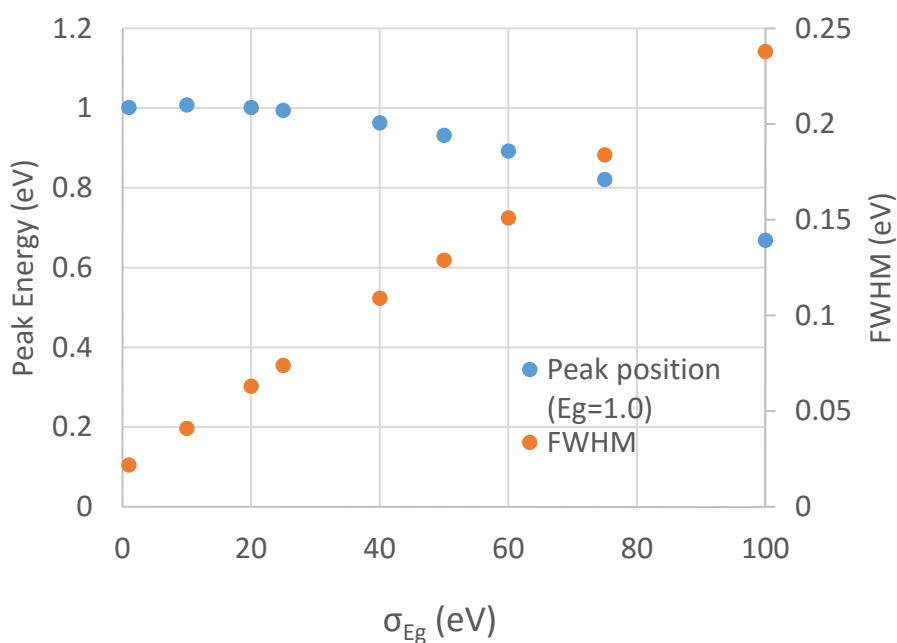


Figure D-3: Calculated PL peak position and FWHM for a semiconductor of 1 eV such as CZTSe with varying degrees of E_g fluctuations at room temperature

E.1.1 Code for Modeling Bandgap Fluctuations:

```

h = 4.1357*10-15 ; (* eVs *)
c = 3*108; (* m/s *)
' = 1 ; (* eV *)
a = 8.617*10-5; (*eV K-1 *)
T = 300; (* K *)

μ = 0.9; (* eV *)
σ = 0.001;

μ1 = 0.9; (* eV *)
σ1 = 0.025;

μ2 = 0.88; (* eV *)
σ2 = 0.05;

μ3 = 0.8; (* eV *)
σ3 = 0.075;

φ1 = π/(h3*c2)*Erfc[(ε-μ)/(σ*a)]*ε2*Exp[-(ε-μ)/(a*T)];
φ1n=φ1/MaxValue[φ1,ε>0.5,ε];
φ2 = π/(h3*c2)*Erfc[(ε-μ1)/(σ1*a)]*ε2*Exp[-(ε-μ1)/(a*T)];
φ2n=φ2/MaxValue[φ2,ε>0.5,ε];
φ3 = π/(h3*c2)*Erfc[(ε-μ2)/(σ2*a)]*ε2*Exp[-(ε-μ2)/(a*T)];
φ3n=φ3/MaxValue[φ3,ε>0.5,ε];
φ4 = π/(h3*c2)*Erfc[(ε-μ3)/(σ3*a)]*ε2*Exp[-(ε-μ3)/(a*T)];
φ4n=φ4/MaxValue[φ4,ε>0.5,ε];

LHS1=ε/.FindRoot[φ1==MaxValue[φ1,ε>0.5,ε]/2,{ε,1.0001}];
RHS1=ε/.FindRoot[φ1==MaxValue[φ1,ε>0.5,ε]/2,{ε,1.2}];
FWHM1=RHS1-LHS1;
max1=FindMaximum[φ1,{ε,1.03,0.7,1.1}];

```

```

Print[" $\phi$ 1: {Y-max, x-max, FWHM}"];
{max1,FWHM1}

LHS2= $\epsilon$ /.FindRoot[ $\phi$ 2==MaxValue[ $\phi$ 2, $\epsilon$ >0.5, $\epsilon$ ]/2,{ $\epsilon$ ,0.9}]
RHS2= $\epsilon$ /.FindRoot[ $\phi$ 2==MaxValue[ $\phi$ 2, $\epsilon$ >0.5, $\epsilon$ ]/2,{ $\epsilon$ ,1.1}]
FWHM2=RHS2-LHS2;
max2=FindMaximum[ $\phi$ 2,{ $\epsilon$ ,1.03,0.7,1.1}];
Print[" $\phi$ 2: {Y-max, x-max, FWHM}"];
{max2,FWHM2}

LHS3= $\epsilon$ /.FindRoot[ $\phi$ 3==MaxValue[ $\phi$ 3, $\epsilon$ >0.5, $\epsilon$ ]/2,{ $\epsilon$ ,0.6}]
RHS3= $\epsilon$ /.FindRoot[ $\phi$ 3==MaxValue[ $\phi$ 3, $\epsilon$ >0.5, $\epsilon$ ]/2,{ $\epsilon$ ,1.0}]
FWHM3=RHS3-LHS3;
max3=FindMaximum[ $\phi$ 3,{ $\epsilon$ ,1.03,0.6,1.1}];
Print[" $\phi$ 3: {Y-max, x-max, FWHM}"];
{max3,FWHM3}

LHS4= $\epsilon$ /.FindRoot[ $\phi$ 4==MaxValue[ $\phi$ 4, $\epsilon$ >0.5, $\epsilon$ ]/2,{ $\epsilon$ ,0.55}]
;
RHS4= $\epsilon$ /.FindRoot[ $\phi$ 4==MaxValue[ $\phi$ 4, $\epsilon$ >0.5, $\epsilon$ ]/2,{ $\epsilon$ ,0.8}];
FWHM4=RHS4-LHS4;
max4=FindMaximum[ $\phi$ 4,{ $\epsilon$ ,1.03,0.6,1.1}];
Print[" $\phi$ 4: {Y-max, x-max, FWHM}"];
{max4,FWHM4}

Plot[{ $\phi$ 1n, $\phi$ 2n, $\phi$ 3n, $\phi$ 4n},{ $\epsilon$ ,0.5,1.2},PlotRange-
>Full,AxesLabel->Automatic,PlotLegends-
>{" $\sigma$ =1meV"," $\sigma$ =25meV"," $\sigma$ =50meV"," $\sigma$ =75meV"}]
Plot[{ $\phi$ 4n},{ $\epsilon$ ,0.6,1.2},PlotRange->Full,AxesLabel-
>{"Energy (eV)"} ]

Plot[{{ $\phi$ 3},{ $\epsilon$ ,0.6,1.2},AxesLabel->Automatic]

```

E.2 Other PL Models

Many aspects of PL were examined, but were not able to be included in this work. Some of these models are shown below.

E.2.1 Change in PL Intensity with Temperature for Defect-related Transitions

PL emission from defects is typically quenched with increasing temperature due to thermalization out of the defect. From measuring PL vs. temperature, an activation energy can be extracted. The PL intensity is graphed as a function of temperature for defects of different energy levels below. Equation from textbook: Wide Bandgap Photovoltaics [51]

$$I_{pldefect} = \frac{1}{1 + a * e^{\frac{-E_a}{k_b * x_1}}}$$

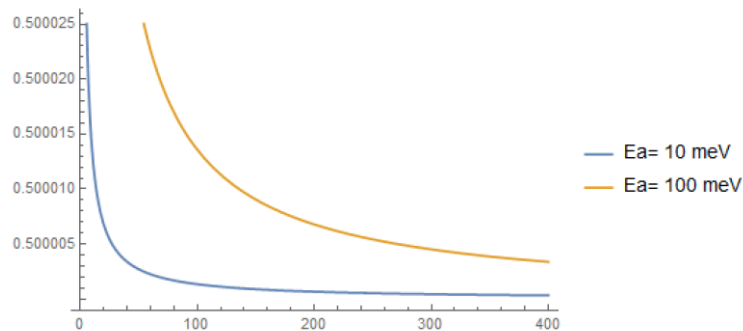


Figure D-4: PL intensity quenching for defect related PL emission as a function of temperature.

E.2.2 PL Intensity for Band-Band Emission as a Function of Temperature

PL intensity for band-band emission is shown below for various temperatures. At higher temperatures PL intensity increases, the PL peak slightly increases as shown in the table (assuming fixed E_g), and the tail at high energy increases significantly. In

reality, competing non-radiative recombination processes result in generally lower PL intensity at higher temperatures. This is due to temperature dependence of defect cross-section.

Equation from textbook: Wide Bandgap Photovoltaics [51]

$$I_{pl} = (E_n - E_g)^{\frac{1}{2}} e^{\frac{-(E_n - E_g)}{k_b T}};$$

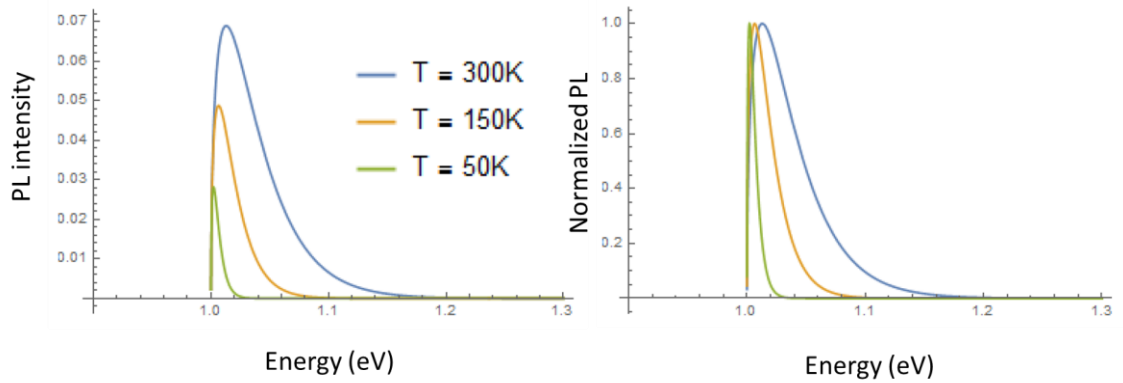


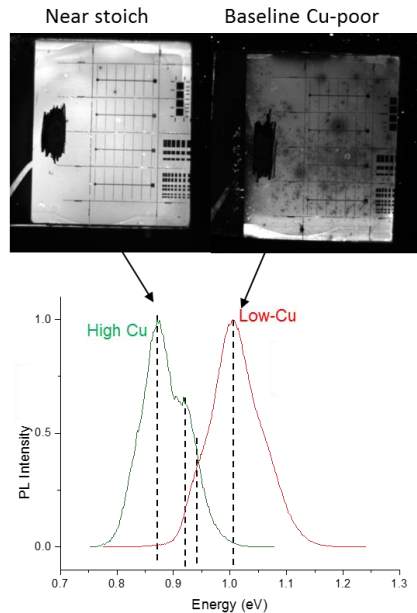
Figure D-5: PL spectra and shape as a function of temperature for band-band emission in ideal semiconductor with $E_g = 1$ eV

Table D-1: Modeled PL peak energy and PL rate from band to band emission

Temp (K)	Peak Energy (eV)	Normalized PL Rate
400	1.0172	115%
300	1.0129	100%
200	1.0086	82%
100	1.0043	58%
50	1.0022	41%
5	1.0002	13%

E.3 PL Intensities for Cu-poor and Near-Stoichiometric Thin Films

Link back to main text Pg. 133



Unlike the single crystal results, PL image intensity obtained with an 808 nm laser was 2x higher for near stoichiometric samples. This is explained by the presence of the CdS junction. Cu-poor samples have lower carrier concentrations, and therefore longer depletion regions. This means the PL spectra will be quenched to a larger extent by carrier separation which occurs for carriers absorbing in or near the depletion region.

One option to reduce the effects of carrier separation on PL is to increase power. Since PL probability is related to the product of holes and electrons, $n \cdot p$, (which is intensity squared), increasing laser intensity will therefore increase the radiative component of recombination more than drift from the space charge region [170].

Appendix F

MODELING XRD OF AZTSe

F.1 Crystal Structure of AZTSe

Link back to main text Pg. 150

One of the largest motivations for AZTSe is a potential reduction in bandtailing due to reduced cation disorder. The larger differential in atomic radius from Ag and Zn cations (atomic radius of Cu=145 pm, Zn=142 pm, while Ag= 165 pm), gives an intuitive explanation for why less Ag-Zn antisites defects would be expected, however this has not been confirmed. The size of these bandtails can be probed by both emission and absorption measurements, but direct characterization of Ag-Zn anti-sites quantities would be desirable. XRD provides one method to examine atomic locations, occupancy and lattice defects. As was discussed for CZTSe, XRD can be used to detect a change in lattice constant for the c-axis which occurs with high quantities of Cu-Zn defects but even random Cu-Zn ordering provides minimal changes in absolute intensity of XRD pattern due to similar scattering factor for Cu and Zn. For AZTSe, the difference in scattering factor between Ag and Zn is somewhat larger (incoming x-rays are scattered by electrons and Ag has an additional 17 electrons). This means changes in cation ordering, and the presence or absence of Ag-Zn defects may be able to be determined through XRD. In addition, the related challenges of determining stannite vs. kesterite crystal structure may be resolvable in the AZTSe system. Very few references exists on AZTSe crystal structure and defects but both first principle calculations and powder

refinement suggest kesterite structure is preferred [150], [171]. The cation ordering in AZTSe has not previously been reported.

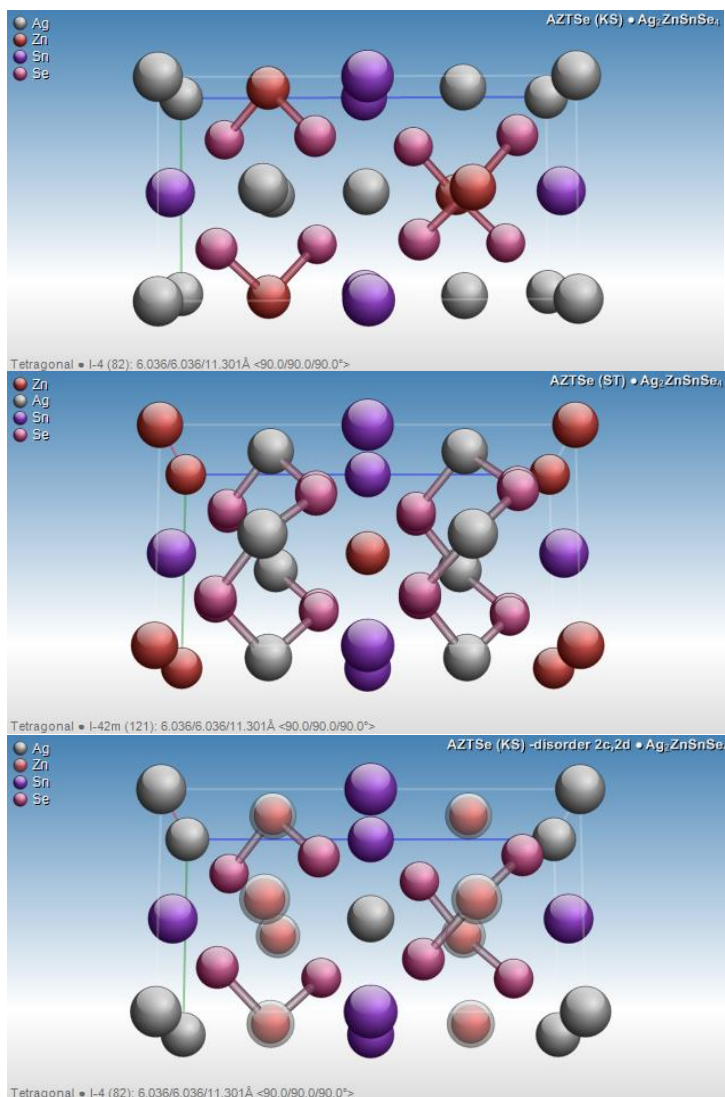


Figure F-1: Atomic models of AZTSe. Top to bottom: kesterite, stannite, and disordered kesterite (random occupancy of 2a and 2c site)

Theoretical XRD models were calculated for AZTSe as a function of crystal structure and cation orderings in order to provide basis for future Rietveld refinements,

as well as to determine what changes can be concluded when qualitatively examining XRD patterns for thin films. The latter point is critical for the larger community, as the vast majority of researchers often lack the tools or time for proper crystal structure refinement.

Lattice parameters and anion displacement²⁴ from Gong et al. were used for the basis of theoretical patterns. Changes in lattice parameters will only result in changes in peak position which doesn't affect the basis of the comparison below. It is also likely that changes from kesterite to stannite, or the presence of large number of Ag-Zn antisites may additionally change lattice parameters as was shown for CZTSe. However this mechanism is harder to predict quantitatively on a theoretical basis and consequently the worst case hardest case for differentiation of patterns is assumed with no change in lattice parameter based on cation arrangement.

F.1.1 Separating Stannite and Kesterite in AZTSe by XRD

The theoretical models for stannite and kesterite are plotted in Figure F-. Standard instrument broadening (FWHM=0.1deg) and peaks from Cu-k-alpha2 peaks were applied to simulate expected XRD measurements. In a powder the intensity ratios between peaks should be equal to the modeled pattern although there is the potential for changes of intensity due to non-random powder orientation, instrumental effects and sample thin-ness. These effects can be negated with proper powder preparation and by

²⁴ Changes in anion displacement were also varied from the literature values ($\mu_x = 0.251$, $\mu_y = 0.23$, $\mu_z = 0.128$), ranging from no displacement to anion values found for CZTSe and mainly small changes in intensity were noted. The largest change was noted in the 101 peak with an increase of up to 0.7% absolute.

examining peaks at similar diffraction angle. Differences in intensity can be seen throughout the pattern (plotted in blue) with up to 2.4% absolute change in intensity for the (204) peak however this change will likely not be detectable in qualitative examination since it represents a 3% relative intensity change in a large peak. The best peaks for identifying stannite and kesterite can be found at low angles. The lower half of Figure F- highlights the lower angle peaks of interest. The (101), (200), and (202) peaks represent the best chance for determining stannite or kesterite crystal structure. For powders, 3 key criteria that can be qualitatively examined:

1. $I(002) > 2x I(101)$ for kesterite but $I(002) < I(101)$ for kesterite.
2. $I(200)$ increases by $\sim 2x$ for stannite
3. $I(202)$ does not appear for stannite.

The 3rd point is likely the most critical for separation of crystal structures. The presence of a peak at 33.6 (202) uniquely identifies the kesterite phase. Thin films can be more difficult to identify due to the potential for preferred orientation however the presence of the (202) peak will still identify kesterite structure in a thin film. The absence of this peak however doesn't necessarily rule out kesterite. The intensity changes in points 1 and 2 can be helpful in the identification of stannite can likely be helpful in separation of kesterite an stannite thin films although they cannot prove either crystal structure due to the potential for preferential orientation on the chosen peaks.

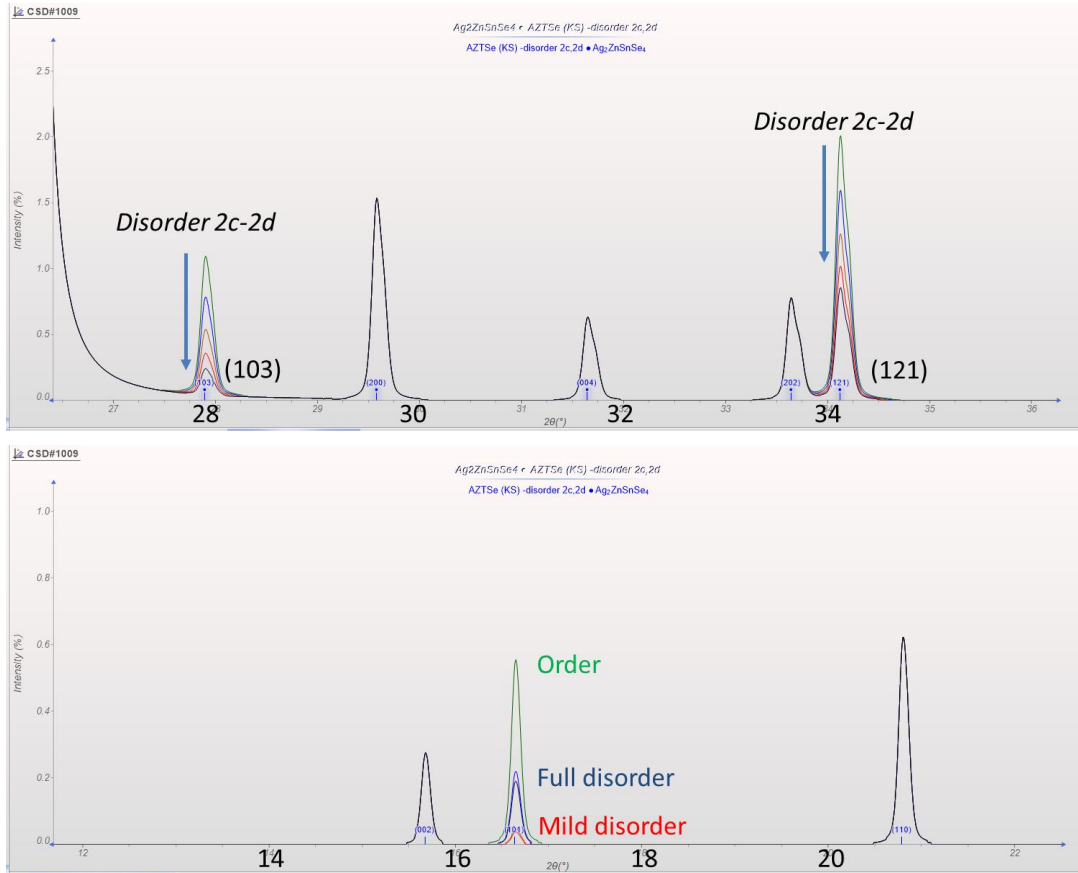


Figure F-3: Modeled XRD pattern for AZTSe as a function of Ag-Zn order. Bottom panels highlights the critical regions of differentiation

Ag-Zn anti-sites provide only small changes throughout the pattern similar to the situation for kesterite vs. stannite. The largest changes can be seen in the (101), (103), and (121) peaks. Three key areas of differentiation are:

1. The 103 peak almost disappears from 1.2% absolute intensity for ordered to ~0.2% absolute intensity for fully disordered –relative to nearby [200] peak which is fixed.

2. The 121 peak decreases from ~2.1% to ~0.9% absolute for the ordered and disordered case respectively while neighboring 202 peak is fixed.
3. The 101 peak reduces significantly with mild amounts of disorder from 0.6% to less than .06% between 25-37.5% antisites occupancy and then increases to 0.25% for full disorder (50% antisites occupancy) which can be compared to neighboring 002 peak.

Despite large changes in relative intensity, the absolute intensity changes are small and therefore would require detailed fine scans with long dwell times in the noted areas to quantify disorder. As previously noted, the clues above may provide some qualitative insight for thin films, the potential for orientation complicates analysis and makes explicit determination of ordering unlikely.

It may be expected that additional changes in lattice expansion may occur with increasing antisites density which would add to the ability to distinguish between ordered and disordered AZTSe phases (as well as kesterite vs. stannite).

To determine both crystal structure and cation ordering in the AZTSe system by peak intensity requires relatively fine XRD scans and more conclusive evidence can be drawn with non-oriented powders. Despite the challenges, the XRD analysis is much improved compared to the case of Cu-Zn ordering in CZTSe which has almost zero change in XRD intensity. The same analysis was performed for CZTSe and the differences in peak height are hard to see graphically. The largest change was less than 0.1% absolute intensity for fully disordered Cu-Zn lattice on 2a-2c sites. Similarly, the largest change for kesterite – stannite (assuming no change in anion displacement) is 0.24% absolute intensity. In the best cases this results in ~20% relative change in the height of very minor peaks which makes definitive determination via XRD unlikely.

Appendix G

MODELING XRD OF V_{Cu} IN CZTSe

G.1 Cu-vacancies in CZTSe Determined by XRD

A key feature in CZTSe is the Cu-poor nature of highly efficient solar cells. Champion device efficiencies have typically had Cu/Zn+Sn ratios of approximately 0.8 which is equivalent to ~20% deficiency in Cu. This deficiency is likely to lead to high numbers of V_{Cu} . Despite strong deviations from stoichiometry, few reports have provided a direct measurement of vacancies and anti-site defects. Limited neutron diffraction data has provided the backbone for most assumptions about the presence and structural location of defects. The lack of XRD data is likely due to the challenging phase purity combined with the difficulties separating Cu and Zn due to similar scattering factors as was mentioned above. Despite the challenges, the main stoichiometric feature of CZTSe, strong Cu-poor nature, can in fact be examined by XRD. To examine this CZTSe patterns were simulated as a function of V_{Cu} concentration and structural position.

Cu in the ordered kesterite CZTSe structure exists on two separate atomic sites. The Cu-Sn plane is the 2a site, while the Cu-Zn plane is the 2c site (analogous to AZTSe seen in Figure F-). Two separate series of models were created. In the first, Figure G-, XRD patterns were modeled with increasing V_{Cu} from 0-30%, split evenly on the 2a and 2c sites.

In the second series (Figure G-), the location of the V_{Cu} was varied from the 2a, 2c, or split evenly on both sites for a fixed $V_{\text{Cu}}=20\%$ and compared to a reference

stoichiometric pattern. $V_{Cu}=20\%$ was chosen since this is near the highly Cu-deficient composition of champion cells.

Certain assumptions have to be made for comparison sake. Lattice size was held constant although it is likely that there would be decrease in lattice size with increasing V_{Cu} . This fact may aid separation between patterns further. Also the anti-site substitutions were ignored. It is likely that the Cu deficiency is made up of a combination of V_{Cu} as well as Zn_{Cu} and Sn_{Cu} . As discussed, Zn_{Cu} will be equivalent to reductions in V_{Cu} (since Zn is essentially indistinguishable from Cu in XRD). Sn_{Cu} will occur in lower numbers than Zn_{Cu} due to chosen Zn rich composition and large changes in atomic size and valence between Sn and Cu. For the above reasons, Sn_{Cu} were not modeled in the comparisons below.

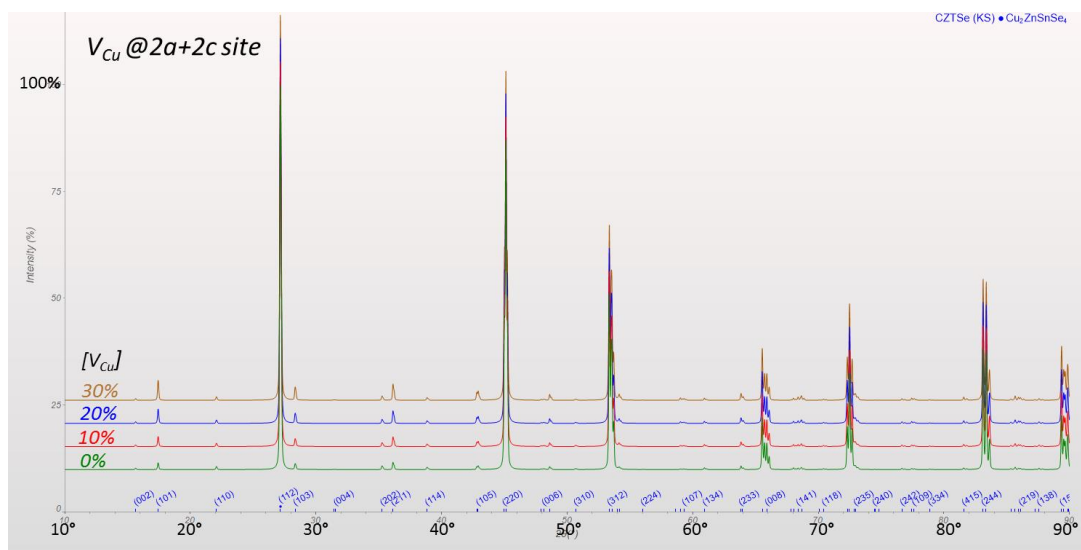


Figure G-1: Modeled XRD pattern for CZTSe as function of V_{Cu} concentration located equally at 2a and 2c sites.

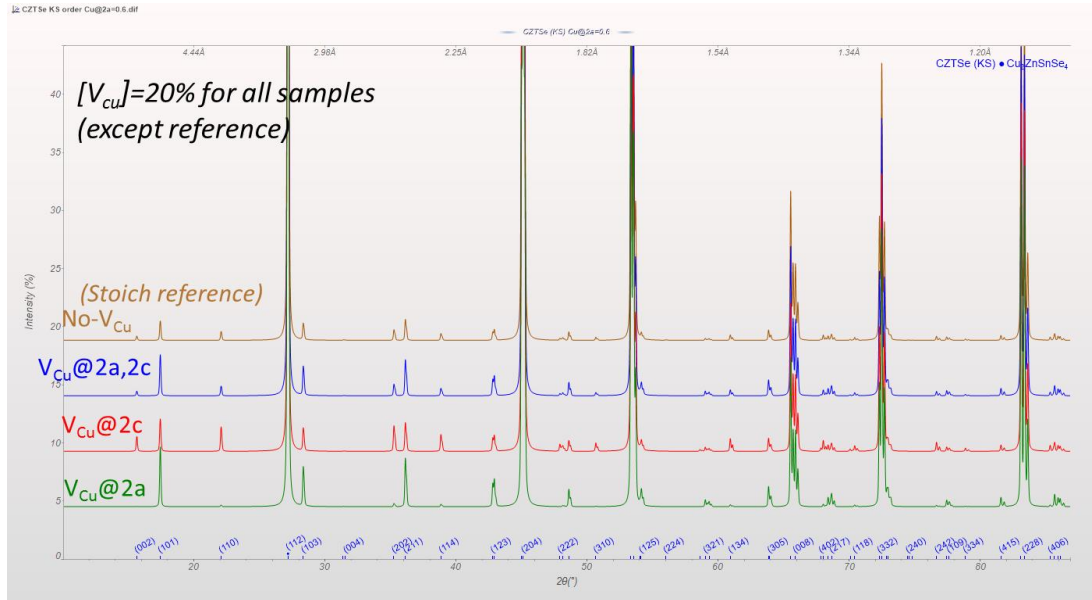


Figure G-2: Modeled XRD pattern for CZTSe as function of V_{Cu} position for fixed 20% V_{Cu}

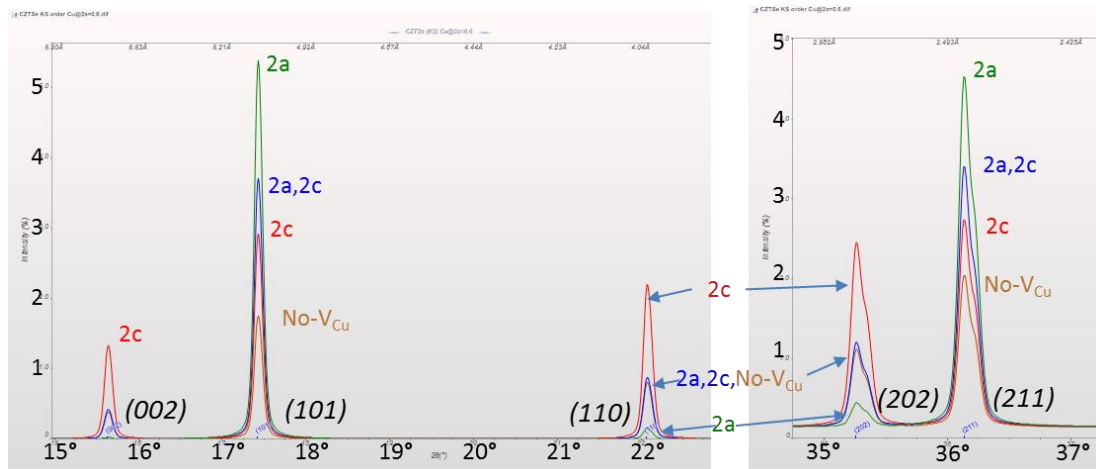


Figure G-3: Key peak changes for modeled XRD pattern for CZTSe as function of V_{Cu} position for fixed 20% V_{Cu}

Similar to the situation for determining the cation location in AZTSe, the best peaks for separation of V_{Cu} location are at low angles. The (101) peak is the largest change in intensity and increases strongly for increasing quantities of V_{Cu} (Figure G-). The location of the V_{Cu} also strongly affects the (101) peak (Figure **Error! Reference source not found.**). The $V_{Cu}@2a$ provides the largest increase in (101) intensity while neighboring peaks like the (002) have the opposite trend with decreasing intensity with $V_{Cu}@2a$ and increasing intensity at $V_{Cu}@2c$. The ratios of these neighboring peaks should provide a method for determining locations of V_{Cu} in the kesterite structure. These models would best be used as alternate structures in a Rietveld refinement.

It is worth re-emphasizing that typical samples with $0.8 = Cu/Zn+Sn$ likely do not translate to modeled 20% V_{Cu} concentration as is expected from the 20% Cu deficiency. Increasing Zn_{Cu} and to a smaller extent other compensating antisites likely reduce the quantity of V_{Cu} . The presented models therefore represent an upper bound for changes in XRD pattern and the analysis might be improved by pairing with accurate measurements of composition.

Appendix H

THIN FILM DEPOSITION

Significant efforts were undertaken to improve evaporation repeatability and uniformity through modified source design and modified substrate heating. These are discussed below.

H.1 Zn Source Design and Effusion Modeling

Link back to main text Pg. 178

Zn sublimates easily and required effusion rates are achieved at $\sim 320^{\circ}\text{C}$, which is 100°C below the melt. Zn nuggets are loaded as source material and as deposition progresses, the nugget surface area changes through both shrinkage and sintering. This causes drift in the effusion rate and curtails repeatability and the ability to do controlled experiments.

In order to improve effusion repeatability, the Zn source design was modified to limit effusion through a rate controlling nozzle with effusion rates calculated by an effusion model. The new source design as well as the predicted effusion rate as a function of rate-restriction nozzle radius are shown below. The Mathematica code for the effusion model is given below for future reference.

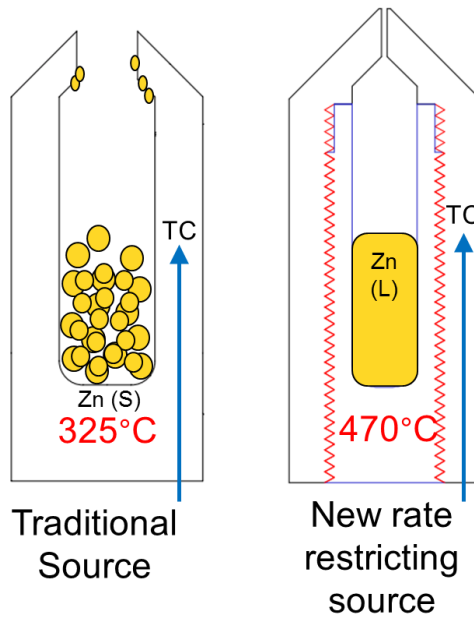


Figure H-1: Source design for Zn bottle and new modification to allow operation above Zn melt

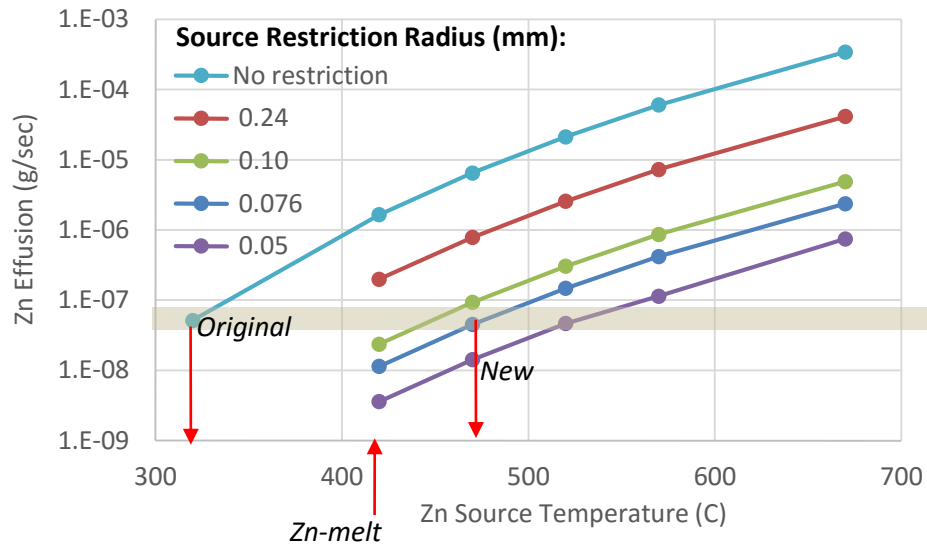


Figure H-2: Modeled Zn effusion rates for normal source and proposed rate-restricting source designs

```
(* Effusion and Vapor pressure calculations Cu, Zn and Sn
(liquid state) *)
```

```
(* CONSTANTS *)
MCu=63.546*^-3;
MZn=65.38*^-3;
MSn=118.71*^-3;
MSe=78.96*^-3;
R= 8.314; (* gas constant [J/K*mol]*)
P2=1*^-5*133; (* pressure [Pa] outside of source nozzle
(i.e. bell jar) during operation *)
```

```
(*Source geometry Constants*)
rNaF=0.0762*^-2; (* [m] --> .052in (originally .03 in,
but drilled out *)
rSe=0.23876*^-2; (* [m] -->.094in *)
rReg=.40386*^-2; (* [m] rad = .159in *)
lNaF=.635*^-2; (* [m] --> *)
lSe=1.03*^-2; (* .406in height *)
lReg=.635*^-2; (* .25 in height *)
SANAf=.5857*^-4; (* [(m^2)] --> .17in rad*)
SASe=2.850*^-4; (* [(m^2)] --> .375in rad*)
SAReg=1.267*^-4; (* [(m^2)] -->.25in rad *)
```

ZINC

```
(* Source material *)
M= MZn; (*molar mass (Zn) *)
Tc= 470; (*temperature of element evap [C] *)
T=Tc+273
```

```
"Vapor pressure of Zn(l) [Pa] @T[°C]"
ee=-6.676;
ff=-1.27;
gg=9.564;
Psat= 10^((ee*1000/T)+ff*Log[10,T]+gg)*750.0675*133 (*
[Pa] calculation of vapor pressure based on temp *)
```

```
(* Source Geometry *)
l= lNaF; (* height of source nozzle [m] (from top
interior of bottle), .25in *)
r=rNaF; (* radius of source nozzle [m], dia=.03in-->
.0762cm *)
SAmelt = SANAf; (* surface area of melt [m] (.34 in dia --
> .4318cm radius) *)
```

```

"Nozzle length/radius (needs to be > 1.5)"
l/Gamma

(* PART 1: NaF bottle effusion constant K calculations
*)
(*for l/Gamma > 1.5 use equation below, in Se source, l/Gamma=8,
in NaF source l/Gamma=16.7 *)
"Effusion constant"
k=(1+(.4*l)/Gamma)/(1+.95*l/Gamma+.15*(l/Gamma)^2) (* constant
related to flow regime *)

(* Net mass rate of evap from surface, P1 = effective
pressure above source *)
Fevap= 1/(4 R T ) (8 R T / pi M)^1/2 (Psat-P1) SAmelt*M ;
(* for flow regime with Kn=lambda/Gamma > 1 use eqt below: *)

Feff=pi Gamma^2 k (M/(2 pi R T))^1/2 (P1-P2); (* mass flow rate
through nozzle [g/sec?] *)
"Pressure inside bottle and effective evaporation rate
(kg/sec?)"
Solve[F==1/(4 R T ) (8 R T / pi M)^1/2 (Psat-P1) SAmelt*M
==pi Gamma^2 k (M/(2 pi R T))^1/2 (P1-P2), {P1, F}]

```

H.2 Substrate Temperature Uniformity

Composition, and therefore electronic properties were found to be sensitive to growth temperature. Composition has an almost step-function change at critical temperatures of ~520°C for our depositions and therefore lower temperatures or strong temperature uniformity are required. The system was further modified so growth temperatures could be mapped and logged across the nine 1x1in substrates during growth. Improved uniformity and temperature control was investigated via modified substrate holders and the addition of heat-spreaders. Improved uniformities were ultimately achieved.

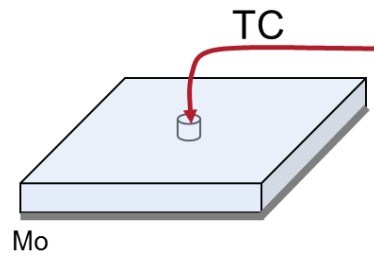


Figure H-3: Depiction of thermocouple position for measuring substrate temperatures.

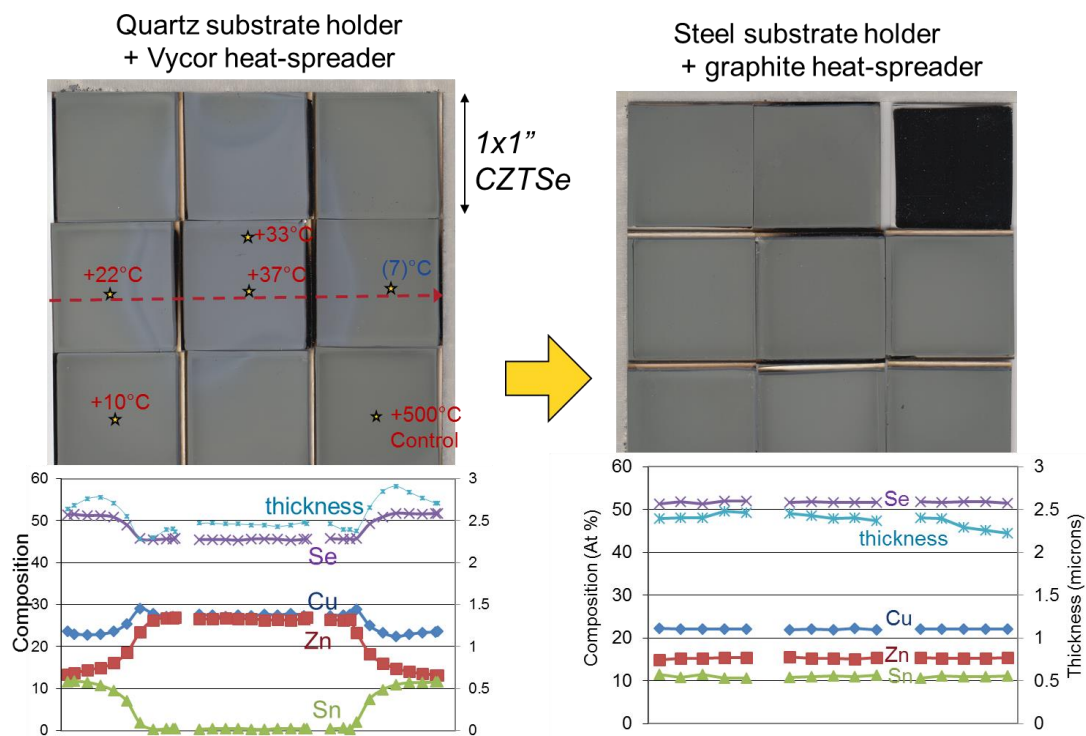


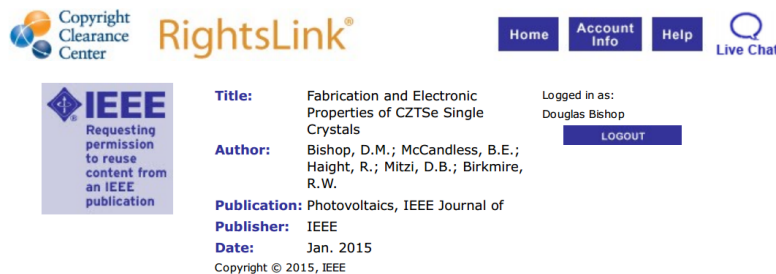
Figure H-4: Temperature uniformity mapped across thin film substrates and resulting composition. Worst case; quartz substrate holder, and best case: metal substrate holder + graphite heat spreader.

Appendix I

PERMISSION, COPYRIGHT, AND REUSE

Small excerpts from Chapter 3 come from a published IEEE paper cited below. Permissions are granted by default for Thesis use. Sa

D. M. Bishop, B. E. McCandless, R. Haight, D. B. Mitzi, and R. W. Birkmire, "Fabrication and Electronic Properties of CZTSe Single Crystals," *IEEE J. Photovoltaics*, pp. 1–5, 2014.



Copyright Clearance Center RightsLink®

Home Account Info Help Live Chat

IEEE Requesting permission to reuse content from an IEEE publication

Title: Fabrication and Electronic Properties of CZTSe Single Crystals

Author: Bishop, D.M.; McCandless, B.E.; Haight, R.; Mitzi, D.B.; Birkmire, R.W.

Publication: Photovoltaics, IEEE Journal of

Publisher: IEEE

Date: Jan. 2015

Copyright © 2015, IEEE

Logged in as: Douglas Bishop

LOGOUT

Thesis / Dissertation Reuse

The IEEE does not require individuals working on a thesis to obtain a formal reuse license, however, you may print out this statement to be used as a permission grant:

Requirements to be followed when using any portion (e.g., figure, graph, table, or textual material) of an IEEE copyrighted paper in a thesis:

- 1) In the case of textual material (e.g., using short quotes or referring to the work within these papers) users must give full credit to the original source (author, paper, publication) followed by the IEEE copyright line © 2011 IEEE.
- 2) In the case of illustrations or tabular material, we require that the copyright line © [Year of original publication] IEEE appear prominently with each reprinted figure and/or table.
- 3) If a substantial portion of the original paper is to be used, and if you are not the senior author, also obtain the senior author's approval.

Requirements to be followed when using an entire IEEE copyrighted paper in a thesis:

- 1) The following IEEE copyright/ credit notice should be placed prominently in the references: © [year of original publication] IEEE. Reprinted, with permission, from [author names, paper title, IEEE publication title, and month/year of publication]
- 2) Only the accepted version of an IEEE copyrighted paper can be used when posting the paper or your thesis on-line.
- 3) In placing the thesis on the author's university website, please display the following message in a prominent place on the website: In reference to IEEE copyrighted material which is used with permission in this thesis, the IEEE does not endorse any of [university/educational entity's name goes here]'s products or services. Internal or personal use of this material is permitted. If interested in reprinting/republishing IEEE copyrighted material for advertising or promotional purposes or for creating new collective works for resale or redistribution, please go to http://www.ieee.org/publications_standards/publications/rights/rights_link.html to learn how to obtain a License from RightsLink.

If applicable, University Microfilms and/or ProQuest Library, or the Archives of Canada may supply single copies of the dissertation.

BACK

CLOSE WINDOW

Copyright © 2016 Copyright Clearance Center, Inc. All Rights Reserved. [Privacy statement](#). [Terms and Conditions](#).
Comments? We would like to hear from you. E-mail us at customer-care@copyright.com

Chapter 5 is mainly reprinted from a publication in MRS Proceedings. The permission is given below.

D. M. Bishop, B. E. McCandless, T. C. Mangan, K. Dobson, and R. Birkmire, "Effects of Growth Conditions on Secondary Phases in CZTSe Thin Films Deposited by Co-evaporation," *MRS Proc.*, vol. 1538, no. 1, pp. 75–82, Jan. 2013.

**CAMBRIDGE UNIVERSITY PRESS LICENSE
TERMS AND CONDITIONS**

Feb 11, 2016

This Agreement between Douglas M Bishop ("You") and Cambridge University Press ("Cambridge University Press") consists of your license details and the terms and conditions provided by Cambridge University Press and Copyright Clearance Center.

License Number	3806080065890
License date	Feb 11, 2016
Licensed Content Publisher	Cambridge University Press
Licensed Content Publication	MRS Online Proceedings Library
Licensed Content Title	Effects of Growth Conditions on Secondary Phases in CZTSe Thin Films Deposited by Co-evaporation
Licensed Content Author	Douglas M. Bishop, Brian E. McCandless, Thomas C. Mangan, Kevin Dobson and Robert Birkmire
Licensed Content Date	Aug 28, 2013
Licensed Content Volume Number	1538
Licensed Content Issue Number	-1
Start page	75
End page	82
Type of Use	Dissertation/Thesis
Requestor type	Author
Portion	Full article
Author of this Cambridge University Press article	Yes
Author / editor of the new work	Yes
Order reference number	None
Territory for reuse	World
Title of your thesis / dissertation	Fabrication and Modification of Defects in Cu ₂ ZnSnSe ₄ Single Crystals and Thin Films
Expected completion date	Feb 2016
Estimated size(pages)	252
Billing Type	Invoice
Billing Address	Douglas M Bishop 27 Beckett Way

Requestor Location	Douglas M Bishop 27 Beckett Way ITHACA, NY 14850 United States Attn: Douglas M Bishop
Billing Type	Invoice
Billing Address	Douglas M Bishop 27 Beckett Way ITHACA, NY 14850 United States Attn: Douglas M Bishop
Total	0.00 USD
Terms and Conditions	

TERMS & CONDITIONS

Cambridge University Press grants the Licensee permission on a non-exclusive non-transferable basis to reproduce, make available or otherwise use the Licensed content 'Content' in the named territory 'Territory' for the purpose listed 'the Use' on Page 1 of this Agreement subject to the following terms and conditions.

1. The License is limited to the permission granted and the Content detailed herein and does not extend to any other permission or content.
2. Cambridge gives no warranty or indemnity in respect of any third-party copyright material included in the Content, for which the Licensee should seek separate permission clearance.
3. The integrity of the Content must be ensured.
4. The License does extend to any edition published specifically for the use of handicapped or reading-impaired individuals.
5. The Licensee shall provide a prominent acknowledgement in the following format:
author/s, title of article, name of journal, volume number, issue number, page references, , reproduced with permission.